UNIVERSIDADE FEDERAL DO RIO GRANDE DO SUL
ESCOLA DE ENGENHARIA
PROGRAMA DE PÓS-GRADUAÇÃO EM ENGENHARIA ELÉTRICA

LUCAS ARAUJO DA COSTA

DEEPER ANALYSES OF FAULT LOCATION ON ELECTRIC POWER SYSTEMS THROUGH THE METHOD OF ELECTROMAGNETIC TIME REVERSAL

Porto Alegre
2023

LUCAS ARAUJO DA COSTA

DEEPER ANALYSES OF FAULT LOCATION ON ELECTRIC POWER SYSTEMS THROUGH THE METHOD OF ELECTROMAGNETIC TIME REVERSAL

Thesis presented to Programa de Pós-Graduação em Engenharia Elétrica of Universidade Federal do Rio Grande do Sul in partial fulfillment of the requirements for the degree of Doctor in Electrical Engineering.
Area: Energy

ADVISOR: Prof. Dr. Daniel da Silva Gazzana

CO-ADVISOR: Prof. Dr. Roberto Chouhy Leborgne

Porto Alegre
2023

LUCAS ARAUJO DA COSTA

DEEPER ANALYSES OF FAULT LOCATION ON ELECTRIC POWER SYSTEMS THROUGH THE METHOD OF ELECTROMAGNETIC TIME REVERSAL

This thesis was considered adequate for the awarding of the degree of Doctor in Electrical Engineering and approved in its final form by the Advisor and the Examination Committee.

Advisor: _____
Prof. Dr. Daniel da Silva Gazzana, UFRGS
Doctor by Universidade Federal do Rio Grande do Sul – Porto Alegre, Brazil

Examination Committee:

Prof. Dr. Ana Vukovic, GGIEMR - The University of Nottingham
Doctor by the University of Nottingham – Nottingham, United Kingdom

Prof. Dr. Felipe Vigolvino Lopes, DEE - UFPB
Doctor by the Universidade Federal de Campina Grande – Campina Grande, Brazil

Prof. Dr. Mariana Resener, PPGEE - UFRGS
Doctor by the Universidade Federal do Rio Grande do Sul – Porto Alegre, Brazil

Coordinator of PPGEE: _____
Prof. Dr. Luis Fernando Alves Pereira

Porto Alegre, June 2023.

DEDICATION

To my mother, father, brother, and sister...

ACKNOWLEDGEMENTS

To God for providing everything and leading me to the end of my doctorate course.
To my family, friends, and colleagues at work and at GMASP for their support.
To Professors Daniel and Roberto for their supervision during all the years of research.
To PPGEE-UFRGS for offering my doctorate course.
To CAPES for the financial support of my research.
To Professor David Thomas for his supervision during the brief time in the UK.
To all at the GGIEMR for having me at the University of Nottingham.
To Mr Rob Gordon for kindly lodging me at his home in Nottingham.
To EMTP Alliance for granting the academic license of EMTP-RV (EMTP®).

ABSTRACT

Fault location has been the object of research in electric power engineering for many decades. A great number of methods have been developed so far, exploring features regarding measured electrical quantities. Most of the methods can be classified into three or four types concerning the way the fault locations are estimated. The research of other methods for fault-location estimation led to the application of the method so-called electromagnetic time reversal (EMTR). The EMTR method was developed and applied to different areas and types of problems before the studies on fault location. The method is based on the time-reversibility property of the equations of the electromagnetic waves in linear, non-dissipative, and time- and frequency-invariant media. Electrical power systems are linear media and can be considered time- and frequency-invariant within a window of time relatively short. The non-dissipative condition is not fulfilled once real power systems have losses. However, previous studies have shown that the EMTR-based fault-location method works even in the presence of losses. The fault-induced travelling waves form the electromagnetic transients (EMTs), whose signal, whether of electrical current or voltage, is taken for the time-reversal transformation. The method's application is divided into direct- and reversed-time stages. In the former, the signal is recorded, and in the latter, the fault location is estimated by a metric. The present thesis aims to continue the research on the application of the EMTR method on fault location in power systems. Deeper analyses are performed to extend the knowledge in the literature about the method's effectiveness and features that influence the method's behaviour. The method is first applied to a simple system through analytical formulations in the frequency domain, as presented in the previous works. Then, the method is evaluated on the same simple system in the time domain, using the numerical model in one software of simulations of electromagnetic transients. More complex time-domain study cases are considered through two more complex power systems after. The first is a dc transmission link, and the second is a power distribution network. Sophisticated models are used for the underground and overhead cables of the systems. Many fault simulations are performed, where the fault location and the fault resistance are varied. The cut-off frequency used to filter the fault-induced EMTs is changed, in addition to the duration of the signal's recording. The dependence of the performance of the method on these features is shown. The rela-

tion to the spectral content of the signal is observed. The distance of the fault to the point where the signals are recorded is the main feature that can hamper the correct estimation of the fault location. From the analyses, the overall conclusion is that the EMTR method has limited accuracy on fault location in conditions and systems like in the studies. The method could not correctly estimate the location of faults farther than around $30\ \mathrm{km}$ from one or two probes where the signals are recorded. More development of the method needs to be done for future applications in similar systems.

Keywords: Electric Power Distribution, Electromagnetic Time Reversal, Electromagnetic Transients, Fault Location, HVDC Transmission.

RESUMO

Localização de faltas tem sido objeto de pesquisa em engenharia de sistemas elétricos de potência por muitas décadas. Um grande número de métodos tem sido desenvolvido, explorando características relacionadas a grandezas elétricas medidas. A maioria dos métodos pode ser classificada em três ou quatro tipos, de acordo com a forma como a localização das faltas são estimadas. A pesquisa sobre outros métodos para estimar a localização de faltas levou à aplicação do método chamado de reversão do tempo eletromagnético (acrônimo *EMTR* em inglês). O método *EMTR* foi desenvolvido e aplicado à diferentes áreas e tipos de problemas antes dos estudos em localização de faltas. O método é baseado na propriedade de reversibilidade no tempo das equações de ondas eletromagnéticas em meios lineares, não dissipativos e invariantes no tempo e na frequência. Os sistemas elétricos de potência são meios lineares e podem ser considerados invariantes no tempo e na frequência dentro de uma janela de tempo relativamente curta. A condição não dissipativa não é satisfeita, uma vez que os sistemas de potência real tenham perdas. No entanto, estudos anteriores mostraram que a localização de falta através do método *EMTR* funciona mesmo na presença de perda. As ondas viajantes induzidas por falhas formam os transitórios eletromagnéticos (acrônimo *EMTs* em inglês), cujo sinal, seja de corrente elétrica ou tensão elétrica, é revertido no tempo. A aplicação do método é dividida em estágios de tempo direto e reverso. No primeiro, o sinal é registrado e, no segundo, a localização da falta é estimada por uma métrica. A presente tese visa dar continuidade à pesquisa sobre a aplicação do método *EMTR* na localização de faltas em sistemas de potência. Análises mais profundas são realizadas para ampliar o conhecimento na literatura sobre a eficácia do método e as características que influenciam seu comportamento. O método é primeiramente aplicado a um sistema simples através de formulações analíticas no domínio da frequência, conforme apresentado em trabalhos anteriores. Em seguida, o método é avaliado no mesmo sistema simples no domínio do tempo, utilizando o modelo numérico em um software de simulações de transitórios eletromagnéticos. Casos de estudo mais complexos no domínio do tempo são posteriormente considerados através de dois sistemas de potência mais complexos. O primeiro é um link de transmissão CC e o segundo é uma rede de distribuição de energia. Modelos sofisticados são usados para os cabos subterrâneos e aéreos dos sistemas. Muitas simulações de falta são realizadas, onde

a localização da falta e a resistência da falta são variadas. A frequência de corte usada para filtrar os *EMTs* induzidos pelas faltas é mudada, bem como a duração do registro do sinal. A dependência do desempenho do método nessas características é mostrada. A relação com o conteúdo espectral do sinal é observada. A distância da falta até o ponto onde os sinais são registrados é a principal característica que pode dificultar a estimativa correta da localização das faltas. A partir das análises, a conclusão geral é que o método *EMTR* tem exatidão limitada na localização de faltas em condições e sistemas como nos estudos. O método não pôde estimar corretamente a localização de faltas a mais de $30\ \mathrm{km}$ de um ou dois medidores onde os sinais são registrados. É necessário maior desenvolvimento do método para aplicações futuras em sistemas reais.

Palavras-chave: Distribuição de Energia Elétrica, Localização de Faltas, Reversão do Tempo Eletromagnético, Transitórios Eletromagnéticos, Transmissão CC.

LIST OF FIGURES

LIST OF TABLES

LIST OF ABBREVIATIONS

ACSR	Aluminium Cable Steel Reinforced
CP	Constant Parameter
DORT	Decomposition of the Time Reversal Operator
DT	Direct Time
EMT	Electromagnetic Transients
EMTP	Electromagnetic Transients Program
EMTR	Electromagnetic Time Reversal
FCSE	Fault-Current Signal Energy
FD	Frequency Dependent
FFT	Fast Fourier Transform
GFL	Guessed Fault Location
GPS	Global Positioning System
HP	High Pass
HVDC	High-Voltage Direct Current
MMC	Modular Multilevel Converter
MTDC	Multi-Terminal Direct Current
RT	Reversed Time
TR	Time Reversal
TR-MUSIC	Time-Reversal-Based Multiple Signal Classification
TW	Travelling Wave
ULM	Universal Line Model
VSC	Voltage Source Converter
WB	Wideband
XPLE	Cross-Linked Polyethylene

LIST OF SYMBOLS

ω	Angular Frequency
$\angle$	Argument of a Function or Variable
$\mathbf{C}$	Capacitance Matrix
$f(t), g(t)$	Continuous-Time Generic Functions
$s(t)$	Continuous-Time Signal (Generic), Specified by Index
$\bar{s}(\hat{t})$	Continuous-Time Signal (Generic), Specified by Index, Time-Reversed
$\mathbf{i}(x,t)$	Continuous-Time Vector of Line Currents
$\mathbf{v}(x,t)$	Continuous-Time Vector of Line Voltages
$i(x,k)$	Discrete-Time Current Signal, Specified by Index
$\mathcal{E}(x)$	Energy Function (Generic), Specified by Index
B_T	Frequency Bandwidth
$V_f(\omega)$	Frequency-Domain Fault-Source Signal
$G(\omega)$	Frequency-Domain Function (Generic)
Z	Frequency-Domain Impedance (Generic), Specified by Index
$V(x,\omega)$	Frequency-Domain Voltage Signal, Specified by Index
R	Frequency-Domain Resistance (Generic), Specified by Index
$\Delta\nu$	Frequency Step
$w(t)$	Hamming Window
$s_w(t)$	Hamming Window Modified
j	Imaginary Unit Number
$h(\boldsymbol{r},t)$	Impulse Response
est	Index of Estimated Fault Location(s)
f	Index of Fault Location(s)
g	Index of Guessed Fault Location(s)
m	Index of Measurement Point(s)
n	Index of Polynomial Order

k	Index of Sample(s)
$\mathbf{L}$	Inductance Matrix
$\sigma(x)$	Integral Function (Generic), Specified by Index
ℓ	Length
x	Linear Position or One-Dimensional Location Specified by Index
$\mathcal{P}(x)$	Maximum-Amplitude Function (Generic), Specified by Index
$\nu_{K,e}$	Minimum Sampling Frequency Required
N_g	Number of Guessed Fault Locations
N	Number of Polynomial Orders
K	Number of Samples
N_{cross}	Number of Times of Crossing
p	Type of Norm
T	Recording Duration
T_e	Residual Synchronisation Error
T_r	Rise Time
Δt	Sampling Time
T_0	Sampling Offset
$\mathcal{R}(x)$	Similarity Function (Generic), Specified by Index
$\sum$	Summation
$\boldsymbol{r}$	Space Coordination (Generic), Specified by Index
Δx	Spatial Accuracy or Step
$\rho(x)$	Spatially Normalised Correlation Function (Generic), Specified by Index
t	Time Variable or Time Instant when Specified by Index
$\hat{t}$	Time Variable Reversed
$H(x, \omega)$	Transfer Function (Generic), Specified by Index
V_o	Voltage Amplitude
$W(\omega)$	Weighting Function
C_W	Weighting Function Normalised

CONTENTS

1 INTRODUCTION

Distribution and transmission lines, substation buses, transformers, capacitor banks, or any other components of an electric power system are all susceptible to occasional short-circuit faults. They can be caused by the degradation of the material of the components of electric power systems over their life span, human, animal and flora contact with exposed system sections, adverse weathering conditions, like wind, rain, and lightning in a storm, and some others. Short-circuit faults can be sorted in different types and natures, regarding, e.g., the number of phases involved and its duration (WESTINGHOUSE ELECTRIC CORPORATION, 1964; SAHA; IZYKOWSKI; ROSOLOWSKI, 2010; SHORT, 2014).

In a generic definition, short-circuit faults are sudden and arbitrary changes in network topology (MAHSEREDJIAN; DINAVAHI; MARTINEZ, 2009), as switching phenomena. They generate, by themselves, abrupt changes and abnormal conditions in the electromagnetic quantities in an electric power system, such as voltages and currents. The fault inception induces a surge wave that travels throughout the system, being distorted along its propagation and reflecting and refracting at any network junctions (or discontinuities) (BEWLEY, 1931; WESTINGHOUSE ELECTRIC CORPORATION, 1964). From each reflection, another wave is produced and, from the sum of all the final travelling waves, the transient behaviour of the electromagnetic quantities is formed, shaped by the natural resonances that characterise the network state (WATSON; ARRILLAGA, 2003; BRANIN, 1967a,b; LEWIS, 1951; MIANO; MAFFUCCI, 2001; PAUL, 2007).

The entire electromagnetic response of an electric power system to a fault is, thereby, very complex and not fully understood, owing to the innumerable influential factors that act whilst the fault-induced electromagnetic waves propagate all over the network. The waveforms of voltages and currents present the transient aspect during the first milliseconds right after the onset of the fault, in which these quantities are highly composed of the switching-resulted, non-industrial, resonant frequencies (AMETANI *et al.*, 2016; SAHA; IZYKOWSKI; ROSOLOWSKI, 2010; SWIFT, 1979; WEDEPOHL; MOHAMED, 1969).

After the transient period of the fault, an under-fault steady state is reached. The fault

drives a high level of current flowing in the circuit path(s) from the system source(s) to the faulted point, which lasts until the fault is cleared (WESTINGHOUSE ELECTRIC CORPORATION, 1964). The protection system can clear the fault and re-close the distribution or transmission line (either only a single phase or all three phases), if the fault is temporary (considering the widespread use of re-closure devices). On the other hand, if the fault is permanent, the fault is cleared, but the re-closure of the distribution or transmission line fails, and the section of the distribution or transmission line remains de-energised (COMMITTEE, 1984; IEEE GUIDE FOR AUTOMATIC RECLOSING ON AC DISTRIBUTION AND TRANSMISSION LINES, 2022; SHORT, 2014).

In the latter case, it is necessary to locate the fault, either by visual inspection or automatically, and, with that, the subsequent action of the utility crew at the faulted point to carry out any required maintenance and remove the fault and, if it is possible, its cause. Still, in the former case, regardless of whether the fault is temporary, weak spots on the lines can also be pinpointed by an automatic fault location process, indicating those demanding further repair. As might be expected, an automatic process will typically expend less time on the location of the fault, for all the human tasks employed on finding out the system's faulted point will not be demanded (SAHA; IZYKOWSKI; ROSOLOWSKI, 2010).

An automatic fault location process is performed through fault-location algorithms. It is usually off-line (it is done "out of the system"), executed through analyses of the waveform records of voltages and/or currents, in contrast to distant protection relaying, which is on-line, done by equipment installed in the system. The algorithms implement any of the many existent methods developed over the years for general or specific applications on systems of different topologies and voltage levels[1]. Classifications of the fault location methods in power systems have sorted them into two, three or four classes[2], according to the type of analysis carried on upon the waveforms, and the necessity of additional information, previous waveform data or knowledge of the system network (SAHA; IZYKOWSKI; ROSOLOWSKI, 2010).

Exploring one of these methods, which is based on the concept of time-reversibility of electromagnetic waves to locate the source of the disturbance from which the waves

[1]Fault location is not an exclusive concept of power system operation. The procedure is also performed on signal and telecommunication transmission networks. However, only research on fault location in power system is considered herein.

[2]The classification into four classes is done, e.g., by (SAHA; IZYKOWSKI; ROSOLOWSKI, 2010) as *apparent-impedance-based* methods, *travelling-wave-based* methods, *high-frequency-based* methods and *knowledge-based* methods, while the classification into two classes, e.g., by (FURSE *et al.*, 2021) as *apparent-impedance-based* methods and *travelling-wave-based methods*, not referring to the *knowledge-based* methods. The *apparent-impedance-based* methods have the denomination of *phasor-based* methods in these works. The classification into two and three classes considers high-frequency-based methods as another type of travelling-wave-based. The latter classification is used in this work and will be commented on in the next chapter.

derived, the so-called Electromagnetic Time Reversal (EMTR), is the aim of the present work. The EMTR method, as it will be better introduced, works with the signature of the fault-induced electromagnetic transients (EMTs), exploring the resonances of the network under a fault through transient simulations in the time domain (ABBOUD, 2012; MANESH *et al.*, 2012; RAZZAGHI *et al.*, 2013a; RAZZAGHI, 2016; RACHIDI; RUBINSTEIN; PAOLONE, 2017; KAFAL *et al.*, 2019; WANG *et al.*, 2022). Works by Razzaghi et al. (2013a; 2017) and Wang et al. (2020a; 2020b), among others, have shown the application of the EMTR method with positive results upon measurement and simulated data, paving the way towards further analyses, on which the studies herein seek to follow.

1.1 Justification

Short-circuit faults are the origin of many issues related to the reliability and stability of electric power systems, affecting economically and operationally utilities and consumers (BOLLEN, 2000). Permanent faults might cause interruptions in power supply over large geographical areas. Loss of production and revenue, besides the inconvenience of the lack of electricity, are yielded. Hence, their typical severe consequences justify the concerns that lead to adopting corrective actions following their occurrence. This is the importance of the fault location, and why fault location procedures are implemented in many real power systems, through any existing methods. Fast and accurate fault location renders reliability and enhances the stability of an electric power system, reducing the duration of outages.

Although the variety of methods and the respective literature on fault location are considerably extensive, the necessity of developing new methodologies still stands to address the weakness of the existing ones and achieve higher accuracy in specific applications. One of the known challenges faced by most current fault location methods, e.g., concerns the effective application in branched networks, the characteristic topology of electric power distribution systems. Moreover, electric power systems in dc operation push the improvement on fault location methods since an entire class of existing methods is not able to be applied to dc systems, regardless of whether it is in ac ones, and also the increasing number of dc installations.

As far as it has been presented, the EMTR fault-location method is suitable to be applied in all types of electric power systems, as inhomogeneous and radially built, as well as in dc networks (RAZZAGHI, 2016; RAZZAGHI *et al.*, 2013a, 2014, 2017; RAZZAGHI; RACHIDI; PAOLONE, 2017). The robustness of the EMTR method, according to previous works, is a key feature motivating the continuity of the related research. Despite the success presented, its application considering more complex systems and conditions hindering the fault location process has not been extensively conducted in the literature up

to now. Numerous parameters regarding real components of electric power systems, their correspondent numerical modelling, and the recording and processing of the signal of the fault-induced EMTs might have a strong impact on fault location through the EMTR method, which has not been completely evaluated in previous research. Therefore, the present work seeks to expand the research towards a better understanding of the capabilities and limitations of this method. Once the trends regarding fault location in the last years often fall in research concerning distribution and dc operated systems, the studies of the present work are built by application of the method to these systems, thus taking a developing method to open problems on fault location research.

1.2 Objectives and Contributions

This work constitutes deeper analyses of the EMTR method applied to fault location in electric power systems from a critical perspective of its effectiveness and suitability. It objectives to assess the dependence of the performance of the EMTR-based fault-location method on some underlying features of its application, for a better understanding of characteristics, strengths, and weaknesses of the method itself and ways to improve its implementation somehow. Likewise, recognise situations where its application will not be recommended at all, given results showing poor performance or inaccuracy in which improvements may be impracticable. A new method requires prior investigation of its merits to ensure its utilisation is reasonable, meaning that satisfactory results will be achieved. This is what is desired with the present thesis on the EMTR fault-location method, advancing in some analyses, however certainly without exploring all possibilities of research.

The whole assessment is carried out through numerical simulations, which enable several fault cases to gather data for many different analyses. These analyses are regarding the systems' topologies, the characteristic of the lines or cables of their networks, the numerical modelling of the systems, the fault location, type and impedance, and the acquisition and filtering of the signal of the fault-induced EMTs, to have the sought wide perspective of the method's behaviour. The results of the application of the method are evaluated for each case considered, and so are the characteristics of the fault-induced EMTs that might be associated with the method's performance.

The contribution of this study to the current literature on the fault-location EMTR-based method is exactly the extensive analysis of the method's sensitives throughout time-domain simulations, in a manner yet not presented in related works so far. The simulations are performed on numerical models of a high-voltage dc (HVDC) transmission system and an electric power distribution system, covering different fault impedances, aiming to take conclusions from cases where fault location research is ongoing. The results, discussion and conclusions of this work might lead to the development of different forms of evaluation of the fault location by the EMTR method or even alternative techniques

based on the EMTR approach. A list of contributions follows:

i) the strong dependence of the EMTR method on the distance from the fault to the point where the signal of the fault-induced EMTs is recorded in a single-end approach is shown: the fault location might not be correctly estimated for longer distances than, e.g., $30\ \mathrm{km}$;

ii) the dependence of the EMTR method on the number of ends of the system where the signal is recorded is shown: the double-end approach of the EMTR method can have higher performance for faults at long distances and correct the drawback referred in (i), however still presenting shortcomings related to faults at some locations;

iii) the dependence of the EMTR method on the fault resistance is shown: the higher the fault resistance, the worse the fault location estimation tends to be in some of the cases studied;

iv) the dependence of the EMTR method on the fault type is shown: the fault location estimation tends to be worse for asymmetric ground faults for some types of systems;

v) the strong dependence of the EMTR method on the spectra content of the signal of the fault-induced EMTs is shown, which is related to the fault distance (i), the fault resistance (iii), and the fault type (iv) in addition to the system topology and parameters of its components: the latter two characteristics define the equivalent system impedance to the fault point and the behaviour of this impedance before high-frequency EMTs.

1.3 Overview

The present thesis is structured into six chapters. Chapter 2 contextualises the research on fault location, describing the classes of current methods, and brings a brief theoretical review of the EMTR method, whilst Chapter 3 presents more deeply the state-of-the-art of the EMTR-based fault-location method, attempting to sort and comment on reference works in the literature on the subject. The detailing of the methodology applied throughout the thesis studies, as the EMTR-method algorithm used in the study cases and which kind of evaluations are performed and how they are done, is described in Chapter 4. The study cases considered in the thesis and the results from the implementation of the EMTR method are shown in Chapter 5, followed by the discussion about the behaviour and performance observed through them. Chapter 6 summarises the overall conclusions of the research on this thesis and points forward possible investigations and developments concerning fault location by the EMTR method. Appendixes A, B, C, D, and E bring more details about the numerical modelling and results related to Chapter 5 that were opted not

to show in that chapter for brevity. Finally, the publications related to this thesis are listed in Appendix F.

2 THEORETICAL BACKGROUND ON FAULT LOCATION AND THE EMTR METHOD

The present chapter briefly describes three classes of fault-location methods applied to electric power systems as found in the respective literature to present the field where the research of this thesis is developed. Fault location on electric power systems is an old issue and has been studied for decades, yielding a large number of publications, of which only a few are herein cited. Different methods have been developed and applied so far, and general classifications for them may be given regarding the form they work to estimate the fault location. Apparent-impedance-based, travelling-wave-based and knowledge-based methods are some likely classifications when a method is singly applied. Likewise, there are integrated approaches when two methods are combined, resulting in a sometimes more sophisticated and accurate way to localise faults (SAHA; IZYKOWSKI; ROSOLOWSKI, 2010).

Besides, this chapter contextualises the time reversal (TR) method citing the works that developed it through the years from the application to signal processing and acoustic waves up to the EMTR on fault location. The TR transformation on recording signals and the EMTR method and its relation and applicability to current and voltage propagation in transmission lines of electric power systems are thus introduced. This knowledge is the foundation of the EMTR-based fault-location method, the research in this thesis. Nonetheless, EMTR is not a method of fault location itself once its application covers different areas. Only one of those is the location of the source of signals. EMTR works specifically on electromagnetic waves, as the method's name suggests, whereas the more generic TR method extends to acoustic waves. The TR method actually started the source location implementation (RACHIDI; RUBINSTEIN; PAOLONE, 2017).

2.1 Fault Location Concepts and Methods

2.1.1 Apparent-Impedance-Based Methods

The proportional dependence of a line impedance with the line length leads to a relation between the recorded voltage and current signals during a fault occurrence with the

distance between the observation and the faulted points. Consequently, the apparent line impedance brings information about the fault position, which characterises the so-called apparent-impedance-based (or just impedance-based or phasor-based) methods. The estimation of the fault position by the knowledge of the apparent total impedance until the fault point is quite similar to the impedance relay functionality, although optimisation and numerical techniques are frequently combined on the methods solutions for less simplified modelling of the system (SAHA; IZYKOWSKI; ROSOLOWSKI, 2010).

Many algorithms work on an impedance-type calculation for the fault location process, some handling only the fundamental frequency component of the signals and others over an entire range of frequencies (ERIKSSON; SAHA; ROCKEFELLER, 1985; JIA; THOMAS; SUMNER, 2012; SALIM *et al.*, 2009; SALIM; SALIM; BRETAS, 2011; TAKAGI *et al.*, 1981, 1982a,b). Moreover, apparent-impedance-based methods can be implemented through single-, double- and multi-end observation points to record the voltage and current signals (SAHA; IZYKOWSKI; ROSOLOWSKI, 2010).

The existing algorithms for the single-end form do not present complexity in the implementation, yet the single-end approaches may be significantly limited in accuracy (ERIKSSON; SAHA; ROCKEFELLER, 1985; KAWADY; STENZEL, 2003; IZYKOWSKI; ROSOLOWSKI; SAHA, 2004).

The double- and multi-end forms, in turn, are much more sophisticated, as they manage information of signals from two or more positions in the system, generally reflecting higher accuracy. They can be synchronised or unsynchronised, regarding whether or not the measurements are obtained in the same instants. The synchronised applications might require additional apparatus through a Global Positioning System (GPS) signal, or similar, to time-stamp the measurements, but both synchronised and unsynchronised versions require communication systems (BRAHMA, 2005; FUNABASHI *et al.*, 2000; GIRGIS; HART; PETERSON, 1992; IZYKOWSKI *et al.*, 2011; NAGASAWA *et al.*, 1992; NOVOSEL *et al.*, 1996; TZIOUVARAS; ROBERTS; BENMOUYAL, 2001; ZAMORA *et al.*, 1996).

The straightforward understanding and relatively simple and less expensive implementation have encouraged the wide use of these methods in systems of all types since their development. They are the most direct approaches to the fault location process, although their accuracy suffers with the influence of many factors, like the fault resistance, line characteristics and source impedances, and can exhibit low performance when applied to networks with distributed generation or dc transmission (SAHA; IZYKOWSKI; ROSOLOWSKI, 2010).

Variations have been made to the algorithms to cope with limitations and disregard assumptions that decrease the accuracy in some applications, mainly on the numerical solution of the linear system of equations formed from the set of samples of the records (FILOMENA *et al.*, 2009; IURINIC *et al.*, 2016; FERRAZ *et al.*, 2016; RAMOS *et al.*,

2017; OROZCO-HENAO *et al.*, 2017, 2018; HERRERA-OROZCO *et al.*, 2017; NUNES *et al.*, 2019). Derived techniques where a switching-generated signal rather than the fault-originated one is used for the fault location have also been presented in the respective literature, thus classified as active methods in opposition to the passive ones (JIA; THOMAS; SUMNER, 2012, 2013a,b; CHRISTOPHER *et al.*, 2013).

2.1.2 Travelling-Wave-Based Methods

Travelling wave theory, once applied to voltages and currents along transmission lines is the basis for fault location algorithms working directly over the fault-induced transients. As earlier introduced, the EMTs generated by a fault observed at a point are an aggregation of all travelling waves arriving there, including the initial forward wave from the faulted point and all waves resulting from successive reflections onto the fault, network junctions, components and terminations and the observation point itself. The fault-generate EMTs enclose information about the fault location in different aspects, and the techniques developed so far vary among each other regarding the type of analysis, either looking at the time-domain behaviour of the signal or the spectral pattern (BO; WELLER; REDFERN, 1999; MAGNAGO; ABUR, 1998; SAHA; IZYKOWSKI; ROSOLOWSKI, 2010; SWIFT, 1979).

Concerning the analyses on the time domain, the approaches work on the time of arrival of the impinging waves onto one, two or multiple observation points, which have also been investigated in distance protection applications (CHRISTOPOULOS; THOMAS; WRIGHT, 1988; CROSSLEY; MCLAREN, 1983; JOHNS, 1980; MCLAREN; RAJENDRA, 1985a,b). Since the time of wave propagation between the faulted point to the record one is directly related to the fault position, knowing the wave propagation velocity, the arrival times can give the fault location information.

Single-end (one observation point) methods focus on estimating the time delay between the instant of arrival of two waves composing the fault-transient signal. The maximum value of the autocorrelation of the forward and backward waves originated by the fault and the reflections, or other timing techniques, enables this time delay to be measured, taking as reference the arrival time of the first pick of the wave (ANCELL; PAHALAWATHTHA, 1992, 1994; ANDO; SCHWEITZER; BAKER, 1985; BO *et al.*, 1996; BO; WELLER; REDFERN, 1999; LEWIS, 1951; LOPES *et al.*, 2015; MAGNAGO; ABUR, 1998; MCLAREN; RAJENDRA, 1985a,b; PAITHANKAR; SANT, 1985; RANJBAR; SHIRANI; FATHI, 1992; SHEHAB-ELDIN; MCLAREN, 1988; STYVAKTAKIS; BOLLEN; GU, 1999).

The two- and multi-ends (two- and multi-observation point) methods return the fault location through the time delay between the impinging waves onto them, with either an unsynchronised or synchronised time stamping. The synchronised methods generally used the GPS signal for the time-stamp reference, as the apparent-impedance-based meth-

ods (IBE; CORY, 1986; DEWE; SANKAR; ARRILLAGA, 1993; YU, 2010). The data exchange is also fundamental.

A classification into types A, B, C and D has been given to the fault locators implementing some of these approaches, according to whether they are single- or two-end and synchronised or unsynchronised. Moreover, there are approaches where the working signal to calculate the fault position is produced using a switching technique instead of the recorded signal of the fault-induced waves. In these cases, the EMT is indirectly associated with the fault, not originating from it, and the fault locator type has been classified as E.

Whatever approach is implemented, the timing is the key point. A filtering process to extract the EMTs from the fault-recorded signal is essential, and many filtering techniques have been used, such as the Fourier transform or the discrete wavelet decomposition, with different variations (SAHA; IZYKOWSKI; ROSOLOWSKI, 2010).

As the component frequencies of a fault-induced signal are a product of the propagation phenomena throughout the entire system, the fault location might else be estimated by analysing the high-frequency range of the signal spectrum. The resonant (or characteristic) frequencies of the signal are directly associated with the fault location, as a fault signature contained in the high-frequency transients. Their identification leads to the estimation of the fault position, and many techniques have been applied to it, such as continuous wavelet transform or spectrum estimation methods (STYVAKTAKIS; BOLLEN; GU, 1999; BORGHETTI *et al.*, 2006, 2008, 2010).

Not only can the fault location in distance terms be obtained from these analyses, but also the faulted section in a branched system, besides the detection and classification of the fault (SALIM *et al.*, 2008; GAZZANA *et al.*, 2014). The lengths of the possible propagation paths for the fault-originated wave, and, as a consequence, the location of the fault, is a function of the wave velocity and number of reflections due to the wave being back to the initial polarity while travelling, which generally comes of an approximation of the reflection coefficients at the faulted-, observation- and junction points by units, -1 and $+1$ (SWIFT, 1979; IURINIC; FERRAZ; BRETAS, 2013). Theoretical frequencies can be calculated and then compared with those estimated from the signal analyses.

Another technique for this class of fault-location methods analyses the overall pattern of the EMT fault-induced signal in time, through correlation between simulated and field-measured signals (AURANGZEB; CROSSLEY; GALE, 2000; FARSHAD; SADEH, 2013; DENG; LI; ZENG, 2018).

Therefore, regardless of also working on the travelling wave theory, all these methods examine in some way the high-frequency content of the fault-induced transients rather than the arrival times of impinging waves.

In general, the application of any travelling-wave method has shown high accuracy in locating the fault, for them are not sensitive to hindering factors affecting apparent-

impedance-based methods, such as fault type, resistance and inception angle, as well as the saturation of the current transformer, the uncertainty about the source parameters, the swing of generation and system load. Furthermore, this accuracy is commonly improved in the two-end approaches, thanks to the superior robustness against inaccuracy sources affecting the single-end forms.

Concerning the analyses on the signal spectrum, one of the drawbacks has been exactly the need for the correct selection of the filters to separate the high-frequency components, which may be specially tuned for a specific fault type or even formed through it, as the case of wavelet mother built from the signal of the fault-induced EMTs (BORGHETTI *et al.*, 2008).

Issues concerning practical applications with time-domain analyses are the need for high sampling frequency (or rate) and the common presence of noise on the recordings, in addition to an adequate recording window and accurate time tagging. In these, the greatest difficulty is likely concerning discerning the impinging waves, to recognise which one originated by the forward propagation from the fault, by reflection onto the fault or by reflection onto the junctions or the extremity of the line (BO; WELLER; REDFERN, 1999; SAHA; IZYKOWSKI; ROSOLOWSKI, 2010).

2.1.3 Other Methods: Knowledge-Based and Integrated Ones

Artificial intelligence has been applied to fault location through sets of data from simulations for training processes in some works. However, a high knowledge of the characteristics of the system is required for the emulation of all interesting possible faulted conditions. Other works have likewise used expert systems and fuzzy logic, which may be combined with neural network implementations (HSU *et al.*, 1991; KUAN; WARWICK, 1992; JÄRVENTAUSTA; VERHO; PARTANEN, 1994; MOMOH; DIAS; LAIRD, 1997; CHEN; MAUN, 2000; GRACIA; MAZON; ZAMORA, 2005).

Moreover, approaches that integrate apparent-impedance- and travelling-wave-based techniques have been presented in the literature (SALIM *et al.*, 2008; GAZZANA *et al.*, 2014). The combination of two classes of methods aims to explore the advantages of each one of them to have higher accuracy and improved fault-location procedures.

2.2 EMTR Concepts

The mathematical description of most physical laws reveals a symmetric character concerning time. In other words, these laws are invariant for the TR transformation represented by the substitution $t \rightarrow -t$, where t is the variable time. This procedure allows retracing a physical system[1] to its previous states in the future. This is the case for the laws represented by second-order differential equations on time (as the sign of

[1] By *physical system* is not meant *physical mean* herein.

time would not mathematically mean). However, it is likewise true for Maxwell's equations (ARTHUR, 2013), which do not have the second-order time-differential dependence (SNIEDER, 2002; POLJAK; NEKHOUL; DRISSI, 2015)[2].

The time-reversal invariance of a physical system is classified as either *time-invariance in the strict sense* or *time-invariance in the soft sense*, according to (RACHIDI; RUBINSTEIN; PAOLONE, 2017). Considering $f(t)$ as a solution for differential equations related to a physical quantity in a system. Additionally, considering that the function $g(t)$ in (1)

$$g(t) = f(-t + 2t^{'}) \tag{1}$$

is also a solution, where $t^{'}$ is the final time instant considered for the evolution of the physical quantity. The system is time-reversal invariant in the strict sense for the physical quantity if no changes are necessary for the related equations. Otherwise, if changes in the related equations are required, the system is time-reversal invariant in the soft sense for the physical quantity. Maxwell's equations are, e.g., TR invariant in the soft sense as defined, while there are other physical laws TR invariant in the strict sense (RACHIDI; RUBINSTEIN; PAOLONE, 2017).

Wave phenomenon is the type of physical system on which TR may be performed. TR works on the transduced signal from the waves, whether acoustic or electromagnetic. The wave field is recorded by a finite number of sensors (one or more). This step may be called *recording*, *direct-time* (DT) or *forward-propagation stage*, in reference to the recording, direct time or forward propagation of the waves, respectively. The TR transformation on the wave signal yields the time-reversed waves (the time-reversed signal). The same sensors retransmitted the time-reversed signal into the medium, which refocus to the source location of the wave field. At there, all TR waves add in phase and the TR field wave reaches its maximum amplitude. This step may be called *reconstruction*, *reversed-time* (RT) or *backward-propagation stage*, in reference to the reconstruction, reversed time or the backward propagation of the waves, respectively (RACHIDI; RUBINSTEIN; PAOLONE, 2017).

The method's performance is sensitive to the medium of the wave propagation. Inhomogeneous physical media, e.g., can allow higher focusing in the TR process than homogeneous media. The multiple reflections and the scattering of the waves are the cause of this. Yet there are more requirements for the observation of the TR invariance. Rigorously, the medium needs to be linear, non-dissipative (*lossless*) and time and frequency invariant for the definition of TR to be valid (FINK, 1992). These ensure that the wave field can propagate in DT or RT directions without variations other than magnitude. Indeed, the back propagation of the TR wave field is likely not exactly a reverse version of the DT propagation, even if no distortions occur. Focusing the time-reversed signal at

[2]The referred laws are those of classical mechanics, including the propagation of mechanic waves and fluids, classical electromagnetism, and quantum mechanics, when there is no dissipation (SNIEDER, 2002).

the source location in the RT stage is what denotes the TR technique.

A reflective target for incident waves can be seen as the "source" of a signal to the TR method. The TR process on the reflective waves from the target will focus right at the target location, maximising the waves' amplitude there (FINK, 1992). Thus, the method works for target localisation.

Unlike wave systems, TR does not practically work on dynamical systems, such as the movement of a particle. The sensitive to the initial conditions of these kind of physical systems makes them not to be TR invariant (RACHIDI; RUBINSTEIN; PAOLONE, 2017).

TR can be related to a matched filter in signal processing. This principle says that the signal $h(-t)$ is the input that maximises the output of a linear system with an impulse response $h(t)$. The convolution $h(t) * h(-t)$ gives the maximum response for $h(t)$ (FINK, 1992).

The TR process was first applied as a signal processing algorithm to cope with distortion in the transmission of images (BOGERT, 1957) and telephone signals (SCHREINER; FUNK; HOPNER, 1965) and for the development of digital filters (KORMYLO; JAIN, 1974). Further, it was demonstrated as a backward-propagation technique of acoustic waves (CASSEREAU; FINK, 1992; DERODE; TOURIN; FINK, 2000; DRAEGER; FINK, 1997; FINK, 1992, 1999; FINK *et al.*, 1989; WU; THOMAS; FINK, 1992) and then extended to electromagnetic ones (LEROSEY *et al.*, 2004; LIU *et al.*, 2005; DE ROSNY; LEROSEY; FINK, 2010; ZHAI *et al.*, 2010). It has become a technique to image reconstruction (KOSMAS; RAPPAPORT, 2005, 2006a,b), localisation of the source of electromagnetic waves in an environment (ALBERT; LIU; MORAN, 2005; LIU *et al.*, 2007; LIU; KROLIK; CARIN, 2007) and electromagnetic component design (FOREST; HOEFER, 1992; SORRENTINO; SO; HOEFER, 1991; SORRENTINO; ROSELLI; MEZZANOTTE, 1993)[3].

The translation in time by $2t^{'}$ in (1) formally exposes that the $g(t)$ follows $f(t)$ in time for a physical system. The TR of a continuous signal $s(t)$ returns exactly $s(-t)$. However, to maintain the causality is necessary to translate $s(-t)$ in time. A time delay equal to the length of the recording time window is added. Thus, for a recording window of length T, the causality is ensured after the TR transformation, yielding $s(T-t)$. This signal-processing operation can be realised either in the time or frequency domain, given the correspondence between the operations in both ones[4]: $s(-t) \leftrightarrow S^{*}(\omega)$ or $s(T-t) \leftrightarrow S^{*}(\omega)e^{j\omega T}$, where $S(\omega)$ is the Fourier transform of $s(t)$ and $S^{*}(\omega)$ the complex conjugate

[3]Better historical appointments about the TR applications and their details can be found in the literature, such as in (DYAB *et al.*, 2013; KAFAL *et al.*, 2019; RACHIDI; RUBINSTEIN; PAOLONE, 2017; RAZZAGHI, 2016; SCOTT, 2010).

[4]The signal reversal in the time domain is related to its complex conjugate in the frequency domain (OPPENHEIM; WILLSKY; YOUNG, 1983).

of $S(\omega)$ (FINK, 1992; RACHIDI; RUBINSTEIN; PAOLONE, 2017; RAZZAGHI, 2016).

The EMTR is based solely on the time reversibility of Maxwell's equations in a linear, isotropic, non-dissipative and time-invariant medium. Besides, the TR transformation requires a change in the sign of the magnetic field and current density to keep the equalities satisfied (JACKSON, 1998; LUGRIN *et al.*, 2014; POLJAK; NEKHOUL; DRISSI, 2015). That is the reason why the *in the soft sense* definition is applied to Maxwell's equations regarding time reversibility (RACHIDI; RUBINSTEIN; PAOLONE, 2017). The EMTR procedure should not be seen as a backward-propagation technique of waves but as a signal processing algorithm (DYAB *et al.*, 2013; POLJAK; NEKHOUL; DRISSI, 2015).

The propagation of voltages and currents on networks of electric power systems, being related to the TR property of Maxwell's equations, also can be submitted to the TR operation. That is strictly true when the system, formed by transmission lines and ground, is lossless (lossless transmission lines and perfectly conducting ground[5]). However, it has likewise been demonstrated to be in lossy cases (lossy transmission lines and/or resistive ground[6]) (LUGRIN *et al.*, 2015; RAZZAGHI *et al.*, 2017).

Those propagations along a lossless single-conductor transmission line are represented by the Telegrapher's equations (2) and (3) (RACHIDI; RUBINSTEIN; PAOLONE, 2017; BEWLEY, 1933)

$$\frac{\partial^2 v(x,t)}{\partial x^2} - L^{'}C^{'}\frac{\partial^2 v(x,t)}{\partial t^2} = 0, \tag{2}$$

$$\frac{\partial^2 i(x,t)}{\partial x^2} - L^{'}C^{'}\frac{\partial^2 i(x,t)}{\partial t^2} = 0, \tag{3}$$

where $v(x,t)$ and $i(x,t)$ are, respectively, the voltage and current at the spatial coordinate x along the line and time coordinate t and L and C are, respectively, the inductance and capacitance per unit of length of the line. The Telegrapher's equations have a form of wave equations and were derived from the conditions of very small signals on the line. It is a propagation modelled across only one dimension. The lossless single-conductor transmission is above a perfectly conducting ground that offers an earth return for the circuit. An equivalent is a lossless two-conductor transmission line, where the second conductor is the return (RACHIDI; RUBINSTEIN; PAOLONE, 2017).

Similarly, the voltage and current along a lossless multi-conductor transmission line are represented by (4) and (5), respectively, (RAZZAGHI *et al.*, 2013a)

$$\frac{\partial^2 \mathbf{v}(x,t)}{\partial x^2} - \mathbf{L}^{'}\mathbf{C}^{'}\frac{\partial^2 \mathbf{v}(x,t)}{\partial t^2} = \mathbf{0}, \tag{4}$$

$$\frac{\partial^2 \mathbf{i}(x,t)}{\partial x^2} - \mathbf{L}^{'}\mathbf{C}^{'}\frac{\partial^2 \mathbf{i}(x,t)}{\partial t^2} = \mathbf{0}, \tag{5}$$

[5]The impedance of the ground is added to the impedance of transmission lines to compute an external impedance of the circuit formed by them (MARTINEZ-VELASCO, 2010). So, one can also refer to this system condition only as given by lossless transmission lines.

[6]*Id.* lossy transmission lines.

where $\mathbf{v}(x,t)$ and $\mathbf{i}(x,t)$ are the vectors of line voltages and currents at the spatial and time coordinates x and t, respectively, and $\mathbf{L}$ and $\mathbf{C}$ are the inductance and capacitance matrices, respectively, per unit of length of the lines[7].

The TR transformation on (4) and (5) yields (6) and (7)

$$\frac{\partial^2 \mathbf{v}(x,-t)}{\partial x^2} - \mathbf{L}'\mathbf{C}'\frac{\partial^2 \mathbf{v}(x,-t)}{\partial t^2} = \mathbf{0}, \tag{6}$$

$$\frac{\partial^2 \mathbf{i}(x,-t)}{\partial x^2} - \mathbf{L}'\mathbf{C}'\frac{\partial^2 \mathbf{i}(x,-t)}{\partial t^2} = \mathbf{0}, \tag{7}$$

respectively. Both $\mathbf{v}(x,t)$ and $\mathbf{v}(x,-t)$ are possible solutions for (6), as well as both $\mathbf{i}(x,t)$ and $\mathbf{i}(x,-t)$ for (7). The applicability of the EMTR to locate the source of any EMTs on power systems, including fault-induced ones, is considered valid from the TR operation on (4) and (5) (RAZZAGHI *et al.*, 2013a).

The EMTR theory suggests that a back-injected signal from the fault-induced EMTs will have all its reflections added up in phase at the right fault position, which thereby would allow the fault location (RAZZAGHI, 2016). Not only the EMTR method utilises the principle of TR to fault location; other methods do the same, as the so-called Decomposition of the TR Operator (DORT in its French acronym, referring to *Décomposition de l'Opérateur de Retournement Temporel*) (ABBOUD, 2012; ABBOUD; COZZA; PICHON, 2013; KAFAL; COZZA; PICHON, 2016a) and TR-based Multiple Signal Classification (TR-MUSIC) (KAFAL; COZZA; PICHON, 2016b; KAFAL; COZZA, 2020). Nonetheless, the DORT and TR-MUSIC methods were applied to the location of soft faults in cable networks, as those of telecommunication ones. The state-of-the-art of the application of the EMTR method to power systems follows in the next chapter.

[7] L and C or $\mathbf{L}$ and $\mathbf{C}$ are functions of the type and the geometry of the conductor and the line itself (AMETANI *et al.*, 2016; MARTINEZ-VELASCO, 2010).

3 STATE-OF-THE-ART OF EMTR-BASED FAULT LOCATION TECHNIQUES

The investigation of the EMTR application on fault location in electric power systems started with the work of (MANESH *et al.*, 2012), and it was developed in (RAZZAGHI *et al.*, 2013a). These works presented the TR transformation and showed its application on a single-conductor lossless transmission line above a ground plane in the frequency domain. Two observation points were considered in (MANESH *et al.*, 2012) and two and also only one in (RAZZAGHI *et al.*, 2013a) to record the signal at line extremities. The recorded signals for a fault were time reversed and back injected into the system at the same points where they were measured, holding the same reflection coefficients there. The correct fault location could be found by evaluating the amplitude or the energy of the fault-current signal through faults at several guessed fault locations (GFLs). Amplitude was the criterion used in (MANESH *et al.*, 2012), whilst energy in (RAZZAGHI *et al.*, 2013a), named fault-current signal energy (FCSE). The GFL where the value of any of these criteria was maximum was the fault location estimated by the EMTR.

The fault location was correctly guessed in (MANESH *et al.*, 2012) in time-domain analyses on the single-conductor line. Otherwise, the simple analyses were performed in (RAZZAGHI *et al.*, 2013a) only in the frequency domain, where the correct estimation was observed for both two and one observation point cases.

The time-domain algorithm for EMTR using the FCSE metric was then presented in (RAZZAGHI *et al.*, 2013a) to be used with signals recorded in real field measurements or simulations, which was the same applied with the amplitude metric in (MANESH *et al.*, 2012). Generally speaking, after a fault incipience in any network location x_f, voltages and/or currents signals $s_m(t)$ are measured by observation points at the positions m. The recordings start at the instant of the detection of the fault at m, t_m, within a window of length $T = K\Delta t$, where K is the number of samples and Δt the sampling time. Each $s_m(t)$ admits the TR transformation, yielding $\bar{s}_m(\hat{t})$, defined for $\hat{t} \in [0, T]$, with $\hat{t} = (T + t_m) - t$. The signals $\bar{s}_m(\hat{t})$ are then back injected into a simulation model of the analysed power system , faults are simulated and a metric is applied.

Following this algorithm, the amplitude metric with the current signal, $\mathcal{P}_i(x_g)$, for the

set of GFLs, x_g, $g = 1, \cdots, N_g$, is computed by (8)

$$\mathcal{P}_i(x_g) = \max\{|i(x_g, k)|\}, \tag{8}$$

whilst the FCSE, $\mathcal{E}_i(x_g)$, by (9)

$$\mathcal{E}_i(x_g) = \sum_{k=1}^{K} i^2(x_g, k), \tag{9}$$

where k is the sample index and $i(x_g, k)$ is the current at a GFL x_g. The estimated fault location, x_{est}, is given by (10) through $\mathcal{P}_i(x_g)$

$$x_{est} = \arg|_{x_g} \max\{\mathcal{P}_i(x_g)\}, \tag{10}$$

and by (11) through $\mathcal{E}_i(x_g)$

$$x_{est} = \arg|_{x_g} \max\{\mathcal{E}_i(x_g)\}. \tag{11}$$

After the simple frequency-domain analyses, Razzaghi et al. (2013a) brought an experimental validation on a reduced-scale setup using real-time simulation. Single transmission-line and T-shape network configurations were built with coaxial cable. One observation point was used in the DT stage. An oscilloscope at a sampling frequency of $1\ \mathrm{GSamples/s}$ took the measurements of the fault-induced EMTs.

In the RT stage, the source injecting back the time-reversed signal is given by a waveform generator at the same sampling frequency of $1\ \mathrm{GSamples/s}$. This one was connected with a lumped resistance to model the behaviour of transformers to high-frequency EMTs. Besides, high impedances were connected to the line ends. The current at the GFLs was measured by a wideband current monitor with a bandwidth of $300\ \mathrm{Hz}$–$200\ \mathrm{MHz}$. The accuracy of the EMTR-based fault-location method was evidenced in this real application. The real fault location was correctly estimated.

Simulations were further conducted in EMTP-RV on an inhomogeneous network of overhead lines and coaxial cables and on a radial distribution network given by the IEEE 34-Bus Test Distribution Feeder (INSTITUTE OF ELECTRICAL AND ELECTRONIC ENGINEERS, 2010), using a single observation point.

For all simulated cases, the fault was correctly located, resulting in $x_{est} = x_f$. That was irrespectively the fault type (considered known due to the protection system action) and fault impedance. The method was able to locate faults in the presence of losses in the system. The lines had the resistive component in both experimental and simulation cases. That has been one indication of its high robustness, even though the time-reversibility is not defined in a lossy medium.

Nowadays, it is worth highlighting that just the case of faults within one section of the distribution system under study was analysed. The section was delimited by transformers

at the extremities, where there was just one branch off the main feeder. So, the location accuracy was evaluated neither over the whole network nor for a highly branched system. Whether the accuracy would be influenced in the presence of noise was another feature not covered.

The same algorithm was used in (RAZZAGHI *et al.*, 2013b) to locate faults on a series-compensated transmission line. Three-phase-to-ground, double-phase-to-ground and single-phase-to-ground faults at three different positions and with two resistance values were simulated in EMTP-RV. A single measurement was used. In all cases, the correct location was successfully estimated.

Razzaghi et al. (2014) either used the same algorithm for faults in a multi-terminal dc (MTDC) network. The method correctly located pole-to-pole and pole-to-ground faults, solid or with resistance, at three different lines. Moreover, the influence of the window length of the recording signal was evaluated for the pole-to-ground fault. Window lengths of 3, 4, 5, 7, and 180 ms were applied. The window length did not have a relevant influence on the method's accuracy.

The application on a lossy medium was more deeply studied in (LUGRIN *et al.*, 2015) and further extended in (RAZZAGHI *et al.*, 2017), and the problem of the non-time-reversibility of the wave equations in the presence of losses was exposed. The fault was computed on a lossy system in the DT stage, whilst three back-propagation models[1] were considered in the RT stage, a lossless, a lossy and an inverted-loss one. Concerning the location accuracy, on both lossy and inverted-loss modelling of the system, the EMTR procedure returned the correct position of the fault; however, the fault was not correctly located with the lossless back-propagation model.

Razzaghi et al. (2017) performed simulations of three types of faults on an inhomogeneous network and a radial three-phase network using EMTP-RV, neglecting either the conductors or ground losses in the back-propagation model. The results showed that neglecting the ground losses affects the accuracy of the fault location when the fault has the ground mode and it is worsened in higher-resistivity soils. Experimental tests on a lossy line and in the presence of noise were further conducted, ascertaining the robustness of the EMTR procedure on applications like that.

Razzaghi, Rachidi and Paolone (2017) also showed the effectiveness of the EMTR method on MTDC and radial networks for many types of faults, including high-impedance ones. The real-time simulator platform implemented in (RAZZAGHI *et al.*, 2016) was applied, which is an inexpensive hardware-in-the-loop system based on a field-programmable gate array. A sampling frequency of 20 MSamples/s was used.

The faulty line in the MTDC network was assumed to be previously known by the fault location system. Therefore, the GFLs were evaluated only along the faulty line.

[1]The back-propagation model is the system model in the RT stage, which can be the same or different from the direct-propagation model, which is the model used in the DT stage.

Pole-to-pole and pole-to-ground faults without impedance and a pole-to-pole fault with impedance were simulated. The radial network is the same modelled in (RAZZAGHI *et al.*, 2017), representing a sub-transmission/distribution one. Three-phase, phase-to-phase, and phase-to-ground faults without impedance and a phase-to-phase fault with impedance were simulated. The knowledge of the faulty line was not considered for those cases, and GFLs along all lines were evaluated.

For the two types of networks, the fault locations were correctly estimated in almost all cases. Additionally, the method identified the faulty line in the radial network. These results may indicate and encourage a widespread utilisation of the method for fault location in any type of network.

One relevant contribution was derived in (CODINO *et al.*, 2017), where an alternative methodology based on the EMTR was presented to estimate the fault location. Instead of using a metric based on the FCSE, Codino et al. (2017) showed that the backward-propagation stage can be performed in just one simulation using an unmatched (or mismatched) back-propagation model to the direct-propagation one.

The back-propagation model does not have the transverse branch representing the fault. The fault location is estimated at the point along the line where the argument of the voltage in the frequency domain is bounded in $[-\frac{\pi}{2}, \frac{\pi}{2}]$. It stands on the fact that, since the network is a highly reflecting medium, the wave reflections on line terminals and junctions contribute altogether much more to the transient signal measured in the forward-propagation stage than the reflection on the fault itself. Thus, the presence of the fault in the backward-propagation stage is unnecessary to the fault location process, and the mismatch between the media of the two stages is admissible.

Codino et al. (2017) still introduced the concept of considering transfer functions to represent the system for the forward-propagation stage, the backward-propagation stage in the unmatched medium, and the whole TR process. In this case, for a fault source at the position x_f in the frequency domain, $V_f(\omega)$, the transfer function in relation to the voltage recorded in one extremity of a line, $V_m(x_f, \omega)$, is given by (12)

$$H_{DT}(x_f, \omega) = \frac{V_m(x_f, \omega)}{V_f(\omega)}, \tag{12}$$

on which the TR transformation yields (13)

$$H^*_{DT}(x_f, \omega) = \frac{V^*_m(x_f, \omega)}{V^*_f(\omega)}. \tag{13}$$

For the unmatched backward-propagation medium, $V^*_f(\omega)$ is applied and the voltage $V(x_g, \omega)$ is measured at the position x_g along the line, with the transfer function given by (14)

$$H_{RT}(x_g, \omega) = \frac{V(x_g, \omega)}{V^*_m(x_f, \omega)}. \tag{14}$$

Thereby, the transfer function for the whole TR process is given by (15)

$$H_{TR}(x_g, \omega) = \frac{V(x_g, \omega)}{V_f^*(\omega)} = H_{DT}^*(x_f, \omega) \cdot H_{RT}(x_g, \omega). \tag{15}$$

The property that establishes the identification of the fault location was demonstrated. That is related to the behaviour of the argument of $H_{TR}(x_g, \omega)$ in all frequencies for a given x_g. With the phase spectrum of $H_{TR}(x_g, \omega)$, according to (16)

$$\begin{aligned} &\text{if } x_g = x_f, \forall\, \omega, \angle H_{TR}(x_g, \omega) \in [-\frac{\pi}{2}, \frac{\pi}{2}], \\ &\text{c.c., } \forall\, x_g \neq x_f, \exists\, \omega : \angle H_{TR}(x_g, \omega) \notin [-\frac{\pi}{2}, \frac{\pi}{2}]. \end{aligned} \tag{16}$$

$x_{est} = x_g$ for the x_g where (16) is satisfied.

The accuracy of the fault location was observed to be intrinsically related to the sampling frequency of the signal (or the bandwidth of the sampling system) through the bounded-phase property. It indicates one criterion to determinate the sampling frequency for a desired accuracy. The minimum required sampling frequency, $\nu_{K,e}$, for a given accuracy $\Delta x_{est} = x_{est} - x_f$, for the estimated fault location, x_{est}, would be simply known by the minimum frequency where $\angle H_{TR}(x_{est}, \omega) \in [-\frac{\pi}{2}, \frac{\pi}{2}]$. In other words, $\nu_{K,e}$ is the minimum sampling frequency needed for any estimated fault location x_{est} to be distinguished from x_f by Δx_{est}. Therefore, the transfer function $H_{TR}(x_{est}, \omega)$ has a bounded phase behaviour at some conditions.

Yet, since the fault source is regarded as a step-like function, whose frequency-domain representation is $V_f(\omega) = \frac{1}{j\omega}$ for the frequency range of interest, the bounded-phase property is verified for $V(x_g, \omega)$ as for $H_{TR}(x_g, \omega)$. It happens just by adding an angle equal to $\frac{\pi}{2}$ to the limits in (16). Thus, the limited region of the argument of $\angle V_f(\omega)$ is $[0, \pi]$ at the right fault location.

The article showed fault location effectiveness from the applicability of the proposed theory on a single-phase inhomogeneous transmission line and a wye-shape inhomogeneous network. Nevertheless, Codino et al. (2017) did not consider more complex systems and did not work on results from experiments or with noise added.

Another alternative EMTR methodology to locate faults without the branch representing the fault in the back-propagation medium was found in (WANG *et al.*, 2017). Wang et al. (2017) used not the argument of the voltage along the line but the energy of the voltage signal as the metric in the evaluation. The fault location is estimated at the point along the line correspondent to the mirror image of the point where the voltage signal energy, $\mathcal{E}_v(x_g)$, is minimum, with reference to the line centre. That is the so-called "mirrored minimum energy" property, which gives x_{est} for a line of length ℓ, knowing the location $x_{g_{min}}$, correspondent to (17)

$$x_{est} = \ell - x_{g_{min}} = \ell - \min_{x_g} \{\mathcal{E}_v(x_g)\}. \tag{17}$$

The mirrored minimum energy property is naturally dependent on the transfer function representing the system since the energy $\mathcal{E}_v(x_g)$ is computed with it.

The results from simulations and experimental measurements showed the effectiveness of this metric on providing the right fault location on a single-phase system, even with a real lossy line. An evident drawback of the metric is that it was developed and only can be used on non-branched systems, so it was not applied to more complex cases.

A validation of the EMTR method to locate generic electromagnetic disturbances on a real overhead distribution line was presented through experiments in (WANG *et al.*, 2018a). A voltage pulse representing the transients originated by faults, lightning, and even conducted intentional electromagnetic interferences, was injected on a full-scale system. The metric FCSE was used to evaluate the disturbance location in the backward-propagation stage by simulations.

The results confirm the efficacy of the EMTR in locating electromagnetic disturbances on power-system overhead lines, including faults. The phase where the disturbance was injected was also identified. However, as the system used is composed of no branches, whether or not the EMTR application to a branched system would be able to reach the same performance observed in this article is open.

The metrics of the maximum amplitude and energy of the fault-current signal was analysed more deeply in (HE *et al.*, 2018). They are respectively derived from the ∞-norm and 2-norm, concepts which were largely employed in studies of electromagnetic pulse.

For a signal $s(t)$ in the time domain, with initial and final instants t_i and t_f, respectively, the p-norm is calculated with (18)

$$\|s(t)\|_{t,p}^{(t_i,t_f)} = \left\{ \int_{t_i}^{t_f} |s(t)|^p \, dt \right\}^{1/p}, \tag{18}$$

with $p = \infty$ for the ∞-norm and $p = 2$ for the 2-norm. They coincide, in a physical sense, respectively, to the absolute amplitude peak and the energy root. Therefore, the criteria used in (RAZZAGHI *et al.*, 2013a) and (MANESH *et al.*, 2012) are the square of the 2-norm and the ∞-norm themself, respectively.

In a rigorous formulation, for the ∞-norm, the fault location might be estimated by (19)

$$x_{est} = \arg|_{x_g} \max \left\{ \|i(x_g,t)\|_{t,\infty}^{(0,T)} \right\}, \tag{19}$$

using the fault current signal $i(x_g,t)$ at a GFL x_g in the backward-propagation stage. Analogously, for the 2-norm, the fault location is estimated by (20)

$$x_{est} = \arg|_{x_g} \max \left\{ \|i(x_g,t)\|_{t,2}^{(0,T)} \right\}. \tag{20}$$

The two metrics were tested in the study with a simulated fault on a lossless transmission line using EMTP-RV and the frequency-domain Baum-Liu-Tesche equation (BAUM

et al., 1977; PAUL, 2007). The accuracy of the fault location estimates and the great resemblance of the results from the two metrics were shown, which was proved by the feature selective validation (INSTITUTE OF ELECTRICAL AND ELECTRONIC ENGINEERS, 2021; ORLANDI *et al.*, 2006). Gaussian noise was added to the results from the Baum-Liu-Tesche simulations in the forward-propagation stage. The results observed using the two metrics in the backward-propagation stage could indicate a higher robustness of the ∞-norm in relation to the 2-norm in noisy conditions.

More Baum-Liu-Tesche simulations were made on a model of a lossy transmission line above a poor-conducting ground. Accuracy was lower the longer the line was considered, although the results still showed low fault location errors using both metrics. Results from two experimental sets were further presented, ratifying the EMTR method with both norms due to the accuracy observed. However, the simulated and experimental systems were simple, without branches and complex components (the case of distribution systems), which may represent a limited assessment.

The EMTR method was evaluated using the similarity property in (WANG *et al.*, 2018b). Wang et al. (2018b) showed that the current signal at the correct fault position during the backward-propagation stage is like the time-reversed signal injected into the system, but with a time delay equal to the wave-propagating time from this point to the measurement one in the forward-propagation stage. This property allows the fault location estimation based on the cross-correlation between the two signals.

The similarity between the applied time-reversed discrete signal, $\bar{i}_m(\hat{k})$ (which was considered to be a current one) and fault-current discrete signal $i(x_g, k)$ at the guessed positions x_g for the set of samples $k = 0, 1, \cdots, K$, is quantified by (21)

$$\mathcal{R}^m_{\bar{i}_m,i}(x_g, l) = \max\left\{\sum_{k=0}^{K} \underset{\max\left[\bar{i}_m(\hat{k})\right]}{\text{nor}} \left[\bar{i}_m(\hat{k})\right] \underset{\max\left[\bar{i}_m(\hat{k})\right]}{\text{nor}} \left[i(x_g, k-l)\right]\right\}, \quad l = 0, \pm1, \pm2, \cdots, \pm(K-1) \tag{21}$$

and the fault location estimated by (22)

$$x_{est} = \arg|_{x_g} \max\left\{\mathcal{R}^m_{\bar{i}_m,i}(x_g, l)\right\}. \tag{22}$$

The article showed the results of simulations on a single-conductor lossless transmission line and an inhomogeneous lossy three-phase network. The use of the similarity characteristic (21) between the signals was observed as one more option of metric for the EMTR method. However, it was not considered the influence of noise on the signals and its applicability to more complex networks.

Orlandi, Rachidi and Paolone (2018) analysed the methodology of (CODINO *et al.*, 2017) for the so-called soft faults, or, in a practical sense, faults with impedance. The fault impedance, Z_f, is resistive ($Z_f = R_f$), whereas in (CODINO *et al.*, 2017) it was considered just the case of a solid fault (or $Z_f = 0$). The capability of the EMTR method

to locate soft faults with different resistances was evaluated on three types of systems (including a microelectronic one). The evaluation is performed through both $\nu_{K,i}$ and the number of times when the argument of $H_{TR}(x, \omega)$ is off $[-\frac{\pi}{2}, \frac{\pi}{2}]$, represented in the article by N_{cross}. Nevertheless, the evaluation of generic complex fault impedances or in more complex systems is open.

After a review of the transfer function model of generic cases where the EMTR method can be applied, the concepts regarding it were explored in (CHEN *et al.*, 2019). At the correct fault location, the respective transfer functions to the direct- and back-propagation mediums are equal, shown as in (23)

$$H_{RT}(x_f, \omega) = H_{DT}(x_f, \omega). \tag{23}$$

Equation (23) is another way to evaluate the guessed fault positions.

The resemblance of (23) as the case of a matched filter was appointed. A consequence of (23) is that the resonance frequencies of $H_{DT}(x_f, \omega)$ and $H_{RT}(x_f, \omega)$ coincide at the matched condition. A mismatch between the back-propagation medium concerning the direct one corresponds to a translation of the resonance frequencies.

Chen et al. (2019) calculated the transfer functions for a single-conductor line for solid and resistive faults, being their resonance frequencies observed through an analytical closed form. Both the transient signal measured at the observation point and the characterisation signal[2] at the actual fault location show the same resonance frequencies. The evaluations were done on a simple system. So, an expansion to more complex ones is valuable.

Other experiments of fault location through the EMTR method were made in (WANG *et al.*, 2020a) for some types of faults in a real radial medium voltage distribution network in operation, composed of overhear lines, underground cables and lateral branches. The faults were intentionally applied on the system with zero and 30-Ω resistances and single and double arc discharge of two different lengths. For data acquisition and data processing, an EMTR-based fault location system was developed and built at only one observation point on the system, coupled with the operation of the relay. The fault location system ran simulations in EMTP-RV in the backward-propagation stage.

The experiment results showed an accuracy of about $250\ \mathrm{m}$ on on-line simulations of the backward-propagation stage and lower than $10\ \mathrm{m}$ on off-line ones, using the FCSE metric. This work is thus considerably important to establish the applicability of the EMTR method in real live distribution systems. Nonetheless, the sampling frequency used in the experiments is relatively high compared to the sampling frequency of the existing commercial fault locators. That is $20\ \mathrm{MSamples/s}$, against $1\ \mathrm{MSamples/s}$, the highest found[3] in (SCHWEITZER ENGINEERING LABORATORIES, 2019a). The

[2]Characterisation signal means the signal used in the back-propagation stage to locate the fault, as the voltage along the line or the fault current.

[3]This commercial fault locator uses the travelling-wave method.

high sampling frequency has also a correspondence with the time step of the backward-propagation simulations. A time step of 50 ns was used, a value significantly low for simulations of EMT caused by faults in electric power systems (pondering the length of the system).

The study presented in (HE; COZZA; XIE, 2020a) showed the EMTR method as a fault-location estimator through the correlation of signals. The article showed that the criteria using the energy or amplitude of the voltage at GFLs in the RT stage are subject to ambiguities. (The use of the energy or amplitude of the voltage instead of the current at GFLs is somewhat equivalent, provided that the fault impedance is not null.) The ambiguities of those criteria can lead to incorrect fault location.

The maximum amplitude of the voltage at a GFL is changed to consider just the maximum that occurs at $t = 0$, given in the frequency domain with (24)

$$\begin{aligned}\mathcal{P}_{v_{t=0}}(x_g) &= \int_{B_T} V_m^*(x_f,\omega) H_{RT}(x_g,\omega) d\omega \\ &= \int_{B_T} V_f^*(\omega) H_{DT}^*(x_f,\omega) H_{RT}(x_g,\omega) d\omega,\end{aligned} \tag{24}$$

where B_T is the bandwidth of $V_m(x_f,\omega)$.

Limiting the analyses around $t = 0$ allows the work with only the coherent part of the time-reversed signal. That is practically deterministic, whereas the remainder of the signal has a random nature, according to the authors. To compare to (24), the voltage at one GFL is expressed in the frequency domain by (25)

$$v_g(x_g,t) = \int_{B_T} V_m^*(x_f,\omega) H_{RT}(x_g,\omega) e^{j\omega t} d\omega. \tag{25}$$

The maximum value is taken among all GFLs.

An exponential charge in the transient was considered for the fault source at the position x_f in the time domain with (26)

$$v_f(t) = V_o\left(1 - e^{-t/T_r}\right), \tag{26}$$

where T_r is the rise time, and whose frequency domain form is given by (27)

$$V_f(\omega) = \frac{V_o/T_r}{j\omega\left(j\omega + 1/T_r\right)}. \tag{27}$$

Moreover, the fault resistance is in series with the fault source.

$\mathcal{P}_{v_{t=0}}(x_g)$ can be computed as the matrix product (28)

$$\begin{bmatrix} \mathcal{P}_{v_{t=0}}(x_1) \\ \vdots \\ \mathcal{P}_{v_{t=0}}(x_{N_g}) \end{bmatrix} = \Delta\nu \begin{bmatrix} H_{RT}(x_1,\omega) \\ \vdots \\ H_{RT}(x_{N_g},\omega) \end{bmatrix} \left[V_m^*(x_f,\omega)\right], \tag{28}$$

where Δf is the discrete step of the frequency. $\mathcal{P}_{v_{t=0}}(x_g)$ gives an estimation of the fault location without the need for RT simulations.

The study pointed out that $\mathcal{P}_{v_{t=0}}(x_g)$ is still subject to bias in the fault-location estimation, like the ∞- and 2-norms. So, another metric was proposed, given by (29)

$$\rho_{VH}(x_g) = \frac{\mathcal{P}_{v_{t=0}}(x_g)}{\sqrt{\mathcal{E}_m(x_f)\mathcal{E}_{RT}(x_g)}}, \tag{29}$$

where $\mathcal{E}_m(x_f)$ and $\mathcal{E}_{RT}(x_g)$ are energies of $V_m(x_f, \omega)$ and $H_{RT}(x_g, \omega)$.

$\rho_{VH}(x_g)$ is a correlation function. It does a local normalisation of $\mathcal{P}_{v_{t=0}}(x_g)$. The value of $\rho_{VH}(x_g)$ for any position is independent of $\mathscr{E}_{RT}(x_g)$ observed at other positions.

Another form presented for (29) is with (30)

$$\rho_{VH}(x_g) = \frac{\left\langle V_f^*(\omega) H_{DT}^*(x_f, \omega) H_{RT}(x_g, \omega) \right\rangle}{\sigma_m(x_f)\sigma_{RT}(x_g)}, \tag{30}$$

where it is used the operator in (31)

$$\langle G(\omega) \rangle = B_T^{-1} \int_{B_T} G(\omega)\, d\omega, \tag{31}$$

for the integral, and $\sigma_m(x_f)$ and $\sigma_{RT}(x_g)$ are given by (32) and (33), respectively

$$\sigma_m^2(x_f) = \left\langle |V_m(x_f, \omega)|^2 \right\rangle, \tag{32}$$

$$\sigma_{RT}^2(x_g) = \left\langle |H_{RT}(x_g, \omega)|^2 \right\rangle. \tag{33}$$

The authors still proposed another metric, $\rho_{VH}(x_g)$, mitigating the influence of $V_m(x_f, \omega)$, given in (34)

$$\rho_{HH}(x_g) = \frac{\langle H_{DT}^*(x_f, \omega) H_{RT}(x_g, \omega) \rangle}{\sigma_{DT}(x_f)\sigma_{RT}(x_g)}, \tag{34}$$

where $\sigma_{DT}(x_f)$ is given by (35)

$$\sigma_{DT}^2(x_f) = \left\langle |H_{DT}^*(x_f, \omega)|^2 \right\rangle. \tag{35}$$

However, as the information of $V_f(\omega)$ is not accessible in real applications, the knowledge of $H_{DT}(x_f, \omega)$ is not actually available. To cope with this, an estimator of $\rho_{HH}(x_g)$ was proposed with (36)

$$\hat{\rho}_{HH}(x_g) = \frac{\langle H_{DT}^*(x_f, \omega) H_{RT}(x_g, \omega) W(\omega) \rangle}{\sigma_{RT}(x_g)\sqrt{\left\langle |H_{DT}(x_f, \omega)|^2 |W(\omega)|^2 \right\rangle}}, \tag{36}$$

where $W(\omega)$, based on the source function (27), is given by (37)

$$W(\omega) = \frac{j2\pi f + 2\pi \hat{f}_c}{j2\pi f + 2\pi \nu_r} = \frac{j\omega/\nu_r + \hat{f}_c/\nu_r}{j\omega/\nu_r + 1}, \tag{37}$$

where ν is the linear frequency and $\nu_r = 1/2\pi T_r$.

The relation between $\rho_{HH}(x_g)$ and $\hat{\rho}_{HH}(x_g)$ is given in (38)

$$\hat{\rho}_{HH}(x_g) = \rho_{HH}(x_g) C_W, \tag{38}$$

with C_W in (39)

$$C_W = \langle W(\omega) \rangle \, / \sqrt{\left\langle |W(\omega)|^2 \right\rangle}. \tag{39}$$

An advantage of $\rho_{VH}(x_g)$, $\rho_{HH}(x_g)$, and $\hat{\rho}_{HH}(x_g)$ is the quantitative meaning. Their values might indicate whether a given GFL is a good guess. As closer to one is the value of any of these criteria for a given GFL, the closer to the correct fault location the GFL would be.

The study tested the criteria of the ∞- and 2-norms, $\mathcal{P}_{v_{t=0}}(x_g)$, $\rho_{VH}(x_g)$, and $\rho_{HH}(x_g)$ in three distribution networks. The data came from time-domain simulations in EMTP-RV. The three networks have three, five, and ten junctions, respectively, off the main line. All lines were modelled as lossless and single phases. The terminations of the networks were modelled as high resistances. The only source in the DT simulations was the fault one, given by (26). The signal in the DT stage was recorded at only one end. The GFLs were spaced by 1 km in all three cases.

Results compared the ∞-norm and $\mathcal{P}_{v_{t=0}}(x_g)$ criteria for a frequency range of 10 kHz to 1000 kHz in the frequency-domain calculations. The performance of $\mathcal{P}_{v_{t=0}}(x_g)$ was higher than the ∞-norm for the estimation of the fault location in all networks. Nonetheless, the overall accuracy was significantly low for the ten-junction network. Only 36% and 15% of all faults were accurately located by the $\mathcal{P}_{v_{t=0}}(x_g)$ and ∞-norm, respectively, in this case.

The criteria of the 2-norm, $\mathcal{P}_{v_{t=0}}(x_g)$, $\rho_{VH}(x_g)$, and $\rho_{HH}(x_g)$ were compared with frequency ranges of 10–100 kHz, 100–1000 kHz, and 10–1000 kHz. The bandwidth of 100–1000 kHz afforded the highest accuracy for any of the first three criteria. The lowest occurred for the range of 10–100 kHz. It evidenced the poor performance when considering low frequencies in the recorded signal. Furthermore, it showed the contribution of frequencies from 100 kHz to 1000 kHz to improve the estimation. The most affected metric by the frequency range was the 2-norm. $\rho_{HH}(x_g)$ showed no dependence on the bandwidth, however.

$\mathcal{P}_{v_{t=0}}(x_g)$ performed much better than the 2-norm, as it was against the ∞-norm. Only 18% of accuracy was observed with the 2-norm for the ten-junction network, while 94% with $\mathcal{P}_{v_{t=0}}(x_g)$ for the bandwidth of 100–1000 kHz. $\rho_{VH}(x_g)$ was more accurate in this case, returning 100%. In all cases, $\rho_{HH}(x_g)$ gave 100% of accuracy. That contrasted with the other criteria. For instance, accuracies of 8%, 36%, and 60% were observed for the 2-norm, $\mathcal{P}_{v_{t=0}}(x_g)$, and $\rho_{VH}(x_g)$, respectively, for the ten-junction network, with the range of 10–100 kHz.

The $\hat{\rho}_{HH}(x_g)$ metric was further tested on the five-junction network, considering different values for ν_r. $\hat{\rho}_{HH}(x_g)$ presented the same accuracy as $\rho_{HH}(x_g)$.

Finally, the study suggested that the non-uniform distribution of the intensity of the transfer functions in space is the cause of the bad performance of the 2-norm and $\mathcal{P}_{v_{t=0}}(x_g)$. It regards the location of the fault to that of the probe. The intensity lowered after a junction. So, the more junctions crossed, the lower the intensity of the transfer functions and bad the accuracy of those criteria.

He, Cozza, and Xie (2020b) presented studies on the spatial resolution of the EMTR method on fault location. The spatial resolution is the minimum spatial distance between the estimated fault location from the actual one that can be resolved by the method. The EMTR method was classified as a fault-location technique based on full-fault transients by the authors. Indeed, the article worked with a general methodology for these methods, for they share the same characteristic. The results and conclusions apply to EMTR so.

The correlation metric given in (40)

$$\rho_{VV}(x_g) = \left(\sqrt{\mathcal{E}_m(x_f)\mathcal{E}_m(x_g)}\right)^{-1} \int_T v_m(x_f,t)v_m(x_g,t)dt, \tag{40}$$

is used in the analyses. In (40), $v_m(x_f,t)$ is the voltage signal recorded at one place of the network for a fault event, $v_m(x_g,t)$ is the voltage signals recorded at the same place as $v_m(x_f,t)$ for faults at the GFLs, and $\mathcal{E}_m(x_f)$ and $\mathcal{E}_m(x_g)$ are the energies of $v_m(x_f,t)$ and $v_m(x_g,t)$, respectively. T is, again, the time interval of the recordings, equal for all. $v_m(x_g,t)$ can be previously recorded, e.g., through simulations, and stored. It would compose a dictionary of $v_m(x_g,t)$ for the GFLs.

In the frequency domain, $\rho_{VV}(x_g)$ can assume the form in (41)

$$\rho_{VV}(x_g) = \left(\sqrt{\mathcal{E}_m(x_f)\mathcal{E}_m(x_g)}\right)^{-1} \int_{B_T} |V_f(\omega)|^2 H^*_{DT}(x_f,\omega)H_{RT}(x_g,\omega)d\omega. \tag{41}$$

$\rho_{VV}(x_g)$ is distinct to $\rho_{VH}(x_g)$. Whilst the argument in the integral of the numerator of (29) is $V^*_f(\omega)H^*_{DT}(x_f,\omega)H_{RT}(x_g,\omega)$, in (41) is $|V_f(\omega)|^2 H^*_{DT}(x_f,\omega)H_{RT}(x_g,\omega)$.

The spatial resolution was related to the difference between fault-induced resonances induced by the actual fault and faults at the GFLs. Additionally, different resonances did not present the same spatial resolution. It stood the influence of the frequency range of the signals. The article showed that wide-band data does not necessarily lead to higher accuracy. If the system is resonating, the fault location might present super-resolution.

The super-resolution was observed on a single-phase and lossless line between two high resistances through the theoretical formulation developed. The fault was represented by (26), but only the flat part of the function spectrum was considered. The influence of frequency ranges covering only one or more fault resonances is shown. As observed in (HE; COZZA; XIE, 2020a) for the location accuracy, low frequencies hinder the spatial

resolution, i.e., of about $10\,\mathrm{kHz}$. Resonances of high degree gave higher spatial resolution. The theoretical results were validated with simulations in EMTP-RV.

Loss of spatial resolution happened when a lateral branch was added to the system. The lateral can influence in such a way that the fault is hard to be located. It occurred when the resonances related to the lateral were next to those of the branch ending with a fault. The lateral partially shunted the fault, and the resonances observed were less sensitive to the fault location. It is a destructive interference. The spatial resolution was evaluated in this case, changing also the values of the reflection coefficients of the terminations. The theoretical formulation was compared to results from simulations in EMTP-RV as in the previous case, with agreement.

The spatial resolution was obtained for a five-junction network with simulations in EMTP-RV. It was modelled with the same parameters as the single-line system. All lines were single-phase and lossless, with high resistances at terminations. The fault was given by (26) again. The results showed that more junctions do not strongly impact the spatial resolution. The loss of spatial resolution was similar to that of one lateral.

The study presented the spatial resolution for a single-phase-to-ground fault in a single three-phase line between two high impedances. The line was represented with the constant-parameter model. Line resistance and a lossy ground were considered, imposing propagation losses. Loss of sensibility to the fault location was observed for some resonances. It is due to interactions between the resonances associated with the two sections of the faulted phase and those from the phases not involved in the fault. The spatial resolution had similar behaviour as the one lateral case. Still, if the line length doubles, the loss in spatial resolution increases, given the propagation losses.

The work in (WANG *et al.*, 2020b) extended that one in (WANG *et al.*, 2018b). The correlation between the signals $\bar{i}_m(\hat{k})$ and $i(x_g, k)$ can likewise be seen as an autocorrelation between the impulse response of the system in the DT stage, as it was shown.

Considering a generic case of many measurement points, for a system with the impulse response $\boldsymbol{h}_{dt_m}((\boldsymbol{r}_0, \boldsymbol{r}_m), -t)$, the autocorrelation is given by $\boldsymbol{\mathcal{R}}_{hh}(\boldsymbol{r}_0, t)$ in (42)

$$\boldsymbol{\mathcal{R}}_{hh}(\boldsymbol{r}_0, t) = \sum_{m=1}^{M} \boldsymbol{h}_{dt_m}((\boldsymbol{r}_0, \boldsymbol{r}_m), -t) \otimes \boldsymbol{h}_{dt_m}((\boldsymbol{r}_0, \boldsymbol{r}_m), t). \tag{42}$$

where $\boldsymbol{r}_0$ and $\boldsymbol{r}_m$ are the space coordinates of the source and the point of measurement m belonging to the set of M measurement points at positions $\{\boldsymbol{r}_1, \cdots, \boldsymbol{r}_m, \cdots, \boldsymbol{r}_M\}$.

The mathematical proving that the current signal at the correct fault position in the backward-propagation stage is a time-delayed quasi-copy of the time-reversed signal applied into the system was further developed in the article, as commented in (WANG *et al.*, 2018b). Demonstrations for closed expressions of the measured voltage in the forward-propagation stage, the time-reversed voltage and the fault current in the backward-propagation stage were calculated for a single-conductor system, although the principles are valid for any.

The correlation $\mathcal{R}^{m}_{\widetilde{i}_m,i}(x_g,l)$ (the similarity metric) was considered in simulations of two types of faults on the IEEE 34-bus test distribution feeder in EMTP-RV. The fault location, impedance and inception angle were stochastic variables among a predefined set. Moreover, the methodology was used on experimental data[4].

Both simulation and experimental results confirmed the accuracy of the EMTR method on fault location and the applicability of the similarity metric, even in relatively difficult cases, such as near zero-crossing faults. The similarity metric may demand a lower computational cost, as indicated in the article, because the window length used in the correlation calculation is half of that used for the FCSE, as an example.

Cozza, He, and Xie (2021a) studied the advantages of filtering on the fault location accuracy of the EMTR method. The technique was treated as one based on full-fault transients, as in (HE; COZZA; XIE, 2020b). The study observed that the fault-induced surges reaching the probe end normally overlapped. Filtering low frequencies of the recorded signal gives surges with compressed duration (shorter time support). Hence, it decreases the overlapping. Filtering is as surge compression.

Using $\rho_{VV}(x_g)$ from (HE; COZZA; XIE, 2020b), the article showed how it improves the fault location. Differences between $v_m(x_f,t)$ and $v_m(x_g,t)$ from GFLs in the correlation are emphasised with the filtering.

The influence of the high-pass filtering was tested with a formulation based on a single-line system. The line was between the high resistance at the probe end representing the transformer and the low resistance of the fault. The fault is modelled by (26).

The recorded signal was given the form in (43)

$$v_m(x_f,t) = e^{-\alpha x_f}\sum_{n=0}^{\infty}\Gamma^n v_f\left(t-(n+1/2)\,T-T_0\right). \tag{43}$$

T is a propagation delay. T_0 is to model the sampling offset of the signal. $T_0\in[0,\Delta t]$. α is the attenuation constant of the line. Γ was called line transmissivity and is given in (44)

$$\Gamma = \Gamma_S\Gamma_T e^{-2\alpha x_f}, \tag{44}$$

where Γ_S and Γ_T are the reflectivity coefficients of the high and low resistances, respectively, at line ends. $v_m(x_f,t)$ was also given in its discrete form by (45)

$$v_m(x_f,k) = e^{-\alpha x_f}\sum_{n=0}^{\infty}\Gamma^n v_f\left(k\Delta t-(n+1/2)\,T-T_0\right). \tag{45}$$

Correspondingly, the discrete form of $\rho_{VV}(x_g)$ was given by (46)

$$\rho_{VV}(x_g) = \left(\sqrt{\mathcal{E}_m(x_f)\mathcal{E}_m(x_g)}\right)^{-1}\sum_{k=1}^{K} v_m(x_f,k)v_m(x_g,k)dt, \tag{46}$$

[4]The experimental data used in this work were the same in (WANG *et al.*, 2020a).

where $v_m(x_g, k)$ is the discrete version of the $v_m(x_g, t)$.

Three types of filters were applied. They all are based on the inverse of the z-transform of the exponential-step surge in (26). They were described by (47),

$$v_{m_{filt}}(x_f, k) = v_m(x_f, k) - \left(1 + e^{-\Delta t/T_r} v_m(x_f, k-1)\right) + e^{-\Delta t/T_r} v_m(x_f, k-2), \quad (47)$$

which came from the finite impulse response that results from the inverse of the z-transform, (48), and (49)

$$v_{m_{filt}}(x_f, k) = v_m(x_f, k) - v_m(x_f, k-1), \quad (48)$$

$$v_{m_{filt}}(x_f, k) = v_m(x_f, k) - 2v_m(x_f, k-1) + v_m(x_f, k-2), \quad (49)$$

through the first- and second-order derivative approximations of (47), respectively.

Filtering the signal with any of the three filters led to higher spatial resolution than when $v_m(x_f, k)$ was not filtered. The spatial resolution was likewise influenced by the sampling frequency for the filtered cases. That did not occur for the unfiltered case. For (48), the spatial resolution changed from 115 m to 87 m, when the sampling frequency increased from 200 kHz to 1 MHz. Applying (47) and (49), higher spatial resolutions were observed, as 40 m and 8 m for the same previous sampling rates, for the first one.

The influence of the fault distance to the probe end on the spatial resolution was either presented. The signal not filtered had spatial resolution two times higher for a fault at 5 km than for a fault at 10 km. The dependence on the fault distance was lowered when applying the filter from (48). Moreover, with the filter from (49), the fault distance almost did not affect the spatial resolution. Filtered signals are so less sensitive to the fault distance.

The spatial resolution for the filtered signal by (49) was observed to be less influenced by the line loss. The improvement was around twenty times against the case with a signal not filtered.

The study also treated the synchronisation of the signals $v_m(x_f, t)$ and $v_m(x_g, t)$ concerning the instants of their surge fronts. It is necessary to have both signals aligned, even if they are equal. The computation of $\rho_{VV}(x_g)$ is not computed correctly if the signals are not synchronised. If there is an offset between the signals, there is a loss of correlation. The effect of an offset on the correlation is worse for filtered signals since their time support is shorter. It causes inaccuracies in the fault location.

A new method of synchronisation was proposed in the article. The method is an alternative to the method of threshold triggering. It uses the estimation of the parameters related to the rising front of the surge from the fault. The threshold method gives the first instant when the signal magnitude is higher than a threshold. This instant is so used to align the signals. The threshold method is prone to errors when applied to noisy and discrete-time signals. Besides, it may give a residual synchronisation error, T_e, due to the sampling offset T_0.

The synchronisation by the surge parameter estimation fits a polynomial to the rising front of the surge transient. Least-square optimisation is used. Polynomial coefficients p_n of a Taylor series are obtained by (50)

$$v_f(t) = V_o\left(1 - e^{-(t-T_e)/T_r}\right) = \sum_{n=0}^{N} p_n t^n, \tag{50}$$

where T_e was added to (26). (50) estimates T_r, T_e, and V_o by (51), (52) and (53)

$$\hat{T}_r \simeq -\frac{p_1}{2p_2}, \tag{51}$$

$$\hat{T}_e^2 + \frac{p_1}{p_2} + \frac{p_0}{p_2} = 0, \tag{52}$$

$$\hat{V}_0 \simeq p_1 \hat{T}_r \left(1 + \frac{\hat{T}_e}{\hat{T}_r}\right)^{-1}. \tag{53}$$

$N = 3$ was chosen in the article.

After having T_e, the Whittaker-Shannon interpolation was done on $v_m(x_g, k)$ to re-sample it and to have $v_m(x_g, k\Delta t + T_e)$ with (54)

$$v_m(x_g, k\Delta t + T_e) = \sum_{l=0} v_m(x_g, k) s_w(k - l - T_e/\Delta t), \tag{54}$$

where $s_w(t) = w(t)sinc(\pi t)$. The Hamming window was chosen for $w(t)$. The number of samples determined the sum limit.

The article showed that the surge-front parameter estimation produces better synchronisation than the threshold triggering. The latter gave imprecise synchronisation of the filtered signals, even when identical. $\rho_{VV}(x_g)$ decreased by increasing the sampling offset when the threshold synchronisation was used. That was improved only by increasing the sampling frequency. However, the sampling offset influenced less the surge-based synchronisation. The spatial resolution was improved even at lower sampling rates.

The methodology was either applied to data from numerical simulations. A three-phase line between two high resistances was modelled in EMTP-RV. The constant-parameter model was used. The fault type and the fault resistance were changed through the simulations.

Results for single-phase-to-ground faults confirmed the improvement brought by the filtering. The spatial resolution was much improved with the filter from the second-order approximation. Otherwise, this improvement also tended to increase proportionally to the sampling frequency. Increasing the sampling frequency for unfiltered signals did not present improvement.

Beyond the phase signals directly recorded in the simulations, the synthetic signal in (55)

$$v_{0_{syn}}(t) = \left\{2v_{0_a}(t) - \left[1 - \sqrt{3}v_{0_b}(t) - (1 + \sqrt{3}v_{0_c}(t))\right]\right\}/3, \tag{55}$$

was used through the computation of $\rho_{VV}(x_g)$. $v_{0_{syn}}(t)$ is composed only by aerial modes. Removing the ground mode yielded higher spatial resolution for the same filtered signals by (49). A different behaviour was observed for the unfiltered signals, where $v_{0_{syn}}(t)$ led to worse results.

The fault location influenced less the results from filtered signals by (49). The spatial resolution was similar for farther and closer faults to the probe end. And this influence was lower using $v_{0_{syn}}(t)$.

Also, the location of single-phase-to-ground faults with high impedance, as $100\ \Omega$, $500\ \Omega$, and $1\ \mathrm{k}\Omega$, was improved using the filtered signals. With unfiltered signals, the location accuracy was much lower for the same high-impedance faults.

Furthermore, the resolution on the location of phase-to-phase and two-phase-to-ground faults was higher using filtered signals. While the accuracy obtained with unfiltered signals for phase-to-phase faults with $100\ \Omega$ was $1\ \mathrm{km}$, with filtered signals was around $26\ \mathrm{m}$, e.g.

Simulations changing T_r in $v_f(t)$ were performed to have cases where the fault surge has smoother transitions. Smoother transitions caused lower resolution using unfiltered signals. Filtered signals yielded resolution much less dependent on the rise time of the fault surge.

A deeper study about the influence of the propagation losses on the accuracy of the EMTR-based fault-location method was presented in (COZZA; HE; XIE, 2021b). The similarity of $v_m(x_f, t)$ and $v_m(x_g, t)$ as given by (56)

$$\mathcal{R}_{VV}(x_g) = \int_T v_m(x_f, t) v_m(x_g, t) dt, \tag{56}$$

and the correlation given by (40) were used to build the theoretical analyses. The fault was represented by (26), as in (HE; COZZA; XIE, 2020a) and (HE; COZZA; XIE, 2020b). Just the frequency range correspondent to its flat part was considered.

The ambiguity in the fault location under regimes of low and high propagation losses was analysed. This classification was given relative to the termination losses. If the propagation loss is negligible compared to termination losses, it is the low regime. Otherwise, if the propagation loss is dominant, it is the high regime. High losses on the propagation led to ambiguity on the fault location. This effect was higher using $\mathcal{P}(x_g)$. Still, even in the low propagation-loss regime, $\mathcal{P}(x_g)$ would present wrong estimations. (40) was much less influenced by the propagation loss, although. For low losses on the propagation, (40) is effective.

Considering only the flat part of the spectrum of (26) is an approximation. Since a model for fault is already used, the study also proposed to calculate the inverse-filter equalisation (57)

$$\hat{H}_{DT}(\omega) = \frac{V_m(x_f, \omega)}{V_f(\omega)}. \tag{57}$$

Then, to work with the similarity of the transfer functions in (58)

$$\mathcal{R}_{\hat{H}H}(x_g) = \int_{B_T} \hat{H}_{DT}(\omega) H_{RT}(x_g, \omega) d\omega, \tag{58}$$

and with the correlation in (59)

$$\rho_{\hat{H}H}(x_g) = \left(\sqrt{\mathcal{E}_{DT}(x_f)\mathcal{E}_{RT}(x_g)} \right)^{-1} \int_{B_T} \hat{H}_{DT}(\omega) H_{RT}(x_g, \omega) d\omega, \tag{59}$$

where $\mathcal{E}_{DT}(x_f)$ is the energy of $\hat{H}_{DT}(\omega)$. $\rho_{\hat{H}H}(x_g)$ is not equal to $\hat{\rho}_{HH}(x_g)$ given in (HE; COZZA; XIE, 2020a). He, Cozza, and Xie (2020a) did not perform an inverse-filter equalisation to have $\hat{H}_{DT}(\omega)$. An approximation of $V_f(\omega)$ by $\hat{V}_f(\omega)$ was done instead. Once $V_f(\omega)$ is unknown, the inverse-filter approach was not considered viable in that study.

Three cases of faults in a single-phase overhead line were analysed, changing the location. The frequency-domain formulation was used. The line model considers the frequency dependence of its parameters. Thus, propagation loss increases with frequency. The line end where $V_m(x_f, \omega)$ is taken terminates in high resistance. At the other end is the fault, with a resistance four orders lower. $\mathcal{R}_{VV}(x_g)$, $\rho_{VV}(x_g)$, $\mathcal{R}_{\hat{H}H}(x_g)$ and $\rho_{\hat{H}H}(x_g)$ were applied to the fault location estimation. The frequency range under analyses was changed. $\mathcal{R}_{\hat{H}H}(x_g)$ and $\rho_{\hat{H}H}(x_g)$ were considered with bandwidths from 1 kHz to 50 kHz and from 1 kHz to 500 kHz. $\mathcal{R}_{VV}(x_g)$ and $\rho_{VV}(x_g)$ with bandwidths from 1 kHz to 500 kHz and from 10 kHz to 500 kHz.

$\mathcal{R}_{\hat{H}H}(x_g)$ and $\rho_{\hat{H}H}(x_g)$ were not able to locate a fault at 0.5 km from the probe end of the line with the 1–50 kHz bandwidth. Yet, they both were with the 1–500 kHz bandwidth. However, similar improvement with larger bandwidth was not observed in all cases for $\mathcal{R}_{\hat{H}H}(x_g)$. $\mathcal{R}_{\hat{H}H}(x_g)$ located faults at 2 km and 16 km with the 1–50 kHz bandwidth, but did not when the bandwidth was increased to 1–500 kHz. $\rho_{\hat{H}H}(x_g)$ gave the right fault location for both latter locations and both bandwidths. $\mathcal{R}_{\hat{H}H}(x_g)$ was much impacted by the bandwidth increase. High-frequency resonances matched with those of some GFLs in the computation of (58) and fault locations other than the right one were estimated. This weakness of $\mathcal{R}_{\hat{H}H}(x_g)$ worsen for larger distances. Indeed, it could occur with the 1–50 kHz bandwidth for bigger distances.

Propagation losses damped resonances of high orders, and it is worsened for more distant locations. Thereby, a limit for improving the spatial resolution by increasing the sampling frequency was identified, related to one distance. Extending the frequency bandwidth did improve the fault location even for $\rho_{\hat{H}H}(x_g)$. High frequencies make propagation losses higher than termination losses.

$V_f(\omega)$ led to loss of accuracy when $\mathcal{R}_{VV}(x_g)$ and $\rho_{VV}(x_g)$ were applied. As also observed in (HE; COZZA; XIE, 2020a), $V_f(\omega)$ is dispersive. Its low-frequency content has an emphasis on its high-frequency one. It may cause estimation inaccuracies. $\mathcal{R}_{VV}(x_g)$

and $\rho_{VV}(x_g)$ only were able to locate the fault at $16\ \mathrm{km}$ with the bandwidth from 1 to 500 kHz. For the 1–500 kHz bandwidth, $\mathcal{R}_{VV}(x_g)$ located the fault at $2\ \mathrm{km}$, whereas $\rho_{VV}(x_g)$ at both $2\ \mathrm{km}$ and $16\ \mathrm{km}$. The advantage of the filter-equalisation to have $\hat{H}_{DT}(\omega)$ was observed, therefore. $\mathcal{R}_{\hat{H}H}(x_g)$ and $\rho_{\hat{H}H}(x_g)$ provided higher accuracy with the 1–50 kHz bandwidth, which means lower sampling frequency.

After, the study presented analyses on a single-phase-to-ground fault at a three-phase line. The line parameters were frequency dependent. Two high resistances were at its ends. The fault had a resistance four orders lower. The same analytical formulation used for the single-phase line was applied. Transformation to modal components was used, decomposing phase coordinates to aerial and ground modes. Aerial and ground modes interact with each other during reflections and refractions. The line presents resonances corresponding to all modes, to the sections of faulted phase (after and before the fault), and to the non-faulted phases.

$\mathcal{R}_{\hat{H}H}(x_g)$ and $\rho_{\hat{H}H}(x_g)$ were applied to estimate the fault location for distances of 2, 16 and $48\ \mathrm{km}$. Bandwidths of 1–50 kHz, 1–500 kHz, and 50–500 kHz were used. $\rho_{\hat{H}H}(x_g)$ rightly located the faults for all three bandwidths. $\mathcal{R}_{\hat{H}H}(x_g)$ located the faults at $2\ \mathrm{km}$ and $16\ \mathrm{km}$ with the bandwidth of 1–50 kHz, and just the fault at $2\ \mathrm{km}$ with 1–500 kHz. With 50–500 kHz, $\mathcal{R}_{\hat{H}H}(x_g)$ did not correctly estimate. The matching of resonances in (58) leads to a wrong location. Furthermore, it leads to an increase in propagation losses. Both were related to these inaccuracies for $\mathcal{R}_{\hat{H}H}(x_g)$.

Spatial resolution of $\rho_{\hat{H}H}(x_g)$ was higher filtering out the frequency content bellow 50 kHz (50–500 kHz bandwidth). Ground mode is stronger in low frequencies, therefore the improvement. Spatial resolution presented different behaviour, however, dependent on the bandwidth and the fault distance.

The applicability of the EMTR-based fault-location method for high-impedance faults was better studied in (AN *et al.*, 2021). A double-ended form of the mirrored-minimum-energy metric from (WANG *et al.*, 2017) is presented. To demonstrate the new technique, the analytical formulation brought by (ORLANDI; RACHIDI; PAOLONE, 2018) is shown to be wrong. So, other two are developed (equivalent to each other) upon a single-conductor transmission line above a ground plane. The validation of the new formulation has been conducted with simulations in EMTP-ATP, revealing much higher agreement in the results compared to the previous one.

The proposed metric was analytically evaluated against the FCSE and the original mirrored-minimum-energy metrics on locating faults of different impedances on the single-conductor system. It includes the value of $1000\ \Omega$, very high impedance considering faults on electric power systems. The accuracy of the technique was likewise compared to a synchronised double-ended travelling-wave location method based on the wavelet transform by simulations.

All results showed that the double-ended method is more reliable and accurate than

the other previous EMTR-based techniques, as well as the wavelet-transform-based one, in the case of faults with high impedance. Still, the new technique was less sensitive against synchronisation errors on the signal recording at both ends. Even so, the system used in the case studies in the article was rather simple, and the fault impedance was real. There was no corroboration of the method efficacy on more complex systems (as three-phase ones and with non-ideal terminations) and fault cases (as high-impedance faults with an imaginary part or non-linear behaviour). Besides, the mathematical proof of the mirrored-minimum-energy metric was not given, as it had not been in (WANG *et al.*, 2017).

4 METHODOLOGY

The methodology of this work is constituted by several analyses of the EMTR method applied to fault location. It follows the methodology presented in previous works (*cf.* Chapter 3) and expands it to bring potential and worthy contributions. The aim is to identify the response and evaluate the method's performance under different conditions for faults in electric power systems, attempting to implement what is presented in a part of the current research from another perspective, not to develop an alternative method. That can raise a deeper understanding of how EMTR works towards the fault location, highlighting the impact of some of the features involved in the fault location process through the method, what may worsen and what may enhance it, why that impact, and how to benefit from it.

The assessment looks at the influence of the parameters of the fault itself, the system where the fault location is carried out, the correspondent numerical modelling of the system, the signal processing involved, and the method's metric for fault-location estimation. Examples of investigations are the fault resistance, the characteristics of the lines and cables, the model used for them, the system topology, and the filtering process on the signal from the fault-induced EMTs. Such analyses neither cover all possibilities of fault occurrences in the life span of any real electric power system nor all kinds of available signal processing techniques. However, they come from a sensitive study, thought to bring relevant information about the application of the method.

The work is mainly based on data from time-domain numerical simulations of *shunt* faults on electric power systems modelled in an EMTP-type program, although analytical analyses corresponding to some found in the literature are first done. The simulations start from less complex analyses to more complex ones regarding the number of variables involved and the size and characteristics of the electric power systems of the study cases. That enables to have different levels of analyses and orderly progress between them. A flowchart of the methodology is in Figure 1.

Figure 1 presents the steps regarding the DT and RT simulations, TR transformation, and metric calculation. These are proper steps of some of the approaches of the EMTR method (RAZZAGHI *et al.*, 2013a; CODINO *et al.*, 2017; WANG *et al.*, 2017; HE *et al.*,

Figure 1 – Methodology's Flowchart

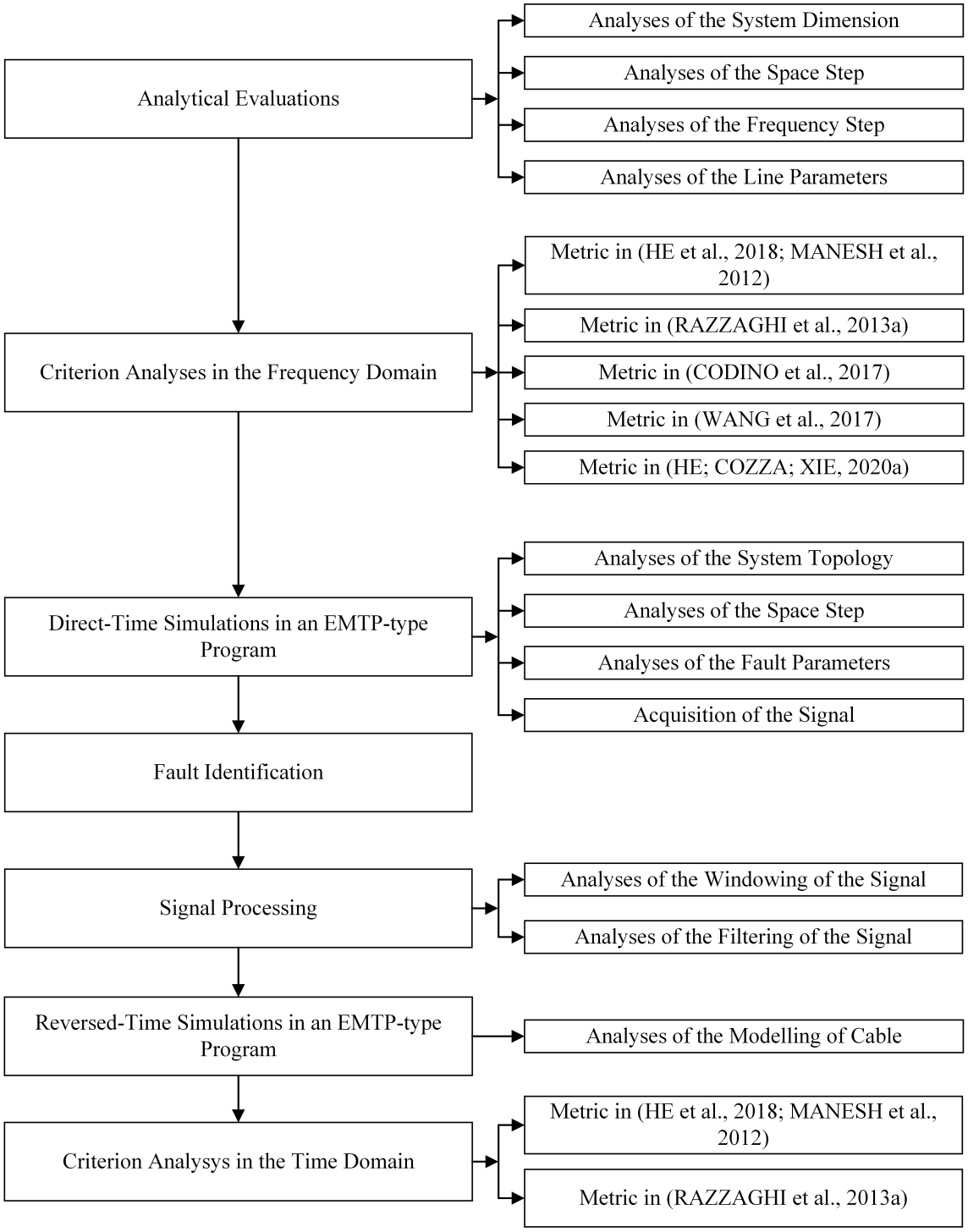

Source: Author

2018; WANG *et al.*, 2020b). The differences between these approaches concern the RT modelling and the metric for the evaluation. The signal processing operations of windowing and filtering can be included as part of the EMTR method, as done in those works. The TR transformation is properly a signal processing technique itself. That is separated in Figure 1 for no analyses are made by changes in its process at this step.

The criteria and methods in (HE; COZZA; XIE, 2020a,b; COZZA; HE; XIE, 2021a,b) use previously recorded signals to calculate correlations. One possibility to have these previous signals is to conduct RT simulations before any fault. In this case, the system has the fault in the RT stage. Those studies represented the fault of the source model. That is not the more conventional approach assumed in fault studies, as already commented. A switch with a fault impedance is the common and simplest model. That is exactly what is used throughout the analyses herein. Therefore, these techniques will not be explored.

Any calculations, plotting and signal processing, including the TR transformation, are implemented in MATLAB® in this thesis.

The basic algorithm of the EMTR methods that use matched media follows the steps:

i. The fault-induced EMTs of the voltage or current signal, $s(t)$, are recorded with a window of length T. That is the DT stage of the method's approaches (RAZZAGHI *et al.*, 2013a; HE *et al.*, 2018; WANG *et al.*, 2020b);

ii. The TR transformation is done on $s(t)$, returning $\bar{s}_m(\hat{t})$;

iii. The GFLs in the electric power system are chosen to evaluate the fault location. $\bar{s}_m(\hat{t})$ is applied as a source in the model of the electric power system for the RT simulations. The location of the time-reversed source is where $s(t)$ was recorded. The reflection coefficient of the DT stage at this location hold. One fault simulation is performed for each GFL at its respective location. A metric is used for the estimation of the fault location. The possible criteria are $\mathcal{E}_i(x_g)$, $\mathcal{P}_i(x_g)$, $\mathcal{P}_v(x_g)$, and $\mathcal{R}_{\bar{i},i}(x_g, l)$. That is the RT stage.

Differently, the basic algorithm of the EMTR methods that use unmatched media (CODINO *et al.*, 2017; WANG *et al.*, 2017; AN *et al.*, 2021) follows the same two first steps above. The difference is in the third one.

iii) Only one fault simulation is performed, not one for each GFL. The possible criteria are $\angle V(x_g, \omega)$ and $\mathcal{E}_v(x_g)$. The location is a given GFL using $\angle V(x_g, \omega)$, and the symmetric location to a given GFL for $\mathcal{E}_v(x_g)$.

Finally, the basic algorithm of the EMTR method that does not work with RT simulations but with the signals and transfer functions for the GFLs stored for each system (HE; COZZA; XIE, 2020a,b; COZZA; HE; XIE, 2021a,b) likewise follows the same two first steps above. The difference is obviously at the third one.

iii) No fault simulation is performed. The possible criteria are: $\mathcal{P}_{v_{t=0}}(x_g)$, $\rho_{VH}(x_g)$, $\rho_{HH}(x_g)$, $\hat{\rho}_{HH}(x_g)$, $\rho_{VV}(x_g)$, $\mathcal{R}_{VV}(x_g)$, $\mathcal{R}_{\hat{H}H}(x_g)$, and $\rho_{\hat{H}H}(x_g)$. The fault location is the GFL where any of these criteria has a maximum.

4.1 Analytical Evaluations

The EMTR-based fault-location method will be first shown in analytical formulations. Similar analyses to those presented in (RAZZAGHI *et al.*, 2013a; CODINO *et al.*, 2017; WANG *et al.*, 2017; CHEN *et al.*, 2019) are analogously produced. The analytical formulations are carried on in the frequency domain for their easier mathematical treatment through algebraic equations. The analyses are performed on two plain transmission systems, where approximations are considered. These analyses set the basis for the method and give insights into the method's behaviour, as commented on previous works in Chapter 3, although they might be much less complex than time-domain studies. The frequency-domain formulations of the EMTR are also presented in the DT and RT stages, despite no simulations are done in their studies.

4.1.1 Analyses of the System Dimension in the Frequency-Domain Studies

The length of the lines of the systems is obviously a question of matter for fault cases. In a real electric power system, the longer the length of a line or cable, the higher the exposition to faults and the larger the range of locations where faults can occur. Still, the measurements of electric voltages and currents are only done at some specific points in real systems. Hence, longer distances between a fault and the measurement point are likely for a system with longer lines or cables. Long-distant faults might impact the fault-location estimation by the EMTR method once the fault-induced EMTs are directly dependent upon the fault distance, owing to the travel of the waves up to the probe point. Therefore, the two plain transmission systems have different line lengths. That proportionates the acknowledgement of the method's reach in spatial dimensions.

4.1.2 Analyses of the Space Step in the Frequency-Domain Studies

Many fault locations along the lines are considered for the evaluations in the frequency domain. These fault locations are evenly spaced between them. Moreover, the GFLs for the RT calculations are equally spaced. The space step is associated with the spatial resolution of the method, i.e. the smallest distance between two fault locations for which the method can discriminate them and give correct estimations. More than one value is used in the studies to assess the impact of the spatial step.

4.1.3 Analyses of the Frequency Step in the Frequency-Domain Studies

The equations in the frequency domain are calculated within a frequency band for discrete frequencies evenly spaced by a frequency step. The frequency step determines the resolution of the quantities in the frequency domain. If the frequency step is larger than given variations in a quantity, this variation is not taken into the calculation, and some spectral information is lost. Therefore, the frequency step is varied to observe its effects on the fault-location estimations.

4.1.4 Analyses of the Line Parameters in the Frequency-Domain Studies

The resistance and reactance of the lines can be altered. The variation represents the reflection of changes in some parameters, such as the configuration of the lines or cables, the geometry and type of the conductors (and insulations, in the case of cables) and the soil resistivity, for instance, among others. These directly impact the EMTs observed.

The influence of the relation between the resistance and the reactance of lines, the R/X relation, is analysed in detail. Starting from the ideally lossless transmission line, the line without resistance, until a typical R/X relation of a distribution line and higher R/X relations, one can have insights into the dependence of the fault location method upon these parameters.

4.2 DT Simulations in EMTP-type Program

After the analytical evaluations of the method and the corresponding comments, several time-domain simulations of short-circuit faults are performed on electric power systems modelled in an EMTP-type tool. The simulations yield data for all analyses ahead, as shown in Figure 1, for no data from measurements are obtained. The EMTP-RV (EMTP®) is chosen as the EMTP-type tool because of the availability of sophisticated models of components of power systems, as the universal line model (ULM) for overhead lines and insulated cables. The set of massive simulations is one of the longest time-spent tasks for the accomplishment of the research in this thesis and, virtually, the most important. Different cases of faults are contemplated, where the fault conditions, the electric power system and the modelling are changed.

4.2.1 Analyses of the System Topology in the Time-Domain Studies

Distribution and transmission systems are modelled for the fault location studies, which have different topologies. Transmission systems normally do not present lateral branches; they usually only interconnect two substations. In this case, there is a single path between the substations for the propagation of forward and backward fault-induced waves, which mostly reflect from the substation transformers. Unlike, distribution systems may be highly branched, with feeders departing from one substation and lateral

branches off them. Each branch adds a path for the fault-induced travelling waves and a junction and an extremity to more reflections and refractions by the waves. Besides, the presence of lateral loads, generally at the lateral branches, leads to changes in the characteristic impedance for a given location of the distribution network. So, the characteristics of the fault-induced EMTs observed in the former type of systems are expected to be different to those of the latter ones, which might influence the performance of the EMTR method.

The evaluations of the EMTR method on both types of systems, transmission and distribution, consider different conductors to observe the influence of the topology and system characteristics on the results. A plain transmission system equivalent to the one used for the analytical evaluation of Section 4.1 is first modelled. After, a dc transmission system forms a more complex case, and then a distribution one. However, the distribution system has the complexity of its topology decreased, where only the first section of the network is used, comprising a part of the main feeder, one lateral branch and a few loads. Therefore, it is not a highly branched case.

4.2.2 Analyses of the Space Step in the Time-Domain Studies

The space step of the actual fault locations and the GFLs are changed for some time-domain cases, as it was for the frequency-domain studies, to have a correspondence between them.

4.2.3 Analyses of the Fault Parameters in the Time-Domain Studies

Short-circuit faults are just modelled as ideal switches connected to resistances. Fault parameters such as the location, type, and resistance are changed. The fault location is the obvious change for each DT simulation. The type of fault is related to how many conductors are involved in the fault. If a dc system, faults involving one pole and ground and only two poles are simulated. If an ac system, faults involving a single phase and ground, only two phases or two phases and ground, or even only three phases and ground are simulated. Fault resistances assume discrete values within a range from low to high values. The fault-inception angles are not changed.

Fault parameters have a direct impact on fault-induced transients. As mentioned above, the location of the fault shapes the induced EMTs. Still, the type of fault determines the modal components induced by the fault. Ground faults yield ground modes, whether faults not involving the ground do not. The strongest contribution of ground modes on the transients' pattern is found for faults involving only a single conductor and ground in its turn, such as pole-to-ground faults in dc and single-line-to-ground faults in ac. The fault resistance contributes to the attenuation of the travelling waves. For high values, the impedance's change at the fault location is less strong in the fault occurrence.

4.2.4 Acquisition of the Signal

The acquisition of the signal is done on the modelled systems. Two situations are considered: the direct acquisition of the voltage signal by a voltage meter and the indirect acquisition of the current signal through a current transformer. In this way, the dependence upon the type of the acquired signal may be known.

The voltage signal is directly taken by a voltage meter in EMTP-RV. This acquisition returns a signal without any limitations in its bandwidth related to a transducer. That might be possible for a large range of frequencies even in real systems, considering the development of new types of transducers, such as low-power voltage transformers and others. Unlike, some attenuation and distortion throughout the frequency range of the signal might be introduced in the acquisition by a current transformer. The modelled of the current transformer is so important for this analysis: the model needs to be properly fitted for frequencies in the order of kHz and MHz.

4.3 Fault Identification

The fault identification (or detection) is made through a simple comparison between the magnitudes of the measured signals within windows of two different times of recording, a previous and the current one. If the difference in the magnitudes is higher than a threshold value, a fault occurrence is assumed. The method is similar to that present in (WANG *et al.*, 2020a). This fault identification method is simple and does not discern between fault-induced and other kinds of EMTs. But the method works properly and is assumed effective for the present studies, as only short-circuit faults are simulated.

4.4 Steps of Signal Processing

The signal of the fault-induced EMTs needs processing. Windowing is necessary to delimit the duration of the signal that will be time reversed. Time-reversed signals must have limited durations to make RT simulations feasible. Filtering is still more necessary. Low-frequency components likely do not contribute to the fault location.

4.4.1 Windowing of the Signal

The windowing of the fault-induced EMTs starts at some samples before the instant of detection of the fault. That allows to cover the first current or voltage step of the forward travelling wave induced by the fault that reaches the recording device. The length of the window is changed. The values chosen range from less than one-tenth of a cycle of the industrial frequency to more than a half cycle.

Longer windows may improve the fault location process (RAZZAGHI *et al.*, 2014) but lead to longer simulations in the RT stage for the same sampling frequency. The

duration of the time-reversal signal used as a source is given just by the length of the window. Longer simulations increase the computational cost and might be a shortcoming for the EMTR methods. Otherwise, shorter windows can shorten the simulation.

4.4.2 Filtering of the Signal

The information about the fault is usually in higher frequencies. Nonetheless, this is relative to the fault distance to the location where the signal is recorded. The first resonant frequency related to the fault is inversely proportional to the travel time from the fault location to the recording point. Low frequencies are so filtered by a high-pass (HP) filter.

The cut-off frequency of the HP filter is changed. Some values from $1\ \mathrm{kHz}$ and above are chosen. That affords to work with signals whose spectrum starts in different frequencies. Which fault-induced resonances compose the spectra of the time-reversed signal might influence the location of the fault. The response of the system is frequency dependent. Besides, the evaluation criteria for the EMTR methods may be very dependent on the frequency components in the signals.

4.5 RT Simulations in EMTP-type Program — Analyses of the Line/Cable Modelling

The line or cable model is a feature under concern for EMT studies. The literature presents different models of lines and cables. Constant-parameter (CP) and frequency-dependent (FD) models have different responses against EMTs. Most of the previous studies on the EMTR method use CP models. A model based on the ULM is used in this work for all DT simulations. In almost all cases, the same model is applied in the RT simulations. However, the CP model is used in the RT simulations of some studies here to observe the behaviour of changing the model.

4.6 Application of Evaluation Metrics

Some of the criteria present in the literature on the EMTR method for fault location are used to estimate the fault location in the frequency- and time-domain evaluations. These are: $\mathcal{E}_i(x_g)$, $\mathcal{P}_i(x_g)$, $\angle V(x_g, \omega)$, $\mathcal{E}_v(x_g)$, and $\rho_{HH}(x_g)$. That enables to verify the performance of each metric for the studied cases.

5 RESULTS AND DISCUSSION

This chapter brings the results of the application of the EMTR method to different cases and forms, as related in the precedent Chapter 1, constituting the contributions of the present thesis. Analytical evaluations of the EMTR method in the frequency domain are first presented according to the respective literature (RAZZAGHI *et al.*, 2013a; CODINO *et al.*, 2017; WANG *et al.*, 2017; CHEN *et al.*, 2019; HE; COZZA; XIE, 2020a). The results of these works are reproduced through the metrics they used for the fault location estimation. Furthermore, some details of the deduction of their respective expressions are shown. The analytical formulations are made over assumptions and simple representations of components of electric power systems, such as high impedances for the transformers at line ends. However, they are all valuable for demonstrating the theoretical basis of the method and indicating its applicability.

Time-domain analyses upon simulation data from numerical modelling of a simple electric power system follow the analytical evaluations aiming to compare their results against those from the analytical ones. These can show if the method works in the time domain according to the analytical results, although not covering all of the same analyses.

More complex time-domain cases are then studied to expand the investigation of the method's capabilities. The EMTR method is applied to an HVDC transmission system and an electric power distribution network, considering sophisticated numerical models for the system components. As related in Chapter 4, the analyses are performed by varying fault parameters, such as the fault location and the fault resistance in the DT simulations (*cf.* Section 4.2.3), and parameters related to the signal processing of the fault-induced EMTs, such as the recording window length (*cf.* Section 4.4.1) and the cut-off frequency applied in the filter (*cf.* Section 4.4.2). The objective is to yield results of the EMTR application from modelling as realistic as possible in different conditions.

A discussion of the EMTR-based fault-location method's strengths and weaknesses is thus built from all analytical and simulation results, as underlined in Section 1.2.

5.1 Single-Conductor Non-Branched Transmission-Line System in the Frequency Domain

Examples of the fault location process through the TR transformation, as presented in (RAZZAGHI *et al.*, 2013a; RAZZAGHI, 2016; RACHIDI; RUBINSTEIN; PAOLONE, 2017), can be made through analytical formulations in the frequency domain (*cf.* Section 4.1). These analyses are made upon a plain system constituted by an overhead single-conductor transmission line of total length ℓ, extended between two transformers, where a fault occurs. Both single- and double-end forms of the EMTR method are formulated herein. The fault-induced EMTs compose the signal under the TR operation.

Let the fault be solid (or of null impedance), at the position x_f, and represented by an ideal source $v_f(t)$, a step-like function in the time domain triggered at the initial instant of analysis (BORGHETTI *et al.*, 2008; RAZZAGHI *et al.*, 2013a). The time-domain representation of the single-conductor transmission-line system and the configuration of the fault are shown in Figure 2.

Figure 2 – Solid fault on a single-conductor transmission-line system in the time domain

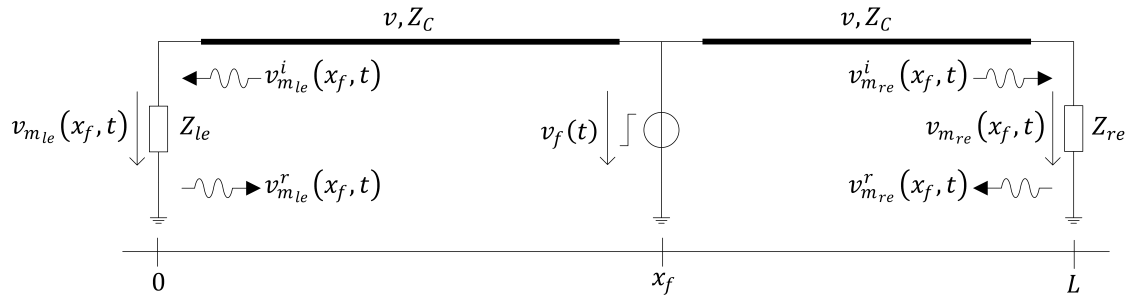

Source: Author

Figure 2 shows the transformers at the line extremities equivalent to high input impedances, Z_{le} and Z_{re}, following the transient approximation (GREENWOOD, 1991).

Still, Figure 2 shows the voltage signals from the fault-induced EMTs, $v_{m_{le}}(x_f,t)$ and $v_{m_{re}}(x_f,t)$, recorded at the left and right ends of the line, whose positions are identified as 0 and L, respectively. The representation corresponds to recordings across the equivalent impedance of the transformers, as done in (RAZZAGHI *et al.*, 2013a). This forms the DT stage of the EMTR method. Only $v_{m_{le}}(x_f,t)$ is considered for the single-end form of the method. Therefore, although Figure 2 shows both extremities of the line as probe ends, $v_{m_{re}}(x_f,t)$ is disregarded in these cases.

The time-domain representation in Figure 2 shows the parameters of the line before high-frequency signals, the phase velocity of the travelling waves through the line, v, and the characteristic (or surge) impedance of the line, Z_C. The propagation constant of the line, γ, is used for analyses in the frequency domain (MIANO; MAFFUCCI, 2001; PAUL,

2007). v, Z_C, and γ are given by (60), (61), and (62), respectively,

$$v = \frac{1}{\sqrt{lc}}, \tag{60}$$

$$Z_C = \sqrt{\frac{z}{y}}, \tag{61}$$

$$\begin{aligned} \gamma &= \sqrt{zy} \\ &= \alpha + j\beta, \end{aligned} \tag{62}$$

where z and y are given by (63) and (64), respectively,

$$z = r + sl, \tag{63}$$

$$y = g + sc, \tag{64}$$

where l, c, r, and g are, respectively, the per-unit-length inductance, capacitance, resistance, and conductance of the line, and s is the frequency in the Laplace domain.

The frequency-domain representation of the system with the fault occurrence is shown in Figure 3.

Figure 3 – Solid fault on a single-conductor transmission-line system in the frequency domain

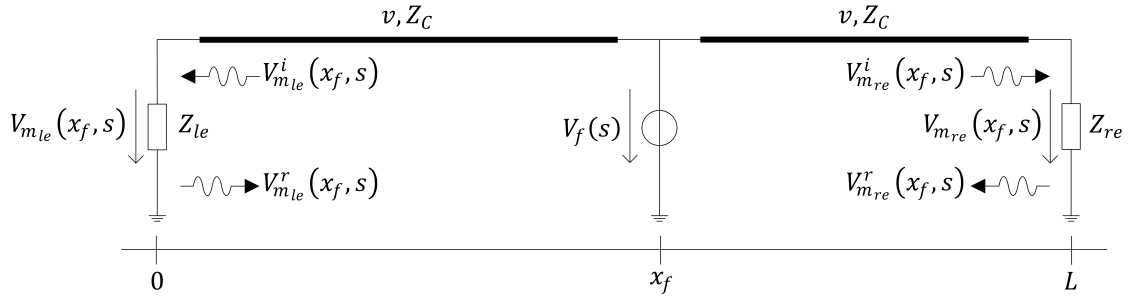

Source: Author

The reflection coefficients at the fault and transformers' positions, designated by f, m_{le} and m_{re}, are given by (65), (66), and (67), respectively,

$$\Gamma_{x_f} = -1, \tag{65}$$

$$\Gamma_{le} = \frac{Z_{le} - Z_C}{Z_{le} + Z_C}, \tag{66}$$

$$\Gamma_{re} = \frac{Z_{re} - Z_C}{Z_{re} + Z_C}. \tag{67}$$

The solid fault allows analysis within the sections $x = [0, x_f]$ and $x = [x_f, L]$ separately. Therefore, one has (68) and (69), (70) and (71), and (72) and (73), for the reflected,

incident and total voltage across the transformers' equivalent impedance, respectively (MIANO; MAFFUCCI, 2001),

$$V^r_{m_{le}}(x_f, s) = \frac{\Gamma_{le} e^{-\gamma x_f}}{1 + \Gamma_{le} e^{-2\gamma x_f}} V_f(s), \tag{68}$$

$$V^r_{m_{re}}(x_f, s) = \frac{\Gamma_{re} e^{-\gamma x_f}}{1 + \Gamma_{re} e^{-2\gamma x_f}} V_f(s), \tag{69}$$

$$V^i_{m_{le}}(x_f, s) = \frac{e^{-\gamma x_f}}{1 + \Gamma_{le} e^{-2\gamma x_f}} V_f(s), \tag{70}$$

$$V^i_{m_{re}}(x_f, s) = \frac{e^{-\gamma x_f}}{1 + \Gamma_{re} e^{-2\gamma x_f}} V_f(s), \tag{71}$$

$$V_{m_{le}}(x_f, s) = \frac{(1 + \Gamma_{le})\, e^{-\gamma x_f}}{1 + \Gamma_{le} e^{-2\gamma x_f}} V_f(s), \tag{72}$$

$$V_{m_{re}}(x_f, s) = \frac{(1 + \Gamma_{re})\, e^{-\gamma x_f}}{1 + \Gamma_{re} e^{-2\gamma x_f}} V_f(s). \tag{73}$$

To analyse the frequency response in the steady state, $s = j\omega$, where ω is the angular frequency, equal to $2\pi f$. One has (74) and (75) (PAUL, 2007)

$$V_{m_{le}}(x_f, \omega) = \frac{(1 + \Gamma_{le})\, e^{-\gamma x_f}}{1 + \Gamma_{le} e^{-2\gamma x_f}} V_f(\omega), \tag{74}$$

$$V_{m_{re}}(x_f, \omega) = \frac{(1 + \Gamma_{re})\, e^{-\gamma x_f}}{1 + \Gamma_{re} e^{-2\gamma x_f}} V_f(\omega). \tag{75}$$

In the RT stage of the double-end form of the EMTR method, the complex conjugate of $V_{m_{le}}(x_f, \omega)$ and $V_{m_{re}}(x_f, \omega)$, $V^*_{m_{le}}(x_f, \omega)$ and $V^*_{m_{re}}(x_f, \omega)$, are injected into a time-reversed version of the system at the same point where both signals were recorded. The impedances Z_{le} and Z_{re} are still present to hold the same reflection coefficient of the original system at these points. In the case of the single-end form of the method, only $V^*_{m_{le}}(x_f, \omega)$ is injected in the RT stage.

Since the steady-state response is now analysed in the RT stage, the fault is considered as a part of the system and not more as a triggered source. However, the location of the fault is unknown, and a range of GFLs is chosen where the response of the time-reversed system to $V^*_{m_{le}}(x_f, \omega)$ and $V^*_{m_{re}}(x_f, \omega)$, or only $V^*_{m_{le}}(x_f, \omega)$, will be evaluated. The double- and single-end configurations are shown in Figures 4 and 5, respectively, where $I(x_g, \omega)$ is the fault current at the GFL x_g.

Again, the fault splits the system into two sections since the fault has no impedance.

Figure 4 – Time-reversed version of the single-conductor transmission-line system given a solid fault in the steady-state frequency domain with the double-end form of the method

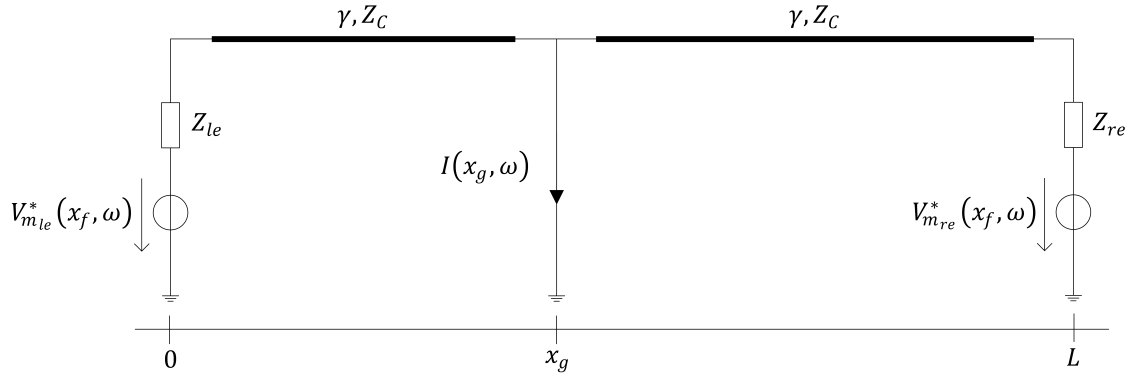

Source: Author

Figure 5 – Time-reversed version of the single-conductor transmission-line system given a solid fault in the steady-state frequency domain with the single-end form of the method

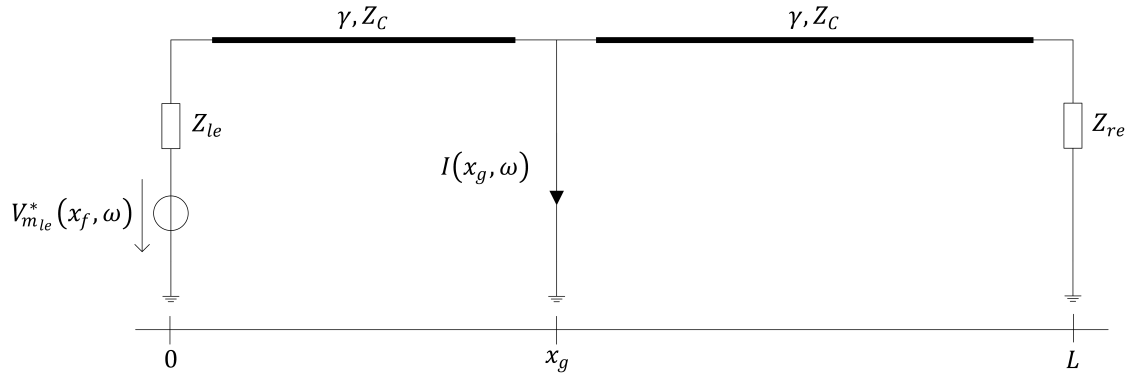

Source: Author

For the double-end form of the method, for any x_g, $I(x_g, \omega)$ is given by (76)

$$
\begin{aligned}
I(x_g,\omega) &= \frac{(1+\Gamma_{le})\, e^{-\gamma x_g}}{Z_{le}\,(1+\Gamma_{le}e^{-2\gamma x_g})} V^*_{m_{le}}(x_f,\omega) \\
&+ \frac{(1+\Gamma_{re})\, e^{-\gamma (L-x_g)}}{Z_{re}\,(1+\Gamma_{re}e^{-2\gamma (L-x_g)})} V^*_{m_{re}}(x_f,\omega) \\
&= \frac{(1+\Gamma_{le})^2 e^{-\gamma\left(x_g-x_f\right)}}{Z_{le}\,(1+\Gamma_{le}e^{-2\gamma x_g})\,(1+\Gamma_{le}e^{2\gamma x_f})} V^*_f(\omega) \\
&+ \frac{(1+\Gamma_{re})^2 e^{-\gamma\left(x_g-x_f\right)}}{Z_{re}\,(1+\Gamma_{re}e^{-2\gamma (L-x_g)})\left(1+\Gamma_{re}e^{2\gamma (L-x_f)}\right)} V^*_f(\omega),
\end{aligned}
\tag{76}
$$

and for the single-end form of the method, $I(x_g, \omega)$ is given by (77)

$$\begin{aligned} I(x_g, \omega) &= \frac{(1+\Gamma_{le})\, e^{-\gamma x_g}}{Z_{le}\,(1+\Gamma_{le} e^{-2\gamma x_g})} V^*_{m_{le}}(x_f, \omega) \\ &= \frac{(1+\Gamma_{le})^2 e^{-\gamma\left(x_g - x_f\right)}}{Z_{le}\,(1+\Gamma_{le} e^{-2\gamma x_g})\,(1+\Gamma_{le} e^{2\gamma x_f})} V^*_f(\omega). \end{aligned} \tag{77}$$

Following (RAZZAGHI *et al.*, 2013a; MANESH *et al.*, 2012; HE *et al.*, 2018), possible metrics for the EMTR application are $\mathcal{E}_i(x_g)$ and $\mathcal{P}_i(x_g)$, in a frequency domain correspondence of those given by (8) and (9), respectively, with (78) and (79)

$$\mathcal{P}_i(x_g) = \max\left\{|i(x_g, \omega_k)|\right\}, \tag{78}$$

$$\mathcal{E}_i(x_g) = \sum_{k=1}^{K} i^2(x_g, \omega_k), \tag{79}$$

where ω_k is a discrete frequency.

$I(x_g, \omega)$ is evaluated for two line lengths, $\ell = 10$ km and $\ell = 1,000$ km, firstly considering lossless lines and all lines' and transformers' parameters independent of the frequency of the signals. The line parameters for the lossless conditions are $Z_T = 100$ kΩ, $c = 10.7$ pF/m, $g = 0$ S, $l = 1.1$ µH/m, and $r = 0\ \Omega$. The fault locations and the GFLs span from 0 km to 10 km, for the case of $\ell = 10$ km, and 0 km to $1,000$ km, for the case of $\ell = 1,000$ km.

The probe ends are at 0 km and 10 km for the 10-km line, and at 0 km and $1,000$ km for the $1,000$-km line, for the double-end form of the method. For the single-end form, the probe end is at 0 km for both line length cases.

Many fault locations in both cases are considered to cover the whole length of lines in the two cases and thus observe the dependence of the method's performance on the location of the fault. The GFLs are at the same positions as the actual fault locations. The frequency range is from 1 kHz to 0.5 MHz. The values of the spatial step of the GFLs, Δx_g, and the frequency step, $\Delta\omega$, are varied to assess their influence. Δx_g assumes the values of 1 km, 100 m, and 10 m for $\ell = 10$ km and 100 km, 10 km, and 1 km for $\ell = 1,000$ km. The actual fault locations are spaced by a distance $\Delta x_f = \Delta x_g$ to have correspondence with the GFLs. Therefore, Δx_g assumes values of 10%, 1%, and 0.1% relative to the line length in both cases, being these values the same for the intervals of the actual fault locations. Still, $\Delta\omega$ assumes the values of $2,000\pi$ rad/s, 200π rad/s, and 20π rad/s in both line-length cases.

With $V_f(\omega) = \frac{1}{j\omega}$ rad^{-1}/s^{-1} (the Fourier transform of the unitary step function that models the fault at the considered frequency range[1]), one has the results in Figures 6 to 17 using $\mathcal{E}_i(x_g)$ and in Appendix A using $\mathcal{P}_i(x_g)$ for the three values of Δx_f and Δx_g

[1]The Fourier transform of the Heaviside function (the unitary step function) is actually equal to $\frac{1}{j\omega} + \pi\delta(\omega)$ (OPPENHEIM; WILLSKY; YOUNG, 1983). So, for $\omega \neq 0$, only the term $\frac{1}{j\omega}$ remains.

and both double- and single-end approaches of the method. The results are shown as *colormap* [*sic*] matrices. The real fault locations, x_f, are along the abscissa axis of the *colormaps* in Figures 6 to 17, whilst the GFLs, x_g, are along the ordinate axis. The values of the axes' points are shown according to the distance of the locations to the probe end at 0 km.

Figure 6 – $\mathcal{E}_i(x_g)$ normalised for $\ell = 10$ km with $\Delta x_f = \Delta x_g = 1$ km and double-end recording

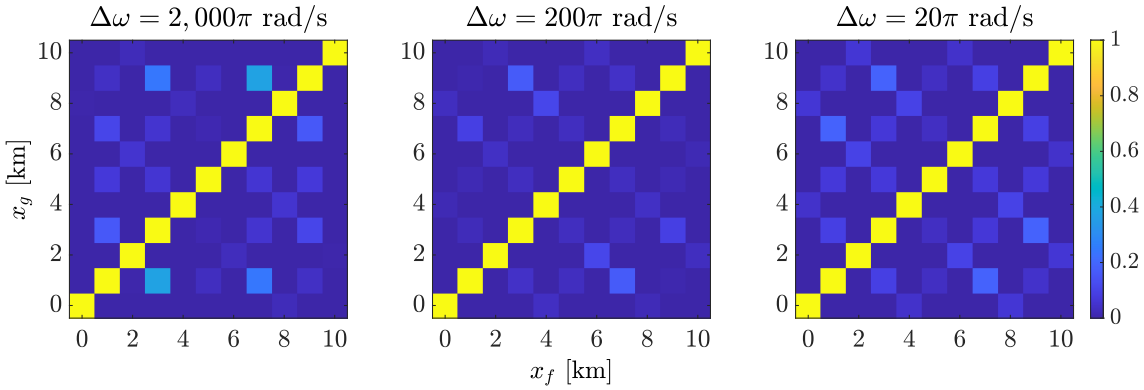

Source: Author

Figure 7 – $\mathcal{E}_i(x_g)$ normalised for $\ell = 10$ km with $\Delta x_f = \Delta x_g = 1$ km and single-end recording

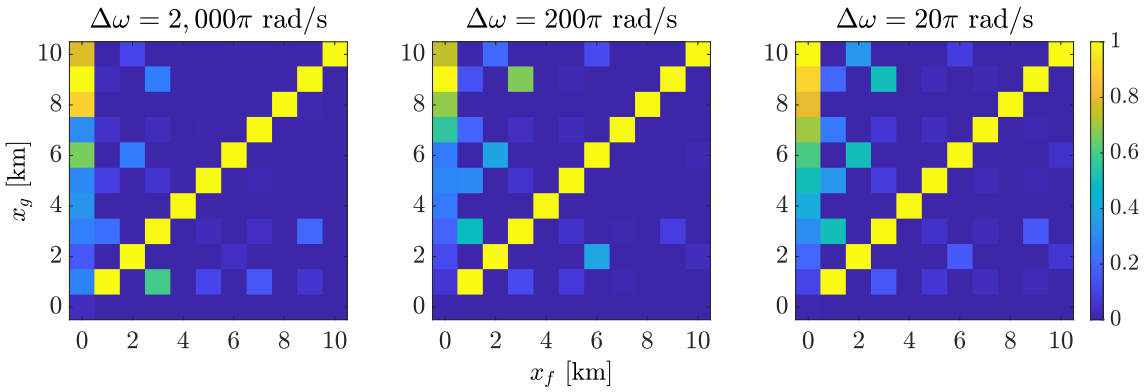

Source: Author

The percentage of correctly estimated fault locations using $\mathcal{E}_i(x_g)$ and $\mathcal{P}_i(x_g)$ for the three values of Δx_f and Δx_g are then shown in Tables 1 to 4.

The actual fault locations were correctly estimated by $\mathcal{E}_i(x_g)$ and $\mathcal{P}_i(x_g)$ for the line of 10 km for $\Delta x_g = 1$ km and the three values of $\Delta\omega$, with the double-end recording, as shown in Table 1. With the single-end recoding, Figure 7 shows an exception for the fault at 0 km, the single probe end. The correct estimation is noticed in the figures where the values of both $\mathcal{E}_i(x_g)$ and $\mathcal{P}_v(x_g)$ criteria along the diagonal from the lower-left corner to

Figure 8 – $\mathcal{E}_i(x_g)$ normalised for $\ell = 1,000$ km with $\Delta x_f = \Delta x_g = 100$ km and double-end recording

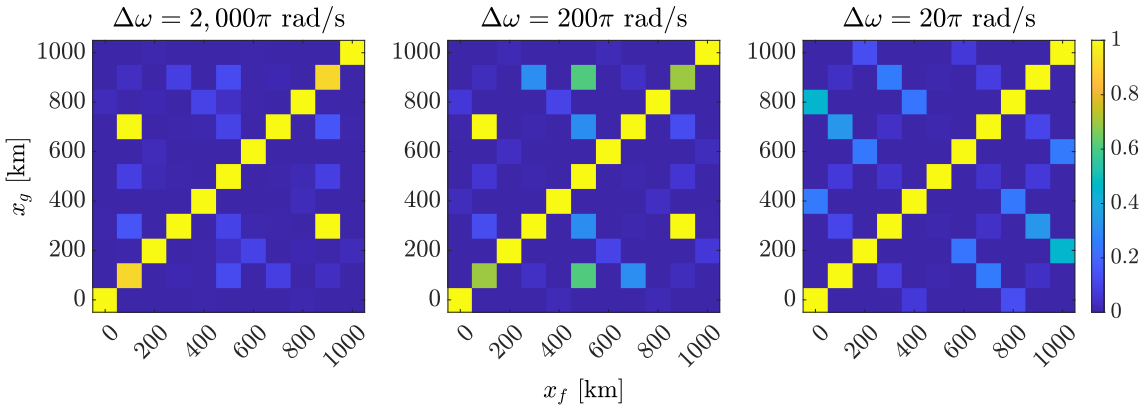

Source: Author

Figure 9 – $\mathcal{E}_i(x_g)$ normalised for $\ell = 1,000$ km with $\Delta x_f = \Delta x_g = 100$ km and single-end recording

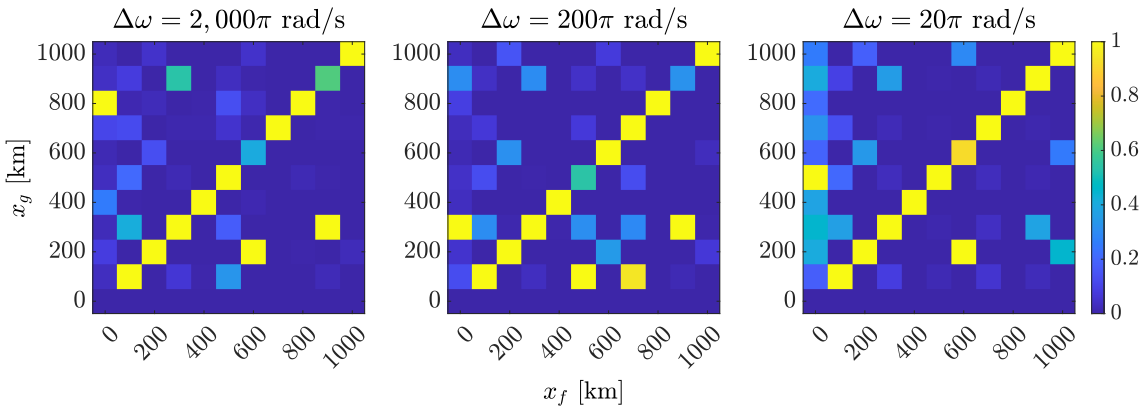

Source: Author

Table 1 – Percentage of fault locations correctly estimated [%] with double-end recording by $\mathcal{P}_i(x_g)$ and $\mathcal{E}_i(x_g)$ for three values of Δx_g and $\Delta\omega$, for $\ell = 10$ km

Δx_g [km]	$\Delta\omega$ [rad/s]					
	$2,000\pi$		200π		20π	
	$\mathcal{P}_v(x_g)$	$\mathcal{E}_v(x_g)$	$\mathcal{P}_v(x_g)$	$\mathcal{E}_v(x_g)$	$\mathcal{P}_v(x_g)$	$\mathcal{E}_v(x_g)$
1	100.00	100.00	100.00	100.00	100.00	100.00
0.1	52.48	64.36	94.06	100.00	100.00	100.00
0.01	14.29	22.68	20.48	44.06	95.60	100.00

the upper-right corner of the *colormap* matrices are higher than at other points (near the

Figure 10 – $\mathcal{E}_i(x_g)$ normalised for $\ell = 10$ km with $\Delta x_f = \Delta x_g = 100$ m and double-end recording

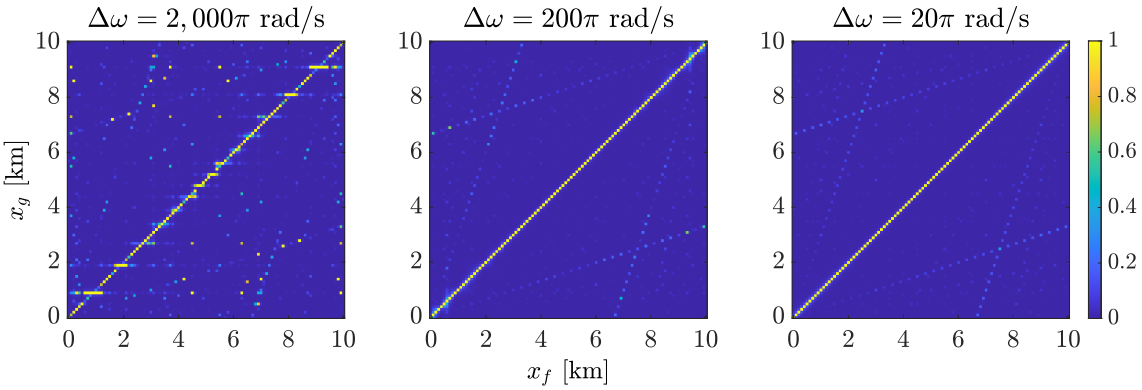

Source: Author

Figure 11 – $\mathcal{E}_i(x_g)$ normalised for $\ell = 10$ km with $\Delta x_f = \Delta x_g = 100$ m and single-end recording

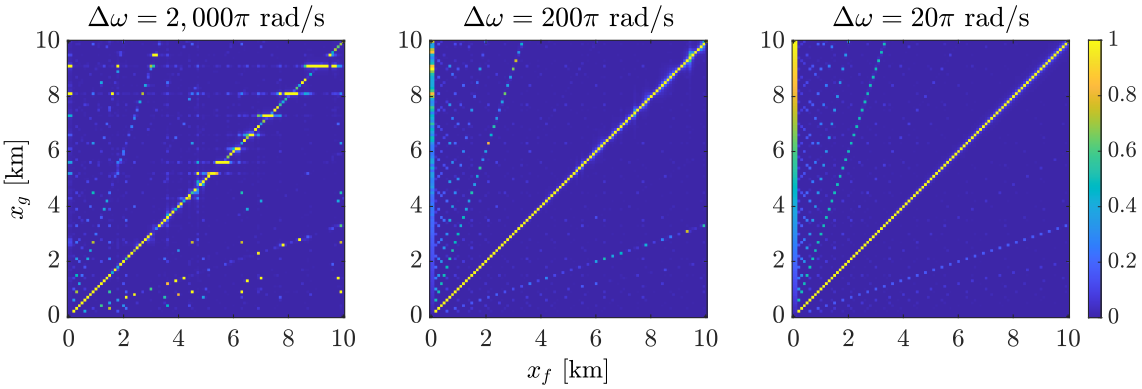

Source: Author

Figure 12 – $\mathcal{E}_i(x_g)$ normalised for $\ell = 1,000$ km with $\Delta x_f = \Delta x_g = 10$ km and double-end recording

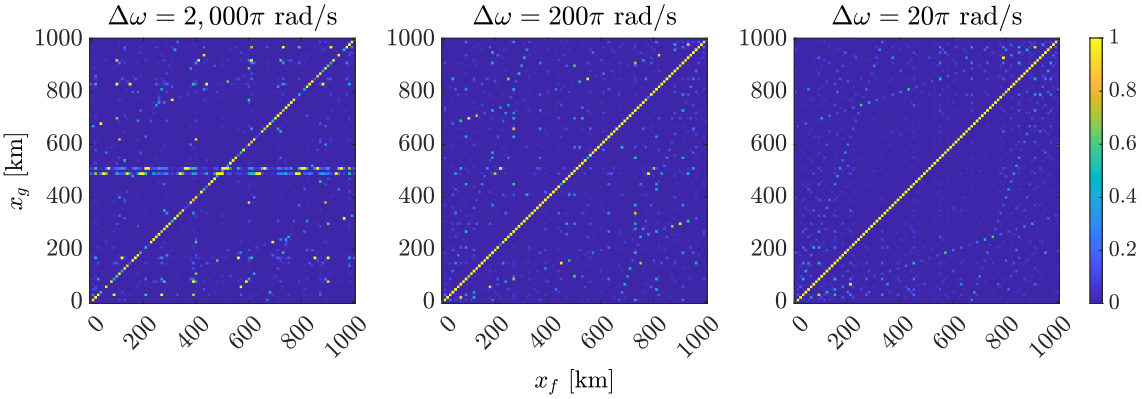

Source: Author

Figure 13 – $\mathcal{E}_i(x_g)$ normalised for $\ell = 1,000$ km with $\Delta x_f = \Delta x_g = 10$ km and single-end recording

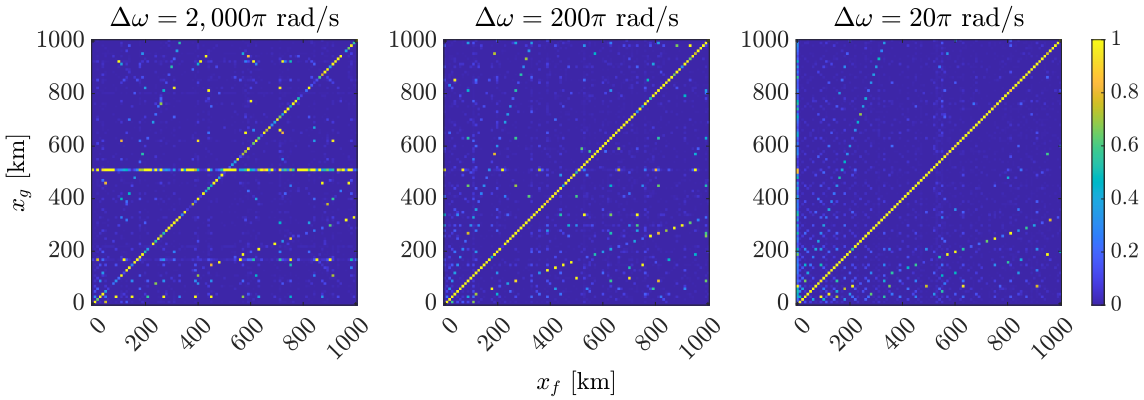

Source: Author

Figure 14 – $\mathcal{E}_i(x_g)$ normalised for $\ell = 10$ km with $\Delta x_f = \Delta x_g = 10$ m and double-end recording

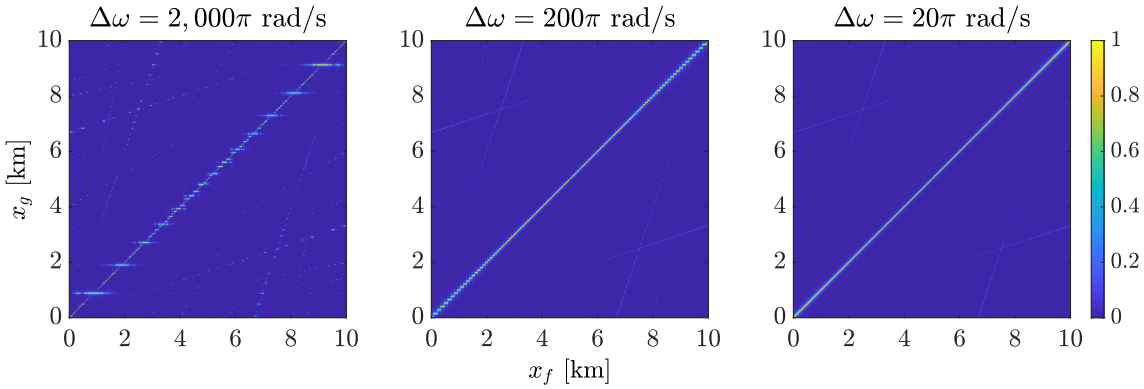

Source: Author

Figure 15 – $\mathcal{E}_i(x_g)$ normalised for $\ell = 10$ km with $\Delta x_f = \Delta x_g = 10$ m and single-end recording

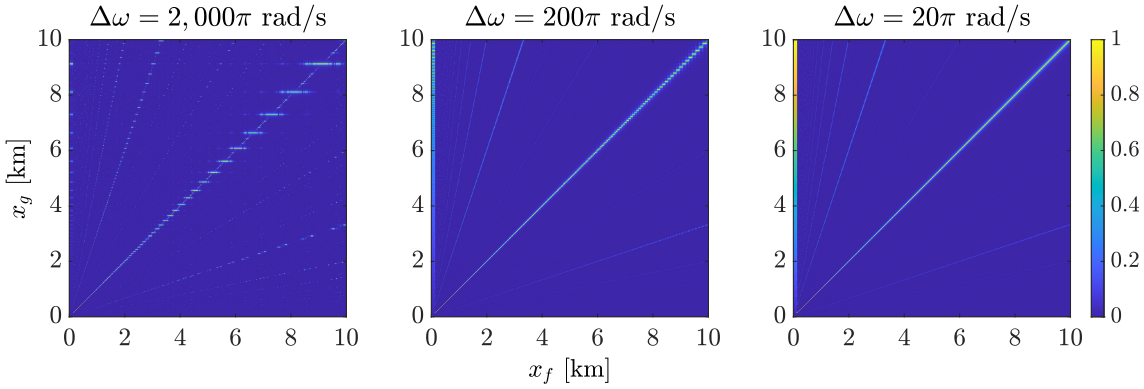

Source: Author

Figure 16 – $\mathcal{E}_i(x_g)$ normalised for $\ell = 1,000$ km with $\Delta x_f = \Delta x_g = 1$ km and double-end recording

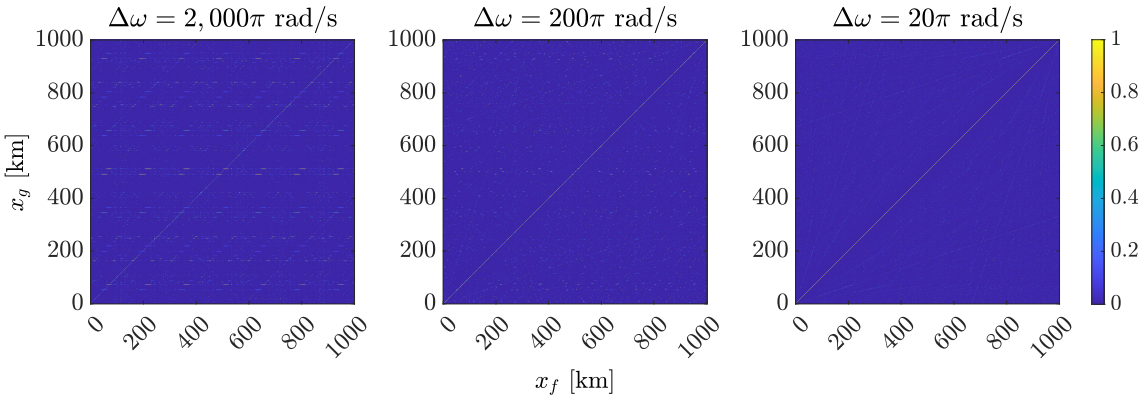

Source: Author

Figure 17 – $\mathcal{E}_i(x_g)$ normalised for $\ell = 1,000$ km with $\Delta x_f = \Delta x_g = 1$ km and single-end recording

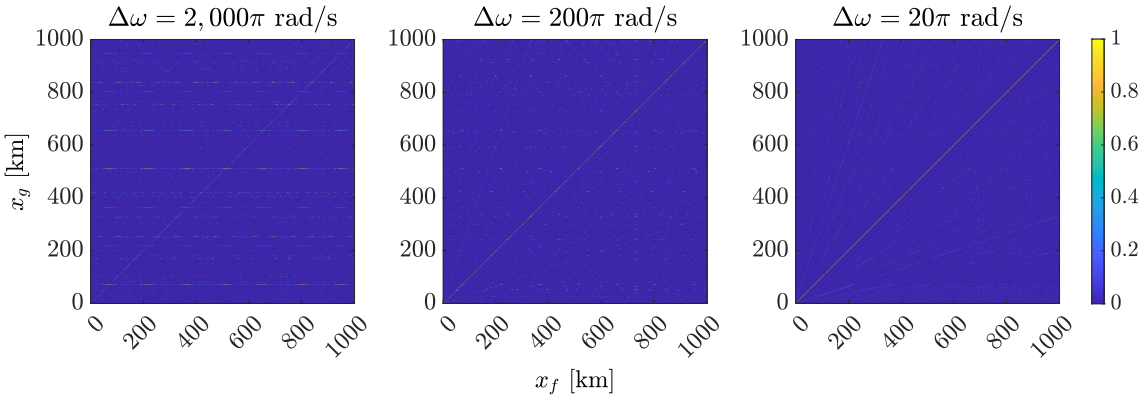

Source: Author

Table 2 – Percentage of fault locations correctly estimated [%] with single-end recording by $\mathcal{P}_i(x_g)$ and $\mathcal{E}_i(x_g)$ for three values of Δx_g and $\Delta\omega$, for $\ell = 10$ km

Δx_g [km]	$\Delta\omega$ [rad/s]					
	$2,000\pi$		200π		20π	
	$\mathcal{P}_v(x_g)$	$\mathcal{E}_v(x_g)$	$\mathcal{P}_v(x_g)$	$\mathcal{E}_v(x_g)$	$\mathcal{P}_v(x_g)$	$\mathcal{E}_v(x_g)$
1	90.91	90.91	90.91	90.91	90.91	90.91
0.1	52.48	57.43	93.07	98.02	98.02	98.02
0.01	12.29	15.38	39.86	49.55	96.30	98.50

yellow colour in the colour bar of the figures).

For both the double- and single-end recordings, for $\Delta x_g = 100$ m, Tables 1 and 2

Table 3 – Percentage of fault locations correctly estimated [%] with double-end recording by $\mathcal{P}_i(x_g)$ and $\mathcal{E}_i(x_g)$ for three values of Δx_g and $\Delta\omega$, for $\ell = 1,000$ km

Δx_g [km]	$\Delta\omega$ [rad/s]					
	$2,000\pi$		200π		20π	
	$\mathcal{P}_v(x_g)$	$\mathcal{E}_v(x_g)$	$\mathcal{P}_v(x_g)$	$\mathcal{E}_v(x_g)$	$\mathcal{P}_v(x_g)$	$\mathcal{E}_v(x_g)$
100	81.82	81.82	72.73	81.82	100.00	100.00
10	47.52	55.45	77.23	94.06	86.14	98.02
1	8.79	12.59	17.58	37.46	35.86	93.21

Table 4 – Percentage of fault locations correctly estimated [%] with single-end recording by $\mathcal{P}_i(x_g)$ and $\mathcal{E}_i(x_g)$ for three values of Δx_g and $\Delta\omega$, for $\ell = 1,000$ km

Δx_g [km]	$\Delta\omega$ [rad/s]					
	$2,000\pi$		200π		20π	
	$\mathcal{P}_v(x_g)$	$\mathcal{E}_v(x_g)$	$\mathcal{P}_v(x_g)$	$\mathcal{E}_v(x_g)$	$\mathcal{P}_v(x_g)$	$\mathcal{E}_v(x_g)$
100	72.73	72.73	63.64	72.73	81.82	81.82
10	35.64	41.58	67.33	84.16	78.22	92.08
1	7.39	8.09	16.38	27.17	30.37	76.52

show that at least 93.07% of the estimations were correct with $\Delta\omega = 200\pi$ rad/s and 98.02% with $\Delta\omega = 20\pi$ rad/s. Figure 10 shows blurs at some points with $\Delta\omega = 2,000\pi$ rad/s for the double-end recording, where the estimations presented deviations around the actual fault location.

A similar behaviour is observed for the single-end recording in Figure 11 for some positions at distances farther than 5 km from the probe end. Still, $\mathcal{P}_i(x_g)$ presented a little worse performance than $\mathcal{E}_i(x_g)$.

For $\Delta x_g = 10$ m, Tables 1 and 2 show that from 95.60% to 100.00% of the actual fault locations were estimated with $\Delta\omega = 20\pi$ rad/s. Deviations around the actual fault location occurred with $\Delta\omega = 2,000\pi$ rad/s and $\Delta\omega = 200\pi$ rad/s for some positions, presenting blurs at some points in Figures 14 and 15. $\mathcal{P}_i(x_g)$ again presented a worse performance than $\mathcal{E}_i(x_g)$.

With the single-end recording, the faults at distances up to 200 m from the probe end for $\Delta x_g = 100$ m, and up to 150 m for $\Delta x_g = 10$ m, were not located with any value of $\Delta\omega$ by either $\mathcal{P}_v(x_g)$ or $\mathcal{E}_i(x_g)$ criteria. That might be related to the spectral characteristics of $V_{m_{le}}(x_f, \omega)$ for close faults to the single probe end: the closer the fault, the higher the resonant frequencies related to the fault in $V_{m_{le}}(x_f, \omega)$. The frequency range considered

might not cover these high frequencies.

For the line of $1,000$ km, the estimations were somewhat worse than the ones for the case of the 10-km line, as observed in Figures 8, 9, 12, 13, 16, and 17, and Tables 3 and 4. Fault locations were correctly estimated for more than 72% of the cases for $\Delta x_g = 100$ km with the three values of $\Delta\omega$; more than 84% and 92% for $\Delta x_g = 10$ km with $\Delta\omega = 200\pi$ rad/s and $\Delta\omega = 20\pi$ rad/s, respectively; and more than 76% for $\Delta x_g = 1$ km with $\Delta\omega = 20\pi$ rad/s by $\mathcal{E}_i(x_g)$ with both forms of recording. The $\mathcal{P}_i(x_g)$ presented a much worse performance than $\mathcal{E}_i(x_g)$, mainly for $\Delta x_g = 1$ km.

For $\Delta x_g = 10$ km with $\Delta\omega = 2,000\pi$ rad/s, there was a trend of $\mathcal{E}_i(x_g)$ and $\mathcal{P}_i(x_g)$ presenting their picks at the GFL corresponding to the middle of the line, 500 km, which is observed by the horizontal line in Figures 12 and 13, for instance. Similar behaviour occurred for $\Delta x_g = 1$ km with $\Delta\omega = 2,000\pi$ rad/s, where the trend of more than one horizontal line is observed.

Therefore, the results indicated a relation between $\Delta\omega$ and Δx_g, which in a time-domain analysis can be translated into a relation between the number of samples of the recorded signal of the fault-induced EMTs and Δx_g. This relation influences the dependence of the estimations of the EMTR method on the fault location and the line length. Considering the single-end recording, the method correctly located faults far from the probe end, as at the right end, even for the case of $\ell = 1,000$ km. However, the performance is not the same for different Δx_g and $\Delta\omega$. The estimations were correct in more cases with $\Delta\omega = 20\pi$ rad/s.

The rather worse behaviour using $\mathcal{P}_i(x_g)$ might be caused by the greater amount of secondary peaks at other positions than the actual fault position presented by $\mathcal{P}_i(x_g)$ in some cases, compared to $\mathcal{E}_i(x_g)$, or the same secondary peaks with a magnitude near the magnitude of the highest one. That is due to the computation of $\mathcal{E}_i(x_g)$, which has a square factor not present in the computation of $\mathcal{P}_i(x_g)$, knowing that $|I(x_g, \omega)| < 1$ A for $|V_f(\omega) = \frac{1}{j\omega}| \; \forall\omega \in [10^3, 5 \times 10^5] \times 2\pi$ rad/s.

The influence of adding loss to the line on the behaviour of $\mathcal{E}_i(x_g)$ and $\mathcal{P}_i(x_g)$ can also be evaluated in the frequency domain. Leaving the lossless condition, the value of resistance, r, of the single-conductor overhead line is varied according to the values of $1/20$, $1/10$, $1/4$, 1, $1/2$, 2, 4, and 10 for the relation between r and the reactive inductance of the line, x_l, considering a frequency of 50 Hz ($x_l = \omega l$)[2,3].

The value of 10 for r/x_l represents an extreme case, perhaps unrealistic in real electric power systems, where the resistive component of the line is very high; $r/x_l = 1/10$ and $r/x_l = 1/4$ represent typical relations of overhead lines of transmission systems, whilst

[2] r/x_l is a dimensionless quantity.

[3] x_l and hence r/x_l are roughly calculated for a constant frequency herein, i.e., $f = 50$ kHz, although a range of frequencies is covered through the analyses. Moreover, r and l are considered not frequency-dependent.

$r/x_l = 1/2$, $r/x_l = 1$, and $r/x_l = 2$ represent typical relations of overhead lines or cables of distribution systems.

Thus, choosing $\Delta\omega = 200\pi$ rad/s, $\Delta x_f = \Delta x_g = 100$ m for $\ell = 10$ km, $\Delta x_f = \Delta x_g = 10$ km for $\ell = 1,000$ km, and holding the same other system parameters of the cases in Figures 6 to 17, one has the results in Appendix A for $\ell = 10$ km and $\ell = 1,000$ km. The percentages of correct estimations of these same cases are then shown in Table 5.

Table 5 – Percentage of fault locations correctly estimated [%] with double- and single-end recordings by $\mathcal{P}_i(x_g)$ and $\mathcal{E}_i(x_g)$ for eight values of r/x_l, for $\ell = 10$ km and $\ell = 1,000$ km

r/x_l	Double End				Single End			
	$\ell = 10$ km		$\ell = 1,000$ km		$\ell = 10$ km		$\ell = 1,000$ km	
	$\mathcal{P}_v(x_g)$	$\mathcal{E}_v(x_g)$	$\mathcal{P}_v(x_g)$	$\mathcal{E}_v(x_g)$	$\mathcal{P}_v(x_g)$	$\mathcal{E}_v(x_g)$	$\mathcal{P}_v(x_g)$	$\mathcal{E}_v(x_g)$
1/20	94.06	100.00	62.38	78.22	92.08	98.02	35.64	49.50
1/10	94.06	100.00	47.52	67.33	92.08	98.02	25.74	34.65
1/4	96.04	100.00	39.60	43.56	92.08	97.03	18.81	20.79
1/2	96.04	98.02	18.81	20.79	94.06	96.04	8.91	8.91
1	92.08	96.04	9.90	10.89	91.09	96.04	4.95	4.95
2	94.06	100.00	7.92	13.86	91.09	98.02	3.96	5.94
4	96.04	98.02	7.92	7.92	95.05	97.03	5.94	6.93
10	98.02	100.00	6.93	3.96	95.05	98.02	6.93	3.96

Table 5 shows that the increase of r did not strongly influence the fault location estimations with the double-end recording for $\ell = 10$ km. More than 96% and 92% over all fault cases were correctly located by $\mathcal{E}_i(x_g)$ and $\mathcal{P}_i(x_g)$, respectively. For $\ell = 1,000$ km, Table 5 shows that the higher r/x_l, the fewer the percentage of correct fault locations over all cases. For instance, with $r/x_l = 1/20$, about 78% and 62% of all estimations were correct by $\mathcal{E}_i(x_g)$ and $\mathcal{P}_i(x_g)$, respectively, whilst these percentages were about 4% and 7%, respectively, with $r/x_l = 10$.

With the single-end recording for $\ell = 10$ km, the results show that increasing r yielded more deviations of the estimations from the actual fault location as farther the fault from the probe end. There is an increase in the magnitude of secondary peaks of $\mathcal{E}_i(x_g)$ and $\mathcal{P}_i(x_g)$, respectively, at other positions different from the actual fault position. Moreover, the peak at the actual fault position widens as r/x_l increases, presenting a likely trend to the loss of accuracy on the fault location by the EMTR method. Nonetheless, almost all actual fault positions were found for all values of r/x_l.

Table 5 shows that above 96% and 91% over all faults had their locations correctly

estimated by $\mathcal{E}_i(x_g)$ and $\mathcal{P}_i(x_g)$, respectively. The higher r/x_l, the closer to the probe end is the farthest x_f, for which the estimation was correct by either $\mathcal{E}_i(x_g)$ or $\mathcal{P}_i(x_g)$ for $\ell = 1,000$ km. Table 5 shows that about 49% and 36% of all faults were correctly located by $\mathcal{E}_i(x_g)$ and $\mathcal{P}_i(x_g)$ with $r/x_l = 1/20$, respectively, and only about 4% and 7% with $r/x_l = 10$.

Given the results for $\ell = 1,000$ km, the EMTR method might have limitations regarding line lengths when lossy lines are considered. That has a higher impact on single-end recording due to the possibility of faults occurring farther away from the probe end. Still, the performance of $\mathcal{P}_i(x_g)$ was slightly worse than that of $\mathcal{E}_i(x_g)$.

The application of the bounded-phase metric introduced in (CODINO *et al.*, 2017) follows the resolution of the back-propagation model of the system without the transverse branch of the fault, taking single-end measurements. This configuration is shown in Figure 18.

Figure 18 – Back-propagation system on the steady-state frequency domain without the transverse branch of the fault

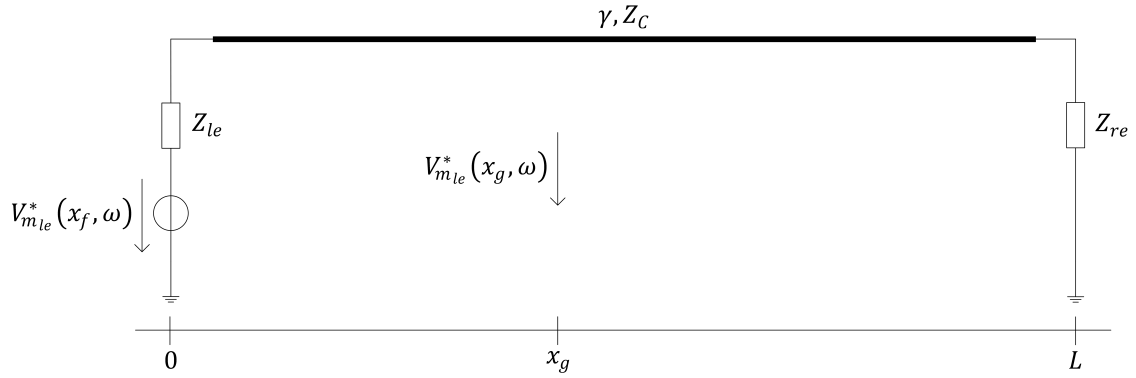

Source: Author

The value of the voltage along the line at any position x_g, $V(x_g, \omega)$, is given by (80) (PAUL, 2007; CODINO *et al.*, 2017)

$$\begin{aligned} V(x_g,\omega) &= (1-\Gamma_{le})\,\frac{e^{-\gamma x_g}+\Gamma_{re}e^{\gamma x_g-2\ell}}{2\,(1-\Gamma_{le}\Gamma_{re}e^{-2\gamma\ell})}V^*_{m_{le}}(x_f,\omega) \\ &= (1-\Gamma_{le}^2)\frac{e^{-\gamma x_g}+\Gamma_{re}e^{\gamma x_g-2\ell}}{2\,(1-\Gamma_{le}\Gamma_{re}e^{-2\gamma\ell})}\left(\frac{e^{-\gamma x_f}}{1+\Gamma_{le}e^{-2\gamma x_f}}\right)^* V_f^*(\omega). \end{aligned} \tag{80}$$

The argument of $V(x_g, \omega)$ is calculated for $\ell = 10$ km and $\ell = 1,000$ km for faults over the whole length of the lines. Δx_f and Δx_g assume the values of 1 km, 100 m, and 10 m, for $\ell = 10$ km, and 100 km, 10 km, and 1 km, for $\ell = 1,000$ km, as in the previous evaluation. Figures 19, 21, and 23 show the minimum values of $\angle V(x_g, \omega)$ within the frequency range for all x_f and x_g as *colormap* matrices for $\ell = 10$ km, for $\Delta x_g = 1$ km,

$\Delta x_g = 100$ m, and $\Delta x_g = 10$ m, respectively. Still, Figures 20, 22, and 24 show the minimum values of $\angle V(x_g, \omega)$ for $\ell = 1,000$ km, for $\Delta x_g = 100$ km, $\Delta x_g = 10$ km, and $\Delta x_g = 1$ km, respectively.

The results for either line length are shown for $\Delta\omega = 2,000\pi$ rad/s, $\Delta\omega = 200\pi$ rad/s, and $\Delta\omega = 20\pi$ rad/s, considering the frequency range from 1 kHz to 0.5 MHz. Since the bounded-phase criterion is $\angle V(x_g, \omega) \in [0, \pi]$ rad $\forall\omega$, the minimum value of $\angle V(x_g, \omega)$ within the frequency range shows if the lower bound of $[0, \pi]$ rad was crossed or not[4]. These minimum values of $\angle V(x_g, \omega) \in [0, \pi]$ were shifted to have only positive values and normalised to have values within $[0, 1]$.

Figure 19 – Argument of $V(x_g, \omega)$ for $\ell = 10$ km with $\Delta x_f = \Delta x_g = 1$ km

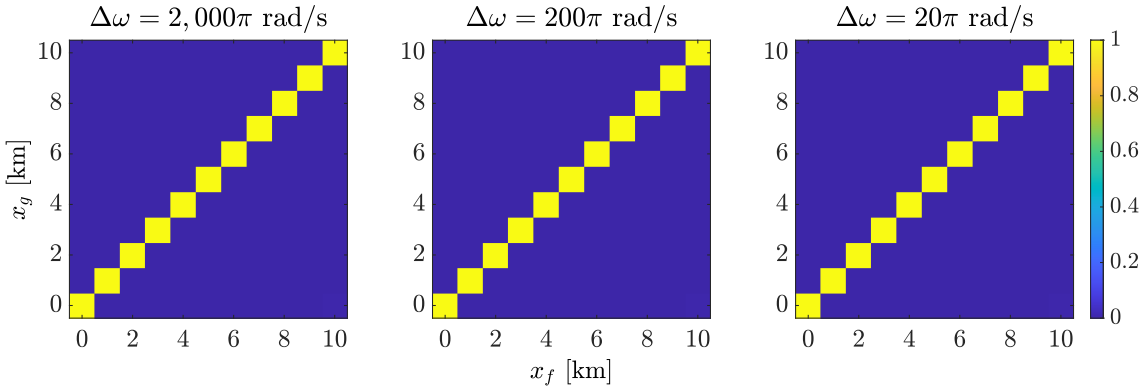

Source: Author

Figure 20 – Argument of $V(x_g, \omega)$ for $\ell = 1,000$ km with $\Delta x_f = \Delta x_g = 100$ km

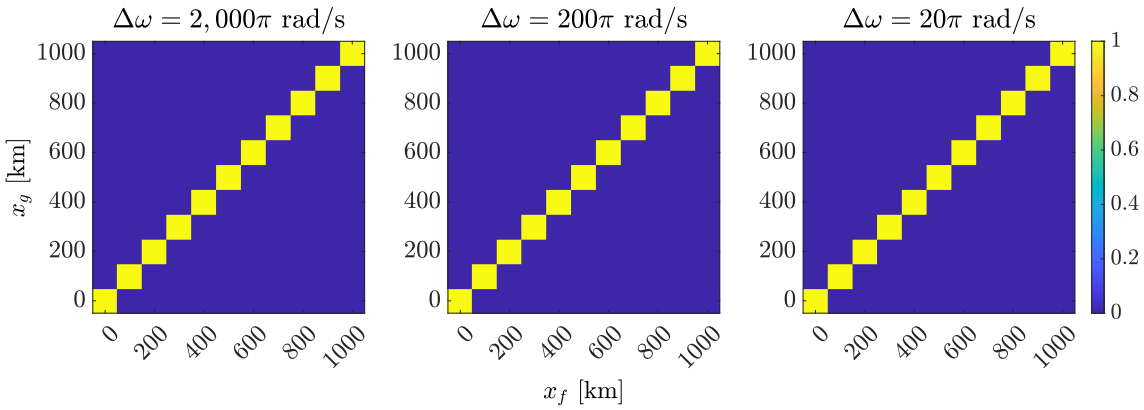

Source: Author

Tables 6 and 7 show the percentages of correct estimations in Figures 19 to 24.

Figures 19 and 21 show that $\angle V(x_g, \omega) \in [0, \pi] \forall\omega$ with $\omega \in [10^3, 5 \times 10^5] \times 2\pi$ rad/s only at the actual fault position, for almost all fault cases with $\ell = 10$ km, for $\Delta x_g = 1$

[4]The numerical computation of the argument returns a value in $[-\pi, \pi]$ rad, so the upper bound, π, can not be crossed.

Figure 21 – Argument of $V(x_g, \omega)$ for $\ell = 10$ km with $\Delta x_f = \Delta x_g = 100$ m

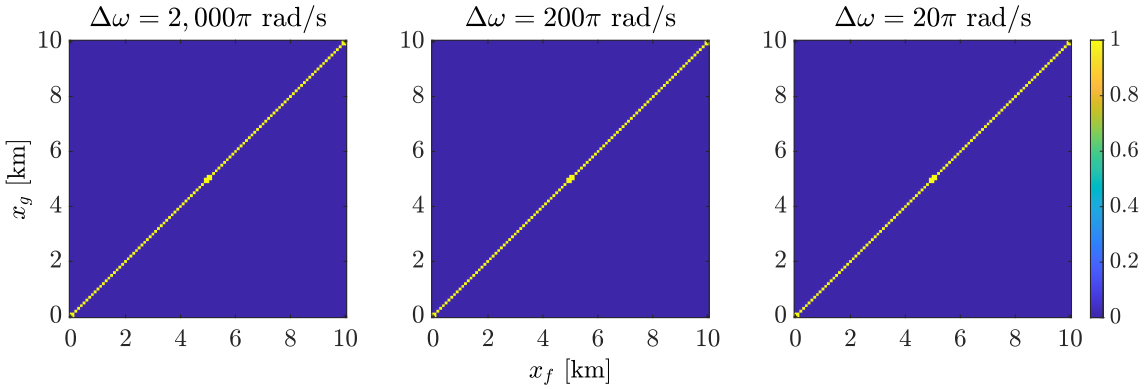

Source: Author

Figure 22 – Argument of $V(x_g, \omega)$ for $\ell = 1,000$ km with $\Delta x_f = \Delta x_g = 10$ km

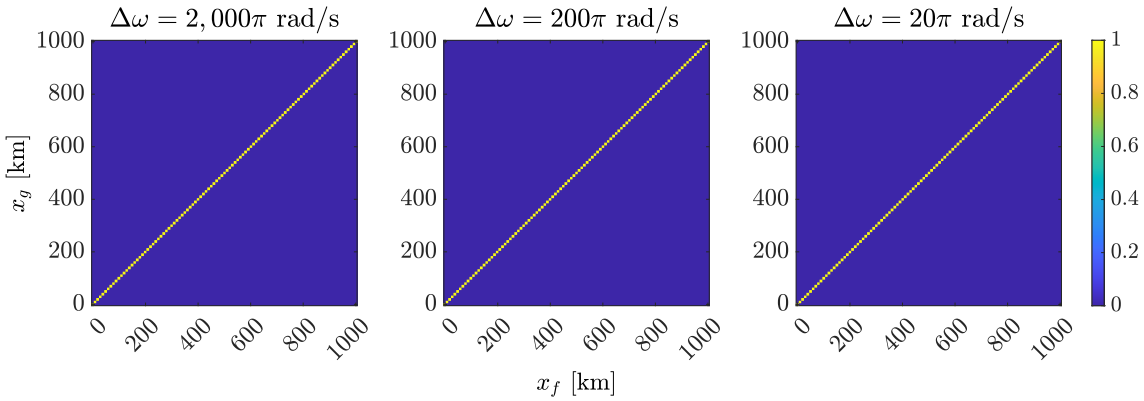

Source: Author

Figure 23 – Argument of $V(x_g, \omega)$ for $\ell = 10$ km with $\Delta x_f = \Delta x_g = 10$ m

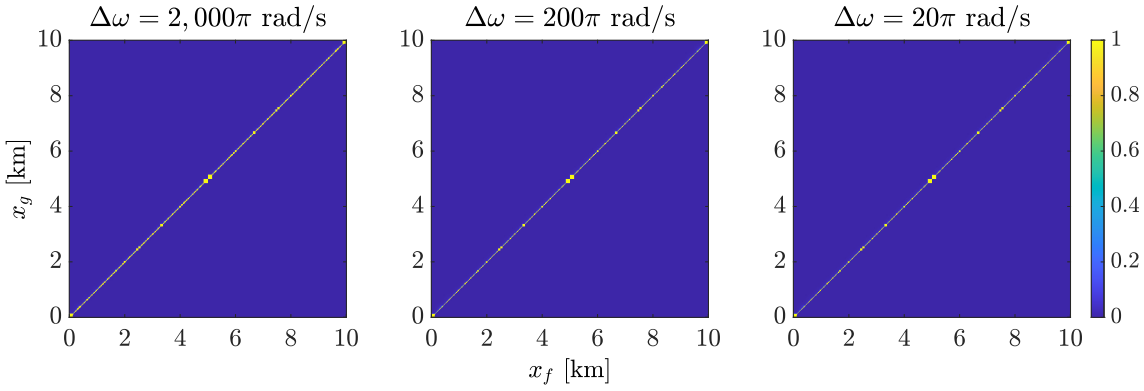

Source: Author

km and $\Delta x_g = 100$ m and the three values $\Delta\omega$. $\angle V(x_g, \omega)$ was bounded in $[0, \pi]$ rad in these cases. Table 6 show that the correct fault locations were estimated in about 100% and 93% of the cases with $\Delta x_g = 1$ km and $\Delta x_g = 100$ m, respectively, for the three

Figure 24 – Argument of $V(x_g, \omega)$ for $\ell = 1,000$ km with $\Delta x_f = \Delta x_g = 1$ km

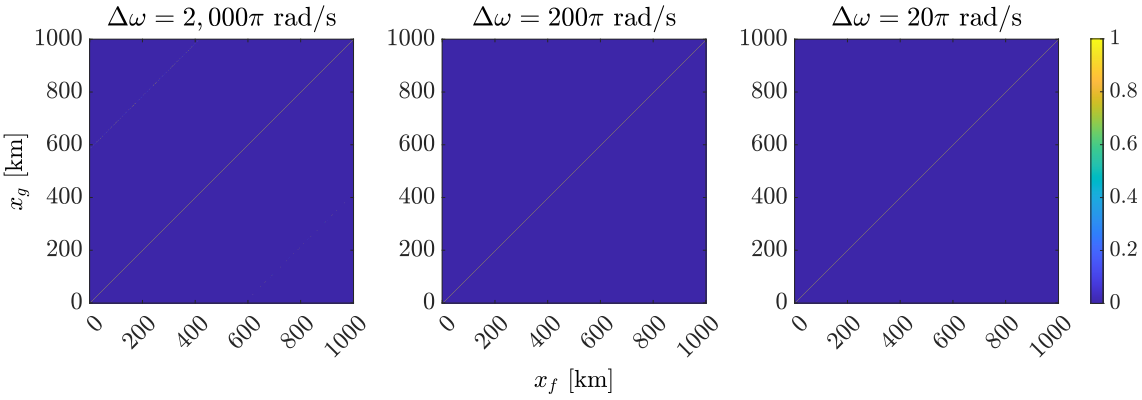

Source: Author

Table 6 – Percentage of fault locations correctly estimated [%] by the bounded-phase criterion for three values of Δx_g and $\Delta\omega$, for $\ell = 10$ km

Δx_g [km]	$\Delta\omega$ [rad/s]		
	$2,000\pi$	200π	20π
100	100.00	100.00	100.00
10	93.07	93.07	93.07
1	6.19	25.57	26.17

Table 7 – Percentage of fault locations correctly estimated [%] by the bounded-phase criterion for three values of Δx_g and $\Delta\omega$, for $\ell = 1,000$ km

Δx_g [km]	$\Delta\omega$ [rad/s]		
	$2,000\pi$	200π	20π
100	100.00	100.00	100.00
10	100.00	100.00	100.00
1	95.60	100.00	100.00

$\Delta\omega$, against only about 6%, 25%, and 26% with $\Delta x_g = 10$ m and $\Delta\omega = 2,000\pi$ rad/s, $\Delta\omega = 200\pi$ rad/s, and $\Delta\omega = 20\pi$ rad/s, respectively.

These results showed that the bounded-phase criterion cannot discriminate between the GFL corresponding to the actual fault location and other ones in fault cases for $\Delta x_f = \Delta x_g = 10$ m and the frequency range $[10^3, 5 \times 10^5] \times 2\pi$ rad/s.

With $\ell = 1,000$ km, Figures 20, 22, and 24 show that the bounded-phase criterion nearly did not wrongly estimate the fault locations. Table 7 that for $\Delta x_g = 10$ km and $\Delta\omega = 2,000\pi$ rad/s, about 96% of the actual fault locations were correctly located; for

the other cases, all actual fault locations were correctly located. This behaviour was due to the longer spatial distance between the GFLs compared to the $\ell = 10\text{-km}$ line cases.

Thereby, the bounded-phase property was verified and worked in both cases of line length, except the cases with $\Delta x_g = 10$ m for $\ell = 10$ km. The smaller frequency where the no-bounded $\angle V(x_g, \omega) \in [0, \pi]$ rad would be observable for a displacement of 10 m from the actual fault location is higher than the upper frequency in the range $[1 \times 10^5, 5 \times 10^5] \times 2\pi$ rad/s, therefore. That respective frequency is a minimum reference for the sampling system if an accuracy of 10 m is desired (CODINO *et al.*, 2017). Its value is not investigated here. In a time-domain analysis, a sampling system of 1 MHz might have the accuracy of 100 m, the next smallest displacement, once the Nyquist frequency is 0.5 MHz, but not 10 m. Nevertheless, 10 m can be seen as very high accuracy, considering the total length of the line (10 km), and then possibly extravagant.

Another observation is that $\Delta\omega$ had little influence on the fault-location estimation by the bounded-phase property. For accuracies of about 100 m, even $\Delta\omega = 2,000\pi$ rad/s could be considered.

The evaluation of the influence of the addition of loss to the line through the value of r/x_l is shown in Figures 25 and 26 for the same eight values of $1/20$, $1/10$, $1/4$, 1, $1/2$, 2, 4, and 10, for $\Delta x_f = \Delta x_g = 100$ m, considering $\ell = 10$ km, and for $\Delta x_f = \Delta x_g = 10$ km, considering $\ell = 1,000$ km, with $\Delta\omega = 200\pi$ rad/s.

Figure 25 – Argument of $V(x_g, \omega)$ for $\ell = 10$ km, $\Delta x_f = \Delta x_g = 100$ m and eight values of r/x_l

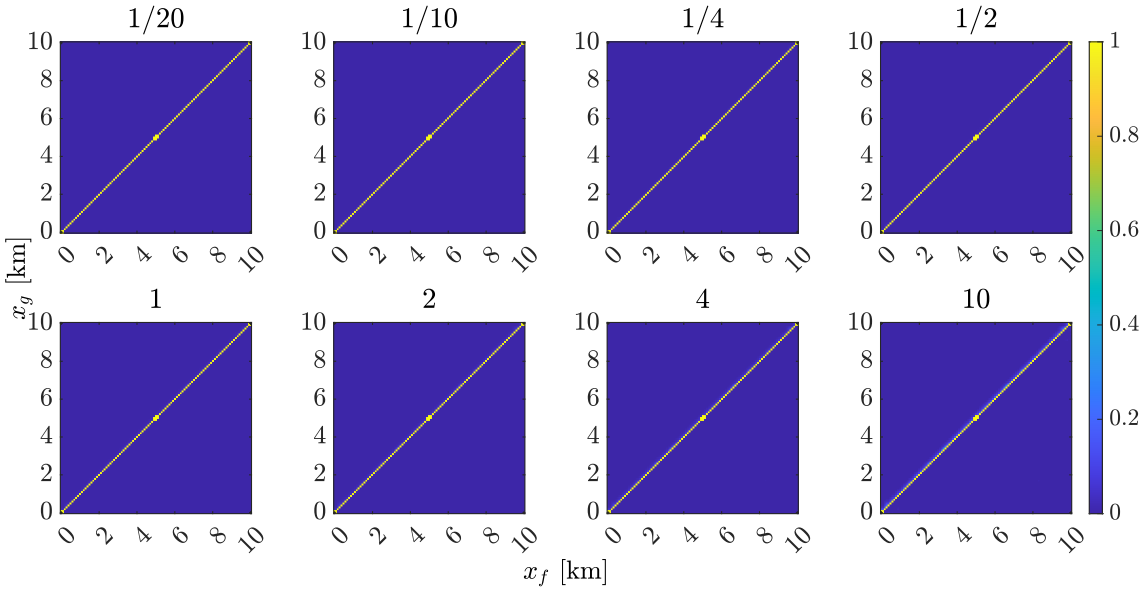

Source: Author

Table 8 presents the percentages of the fault locations correctly estimated in Figures 25 and 26.

Figure 26 – Argument of $V(x_g, \omega)$ for $\ell = 1,000$ km, $\Delta x_f = \Delta x_g = 100$ m and eight values of r/x_l

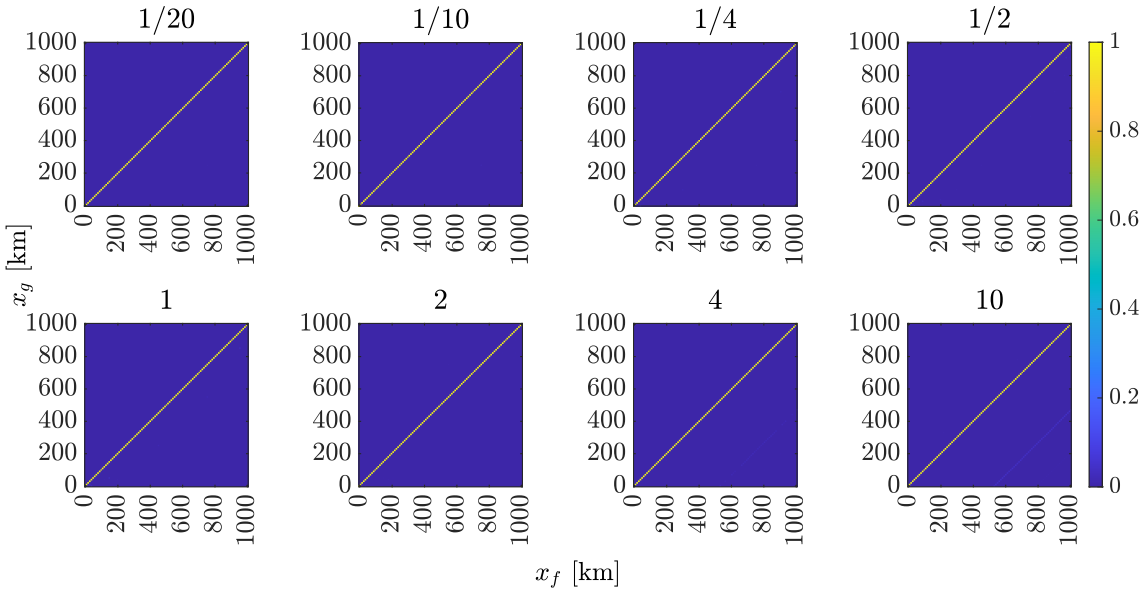

Source: Author

Table 8 – Percentage of fault locations correctly estimated [%] by the bounded-phase criterion for eight values of r/x_l, for $\ell = 10$ km and $\ell = 1,000$ km

r/x_l	$\ell = 10$ km	$\ell = 1,000$ km
1/20	93.07	100.00
1/10	93.07	100.00
1/4	93.07	100.00
1/2	93.07	100.00
1	93.07	100.00
2	93.07	100.00
4	93.07	100.00
10	93.07	100.00

Figures 25 and 26 and Table 8 show that the resistance of the lines did not decrease the accuracy of the fault-location estimation by the bounded-phase property for both line lengths, given the values of Δx_g and $\Delta\omega$. The same cases of correctly located faults for the lossless condition in Figures 21 and 22 with $\Delta\omega = 200\pi$ rad/s were correctly located for any value of r/x_l.

Likewise, evaluating the fault location with the mirrored minimum energy metric of Wang et al. (2017) for single-end measurements, one has the *colormap* matrices of the values of $\mathcal{E}_v(x_g)$ for x_f *versus* x_g in Figures 27 to 32, for $\ell = 10$ km, considering $\Delta x_f = \Delta x_g = 1$ km, $\Delta x_f = \Delta x_g = 100$ m, and $\Delta x_f = \Delta x_g = 10$ m, and $\ell = 1,000$ km,

considering $\Delta x_f = \Delta x_g = 100$ km, $\Delta x_f = \Delta x_g = 10$ km, and $\Delta x_f = \Delta x_g = 1$ km, for $\Delta\omega = 2,000\pi$ rad/s, $\Delta\omega = 200\pi$ rad/s, and $\Delta\omega = 20\pi$ rad/s, with ω within the range $[10^3, 5 \times 10^5] \times 2\pi$ rad/s.

Figure 27 – $\mathcal{E}_v(x_g)$ for $\ell = 10$ km with $\Delta x_f = \Delta x_g = 1$ km

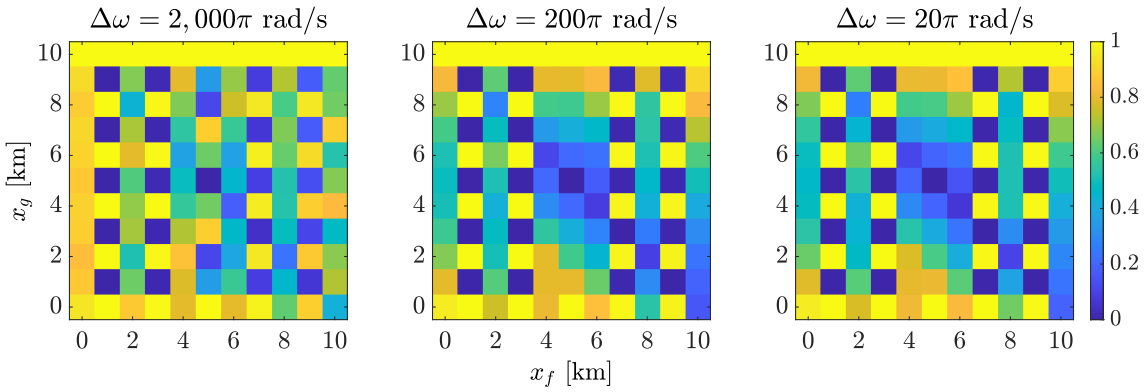

Source: Author

Figure 28 – $\mathcal{E}_v(x_g)$ for $\ell = 1,000$ km with $\Delta x_f = \Delta x_g = 100$ km

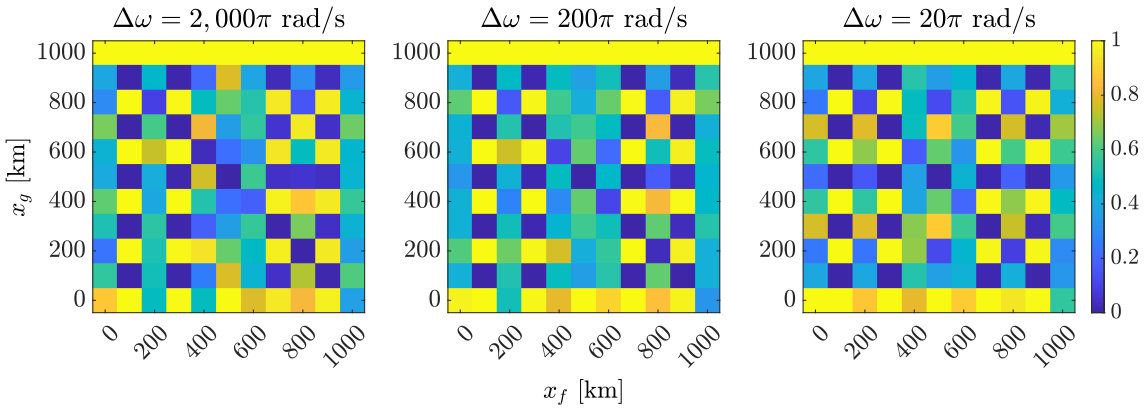

Source: Author

Tables 9 and 10 show the percentages of the cases $\mathcal{E}_v(x_g)$ gave the correct fault location in Figures 27 to 32.

Figures 27 to 32, and Tables 9 and 10 show that $\mathcal{E}_v(x_g)$ was minimum at mirrored positions to the actual faulted ones concerning the line centre for more than 90% of the fault cases with $\Delta x_g = 1$ km and $\Delta x_g = 100$ m and with the three values of $\Delta\omega$ for $\ell = 10$ km, and more than 85% with all values of Δx_g and $\Delta\omega$ for $\ell = 1,000$ km.

The fault at the probe end was not located in any case. The lower performance of the $\mathcal{E}_v(x_g)$ metric with $\Delta x_g = 10$ m for $\ell = 10$ km might be just related to this small spatial step between two adjacent faulted points. The minimum of $\mathcal{E}_v(x_g)$ are at the points of the diagonal from the upper-left corner to the lower-right corner of Figures 27 and 32. However, these minimums are not so evident in all cases in the figures.

Figure 29 – $\mathcal{E}_v(x_g)$ for $\ell = 10$ km with $\Delta x_f = \Delta x_g = 100$ m

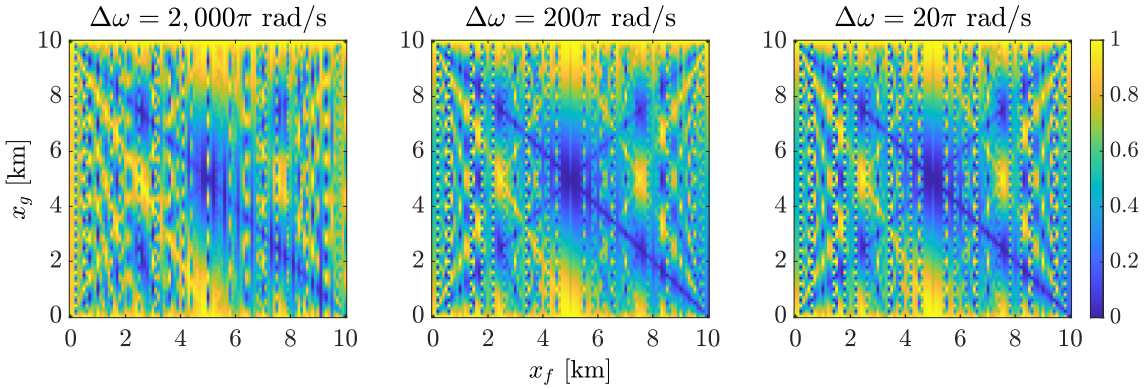

Source: Author

Figure 30 – $\mathcal{E}_v(x_g)$ for $\ell = 1,000$ km with $\Delta x_f = \Delta x_g = 10$ km

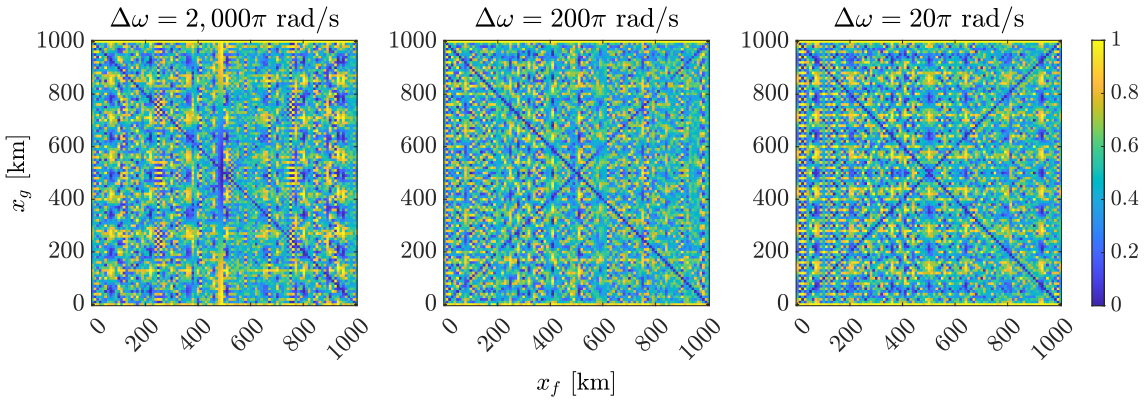

Source: Author

Figure 31 – $\mathcal{E}_v(x_g)$ for $\ell = 10$ km with $\Delta x_f = \Delta x_g = 10$ m

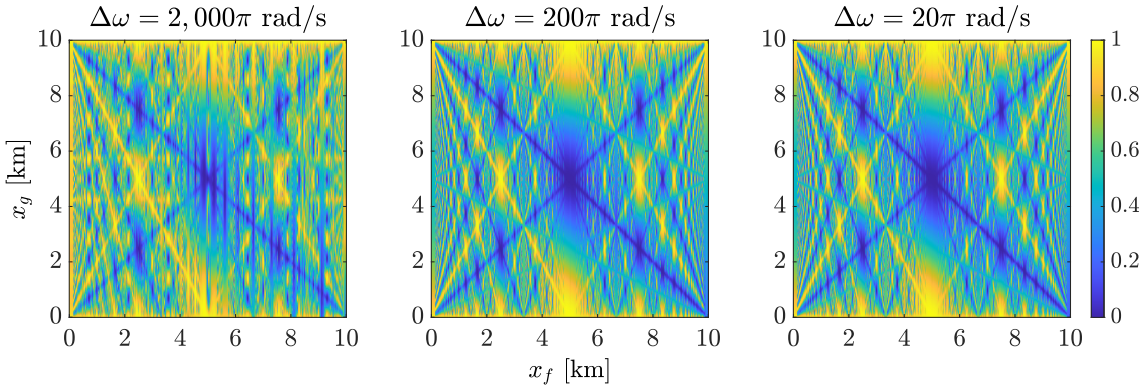

Source: Author

Many secondary minimums occurred for faults on the lines of both lengths; for instance, a diagonal of secondary minimums from the upper-right corner to the lower-left corner was formed in the figures.

Figure 32 – $\mathcal{E}_v(x_g)$ for $\ell = 1,000$ km with $\Delta x_f = \Delta x_g = 1$ km

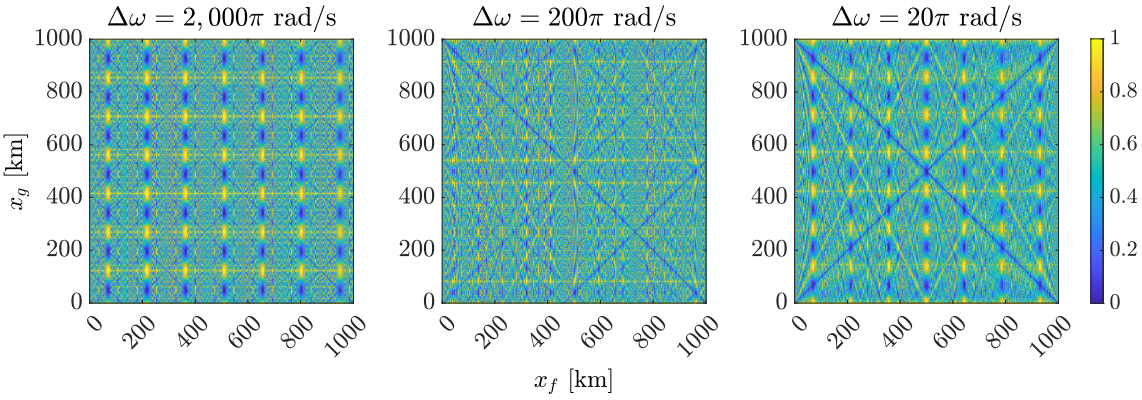

Source: Author

Table 9 – Percentage of fault locations correctly estimated [%] by $\mathcal{E}_v(x_g)$ for three values of Δx_g and $\Delta\omega$, for $\ell = 10$ km

Δx_g [km]	$\Delta\omega$ [rad/s]		
	$2,000\pi$	200π	20π
100	90.91	90.91	90.91
10	95.05	96.04	94.06
1	42.46	60.54	58.94

Table 10 – Percentage of fault locations correctly estimated [%] by $\mathcal{E}_v(x_g)$ for three values of Δx_g and $\Delta\omega$, for $\ell = 1,000$ km

Δx_g [km]	$\Delta\omega$ [rad/s]		
	$2,000\pi$	200π	20π
100	81.82	90.91	81.82
10	94.06	98.02	97.03
1	85.11	99.70	98.90

The results also showed that $\mathcal{E}_v(x_g)$ might be dependent on $\Delta\omega$, although not in a degree that worsened or improved its performance.

The influence of r/x_l on $\mathcal{E}_v(x_g)$, considering the lossy line, is then shown in Figures 33 and 34 for the eight values of $1/20$, $1/10$, $1/4$, 1, $1/2$, 2, 4, and 10, again, for $\ell = 10$ km and $\Delta x_f = \Delta x_g = 100$ m, and $\ell = 1,000$ km and $\Delta x_f = \Delta x_g = 10$ km, with $\Delta\omega = 200\pi$ rad/s.

Table 11 present the percentages of correct estimations by the $\mathcal{E}_v(x_g)$ metric in Figures 33 and 34.

Figure 33 – $\mathcal{E}_v(x_g)$ normalised for $\ell = 10$ km and eight values of r/x_l

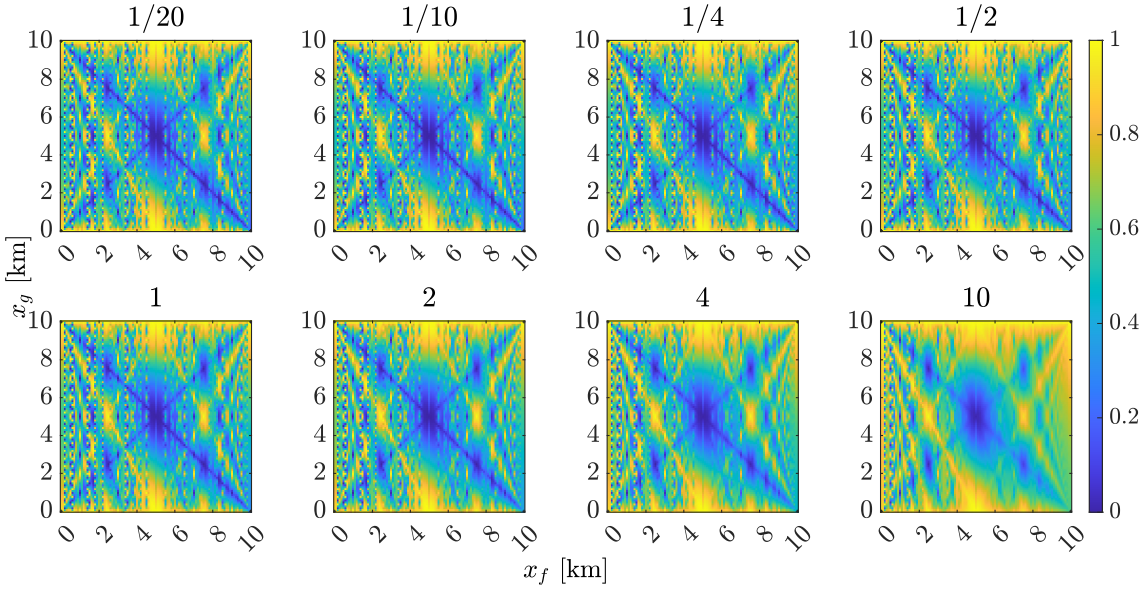

Source: Author

Figure 34 – $\mathcal{E}_v(x_g)$ normalised for $\ell = 1,000$ km and eight values of r/x_l

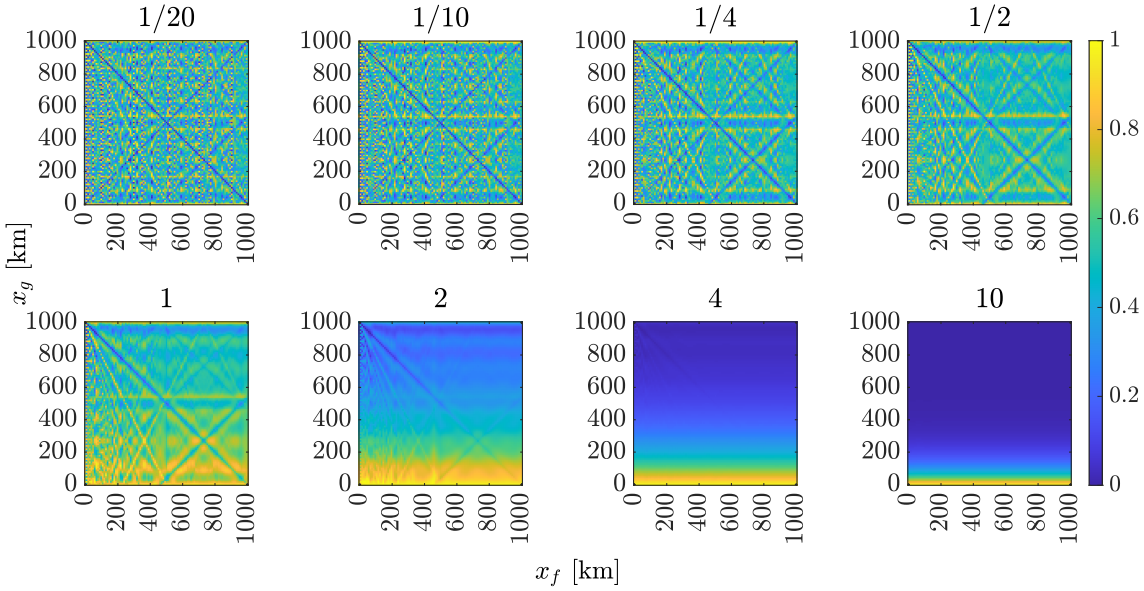

Source: Author

By Figure 33 and Table 11, for $\ell = 10$ km, the fault-location estimations through $\mathcal{E}_v(x_g)$ were not impacted by the resistance of the lines. Faults at up to around 400 m or 600 m were not located in any case. The minimum amount was about 93% of all faults correctly located when $r/x_l = 10$.

Yet, for $\ell = 1,000$ km, Figure 34 and Table 11 show that the correct fault positions were estimated mainly for r/x_l relations lower than 1. For r/x_l equal to 1, 2, 10, and 10, only the faults nearer than 55 km, 26 km, 12 km, and 8 km, respectively, from the

Table 11 – Percentage of fault locations correctly estimated [%] by $\mathcal{E}_v(x_g)$ for eight values of r/x_l, for $\ell = 10$ km and $\ell = 1,000$ km

r/x_l	$\ell = 10$ km	$\ell = 1,000$ km
$1/20$	95.05	98.02
$1/10$	95.05	98.02
$1/4$	95.05	97.03
$1/2$	94.06	90.10
1	94.06	51.49
2	93.07	24.75
4	93.07	10.89
10	93.07	6.93

probe end, were correctly located. Over the number of cases, only about 51% and 7% of the faults were correctly located when $r/x_l = 1$ and $r/x_l = 10$, respectively, while about 90% were when $r/x_l = 1/2$. That indicates some drawback of the $\mathcal{E}_v(x_g)$ metric for distant faults to the probe end when losses are considered. However, as real long lines generally have low values of r/x_l, this drawback might not strongly impact the metric's estimations.

The faults at the line extremities were not located.

As done in (CHEN *et al.*, 2019; WANG *et al.*, 2020b), one can analyse the resemblance between the transfer functions $H_{DT}(x_f, \omega) = \frac{V_f(\omega)}{V_m(x_f,\omega)}$ and $H_{RT}(x_g, \omega) = \frac{I(x_g,\omega)}{I^*_m(x_f,\omega)}$, where $I^*_m(\omega) = \frac{V^*_m(\omega)}{Z_T}$, to have the GFL where $H_{DT}(x_f, \omega) = H_{RT}(x_g, \omega)$, according to the single-end form of the method shown in Figure 5. That can also be performed by the calculation of the correlation $\rho_{HH}(x_g)$ in (34), as in (HE; COZZA; XIE, 2020a).

Following this latter approach, $H_{DT}(x_f, \omega)$, $H_{RT}(x_g, \omega)$, and $\rho_{HH}(x_g)$ are calculated for $\ell = 10$ km, considering Δx_f and Δx_g equal to 1 km, 100 m, and 10 m, and for $\ell = 1,000$ km, considering 100 km, 10 km, and 1 km, as for the previous evaluations. $\Delta\omega$ varies between $2,000\pi$ rad/s, 200π rad/s, and 20π rad/s, with ω within the range $[10^3, 5 \times 10^5] \times 2\pi$ rad/s.

$\rho_{HH}(x_g)$ for each case is then shown in Appendix A.

$\rho_{HH}(x_g)$ is maximum when $x_f = x_g$ for any value of $\Delta x_g = 1$ and $\Delta\omega$. The percentage of correct estimations is 100% in all cases. In fact, it needs to occur, since $H_{DT}(x_f, \omega) = H_{RT}(x_g, \omega)$ in these cases. The transfer functions for the faults in the DT and RT stages are equal, and the correlation between them is maximum.

$\rho_{HH}(x_g)$ for $\ell = 10$ km and $\ell = 1,000$ km, with Δx_g equal to 100 m and 10 m respectively, and with $\Delta\omega = 200\pi$ rad/s, are else plotted in figures presented in Appendix A for r/x_l equal to the eight values of $1/20$, $1/10$, $1/4$, 1, $1/2$, 2, 4, and 10, for the lossy

condition.

The results show that increasing r/x_l does not impact the fault-location estimations by the correlation $\rho_{HH}(x_g)$. The percentage of correct estimations is 100% in all cases either.

The applicability of the EMTR method on fault location in a single-conductor non-branched system was thus verified through the analytical formulation in the frequency domain with the metrics proposed in (RAZZAGHI *et al.*, 2013a; CODINO *et al.*, 2017; WANG *et al.*, 2017; CHEN *et al.*, 2019; WANG *et al.*, 2020b), considering different $\Delta\omega$, Δx_g, and r/x_l when applied. Yet, the analytical evaluations are limited as many assumptions were taken for its formulation; analyses in the time domain are necessary to draw conclusions about the performance of the method.

5.2 Single-Conductor Non-Branched Transmission-Line System in Time-Domain Simulations

A time-domain evaluation of the EMTR method follows the analytical one (*cf.* Section 4.2). The method is applied to a numerical model equivalent to the 10-km overhead single-conductor transmission line between two transformers of the analytical evaluation. The EMTP-RV is used as the EMTP-type tool for the numerical modelling and the fault simulations, yielding the data of the fault-induced EMTs for the analyses.

The CP transmission-line model is employed (*CP line/cable m-phase* part in the software), with the same parameters of the lossless condition, $c = 10.7\ \mathrm{pF/m}$, $g = 0\ \mathrm{S}$, $l = 1.1\ \mu\mathrm{H/m}$, and $r = 0\ \Omega$. Line sections of $100\ \mathrm{m}$ are used for the conductor, returning an amount of 101 fault locations along the 10-km line, where $\Delta x_f = \Delta x_g = 100\ \mathrm{m}$.

Identical high impedances of $100\ \mathrm{k}\Omega$ from the analytical evaluation are placed at both line extremities to model the transformers, with the transformer parameters also independent of the frequency.

The time step is chosen as $0.1\ \mu\mathrm{s}$. This value is lower than the propagation delay of the CP line sections of $100\ \mathrm{m}$ for the given parameters[5].

Faults are simulated at all 101 fault locations in both DT and RT stages. The fault is solid and modelled by a unitary voltage step function in the DT stage, like the analytical case of Figure 2, using the *DC voltage source* part of the software. The voltage step occurs at the simulation time equal to $0\ \mathrm{s}$ and lasts for the whole duration of the DT simulations. In the RT stage, the fault is modelled as just a connection to the ground.

The voltage signals are recorded. Both double- and single-end recordings are tested.

[5]The propagation delay for the CP line model is the time it takes an electromagnetic wave to travel from one end of a line section to the other, given the length of the line section and the velocity of the wave. Additionally, the wave velocity for the CP model is the phase velocity, v, only related to the line section's parameters.

In the double-end recording, the probe ends are at the positions corresponding to 0 km and 10 km. The probe end is at 0 km in the single-end form. Three durations for the recording window are applied in both types of recording, $T = 1$ ms, $T = 10$ ms, and $T = 100$ ms, to evaluate its influence on the method's performance (*cf.* Section 4.4.1). These values of T correspond to $\Delta\omega = 2,000\pi$ rad/s, $\Delta\omega = 200\pi$ rad/s, and $\Delta\omega = 20\pi$ rad/s, respectively, given that $\Delta\omega = 2\pi\frac{1}{T}$ by signal analysis (OPPENHEIM; WILLSKY; YOUNG, 1983).

In the RT stage of the double-end form of the method, two sources inject back into the system the time-reversed version of voltage signals recorded at the two probes in the DT stage. The sources are at both system ends, upstream of the high impedances. Similarly, in the single-end form of the method, only a single source injects back the time-reversed signals at the same side of the system where the signals were recorded. The *Table function voltage source* part is used to model these sources. This part injects the samples of the time-reversed signals following a two-column table of time and voltage data pairs in a generated file in MATLAB® with the extension "dat".

The $\mathcal{E}_i(x_g)$ and $\mathcal{P}_i(x_g)$ criteria are applied to estimate the fault location (*cf.* Section 4.6), as given by (8) and (9).

The results yielded by $\mathcal{E}_i(x_g)$ and $\mathcal{P}_i(x_g)$ are shown as *colormap* matrices in Figures 35 to 38.

Figure 35 – $\mathcal{E}_i(x_g)$ normalised for $\ell = 10$ km with $\Delta x_f = \Delta x_g = 100$ m in the time-domain analyses and double-end recording

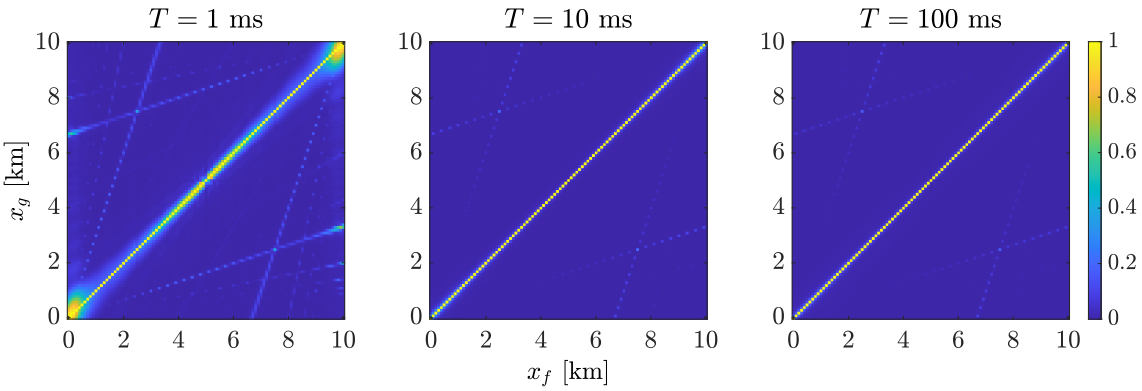

Source: Author

All fault locations were correctly estimated by $\mathcal{E}_i(x_g)$ with the double-end recording, regardless of the value of T, as shown in Figure 35, and the $\mathcal{P}_i(x_g)$ metric only returned wrong fault location estimations for the line extremities, $x_f = 0$ km and $x_f = 10$ km, where the probes are, and only when $T = 1$ ms, as shown in Figure 37.

With the single-end recording, Figure 36 shows that all fault locations from 200 m to 10 m were correctly estimated by $\mathcal{E}_i(x_g)$ regardless of the value of T. The exceptions of the first two x_f agreed with the results observed in the analytical evaluation in Figure

Figure 36 – $\mathcal{E}_i(x_g)$ normalised for $\ell = 10$ km with $\Delta x_f = \Delta x_g = 100$ m in the time-domain analyses and single-end recording

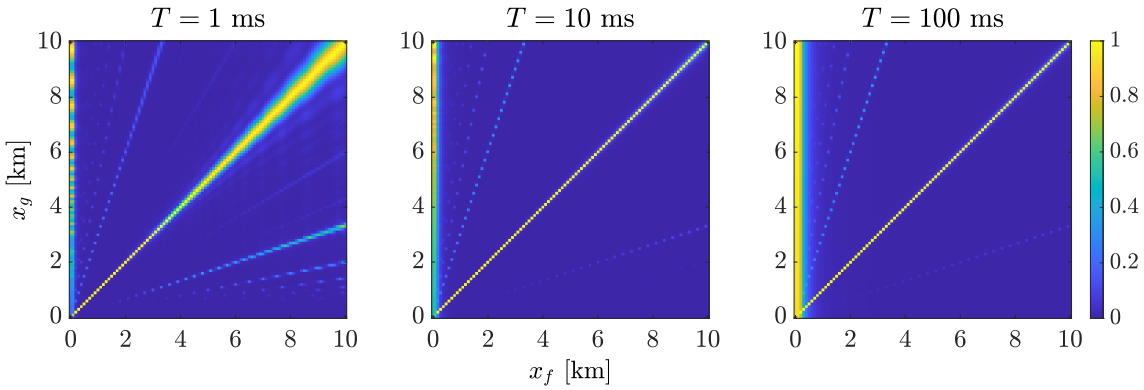

Source: Author

Figure 37 – $\mathcal{P}_i(x_g)$ normalised for $\ell = 10$ km with $\Delta x_f = \Delta x_g = 100$ m in the time-domain analyses and double-end recording

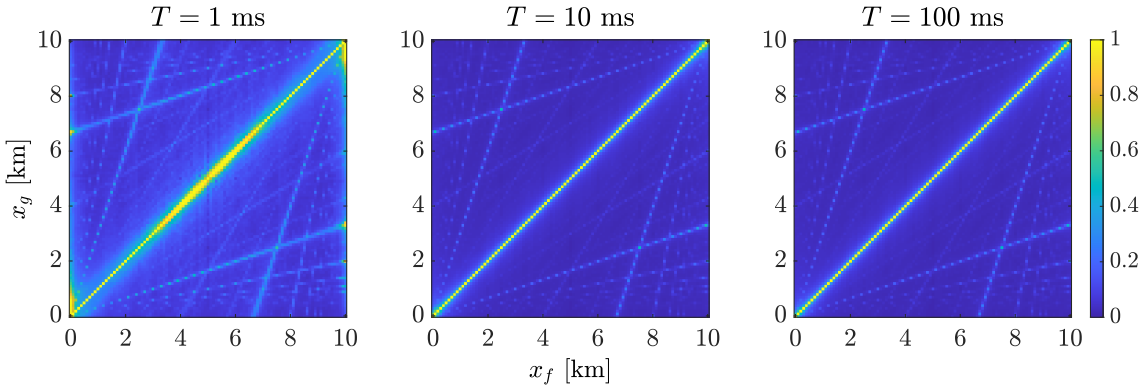

Source: Author

Figure 38 – $\mathcal{P}_i(x_g)$ normalised for $\ell = 10$ km with $\Delta x_f = \Delta x_g = 100$ m in the time-domain analyses and single-end recording

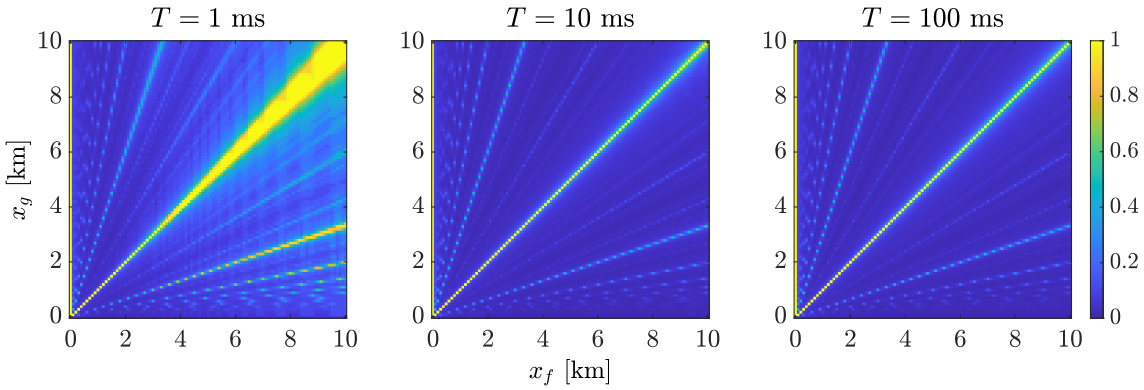

Source: Author

11. The fault-location estimations by $\mathcal{P}_i(x_g)$ were correct for all faults excepting that at the probe-end for $T = 10$ ms and $T = 100$ ms. For $T = 1$ ms, wrong estimations were returned for faults farther than nearly 5 km from the probe end.

The behaviour related to the wrong estimations by $\mathcal{P}_i(x_g)$ in the single-end recording with $T = 1$ ms is observed in Figure 38 by the magnitude picks increasingly spreading out of the diagonal line as farther the fault location is from the probe end for $T = 1$ ms. The magnitude picks in these cases did not always occur when $x_f = x_g$. The increasingly spreading out of the magnitude picks from the diagonal line is also observed in Figure 36 for $\mathcal{E}_i(x_g)$, however not as intense as for $\mathcal{P}_i(x_g)$, i.e., in a degree that might lead to wrong estimations.

Yet, for double-end recording, Figures 35 and 37 show that there was only little concentration of high magnitude values of $\mathcal{E}_i(x_g)$ and $\mathcal{P}_i(x_g)$ around the middle positions of the line with $T = 1$ ms, however without leading to wrong estimations.

Thereby, the results corroborate the influence of T or, in other words, of $\Delta\omega$ on the fault-location estimations, and so does the dependence on the metric applied to the estimations.

5.3 Point-to-Point HVDC Transmission System in Time-Domain Simulations

HVDC transmission systems connecting point-to-point converter stations are similar cases to single-conductor transmission-line systems with earth return (HE; COZZA; XIE, 2020b) and are prone to the application of the EMTR method. The positive pole can be seen as the single conductor, while the negative pole can be as the earth. However, more possible fault conditions can occur in the HVDC system than in the single-conductor one once there are faults involving one or the two poles and ground. Thus, a third conductor aside from the poles is in the system. Faults involving only the two poles are like the condition of the single-conductor fault to ground indeed.

Therefore, another case study is given by fault simulations on a numerical model of a point-to-point HVDC transmission link modelled in EMTP-RV[6] as in the analyses in Section 5.2. Voltage source converters (VSC) in the modular multilevel converter (MMC) technology form the converter stations at both link ends of the system. Figure 39 depicts the VSC-based HVDC system, the converter stations and the ac equivalent sources.

The HVDC link is done through an underground insulated cable. The cable link is

[6]The system, already modelled in two versions, comes with EMTP-RV for fault and power flow simulations. It is one example of the potential of numerical modelling of the software. It presents the sophisticated models of converter stations and underground cables available for the user and the capabilities of advanced numerical representation and simulation of HVDC systems in general. There are no external references to the system on the EMTP-RV documentation.

Figure 39 – Point-to-Point HVDC Transmission System

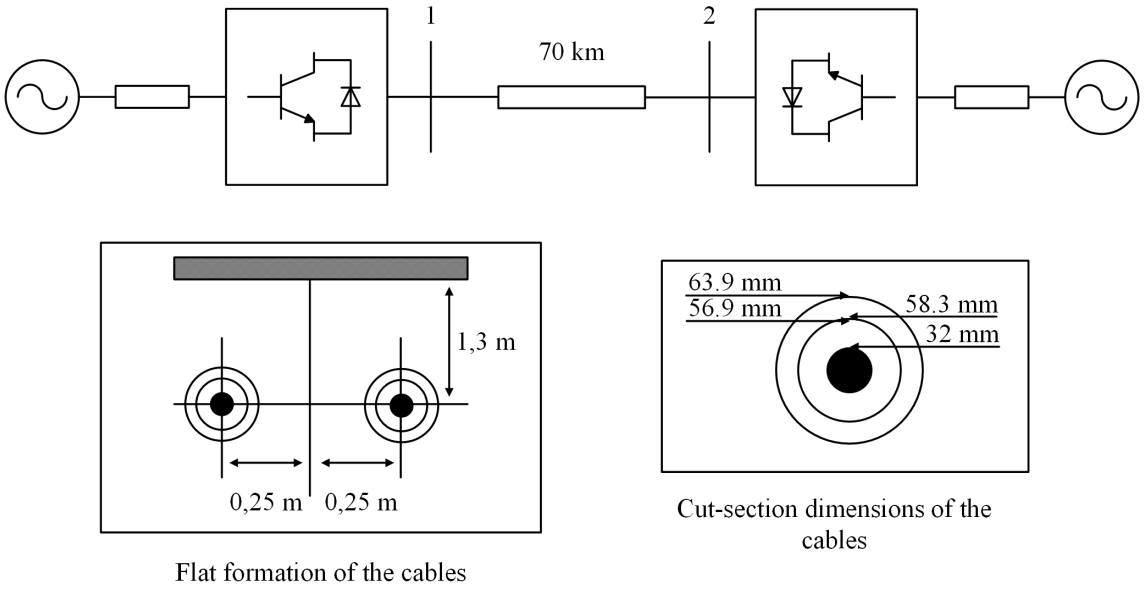

Source: Author

copper, with aluminium tape and cross-linked polyethylene (XPLE) insulation, set in a flat arrangement. The length and cut-section dimensions of the cable link are both shown in Figure 39.

The cable is represented by the wideband (WB) line model, which is the most sophisticated model available in EMTP-RV by the *line/cable data* part of the software, and it is based on the UML. It models the frequency dependence of cable parameters within a wide bandwidth. The parameters for the WB model are shown in Table 12. The resistivity of the core's copper and the tape's aluminium is calculated at $75\ ^{\circ}\mathrm{C}$. There are two single-core cables. The options of *cable model correction* and *dc correction* are selected in the model.

The systems on the ac side are represented by equivalent sources. They both operate rms line-to-line voltages of $400\ \mathrm{kV}$ in $50\ \mathrm{Hz}$ and have both short-circuit powers of $10,000\ \mathrm{MVA}$ and ratios of 12 for the relation between the inductive reactance to the resistance of their equivalent impedance.

The *MMC station* part of EMTP-RV is used for the converter stations in a mono-polar configuration, whose data is shown in Table 13. The two converter stations are connected to busbars 1 and 2 in Figure 39. The pole-to-pole voltage at the dc side is $640\ \mathrm{kV}$.

Double- and single-end forms of the EMTR method are applied (*cf.* Section 4.2.4) to assess the influence of the double- and single-end measurements on the results. The voltage is chosen for the recording signal $s(t)$ in both cases. The probe end in the single-end form is at busbar 1 in Figure 39. The two are at both busbars 1 and 2 in the double-end form.

Table 12 – Data of the WB cable model

Core conductor's resistivity	$1.78 \times 10^{-8}\ \Omega\,\mathrm{m}$
Tape conductor's resistivity	$2.83 \times 10^{-8}\ \Omega\,\mathrm{m}$
Conductors' relative permeability	1
Conductors' relative permittivity	1
Insulators' relative permittivity	2.5
Insulators' loss factor	0.0004
Soil's resistivity	$100\ \Omega\,\mathrm{m}$
Soil's relative permeability	1
Soil's relative permittivity	1
Minimum frequency of the range	0.01 Hz
Maximum frequency of the range	100×10^{6} Hz
Points/decade	20
Number of decades	10
Convergence tolerance	1%
Residue/Pole threshold	1000

Table 13 – Data of the VSC-MMC station

Rated power	1000 MVA
AC primary voltage	400 kV
AC secondary voltage	320 kV
Transformer reactance	0.18 pu
Transformer resistance	0.001 pu
MMC arm inductance	0.15 pu
Capacitor energy in each Submodule (SM)	$40\ \mathrm{kJ/MVA}$
Number of submodules per arm	400
Conduction losses of each IGBT/diode	$0.001\ \Omega$
Connect star point reactor	1

Two lengths for the recording window T are chosen for the TR process, 10 ms and 1 ms (*cf.* Section 4.4.1) in the two forms of the method used, to observe the influence of the recording duration. The length of 10 ms was considered based on (RAZZAGHI *et al.*, 2014), where it is said that the protection system operation in an MTDC network must happen in less than 10 ms after the fault to prevent the power converters from damage. The recording duration of 1 ms is shorter than the lowest evaluated in (RAZZAGHI *et al.*, 2014) (3 ms) and shorter than the time until any common protection system trips. Notwithstanding, a 1-ms length would be fitting if modern relays were used, whose con-

figured tripping times can be even faster than 1 ms (KASZTENNY; ROSTRON, 2018; SCHWEITZER ENGINEERING LABORATORIES, 2019b). Still, the recordings are taken without any consideration of a trip operation occurring along the recording process. The protection system is not considered and modelled. Thus, only the fault-induced EMTs are taken and not the EMTs induced by the breaker opening.

To have T, the signal can be recorded within successive windows of 10 ms or 1 ms until the fault is detected. The identification of the fault is given by the variation in the magnitude of the recorded voltage, comparing each recording window to its subsequent one (*cf.* Section 4.3). The fault is detected if such variation is higher than 1 kV. Thereby, the detection of the fault actually determines T, which starts some samples before the instant of the fault detection and finishes 10 ms or 1 ms after, often overlapping two recording windows. Figure 40 exemplifies the process for $T = 1$ ms.

Figure 40 – Example of Recording the Signal

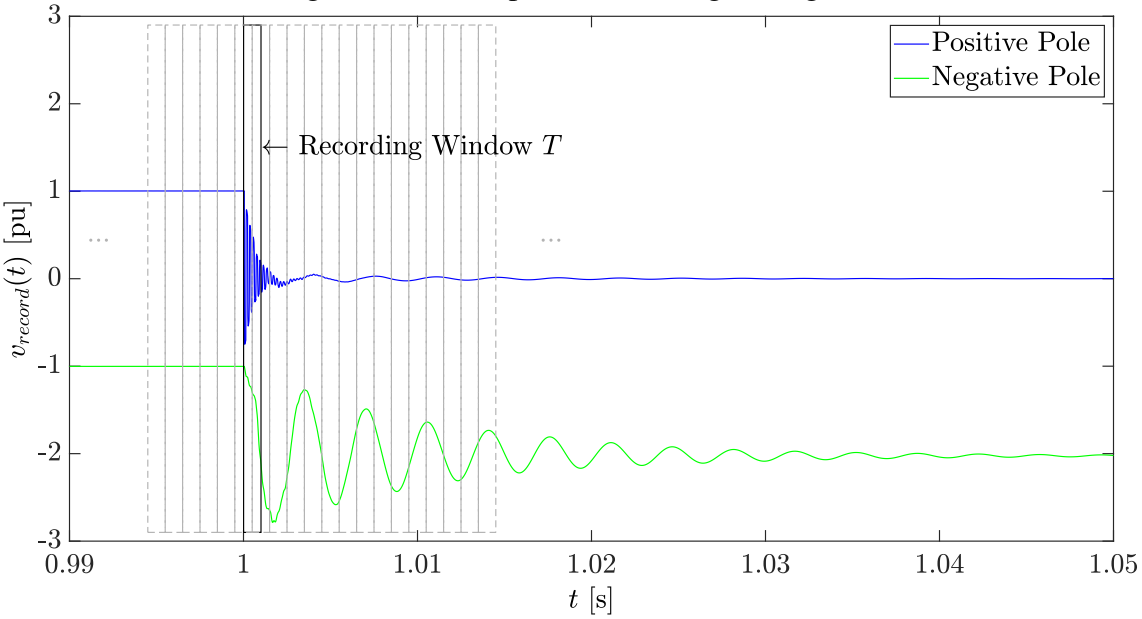

Source: Author

The time step of the DT simulations is chosen as 1 µs, and then each one of the 10-ms and 1-ms windows has $10,000$ and $1,000$ samples, respectively. 1 µs of time step poses a limit to observe transitions on the fault-induced EMTs: those transitions lasting less than 1 µs and between two samples are not taken (COSTA *et al.*, 2020).

An HP filter is applied to the recorded fault-induced EMTs after windowing, as said in Section 4.4.2. A Butterworth filter of 5th order is used, changing the cut-off frequency between the values of 1 kHz, 3 kHz, and 5 kHz to evaluate its impact on the results of the method.

Pole-to-ground and pole-to-pole faults are simulated every 1 km along the cable in the DT stage. So, seventy locations are evaluated, starting at 1 km from busbar 1. The values of fault resistances considered are 1 Ω, 5 Ω, 10 Ω, and 50 Ω. Thus, the influence of the

fault location and fault resistance on the results are else observed (*cf.* Section 4.2.3) as the influence of the filter's cut-off frequency.

The same seventy fault locations are chosen for the GFLs. In any case, faults in the RT simulations have a resistance of $1\ \Omega$.

The time step in the RT simulations is equally $1\ \mu s$. The sampling of the time-reversal signal is not changed in relation to the recorded signal, i.e., no operation of down- or up-sampling is performed on it.

Both $\mathcal{P}_i(x_g)$ and $\mathcal{E}_i(x_g)$ criteria are applied to estimate the fault location, assessing the impact of the metric (*cf.* Section 4.6).

Therefore, there are twelve cases of DT simulations where the cut-off frequency of the HP filter is changed between the values of $1\ \mathrm{kHz}$, $3\ \mathrm{kHz}$, and $5\ \mathrm{kHz}$, with a fault resistance of $1\ \Omega$ in all, using double- and single-end measurements and the WB model for the cable in both DT and RT stages; there are twelve cases of DT simulations where the fault resistance is changed between the values of $5\ \Omega$, $10\ \Omega$, and $50\ \Omega$, applying $1\ \mathrm{kHz}$ for the cut-off frequency of the HP filter in all, also using double- and single-end measurements and the WB model in both DT and RT stages; and, there are six cases of DT simulations where the cut-off frequency of the HP filter is again changed between the values of $1\ \mathrm{kHz}$, $3\ \mathrm{kHz}$, and $5\ \mathrm{kHz}$, with a fault resistance of $1\ \Omega$ in all, but using only single-end measurements and the WB model only in the DT stage, while the CP model in the RT stage. These last evaluations are for analysing the influence of changing the cable model in the RT simulations (*cf.* Section 4.5).

The details of the numerical modelling of the system in EMTP-RV and simulation parameters are in Appendix B.

Figures 41 to 56 present as *colormap* matrices the results for the application of $\mathcal{P}_i(x_g)$ and $\mathcal{E}_i(x_g)$ criteria for the cases where the cut-off frequency of the HP filter is changed, and the WB model is used in both DT and RT stages.

For double-end measurements, for both pole-to-ground and pole-to-pole faults, both $\mathcal{P}_i(x_g)$ and $\mathcal{E}_i(x_g)$ criteria, both of recording durations $T = 10\ \mathrm{ms}$ and $T = 1\ \mathrm{ms}$, and with any of the three cut-off frequencies, the behaviour of the method was almost symmetric regarding the half length of the link, as shown in Figures 41, 42, 45, 46, 49, 50, 53, and 54. The same is not observed in Figures 43, 44, 47, 48, 51, 52, 55, and 56 for single-end measurements, where the results changed as far from the single probe end was the fault location, also for both pole-to-ground and pole-to-pole faults, both $\mathcal{P}_i(x_g)$ and $\mathcal{E}_i(x_g)$ criteria, both of recording durations $T = 10\ \mathrm{ms}$ and $T = 1\ \mathrm{ms}$, and with any of the three cut-off frequencies.

For both double- and single-end recordings in any condition, the picks of the maximum magnitude of both $\mathcal{P}_i(x_g)$ and $\mathcal{E}_i(x_g)$ were partially at points around the diagonals of the *colormap* matrices, but not exactly at their, and partially at other off points from the diagonals. Also, the influence of the cut-off frequency of the HP filter is observed in

Figure 41 – Results by $\mathcal{P}_i(x_g)$ for pole-to-ground faults with different cut-off frequencies, double-end recording and $T = 10$ ms

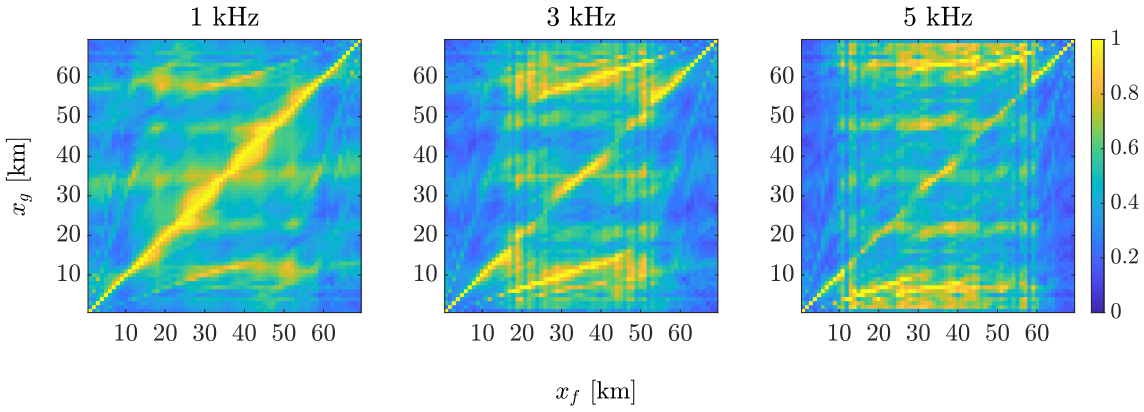

Source: Author

Figure 42 – Results by $\mathcal{P}_i(x_g)$ for pole-to-ground faults with different cut-off frequencies, double-end recording and $T = 1$ ms

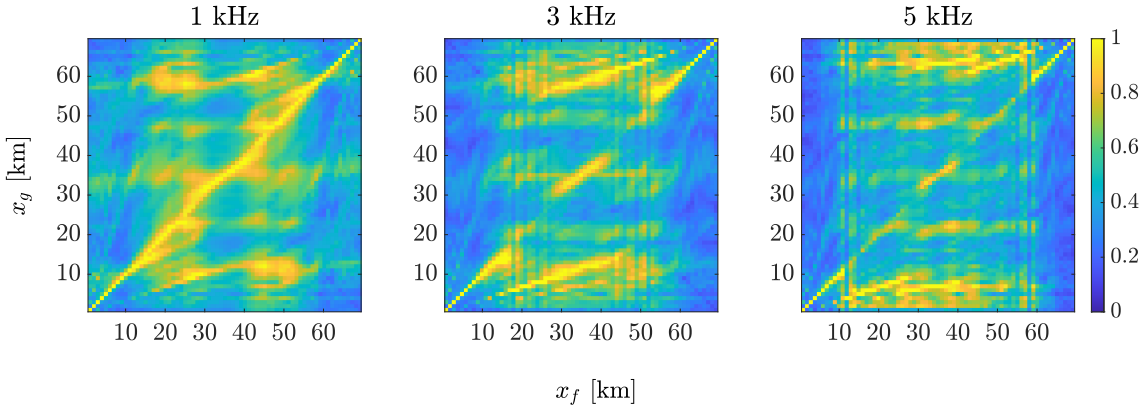

Source: Author

all Figures 41 to 56, regardless of the form of the method, if double- or single-end.

The average and maximum errors on the fault-location estimation in the cases of Figures 41 to 56 are summarised in Tables 14 to 17. Tables 14 and 15 show them of pole-to-ground faults with double-end measurements; Tables 16 and 17 of pole-to-ground faults with single-end measurements; Tables 18 and 19 of pole-to-pole faults with double-end measurements; and, Tables 20 and 21 of pole-to-pole faults with single-end measurements. The cut-off frequency is denoted in all tables by ν_c.

The average and maximum errors by both $\mathcal{P}_i(x_g)$ and $\mathcal{E}_i(x_g)$ in Table 14 and by $\mathcal{P}_i(x_g)$ in Table 18 with double-end recording and $T = 10$ ms were relatively low, i.e., lower than 5%, taken as a threshold value for error, specific for the cut-off frequency at 1 kHz. The filtering at 3 kHz and 5 kHz led to average and maximum errors up to more than forty times higher than the filtering at 1 kHz in these cases.

Figure 43 – Results by $\mathcal{P}_i(x_g)$ for pole-to-ground faults with different cut-off frequencies, single-end recording and $T = 10$ ms

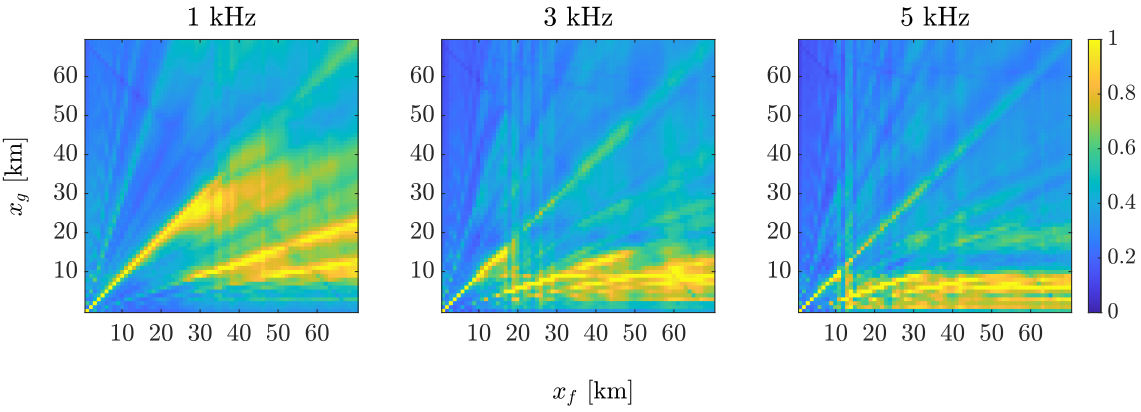

Source: Author

Figure 44 – Results by $\mathcal{P}_i(x_g)$ for pole-to-ground faults with different cut-off frequencies, single-end recording and $T = 1$ ms

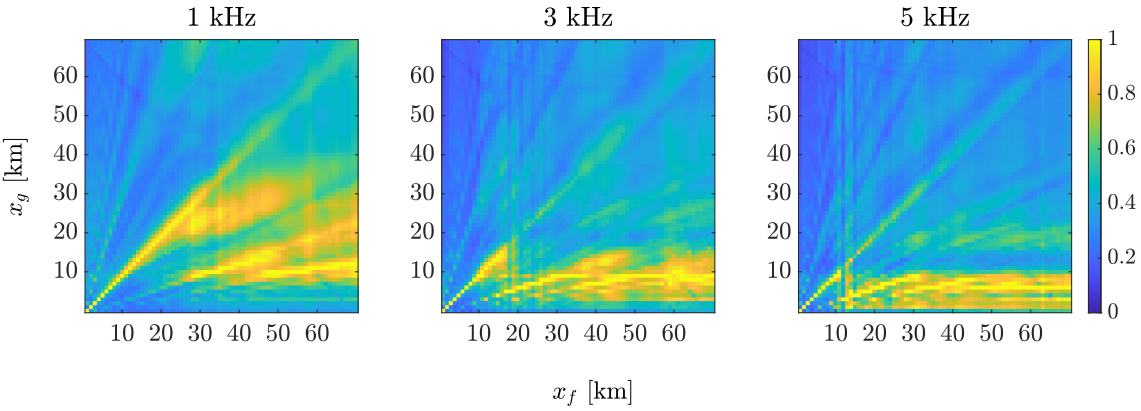

Source: Author

Table 14 – Representative results for pole-to-ground faults with different cut-off frequencies, double-end recording and $T = 10$ ms

ν_c [kHz]	$\mathcal{P}_i(x_g)$		$\mathcal{E}_v(x_g)$	
	Average Error [%]	Maximum Error [%]	Average Error [%]	Maximum Error [%]
1	0.37	2.8	0.50	1.43
3	12.13	42.86	14.95	58.57
5	17.16	45.71	15.94	44.28

The average and maximum errors with $T = 1$ ms for $\nu_c = 1$ kHz were higher than with $T = 10$ ms for pole-to-ground faults by both $\mathcal{P}_i(x_g)$ and $\mathcal{E}_i(x_g)$ and for pole-to-pole faults by $\mathcal{P}_i(x_g)$, according to Tables 15 and 19. The average errors by $\mathcal{P}_i(x_g)$ and $\mathcal{E}_i(x_g)$, for instance, were about ten and two times higher in Table 15 compared to Table 14 and

Figure 45 – Results by $\mathcal{E}_i(x_g)$ for pole-to-ground faults with different cut-off frequencies, double-end recording and $T = 10$ ms

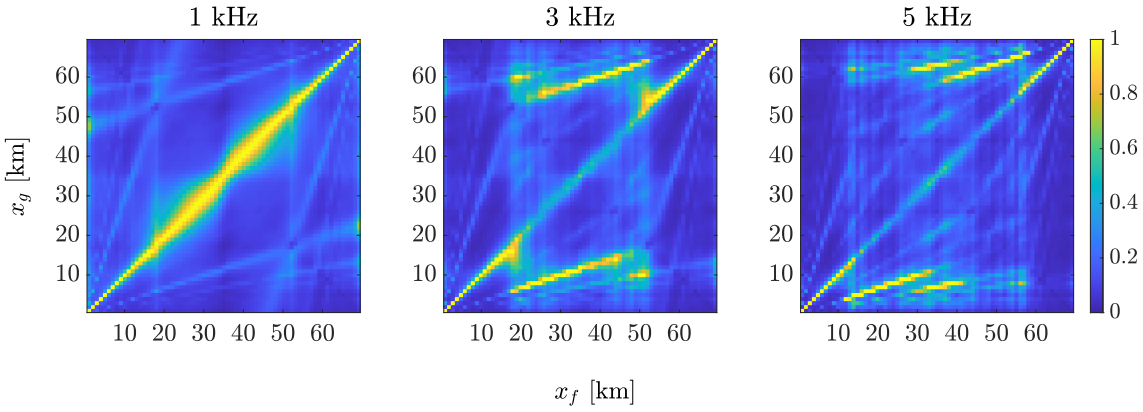

Source: Author

Figure 46 – Results by $\mathcal{E}_i(x_g)$ for pole-to-ground faults with different cut-off frequencies, double-end recording and $T = 1$ ms

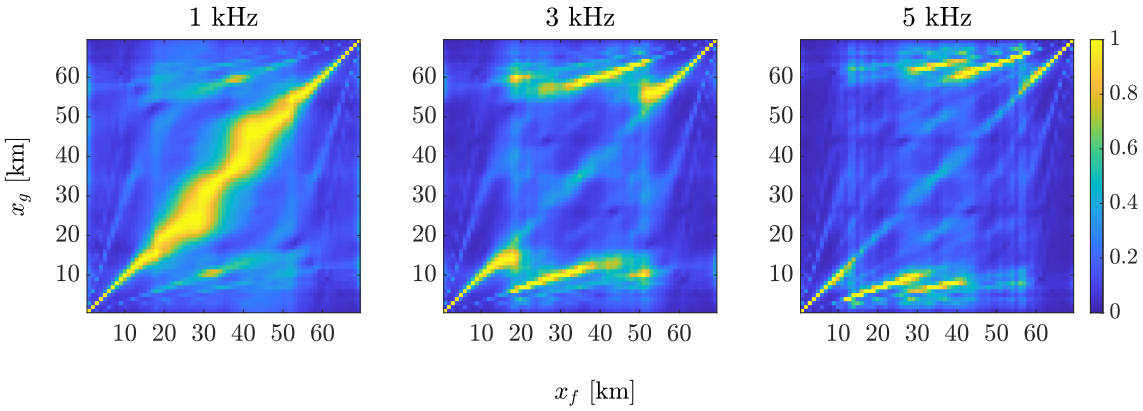

Source: Author

Table 15 – Representative results for pole-to-ground faults with different cut-off frequencies, double-end recording and $T = 1$ ms

ν_c [kHz]	$\mathcal{P}_i(x_g)$		$\mathcal{E}_v(x_g)$	
	Average Error [%]	Maximum Error [%]	Average Error [%]	Maximum Error [%]
1	3.56	27.14	1.12	5.71
3	13.10	38.57	13.81	58.57
5	17.14	45.71	16.31	44.28

by $\mathcal{P}_i(x_g)$ about eight times higher in Table 19 compared to Table 18.

Higher average and maximum errors were found for the filtering at 3 kHz and 5 kHz in Tables 15 and 19 by both criteria. This differs from the results by $\mathcal{E}_i(x_g)$ for pole-to-pole faults with $T = 10$ ms in Table 18, where the maximum error with $\nu_c = 1$ kHz was

Figure 47 – Results by $\mathcal{E}_i(x_g)$ for pole-to-ground faults with different cut-off frequencies, single-end recording and $T = 10$ ms

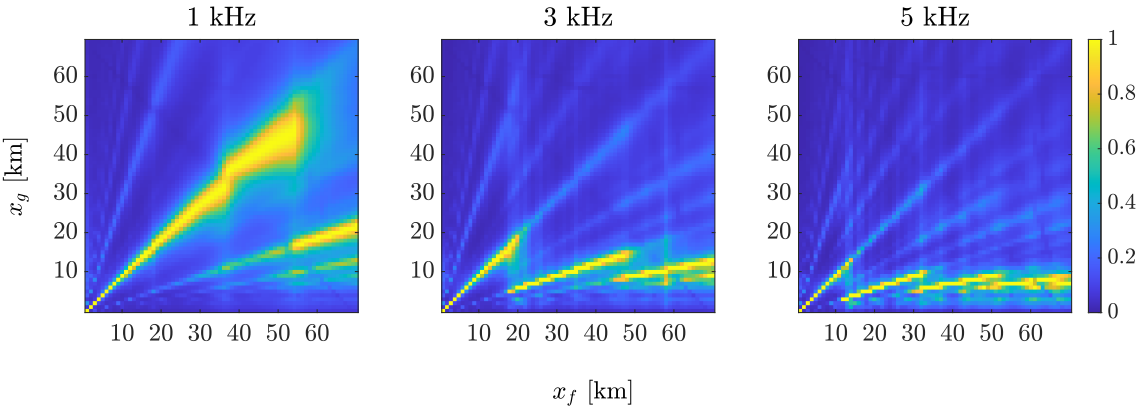

Source: Author

Figure 48 – Results by $\mathcal{E}_i(x_g)$ for pole-to-ground faults with different cut-off frequencies, single-end recording and $T = 1$ ms

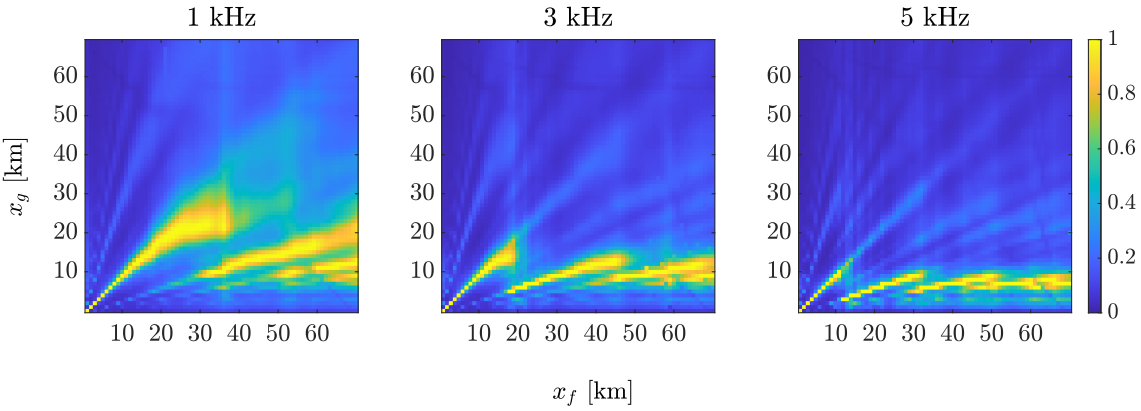

Source: Author

Table 16 – Representative results for pole-to-ground faults with different cut-off frequencies, single-end recording and $T = 10$ ms

ν_c [kHz]	$\mathcal{P}_i(x_g)$		$\mathcal{E}_v(x_g)$	
	Average Error [%]	Maximum Error [%]	Average Error [%]	Maximum Error [%]
1	29.41	78.47	15.69	67.14
3	37.39	85.71	35.20	84.28
5	40.75	90.00	39.82	88.57

higher than with 3 kHz and 5 kHz.

The average and maximum errors by $\mathcal{P}_i(x_g)$ and $\mathcal{E}_i(x_g)$ with single-end recording were in general much higher from those with double-end recording, as seen in Tables 16, 17, 20, and 21 compared to Tables 14, 15, 18, and 19, respectively.

Figure 49 – Results by $\mathcal{P}_i(x_g)$ for pole-to-pole faults with different cut-off frequencies, double-end recording and $T = 10$ ms

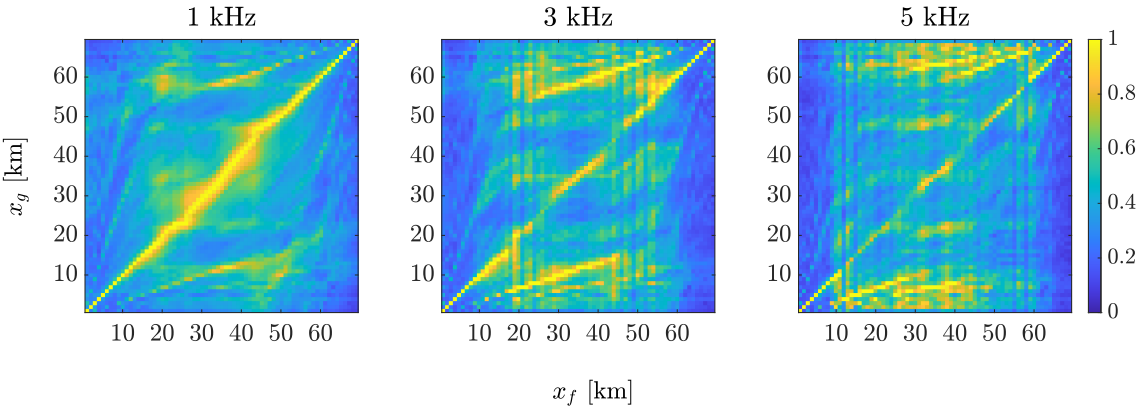

Source: Author

Figure 50 – Results by $\mathcal{P}_i(x_g)$ for pole-to-pole faults with different cut-off frequencies, double-end recording and $T = 1$ ms

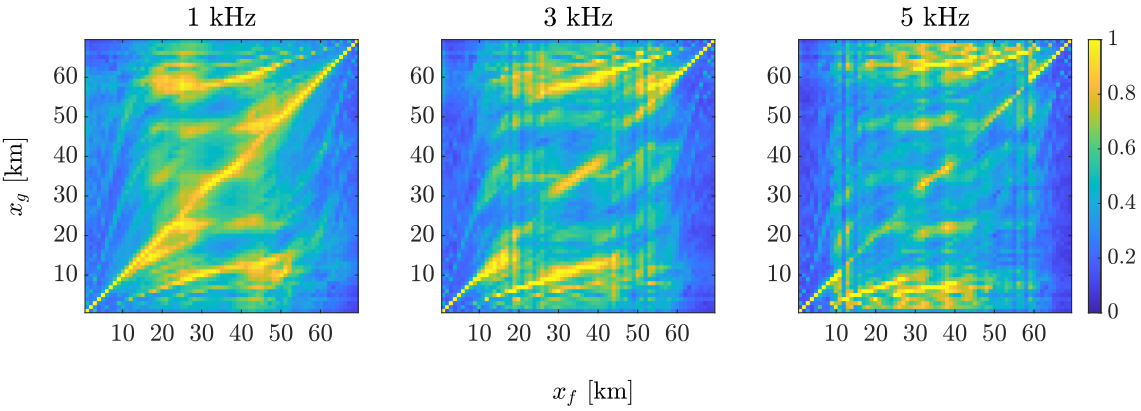

Source: Author

Table 17 – Representative results for pole-to-ground faults with different cut-off frequencies, single-end recording and $T = 1$ ms

ν_c [kHz]	$\mathcal{P}_i(x_g)$		$\mathcal{E}_v(x_g)$	
	Average Error [%]	Maximum Error [%]	Average Error [%]	Maximum Error [%]
1	32.20	81.43	30.18	81.43
3	38.20	85.71	36.37	85.71
5	40.79	90.00	39.94	88.57

With $T = 10$ ms, the average errors by $\mathcal{P}_i(x_g)$ and $\mathcal{E}_i(x_g)$ with $\nu_c = 1$ kHz in Table 16 were up to eighty and forty times higher than in Table 14, respectively, and about forty and eight times higher in Table 20 than in Table 14, respectively. With $T = 1$ ms, the differences between the average errors in Tables 17 and 15 with $\nu_c = 1$ kHz were about

Figure 51 – Results by $\mathcal{P}_i(x_g)$ for pole-to-pole faults with different cut-off frequencies, single-end recording and $T = 10$ ms

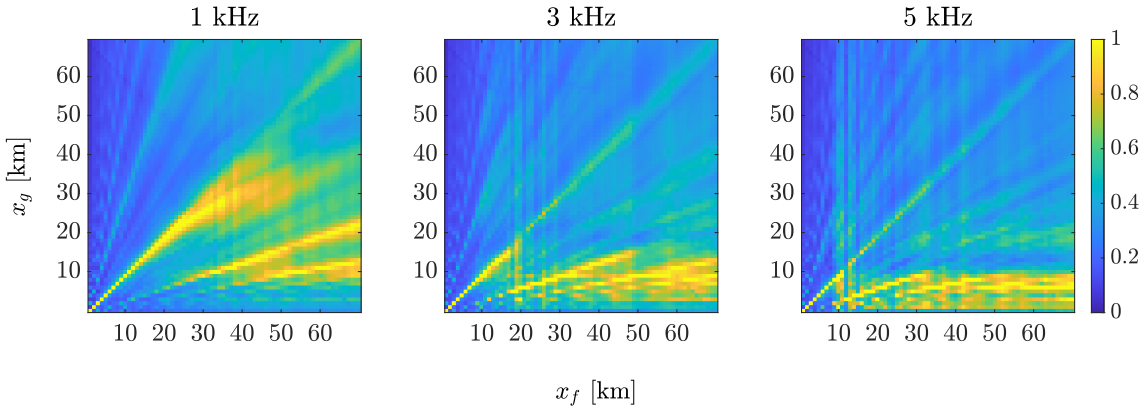

Source: Author

Figure 52 – Results by $\mathcal{P}_i(x_g)$ for pole-to-pole faults with different cut-off frequencies, single-end recording and $T = 1$ ms

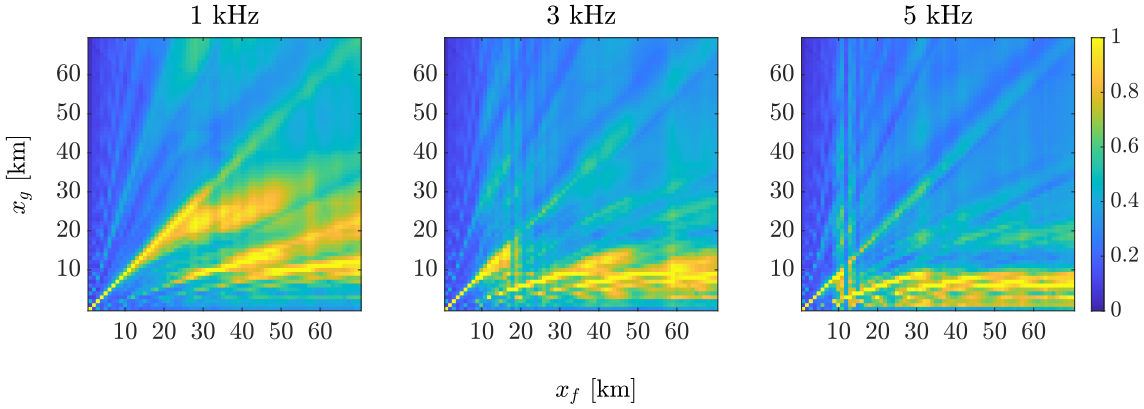

Source: Author

Table 18 – Representative results for pole-to-pole faults with different cut-off frequencies, double-end recording and $T = 10$ ms

ν_c [kHz]	$\mathcal{P}_i(x_g)$		$\mathcal{E}_v(x_g)$	
	Average Error [%]	Maximum Error [%]	Average Error [%]	Maximum Error [%]
1	0.66	4.28	1.99[1]	67.14[2]
3	13.06	42.86	12.48	57.14
5	16.75	45.71	16.19	45.71

[1,2] The fault at 2 km from busbar 1 was estimated by $\mathcal{E}_v(x_g)$ 47 km away, which is a discrepant result compared to the others. The average and maximum errors would be 1.03% and 2.86% if this result was not considered.

Figure 53 – Results by $\mathcal{E}_i(x_g)$ for pole-to-pole faults with different cut-off frequencies, double-end recording and $T = 10$ ms

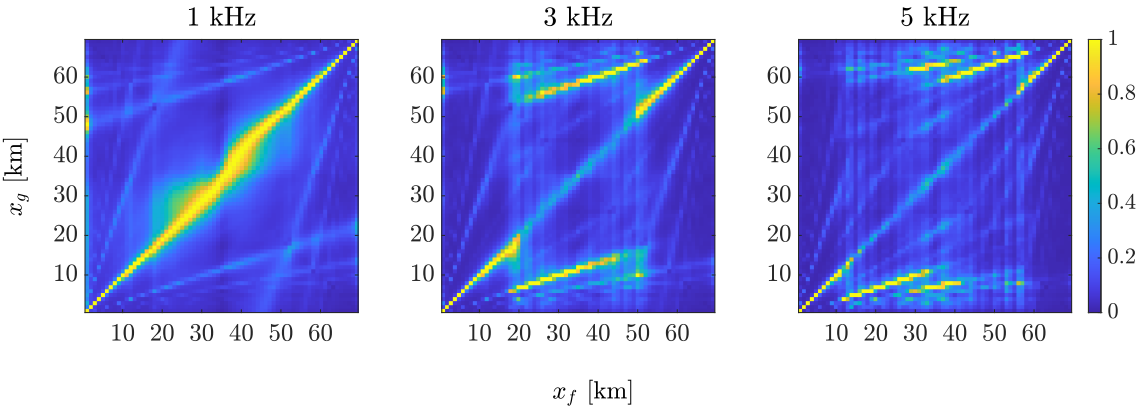

Source: Author

Figure 54 – Results by $\mathcal{E}_i(x_g)$ for pole-to-pole faults with different cut-off frequencies, double-end recording and $T = 1$ ms

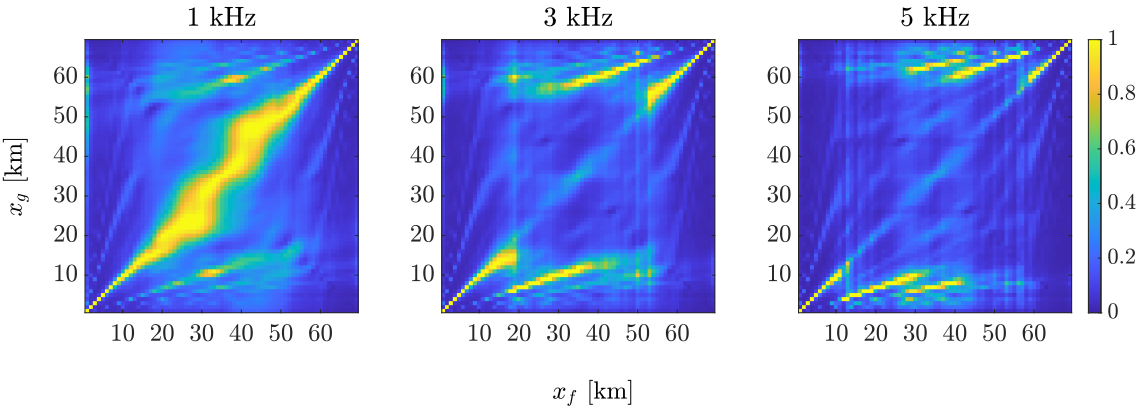

Source: Author

Table 19 – Representative results for pole-to-pole faults with different cut-off frequencies, double-end recording and $T = 1$ ms

ν_c [kHz]	$\mathcal{P}_i(x_g)$		$\mathcal{E}_v(x_g)$	
	Average Error [%]	Maximum Error [%]	Average Error [%]	Maximum Error [%]
1	5.42	45.71	1.68	8.57
3	14.12	38.57	13.17	32.86
5	17.31	45.71	16.65	45.71

nine and thirty times for the same criteria, respectively, and almost six and twenty times in Tables 21 and 19.

The average and maximum errors are also higher for both $T = 10$ ms and $T = 1$ ms with filtering at 3 kHz and 5 kHz and single-end measurements, although the differences

Figure 55 – Results by $\mathcal{E}_i(x_g)$ for pole-to-pole faults with different cut-off frequencies, single-end recording and $T = 10$ ms

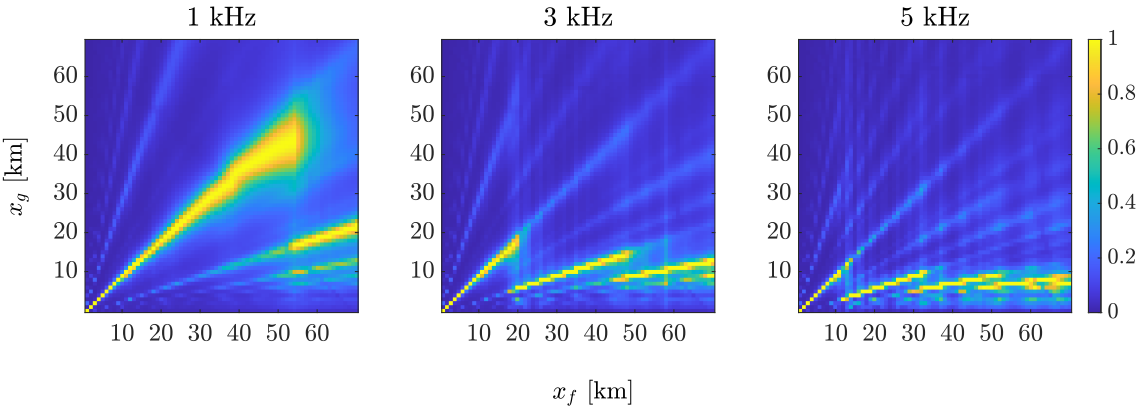

Source: Author

Figure 56 – Results by $\mathcal{E}_i(x_g)$ for pole-to-pole faults with different cut-off frequencies, single-end recording and $T = 1$ ms

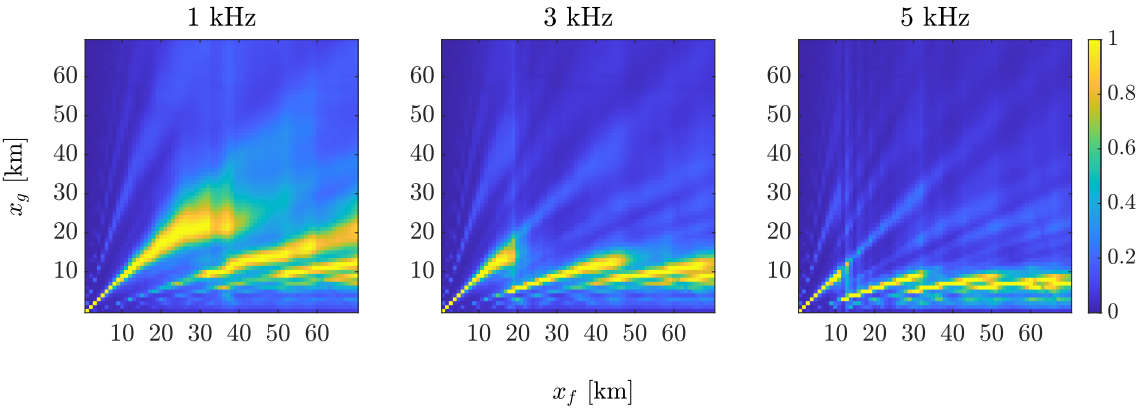

Source: Author

Table 20 – Representative results for pole-to-pole faults with different cut-off frequencies, single-end recording and $T = 10$ ms

ν_c [kHz]	$\mathcal{P}_i(x_g)$		$\mathcal{E}_v(x_g)$	
	Average Error [%]	Maximum Error [%]	Average Error [%]	Maximum Error [%]
1	28.55	77.14	16.65	67.14
3	37.18	85.71	35.26	84.28
5	40.61	90.00	39.71	88.57

to the values with $\nu_c = 1$ kHz were smaller than those for the double-end recording.

By Tables 14 to 21, the recording window with the length of 10 ms provided much higher accuracy for the method than the length of 1 ms only for the double-end recording and cut of lower frequencies off at 1 kHz, especially by $\mathcal{P}_i(x_g)$, given the exception in

Table 21 – Representative results for pole-to-pole faults with different cut-off frequencies, single-end recording and $T = 1$ ms

ν_c [kHz]	$\mathcal{P}_i(x_g)$		$\mathcal{E}_v(x_g)$	
	Average Error [%]	Maximum Error [%]	Average Error [%]	Maximum Error [%]
1	32.08	81.43	31.28	81.43
3	38.31	85.71	36.51	85.71
5	40.71	90.00	40.20	88.57

Table 20. The longer recording window did not present an advantage for the other cases, comparing the values of average and maximum errors.

For $\nu_c = 1$ kHz, higher average error resulted by $\mathcal{E}_i(x_g)$ than by $\mathcal{P}_i(x_g)$ in Table 14; in Table 18, both average and maximum errors were higher by $\mathcal{E}_i(x_g)$ than by $\mathcal{P}_i(x_g)$; in Tables 15 to 17 and 19 to 21 the average and maximum errors by $\mathcal{E}_i(x_g)$ were smaller or equal to those by $\mathcal{P}_i(x_g)$. These results show that the $\mathcal{E}_i(x_g)$ metric might return more accurate estimations than $\mathcal{P}_i(x_g)$ for $T = 1$ ms.

All the results presented the sensitivity of the method related to the filter cut-off frequency, the form of the method regarding the number of recording ends, and the length of the recording window.

An important behaviour of the method in these cases is shown by the similarity of Figures 41 and 49, Figures 42 and 50, Figures 43 and 51, Figures 44 and 52, Figures 45 and 53, Figures 46 and 54, Figures 47 and 55, Figures 48 and 56. They are almost identical to each other. It shows that the performance of the method was not influenced by the fault type in the evaluated cases, although it was very influenced by the fault distance to the probe end and the cut-off frequency of the filter.

Therefore, for these cases, the method was not dependent on the characteristics related to the modes present in the recorded signal, following a phase-to-modal transformation of it. Pole-to-ground faults induce EMTs composed of aerial and ground modes, whilst pole-to-pole faults only induce the aerial mode. The ground mode has a slower propagation velocity than aerial modes. Moreover, the frequency dependence of cable parameters is acknowledged as stronger for the ground mode. Its consideration by the WB line model could strongly impact the induced EMTs by ground faults, and thus worse results for pole-to-ground faults could be expected. Nevertheless, that was not confirmed.

The results for the cases where the fault resistance is changed and the WB model is used in both DT and RT stages are shown in Appendix C by the application of $\mathcal{P}_i(x_g)$ and $\mathcal{E}_i(x_g)$ criteria, likewise.

The results show very similar behaviour for the application of the double- and single-end form of the EMTR method to pole-to-ground and pole-to-pole faults across a resistance of $5\ \Omega$ than that observed in Figures 41 to 56 for the filtering at the cut-off frequency

of 1 kHz, where the fault resistance was 1Ω. However, the method lost performance for the faults across resistances of $10\ \Omega$ and $50\ \Omega$. Only a few faults near the probe end were correctly located in the cases of 10-Ω faults of both types with both values of T, and fewer ones irregularly distanced in the cases of 50-Ω faults. Therefore, fault resistances of about $10\ \Omega$ and higher influenced the method to wrong estimations.

The symmetry is again observed for double-end measurements.

Tables 22 to 29 show the average and maximum errors in the estimation of the fault locations considering the change in the fault resistance. Tables 22 and 23 of pole-to-ground faults using double-end measurements; Tables 24 and 25 of the same faults but using single-end measurements; Tables 26 and 27 of the pole-to-pole faults across the three values of resistance, using double-end measurements; and, Tables 28 and 29 of the same faults but using single-end measurements.

Table 22 – Representative results for pole-to-ground faults with different resistances, double-end recording and $T = 10$ ms

r_f [Ω]	$\mathcal{P}_i(x_g)$		$\mathcal{E}_v(x_g)$	
	Average Error [%]	Maximum Error [%]	Average Error [%]	Maximum Error [%]
5	17.99	77.14	7.27	67.14
10	27.08	77.14	14.57	80.00
50	42.07	81.43	27.58	48.57

Table 23 – Representative results for pole-to-ground faults with different resistances, double-end recording and $T = 1$ ms

r_f [Ω]	$\mathcal{P}_i(x_g)$		$\mathcal{E}_v(x_g)$	
	Average Error [%]	Maximum Error [%]	Average Error [%]	Maximum Error [%]
5	25.09	78.57	6.42	81.43
10	29.38	78.57	20.52	81.43
50	42.19	81.43	24.62	48.57

Tables 22 to 25 show that the average error was about 2.27% and 1.42% higher than the threshold of 5% only in the cases of 5-Ω faults, using double-end recording with the $\mathcal{E}_v(x_g)$ metric. The $\mathcal{P}_i(x_g)$ metric returned average errors of 17.90% and 25.09% in the same cases. In the cases of fault resistances of $10\ \Omega$ and $50\ \Omega$, the average errors were also higher than 14%. The average errors were higher than 20% using single-end measurements. And in all cases, the maximum errors were higher than 67%.

Yet, Table 26 shows the average error about 1.92% and 2.14% higher than 5% in the cases of faults across resistances of $5\ \Omega$ and $10\ \Omega$, whilst Table 27 present a value 1.92%

Table 24 – Representative results for pole-to-ground faults with different resistances, single-end recording and $T = 10$ ms

r_f [Ω]	$\mathcal{P}_i(x_g)$		$\mathcal{E}_v(x_g)$	
	Average Error [%]	Maximum Error [%]	Average Error [%]	Maximum Error [%]
5	32.31	84.28	20.73	68.57
10	34.65	84.28	28.35	80.00
50	34.26	82.86	29.63	77.14

Table 25 – Representative results for pole-to-ground faults with different resistances, single-end recording and $T = 1$ ms

r_f [Ω]	$\mathcal{P}_i(x_g)$		$\mathcal{E}_v(x_g)$	
	Average Error [%]	Maximum Error [%]	Average Error [%]	Maximum Error [%]
5	32.92	81.43	31.94	81.43
10	34.61	82.86	32.37	81.43
50	34.24	82.86	29.28	77.14

Table 26 – Representative results for pole-to-pole faults with different resistances, double-end recording and $T = 10$ ms

r_f [Ω]	$\mathcal{P}_i(x_g)$		$\mathcal{E}_v(x_g)$	
	Average Error [%]	Maximum Error [%]	Average Error [%]	Maximum Error [%]
5	9.65	78.57	5.92	67.14
10	23.60	78.57	7.14	78.57
50	41.86	80.00	37.49	81.43

Table 27 – Representative results for pole-to-pole faults with different resistances, double-end recording and $T = 1$ ms

r_f [Ω]	$\mathcal{P}_i(x_g)$		$\mathcal{E}_v(x_g)$	
	Average Error [%]	Maximum Error [%]	Average Error [%]	Maximum Error [%]
5	16.27	80.00	5.92	80.00
10	26.25	80.00	10.52	81.43
50	42.48	80.00	31.59	81.43

higher only in the cases of faults with $5\ \Omega$, using double-end recording with the $\mathcal{E}_v(x_g)$ metric. Pole-to-pole faults trended to be less influenced by fault resistance than pole-to-ground ones for the same metric and form of the method. Even the $\mathcal{P}_i(x_g)$ metric shows a lower average error than 10% in Table 26. All other cases of fault resistances with double-

Table 28 – Representative results for pole-to-pole faults with different resistances, single-end recording and $T = 10$ ms

r_f [Ω]	$\mathcal{P}_i(x_g)$		$\mathcal{E}_v(x_g)$	
	Average Error [%]	Maximum Error [%]	Average Error [%]	Maximum Error [%]
5	31.51	80.00	17.24	67.14
10	32.82	80.00	21.10	80.00
50	35.12	82.86	28.73	84.28

Table 29 – Representative results for pole-to-pole faults with different resistances, single-end recording and $T = 1$ ms

r_f [Ω]	$\mathcal{P}_i(x_g)$		$\mathcal{E}_v(x_g)$	
	Average Error [%]	Maximum Error [%]	Average Error [%]	Maximum Error [%]
5	32.69	81.43	31.98	81.43
10	33.02	81.43	32.59	81.43
50	35.10	82.86	30.65	84.28

end measurements and any case with a single end, with both criteria, presented average errors from 10% to about 42%.

Thereby, the results showed that pole-to-pole faults trended to be a little less impacted by a fault resistance higher than 5 Ω and the criteria applied for double-end recording and $T = 10$ ms. Nevertheless, the results for pole-to-ground and pole-to-pole faults for the three values of fault resistances are very similar to each other. The average and maximum errors in Tables 22 to 25 are similar to those in Tables 26 to 29. That shows again that the fault type did not strongly influence the performance of the method in general, in a similar way as that observed before.

The cases where the cut-off frequency of the HP filter is changed and the WB model is used only in the DT, while the CP model in the RT stage, have the results shown in Appendix C.

The performance of the method for the cases where the CP model is used in the RT stage is almost the same as observed in the cases where the WB model is used in both DT and RT stages, comparing each analogous case. The differences are at the farthest fault location correctly estimated, which sometimes is closer to the probe end using the CP or the WB model for a given frequency and metric, and other intermediate locations before the farthest. Using the WB model, e.g., $\mathcal{E}_i(x_g)$ located faults at the same or farther distances than when the CP model was used.

Tables 30 and 31 summarises the results for pole-to-ground faults in the cases where the CP model is used in the RT simulations, whilst Tables 32 and 33 those for pole-to-pole

faults.

Table 30 – Representative results for pole-to-ground faults with different cut-off frequencies and $T = 10$ ms, changing the cable model in the RT stage

ν_c [kHz]	$\mathcal{P}_i(x_g)$		$\mathcal{E}_v(x_g)$	
	Average Error [%]	Maximum Error [%]	Average Error [%]	Maximum Error [%]
1	28.43	78.57	16.26	67.14
3	37.18	85.71	35.02	85.71
5	40.55	90.00	39.73	88.57

Table 31 – Representative results for pole-to-ground faults with different cut-off frequencies and $T = 1$ ms, changing the cable model in the RT stage

ν_c [kHz]	$\mathcal{P}_i(x_g)$		$\mathcal{E}_v(x_g)$	
	Average Error [%]	Maximum Error [%]	Average Error [%]	Maximum Error [%]
1	31.92	81.43	31.22	81.43
3	38.00	85.71	36.75	85.71
5	39.24	90.00	37.86	88.57

Table 32 – Representative results for pole-to-pole faults with different cut-off frequencies and $T = 10$ ms, changing the cable model in the RT stage

ν_c [kHz]	$\mathcal{P}_i(x_g)$		$\mathcal{E}_v(x_g)$	
	Average Error [%]	Maximum Error [%]	Average Error [%]	Maximum Error [%]
1	29.00	78.57	17.22	67.14
3	37.08	85.71	35.37	85.71
5	40.90	88.57	40.02	88.57

Table 33 – Representative results for pole-to-pole faults with different cut-off frequencies and $T = 1$ ms, changing the cable model in the RT stage

ν_c [kHz]	$\mathcal{P}_i(x_g)$		$\mathcal{E}_v(x_g)$	
	Average Error [%]	Maximum Error [%]	Average Error [%]	Maximum Error [%]
1	32.55	85.71	32.39	85.71
3	38.43	85.71	36.79	85.71
5	40.92	90.00	40.47	88.57

Comparing Tables 30 to 33 to Tables 16, 17, 20, and 21, the average and maximum errors trended to be higher with the CP line model in the RT stage, mainly for pole-to-pole faults. That shows that the non-dependence of the line parameters on the signal frequency of the CP model did not present advantages against the change between the line models used in the DT and RT stages.

Characteristics of resonance frequencies of the fault-induced EMTs and possible destructive overlap between resonances might be the cause of the wrong estimations for faults at far distances from the double or single probe ends, as observed in (HE; COZZA; XIE, 2020b). Also, those characteristics are not only related to the fault distance but to the fault resistance.

The characteristics of some faults in the frequency domain can be analysed with the amplitude spectrum. The pole-to-ground faults at 10 km and 50 km in the DT stage of the cases where the cut-off frequency of the HP filter and the fault resistance are changed were chosen as examples. The spectral amplitude of the recording signals for the pole-to-ground faults at 10 km and 50 km, unfiltered and filtered with the cut-off frequencies of 1 kHz, 3 kHz, and 5 kHz, are thus shown in Figures 57 and 59 for $T = 10$ ms, and in Figures 58 and 60 for $T = 1$ ms, respectively. The amplitudes are shown normalised relatively to the maximum magnitude in any case to enable a better comparison.

Figure 57 – Magnitude spectra of the recorded voltages at the positive pole for the pole-to-ground faults at 10 km from the probe end with $T = 10$ ms for different cut-off frequencies

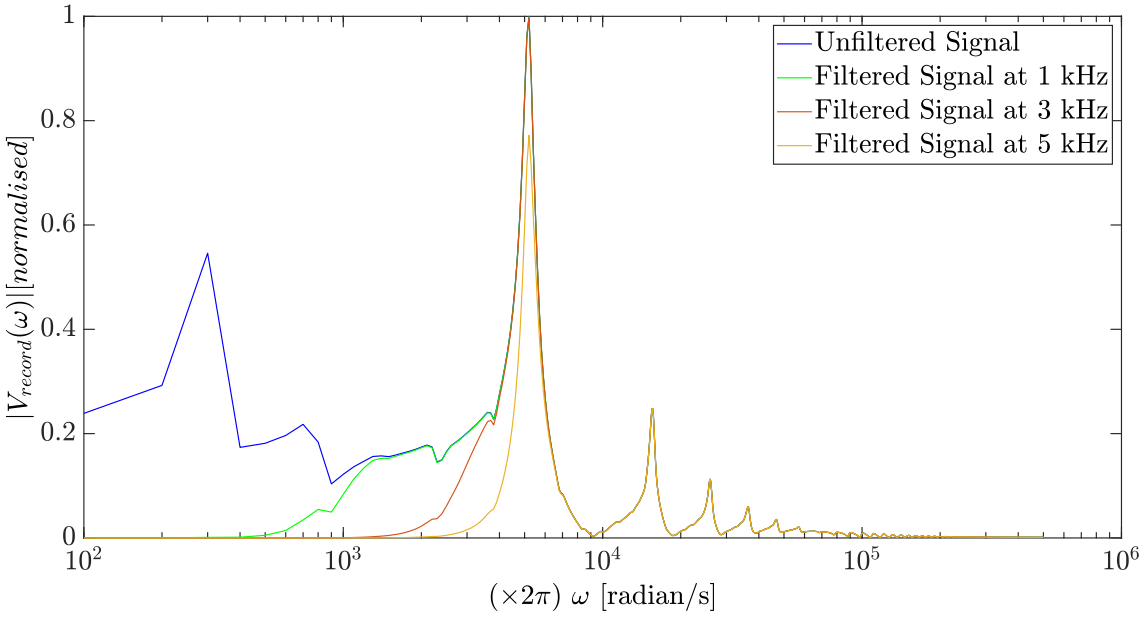

Source: Author

Figure 58 – Magnitude spectra of the recorded voltages at the positive pole for the pole-to-ground faults at $10\ \mathrm{km}$ from the probe end with $T = 1\ \mathrm{ms}$ for different cut-off frequencies

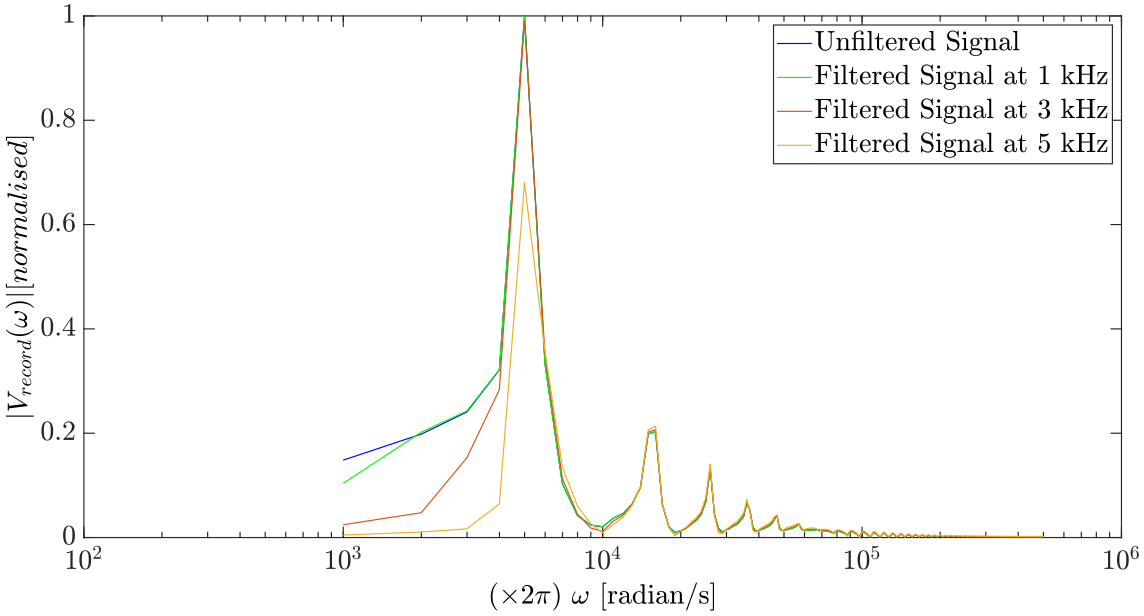

Source: Author

Figure 59 – Magnitude spectra of the recorded voltages at the positive pole for the pole-to-ground faults at $50\ \mathrm{km}$ from the probe end with $T = 10\ \mathrm{ms}$ for different cut-off frequencies

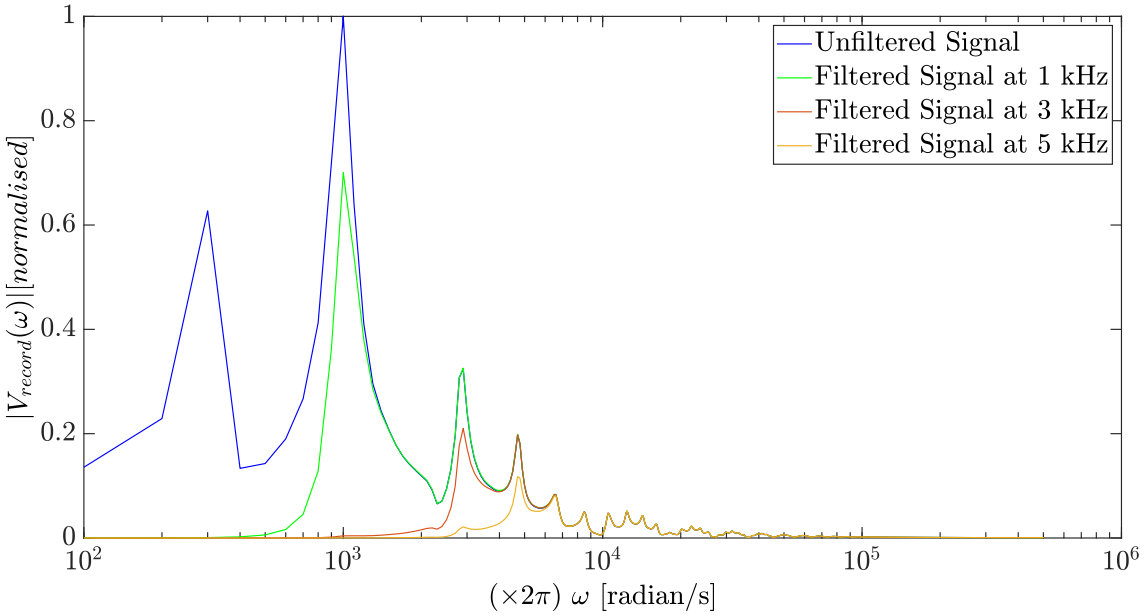

Source: Author

The number of samples of a digital signal determines the frequency step, $\Delta\omega$ in a fast Fourier transform (FFT), as mentioned in Sections 5.1 and 5.2 (although an FFT was not specified). With $T = 10\ \mathrm{ms}$, $\Delta\omega = 200\pi\ \mathrm{rad/s}$, and the magnitude spectra have relevant

Figure 60 – Magnitude spectra of the recorded voltages at the positive pole for the pole-to-ground faults at 50 km from the probe end with $T = 1$ ms for different cut-off frequencies

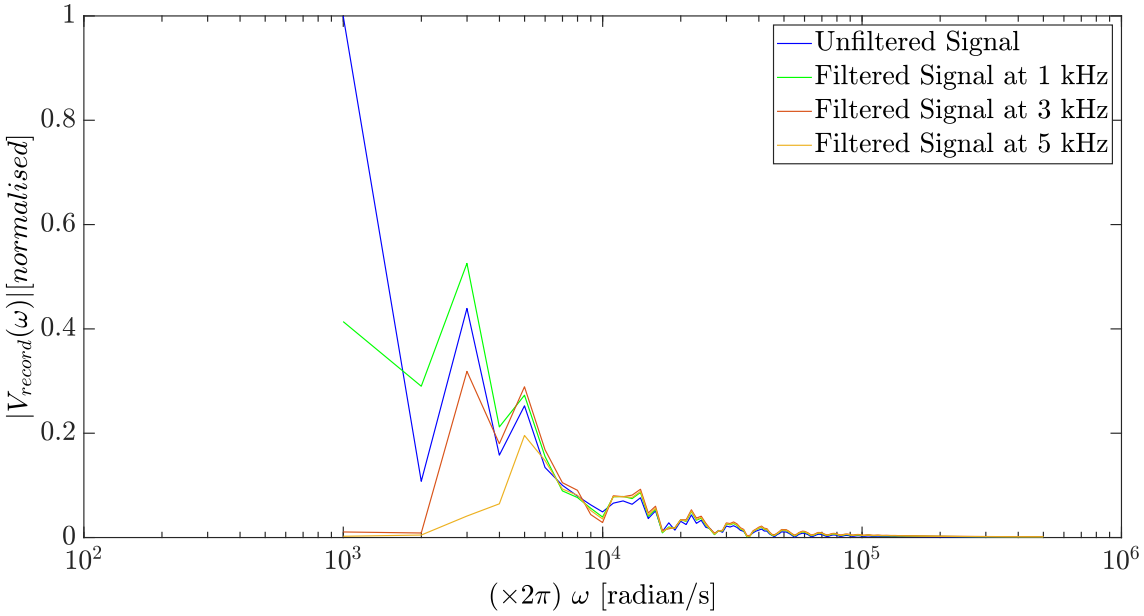

Source: Author

magnitudes within about 200π rad/s to $1,000\pi$ rad/s in Figures 57 and 59; with $T = 1$ ms, $\Delta\omega = 2,000\pi$ rad/s, and this bandwidth begins from about $2,000\pi$ rad/s, instead of 200π rad/s, in Figures 58 and 60.

The frequency resonance with the highest magnitude induced by the fault in Figures 57 and 58 is at about $10,000\pi$ rad/s. Figure 57 shows a lower frequency resonance of around 600π rad/s, however, which is filtered by any of the cut-off frequencies chosen. Figure 58 does not present it. Figure 59 shows the resonance with the highest magnitude at a frequency lower than $2,000\pi$ rad/s. The same resonance is cut with $T = 1$ ms, as shown in Figure 60. Thus, the duration of 1 ms for the recording window may influence the method's performance for the fault at 50 km. Since the first resonance is not completely covered, some spectral content of the fault-induced signal might be lost in this case.

The filtering decreases the magnitude of the resonances in Figures 57 to 60, apart from the cutting of the lower frequencies than the cut-off ones, following the filter's curve. The worst performance of the method in Figures 43, 44, 55, and 56 may caused by that loss of spectral content in the signal from distant faults to the single probe end, given by the filtering at frequencies higher than 1 kHz. Loss of spectral content by the lower magnitudes of the resonances is loss of spectral energy, which occurs more for the filtered signals in Figures 59 and 60 than in Figures 57 and 58, due to the farther distance. This can also be extended to double-end recording cases: for certain positions where the fault is relatively far from both probe ends, the higher the filter's frequency cutting off and decreasing the spectral information, the worse the method's performance.

Additionally, there is a partial overlap between adjacent resonances in Figures 59 and 60, which does not occur in Figures 57 and 58. Indeed, the spectral separation between each resonance in Figures 59 and 60 is narrower than in Figures 57 and 60. The overlap of resonances might cause worse estimations by the EMTR method, for it is associated with loss of resolution in the fault location (HE; COZZA; XIE, 2020b; COZZA; HE; XIE, 2021b).

The magnitude spectra of the signals from pole-to-ground faults in the DT stage across resistances of $5\ \Omega$, $10\ \Omega$, and $50\ \Omega$, at the same locations of 10 km and 50 km from the single probe end, filtered at 1 kHz, are shown in Figures 61 and 63 for $T = 10$ ms, and in Figures 62 and 64 for $T = 1$ ms, respectively.

Figure 61 – Magnitude spectra of the recorded voltages at the positive pole for the pole-to-ground faults at 10 km from the probe end with $T = 10$ ms for different fault resistances

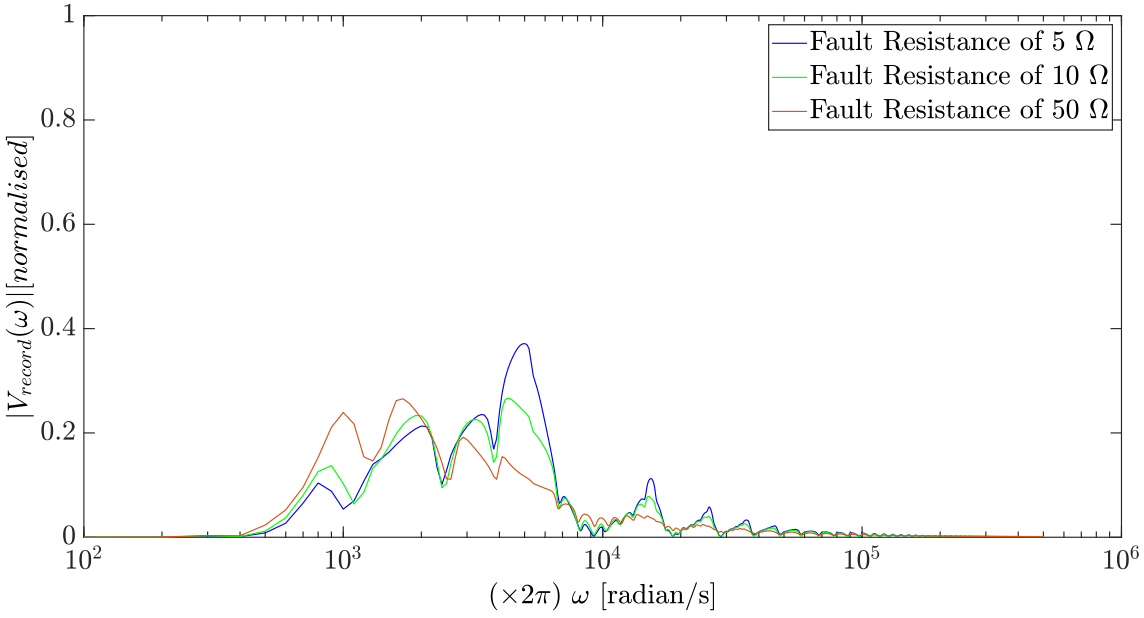

Source: Author

Comparing Figures 61 to 64 to the 1-kHz filtered cases in Figures 57 to 60, the resonances' magnitudes decrease for the fault resistances higher than $1\ \Omega$, which is more evident in the resonance with the highest magnitude in Figures 57 to 60. Moreover, the resonances at lower frequencies than those with the highest magnitude in Figures 57 and 58 increased in magnitude in Figures 61 and 62 with the increase of the fault resistance, while that earlier highest-magnitude one decreased. The performance of the method worsened for fault resistances of $5\ \Omega$, $10\ \Omega$, and $50\ \Omega$ compared to the cases with a fault resistance of $1\ \Omega$, which might be related to these changes in the spectrum content.

Figure 62 – Magnitude spectra of the recorded voltages at the positive pole for the pole-to-ground faults at $10\ \mathrm{km}$ from the probe end with $T = 1\ \mathrm{ms}$ for different fault resistances

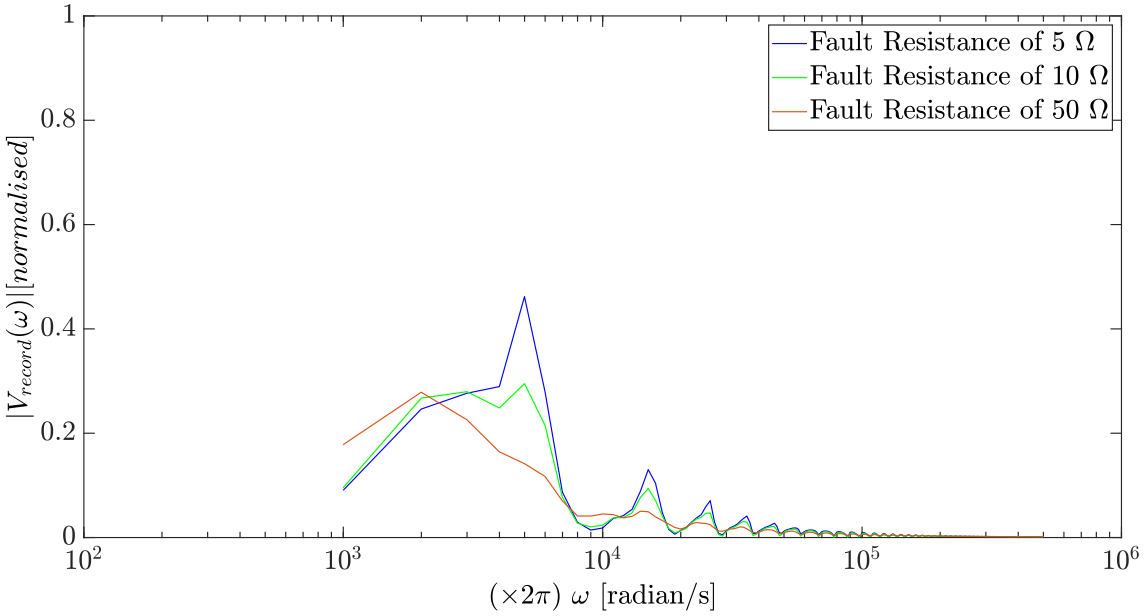

Source: Author

Figure 63 – Magnitude spectra of the recorded voltages at the positive pole for the pole-to-ground faults at $50\ \mathrm{km}$ from the probe end with $T = 10\ \mathrm{ms}$ for different fault resistances

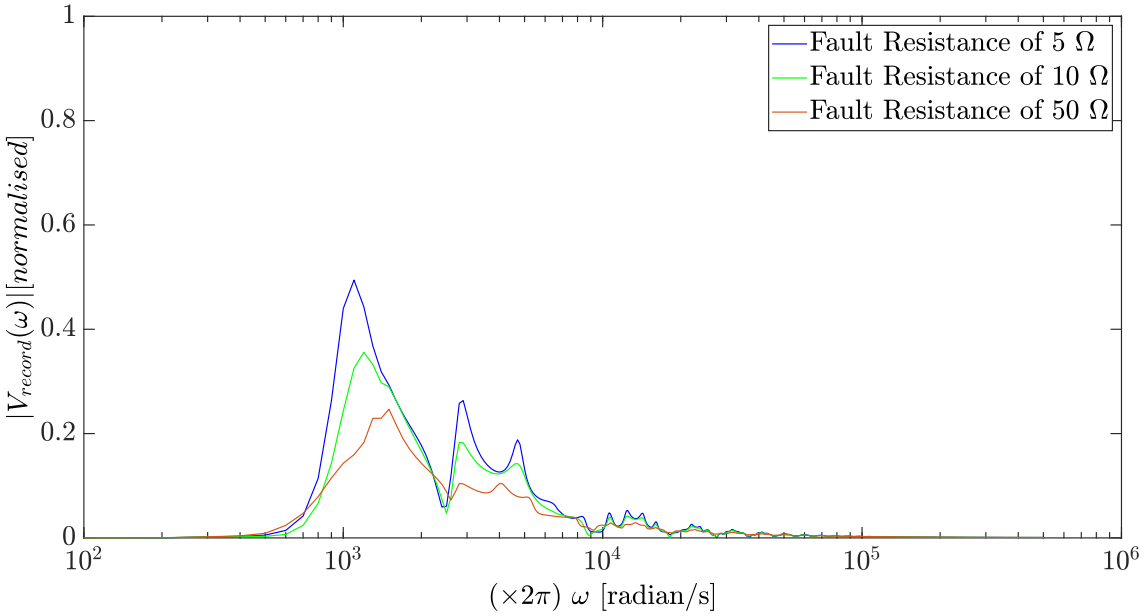

Source: Author

Figure 64 – Magnitude spectra of the recorded voltages at the positive pole for the pole-to-ground faults at $50\ \mathrm{km}$ from the probe end with $T = 1\ \mathrm{ms}$ for different fault resistances

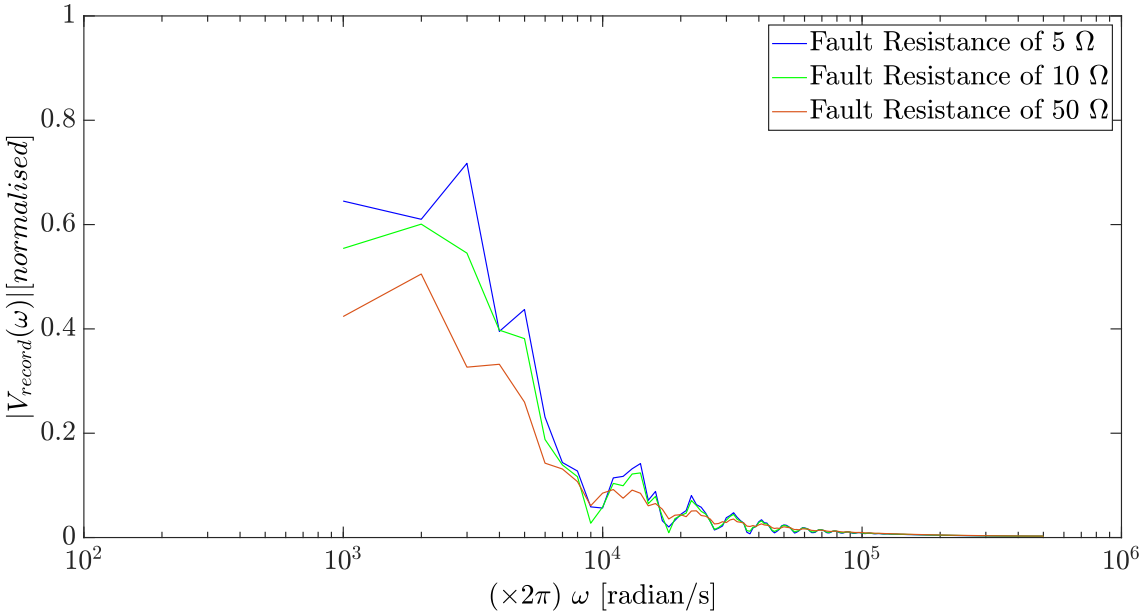

Source: Author

5.4 Electric Power Distribution Network in Time-Domain Simulations

Electric power distribution networks are hard cases for fault location techniques, mainly single-end ones. As aforementioned, due to the common radial and branched topology, multiple estimations may arise from an automatic fault location procedure. The deeper analyses of the EMTR method are likewise extended to a radial electric power distribution system (*cf.* Section 4.2.1) to observe the behaviour of the method. Again, data from fault simulations on the numerical model of the network is used. The IEEE 34 Node Test Feeder depicted in Figure 65 is chosen for the case studies. The network is composed of overhead lines (overhead non-insulated cables or wires), and it has voltage regulators and capacitor banks in its whole form.

As the previous study presented in Section 5.3, the modelling is done in EMTP-RV. Not the whole distribution network is utilised throughout the simulations, although. The section of the network under evaluation is formed by the part of the main feeder and the lateral branch that includes all the nodes upstream of the voltage regulator "Reg1": 800, 802, 808, 810, 812, 814i. That is also the same section of the network in Figure 65 used in studies in (RAZZAGHI *et al.*, 2013a). The main feeder is three-phase. The lateral branch is only at phase *b*[7].

As in Section 5.3, the system upstream of the transformer "Tr1" in Figure 65 is repre-

[7]The electrical phases of a three-phase system are denominated in EMTP-RV as *a*, *b*, *c*, or *A*, *B*, *C*.

Figure 65 – IEEE 34 Node Test Feeder

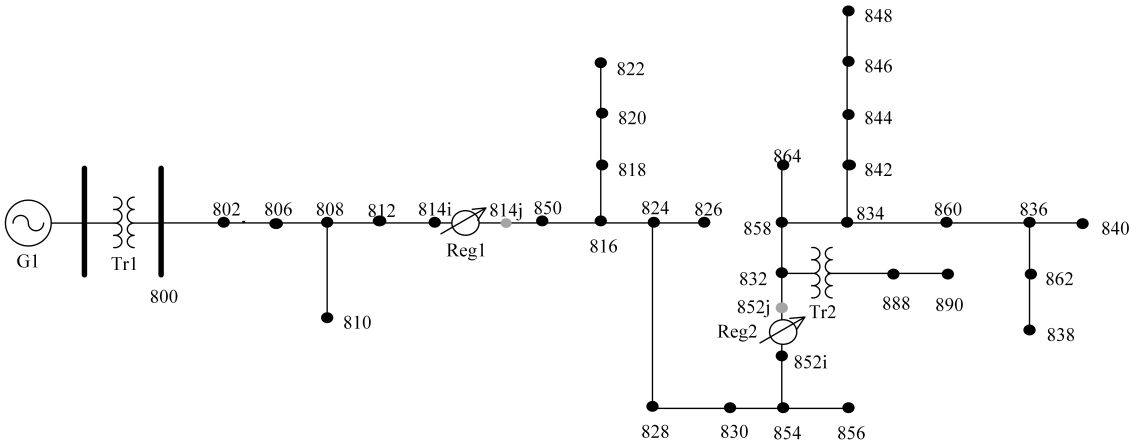

Source: Adapted from (INSTITUTE OF ELECTRICAL AND ELECTRONIC ENGINEERS, 2010)

sented by an equivalent source, whose rms line-to-line voltage is $69\ \mathrm{kV}$ in $60\ \mathrm{Hz}$. It has a short-circuit power of $3,000\ \mathrm{MVA}$ and a ratio of 2.5 for the relation between the inductive reactance to the resistance of the equivalent impedance.

The WB model is considered to model all the overhead lines of the network section to have the frequency dependence considered. That is a different choice than in (RAZZAGHI *et al.*, 2013a), where only the CP model was used. Therefore, different results are expected. All lines' conductors are of the aluminium cable steel reinforced (ACSR) type. The resistance of the aluminium is taken for $50\ ^{\circ}\mathrm{C}$, as shown in (WESTINGHOUSE ELECTRIC CORPORATION, 1964), according to the data in (INSTITUTE OF ELECTRICAL AND ELECTRONIC ENGINEERS, 2010). The general parameters used for the wideband model are shown in Table 34. The resistance of the conductors is shown for the two overhead line configurations present in the network section. The options of *proximity effect*, *earth return path*, and *dc correction* are selected in the model herein.

The transformer "Tr1" is modelled with the *three-phase nameplate input* part in EMTP-RV, which is given by three separate single-phase transformer units. The stray capacitances between the transformer' windings of the high and low voltage sides, as well as between the windings of both sides to the ground, are modelled by external capacitances, in a "Pi" representation, as in (BORGHETTI *et al.*, 2008), but with different values here. These capacitance values are given according to the power and high and low voltage level of "Tr1" and are shown in Table 35.

The faults are simulated at the nodes and intermediate points along the lines. The intermediate points are evenly spaced from each other sectionalising the lines between the nodes 806 to 808, 808 to 810, 808 to 812, and 812 to 814i. The line 806-808 is divided into twelve sections of about $819\ \mathrm{m}$; the line 808-810 is divided into two sections

Table 34 – Data of the wideband models of the lines

DC resistance of the line conductors for the configuration 300	$6.05 \times 10^{-4}\,\Omega\,\mathrm{m}^{-1}$
DC resistance of the line conductors for the configuration 303	$15.34 \times 10^{-4}\,\Omega\,\mathrm{m}^{-1}$
Conductors' relative permeability	1
Conductors' relative permittivity	1
Soil's resistivity	$100\,\Omega\,\mathrm{m}$
Soil's relative permeability	1
Soil's relative permittivity	1
Minimum frequency of the range	0.001 Hz
Maximum frequency of the range	10×10^6 Hz
Points/decade	10
Number of decades	10
Convergence tolerance	1%

Table 35 – Data of the Stray Capacitances of the Transformer "Tr1"

Capacitance Between High-Voltage Side to Ground	≈ 2.46 nF
Capacitance Between Low-Voltage Side to Ground	≈ 3.80 nF
Capacitance Between High- and Low-Voltage Sides	≈ 1.63 nF

of about $884\,\mathrm{m}$; the line 808-812 is divided into fourteen sections of about $816\,\mathrm{m}$; and the line 812-814i is divided into twelve sections of about $755\,\mathrm{m}$.

Figure 66 thereby shows the modelled section of the network in EMTP-RV. The whole length of the lines and the number indexes of the locations, where faults are simulated, are presented along with the lines, in addition to the number indexes representative of the nodes.

Single-end measurements are used only and thus a single-end form of the method. The current measured through a current transformer is the recording signal $s(t)$ (*cf.* Section 4.2.4). The current transformer is given by the *CT* part in EMTP-RV in its three-phase wye-connected version and with a transformation ratio of $200/5$. The magnetisation branch of the current transformer is included in the model and then the non-linearity of the transformation curve is considered to resemble real current transformers. The probe end is at the substation busbar 800 in Figure 65.

The recording window T lasts $1\,\mathrm{ms}$ (*cf.* Section 4.4.1), as in Section 5.3. In the context of general protection practices applied to electric power distribution systems, $1\,\mathrm{ms}$ of recording duration is much shorter than the time until the relay trips. Even a recording window of $10\,\mathrm{ms}$, for instance, would already be shorter than the tripping time of a realistic case of protection system with a *fuse saving* scheme (adopted in many electric

Figure 66 – First Section Studied of the IEEE 34 Node Test Feeder

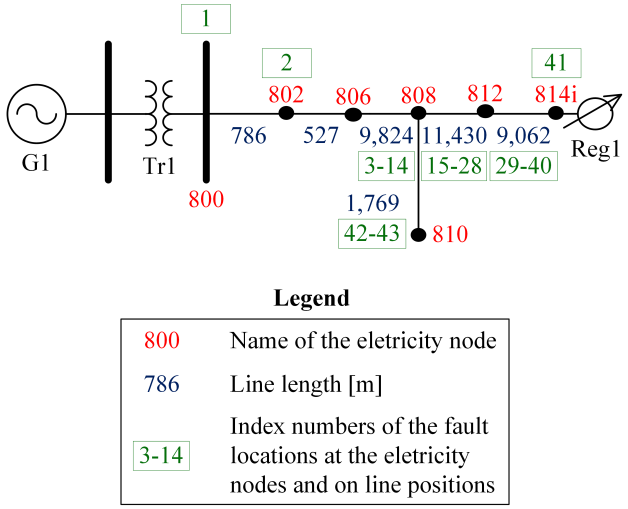

Source: Adapted from (INSTITUTE OF ELECTRICAL AND ELECTRONIC ENGINEERS, 2010)

power distribution systems to have the clearing of the fault before an expulsion fuse blows in a high fault current) (SHORT, 2014). However, the same consideration about modern relays in Section 5.3 applies here for the chosen window length of 1 ms. Again, only the fault-induced EMTs are recorded long before the breaker opening.

Once more, T can be taken recording the signal within successive windows of 1 ms, starting some samples before the instant of the fault identification and finishing 1 ms after, which can overlap two recording windows. Now, the fault detection is given by the variation in the magnitude of the recorded current, also comparing previous recording windows to the present one (*cf.* Section 4.3)[8].

The time step of the DT simulations is now 100 ns, and so the 1-ms windows have $10,000$ samples. The shorter the time step, the longer the computational cost to simulate for the same maximum time of the simulation. However, with the chosen time step of 100 ns, more transitions on the fault-induced EMTs are observed than in the cases of Section 5.3, except those shorter than 100 ns and which occur between two samples (COSTA *et al.*, 2020).

An HP Butterworth filter of 5th order is applied to the recorded EMTs after windowed, as in Section 5.3 (*cf.* Section 4.4.2). The value of the cut-off frequency is similarly changed to evaluate its influence on the method's performance, now between the values of 1 kHz, 3 kHz, 5 kHz, 7 kHz, and 9 kHz.

As in the study in Section 5.3, the fault resistance is changed in the DT simulations.

[8] As aforesaid in Section 4.3, the fault-identification method in the present work is simple. Fault detection is a different problem, and solutions are presented in the literature.

The values chosen are $1\ \Omega$, $5\ \Omega$, $10\ \Omega$, $20\ \Omega$, $50\ \Omega$, and $100\ \Omega$. The evaluation of the change in the resistance value is now done for each value of the cut-off frequency of the HP filter.

All nodes in Figure 66 are equally chosen for the GFLs. Faults in the RT simulations have the same resistance of $1\ \Omega$ in any case.

The time step in the RT simulations is again the same as the DT simulation, as in Section 5.3, i.e., $100\ \mathrm{ns}$, and the signal is not down- or up-sampled.

The same $\mathcal{P}_i(x_g)$ and $\mathcal{E}_i(x_g)$ criteria are applied to the fault location estimations, evaluating the dependence of the method's performance on the metric (*cf.* Section 4.6), as in Section 5.3.

In summary, single-phase-to-ground, phase-to-phase, double-phase-to-ground, and three-phase-to-ground faults are simulated in the DT stage with fault resistances of $1\ \Omega$, $5\ \Omega$, $10\ \Omega$, $20\ \Omega$, $50\ \Omega$, and $100\ \Omega$, and using $1\ \mathrm{kHz}$, $3\ \mathrm{kHz}$, $5\ \mathrm{kHz}$, $7\ \mathrm{kHz}$, and $9\ \mathrm{kHz}$ for the cut-off frequency of the HP filter applied to the recorded signals.

The details of the numerical modelling of the network in EMTP-RV and simulation parameters are in Appendix D.

Results for the application of both $\mathcal{P}_i(x_g)$ and $\mathcal{E}_i(x_g)$ criteria for the different types of faults, fault resistances, and cut-off frequencies are presented in Appendix E by *colormap* matrices as in Section 5.3. Still, the average errors of the fault-location estimation for each fault type by the two metrics are summarised in Tables 36 to 39 bellow.

Table 36 – Average errors [%] in the fault location for single-phase-to-ground faults by $\mathcal{P}_i(x_g)$ and $\mathcal{E}_i(x_g)$

r_f [Ω]	ν_c [kHz]									
	1		3		5		7		9	
	$\mathcal{P}_i(x_g)$	$\mathcal{E}_v(x_g)$	$\mathcal{P}_i(x_g)$	$\mathcal{E}_v(x_g)$	$\mathcal{P}_i(x_g)$	$\mathcal{E}_v(x_g)$	$\mathcal{P}_i(x_g)$	$\mathcal{E}_v(x_g)$	$\mathcal{P}_i(x_g)$	$\mathcal{E}_v(x_g)$
1	14.63	27.52	9.90	9.52	23.69	20.27	38.41	36.86	44.64	44.31
5	16.33	32.17	10.09	10.95	25.52	20.44	38.41	36.96	45.34	44.60
10	15.82	33.07	10.02	11.14	24.64	19.36	40.16	37.46	45.34	44.91
20	19.15	32.64	9.90	11.07	24.83	19.36	40.16	38.16	45.57	45.10
50	22.34	29.13	10.34	11.76	25.58	17.85	41.74	39.42	46.14	45.29
100	20.12	29.44	10.34	15.97	24.76	19.36	43.36	44.91	46.07	45.61

As the cases in Section 5.3, the influence of fault distance to the probe end is evident. The method estimated the correct fault location only for a few faults near the probe end, again noticing by the values of both $\mathcal{P}_i(x_g)$ and $\mathcal{E}_i(x_g)$ criteria along the diagonal of the *colormap* matrices. That was for all four types of faults, single-phase-to-ground, phase-to-phase, double-phase-to-ground, and three-phase-to-ground.

Comparing Tables 36 to 39, for the same fault resistance and cut-off frequency, different results for each fault type are observed. The lowest average errors were found for

Table 37 – Average errors [%] in the fault location for phase-to-phase faults by $\mathcal{P}_i(x_g)$ and $\mathcal{E}_i(x_g)$

r_f [Ω]	ν_c [kHz]									
	1		3		5		7		9	
	$\mathcal{P}_i(x_g)$	$\mathcal{E}_v(x_g)$	$\mathcal{P}_i(x_g)$	$\mathcal{E}_v(x_g)$	$\mathcal{P}_i(x_g)$	$\mathcal{E}_v(x_g)$	$\mathcal{P}_i(x_g)$	$\mathcal{E}_v(x_g)$	$\mathcal{P}_i(x_g)$	$\mathcal{E}_v(x_g)$
1	7.48	7.38	6.82	8.42	34.12	37.86	27.57	41.08	32.23	41.08
5	7.95	9.41	6.82	8.46	34.12	37.96	29.88	41.18	31.79	41.18
10	8.59	10.42	6.82	8.46	34.12	37.96	29.88	41.18	31.79	41.18
20	8.18	8.81	6.94	9.61	34.64	38.32	28.55	41.54	31.75	41.54
50	11.21	12.40	9.55	9.74	35.59	38.55	31.29	42.18	32.50	42.18
100	17.79	17.93	9.99	9.94	35.21	40.57	35.11	42.33	36.93	43.03

Table 38 – Average errors [%] in the fault location for double-phase-to-ground faults by $\mathcal{P}_i(x_g)$ and $\mathcal{E}_i(x_g)$

r_f [Ω]	ν_c [kHz]									
	1		3		5		7		9	
	$\mathcal{P}_i(x_g)$	$\mathcal{E}_v(x_g)$	$\mathcal{P}_i(x_g)$	$\mathcal{E}_v(x_g)$	$\mathcal{P}_i(x_g)$	$\mathcal{E}_v(x_g)$	$\mathcal{P}_i(x_g)$	$\mathcal{E}_v(x_g)$	$\mathcal{P}_i(x_g)$	$\mathcal{E}_v(x_g)$
1	9.96	11.63	7.06	7.24	31.88	35.13	23.08	39.75	30.62	40.32
5	10.97	14.86	7.13	7.55	33.00	35.26	23.14	40.19	30.80	40.19
10	10.37	15.45	7.06	9.52	32.75	35.84	25.68	40.78	32.25	40.78
20	12.48	16.55	6.99	9.51	33.13	38.11	29.73	41.32	32.15	41.32
50	17.56	17.19	8.05	10.20	34.39	37.94	33.61	41.16	36.09	42.55
100	22.35	18.47	9.44	12.43	34.96	40.09	36.58	43.60	37.62	43.60

Table 39 – Average errors [%] in the fault location for three-phase-to-ground faults by $\mathcal{P}_i(x_g)$ and $\mathcal{E}_i(x_g)$

r_f [Ω]	ν_c [kHz]									
	1		3		5		7		9	
	$\mathcal{P}_i(x_g)$	$\mathcal{E}_v(x_g)$	$\mathcal{P}_i(x_g)$	$\mathcal{E}_v(x_g)$	$\mathcal{P}_i(x_g)$	$\mathcal{E}_v(x_g)$	$\mathcal{P}_i(x_g)$	$\mathcal{E}_v(x_g)$	$\mathcal{P}_i(x_g)$	$\mathcal{E}_v(x_g)$
1	6.60	10.27	5.32	6.88	13.49	30.59	10.07	38.98	12.75	39.71
5	7.73	15.33	5.32	6.85	17.08	32.21	10.07	39.08	12.75	39.81
10	7.07	11.99	5.38	6.85	17.71	31.20	12.17	39.04	13.25	40.03
20	9.44	16.12	5.38	6.28	22.13	32.21	15.22	39.29	15.95	40.78
50	16.08	20.68	5.55	6.97	28.97	36.20	19.09	42.23	24.13	43.77
100	22.64	18.81	7.00	11.57	32.52	39.90	32.41	44.65	31.55	44.65

the cases of three-phase-to-ground faults, whereas the highest average errors for single-phase-to-ground faults, as shown in Tables 39 and 36, respectively. The lowest errors occurred specifically with $\mathcal{P}_i(x_g)$ and the cut-off frequency of 3 kHz in Table 39, which are up to 47% lower than the errors in Table 36. The second-best results were found for

phase-to-phase faults, followed by the results for double-phase-to-ground ones.

That shows the influence of the modal components of the fault-induced EMTs on the fault-location estimations for the cases in the distribution-network section, which contrasts with what was observed in Section 5.3 with the HVDC transmission link. As mentioned in Section 5.3, the ground mode has slower propagation than the aerial modes. Since the WB line model considers the frequency dependence of the line parameters within a wide range, the compound of components of different velocities in the EMTs influenced the results, as aforesaid. Likely, this did not occur for the HVDC transmission system due to the characteristics of the insulated cable ensuring much lower coupling between the poles and the poles and ground than there is between the phases and phases and ground in the distribution network.

The asymmetric pole-to-ground fault in the HVDC system induces fewer EMTs in the non-fault pole than the asymmetric single-phase-to-ground fault in the section of the distribution network, for instance. Again, looking at the ac cases, three-phase-to-ground faults are symmetric and tend to induce only aerial modes. That did not occur for these fault cases because the distribution network in Figure 65 is not balanced regarding the impedance of the phase conductors and loads. Thereby, components of the ground mode are likewise induced by the three-phase-to-ground faults, although with a much lower magnitude than those of the aerial modes. The asymmetric ground faults induce high magnitudes of the ground mode otherwise. Single-phase-to-ground faults are the worst case, compared to the double-phase-to-ground ones, because only one phase is involved, and then higher asymmetry.

The dependence on the fault resistance is observed to be not as strong as that on the fault location or the fault type up to some value of resistance in these cases. The performance of the method was similar for fault resistances of $1\ \Omega$, $5\ \Omega$, $10\ \Omega$, and $20\ \Omega$, for a given metric and cut-off frequency, for all fault types. Most of the fault locations correctly estimated for a resistance of $1\ \Omega$ are also for these other resistances by the application of $\mathcal{P}_i(x_g)$ or $\mathcal{E}_i(x_g)$. The cases with fault resistances of $100\ \Omega$ tended to present the worst performance, however, together with the 50-Ω cases, that presented the second worst results. For phase-to-phase and three-phase-to-ground faults, e.g., the average errors in Tables 37 and 39 for fault resistances of $100\ \Omega$ were up to more than two and three times higher than those for fault resistances of $1\ \Omega$, respectively, with the cut-off frequency of $1\ \mathrm{kHz}$.

The method's performance was very influenced by the cut-off frequency: the results from the method's application were lower with the filtering at $3\ \mathrm{kHz}$ for all fault types, for the same fault resistance and metric. The performance was decreased for the cut-off frequencies higher than $3\ \mathrm{kHz}$. Some of the worst results occurred with the filtering at 5 kHz, with can be observed comparing Tables 37 to 39.

Table 38 shows that the average errors for the filtering at $5\ \mathrm{kHz}$ were up to more than

four times higher than those for the filtering at 3 kHz, with the same metric and for the same fault resistance. Still, the filtering at 1 kHz might not filter out the low-frequency components related to the industrial frequency and others above.

That shows that the spectral content of the fault-induced EMTs is associated with the fault location in the evaluated section of the distribution network as it was in the cases in Section 5.3. The filtering process at one of the evaluated cut-off frequencies might lead or not to correct estimations of the fault locations. Which cut-off frequency would be a good choice seemed not to be something possible to infer without previous evaluation by, e.g., simulation data as done here, nonetheless.

The applied metric rather impacted the results. The farthest fault locations correctly estimated by $\mathcal{E}_i(x_g)$ were invariably closer to the probe end than those estimated by $\mathcal{P}_i(x_g)$. The highest differences between the results from both metrics can be seen in Tables 36 and 39. Tables 36 and 39 show average errors up to about two times higher with $\mathcal{E}_i(x_g)$ than with $\mathcal{P}_i(x_g)$, e.g., for the cut-off frequency of 1 kHz and fault resistance of $5\ \Omega$. That is not a pattern observed for all cases, although. Moreover, conversely, the estimations were worse with $\mathcal{P}_i(x_g)$ than with $\mathcal{E}_i(x_g)$ for single-phase-to-ground faults with filtering at 5 kHz and 7 kHz. $\mathcal{P}_i(x_g)$ seems to be a better option, however, as it was observed in Section 5.3.

The different behaviour for estimations with the cut-off frequency 1 kHz than with the others reflects the influence of the spectral content alteration given by the filtering process on the method. The results show that whilst the highest pick of the metrics fell at the wrong location, some of the secondary ones fell at the correct location. How to discern the correct estimation from the metric picks other than the primary one is a point of improvement on $\mathcal{P}_i(x_g)$ and $\mathcal{E}_i(x_g)$, once they both use only the primary one.

Faults at nodes near the probe end were located in many cases by $\mathcal{P}_i(x_g)$ and $\mathcal{E}_i(x_g)$, as expected due to the proximity to the probe end. However, it was not in all cases. Single-phase-to-ground, double-end-to-ground, and three-phase-to-ground faults at nodes near the probe end were not correctly located using $\mathcal{P}_i(x_g)$ and the cut-off frequency of 1 kHz in some cases, as for fault resistances of $100\ \Omega$. The $\mathcal{E}_i(x_g)$ metric returned the worst performance, with no fault correctly located in these same cases.

The farthest fault location correctly estimated by $\mathcal{P}_i(x_g)$ for single-phase-to-ground and three-phase-to-ground faults were at nodes 812(5)[9] and 814i, respectively. This correct estimation occurred without being in sequence from correct estimations of fault locations at previous nodes, with a fault resistance of $1\ \Omega$, $10\ \Omega$, and $20\ \Omega$, for the single-phase-to-ground faults, and with a fault resistance of $20\ \Omega$ for the three-phase-to-ground faults,

[9]The number in brackets refers to the line section the node is. As the node names in Figure 65 refer to the system without the sectionalised lines to yield intermediate points, as in Figure 66, the original downstream node of the line and the section number is used to refer to the downstream node of the sections. For instance, 812(5) means the downstream node of the fifth section of line 812-814i.

for a cut-off frequency of 1 kHz. Nevertheless, this result for the three-phase-to-ground faults may be due to the effects of the extremity of the line.

Another far correct fault-location estimation for three-phase-to-ground faults was at 812(11), with the filtering at 7 kHz and the fault resistances of $1\ \Omega$ and $5\ \Omega$. Otherwise, following a sequence from correct estimations of fault locations at previous nodes, the farthest fault location by $\mathcal{P}_i(x_g)$ for single-phase-to-ground and three-phase-to-ground faults were at nodes 806(8) and 812(1), respectively. It occurred with fault resistances of $1\ \Omega$, $5\ \Omega$, $10\ \Omega$, and $20\ \Omega$, and a cut-off frequency of 3 kHz for single-phase-to-ground faults, and with fault resistances of $1\ \Omega$ and $10\ \Omega$, and a cut-off frequency of 9 kHz for three-phase-to-ground faults.

The $\mathcal{E}_i(x_g)$ metric presented correct estimations for faults closer to the probe end than those by $\mathcal{P}_i(x_g)$. The farthest fault location by $\mathcal{E}_i(x_g)$ for single-phase-to-ground faults was at node 812(5), which occurred with fault resistances of $1\ \Omega$, $20\ \Omega$, and $50\ \Omega$, and the cut-off frequency of 1 kHz. For three-phase-to-ground faults, the farthest fault location by $\mathcal{E}_i(x_g)$ was at node 812(8), which occurred with the fault resistance of $50\ \Omega$ and the cut-off frequency of 1 kHz. However, the correct estimation was not in sequence with correct estimations of fault locations at previous nodes.

Looking only at single-phase-to-ground faults, which are the worst cases, the analysis of the amplitude spectrum of some fault cases can give some understanding of the cause of the wrong estimations of the fault locations for faults at far distances, as done in Section 5.3. The single-phase-to-ground faults at nodes 802, 806(1), 808(1), 812(1), and 814i were chosen for this analysis.

The spectral amplitude of the recording signals for the single-phase-to-ground faults at nodes 806, 808, 850, 816, 824, and 818 in the DT stage, across the resistance of $1\ \Omega$, unfiltered and filtered with the cut-off frequencies of 1 kHz, 3 kHz, 5 kHz, 7 kHz, and 9 kHz, are shown in Figures 67 to 71.

As observed in Section 5.3, the number of samples and the frequency step are related to each other in the FFT. The same $\Delta\nu = 1$ kHz is obtained with the time step of 100 ns, i.e., the sampling frequency of 10 MHz, and $T = 1$ ms. Still, the Nyquist frequency determines the maximum frequency in the bandwidth. Then, the bandwidth in Figures 67 to 71 is within about 1 kHz to 5 MHz.

The single-phase-to-ground faults at nodes 802 and 806(1) presented in Figures 67 to 71 the first resonance of the fault-induced EMTs at a frequency higher than 10 kHz, whether those at nodes 808(1), 812(1) and 814i have the first resonance of the fault-induced EMTs at a frequency between 1 kHz to 10 kHz.

Figures 67 to 71 show in more detail the region in the spectra between 10 kHz to 1 MHz, where there are the resonance frequencies of the closest faults to the probe end. The frequency components lower than 1 kHz present in the recorded signals are not from the fault-induced EMTs, e.g., the industrial frequency.

Figure 67 – Magnitude spectra of the recorded currents by the current transformer for the single-phase-to-ground faults at node 802 across the resistance of 1 Ω for different cut-off frequencies

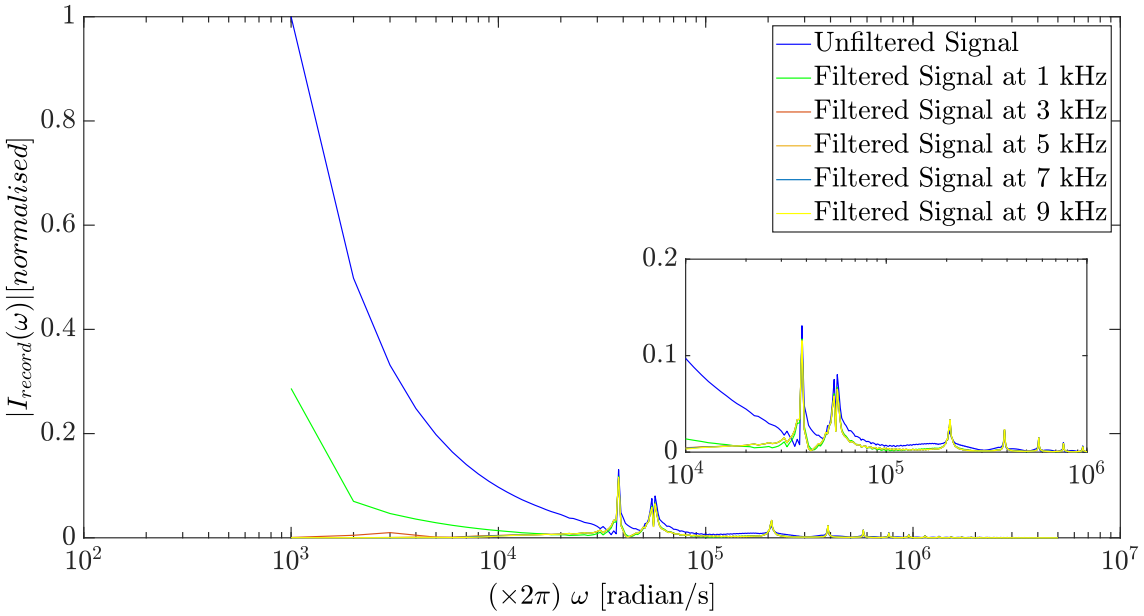

Source: Author

Figure 68 – Magnitude spectra of the recorded currents by the current transformer for the single-phase-to-ground faults at node 806(1) across the resistance of 1 Ω for different cut-off frequencies

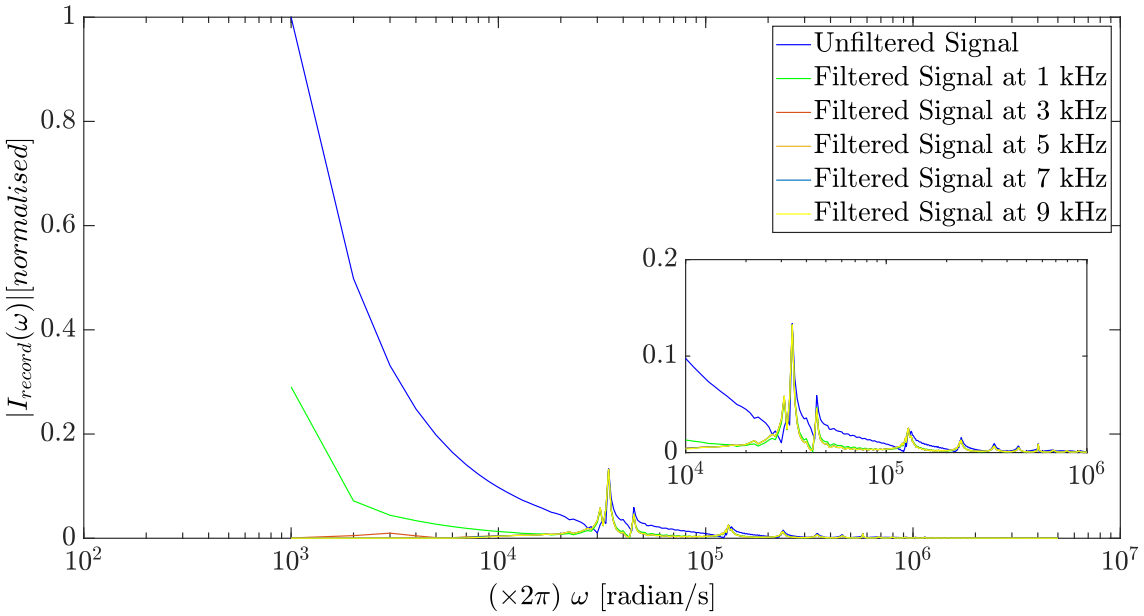

Source: Author

The filtering at the cut-off frequencies from 1 kHz to 9 kHz virtually does not change the spectral content within the region from 10 kHz to 1 MHz. However, it does in the

Figure 69 – Magnitude spectra of the recorded currents by the current transformer for the single-phase-to-ground faults at node 808(1) across the resistance of 1 Ω for different cut-off frequencies

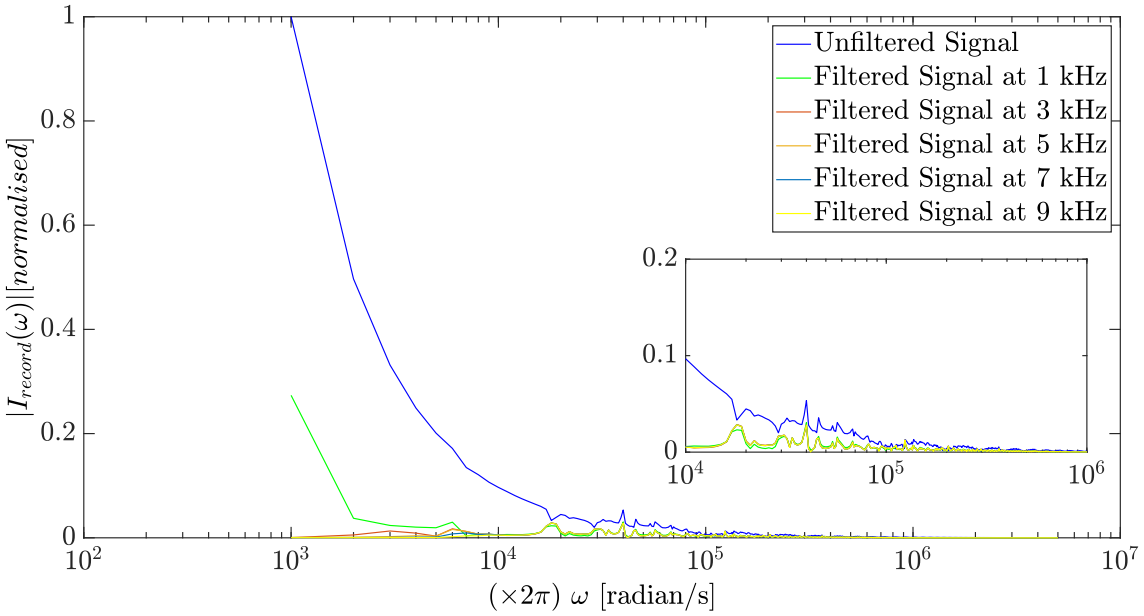

Source: Author

Figure 70 – Magnitude spectra of the recorded currents by the current transformer for the single-phase-to-ground faults at node 812(1) across the resistance of 1 Ω for different cut-off frequencies

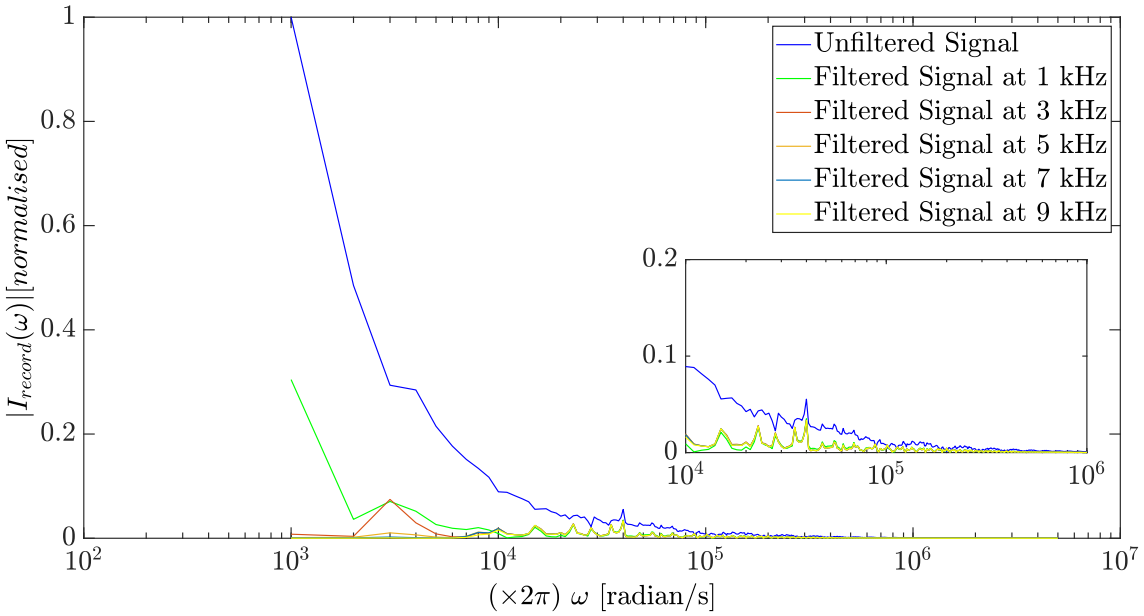

Source: Author

range between 1 kHz to 10 kHz. The first induced resonances of the faults at nodes 808(1), 812(1) and 814i have their magnitude decreased by the filtering process, which

Figure 71 – Magnitude spectra of the recorded currents by the current transformer for the single-phase-to-ground faults at node 814i across the resistance of 1 Ω for different cut-off frequencies

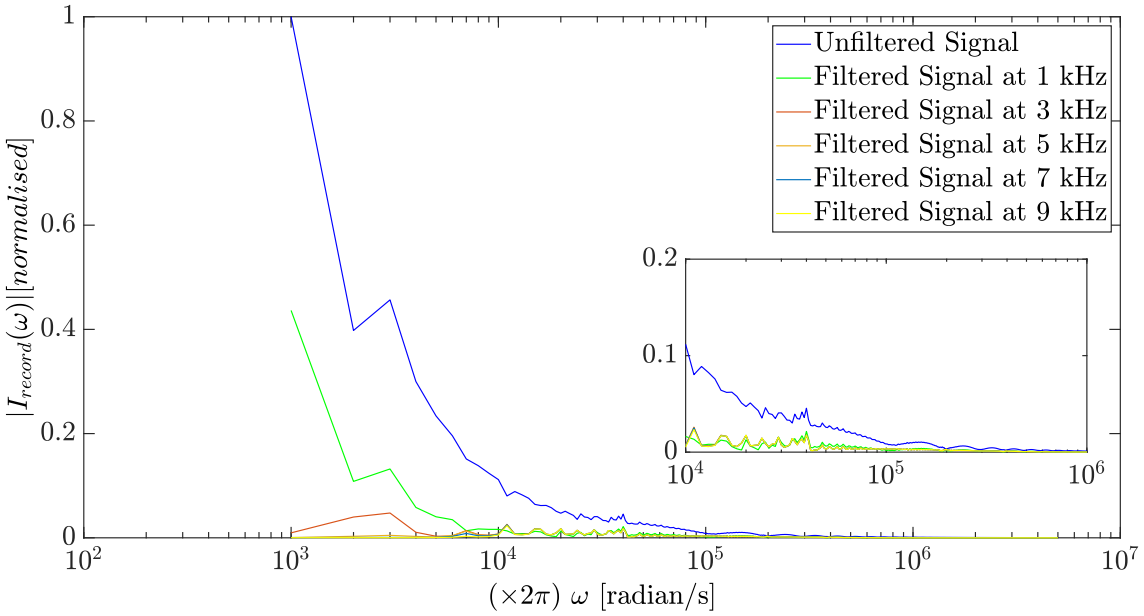

Source: Author

occurs progressively as higher is the cut-off frequency. The filtering at 1 kHz leaves much of the frequency components of the unfiltered signal in the filtered one in Figures 69 and 71, whereas the filtering at 3 kHz is a better option, for which the low-frequency components are filtered and the first induced resonance is not.

Comparing Figures 67 to 71, one observes the decrease of the magnitude of the resonances as far from the probe end is the node, together with the shifting of the resonance frequencies. A contribution to the decrease in the magnitude of the resonances might be the passing through the single-phase lateral 808–810 off the main feeder at phase *b* of node 808(1). This lateral 808–810 just affects the fault-induced EMTs by a single-phase-to-ground fault at phase *a* due to the coupling between the phases, not as direct as a lateral at the same faulted phase, but might affect the EMTs induced by the other types of faults. The decrease in the magnitude of the fault-induced resonances may be thus the main cause of the wrong estimations of the fault locations.

Looking at the spectral content in frequencies higher than 100 kHz in Figures 67 to 71, the loss of information is evident, for the magnitudes at those frequencies are much more attenuated in Figures 69 to 71 than in Figures 67 and 68. The partial overlap between adjacent resonances observed in Section 5.3 also seems to occur.

The magnitude spectra for the EMTs from the faults at nodes 802, 806(1), 808(1), 812(1), and 814i, across the resistances of 5 Ω, 10 Ω, 20 Ω, 50 Ω, and 100 Ω, filtered with the cut-off frequency of 1 kHz, are presented in Figures 72 to 76.

Figure 72 – Magnitude spectra of the recorded currents by the current transformer for the single-phase-to-ground faults at node 802 for different fault resistances with the cut-off frequency of 1 kHz

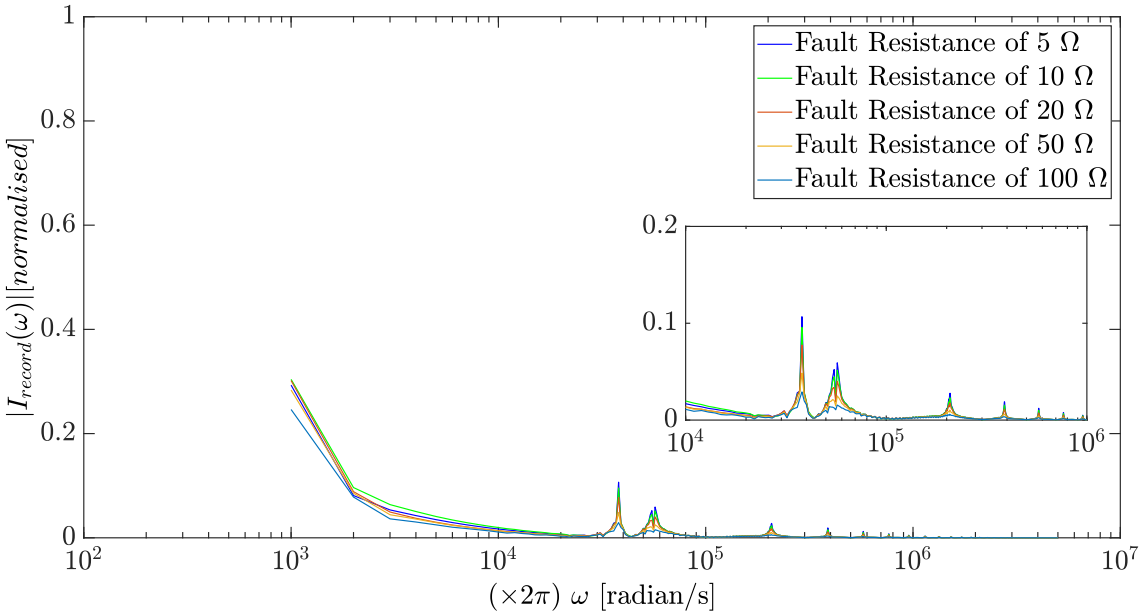

Source: Author

Figure 73 – Magnitude spectra of the recorded currents by the current transformer for the single-phase-to-ground faults at node 806(1) for different fault resistances with the cut-off frequency of 1 kHz

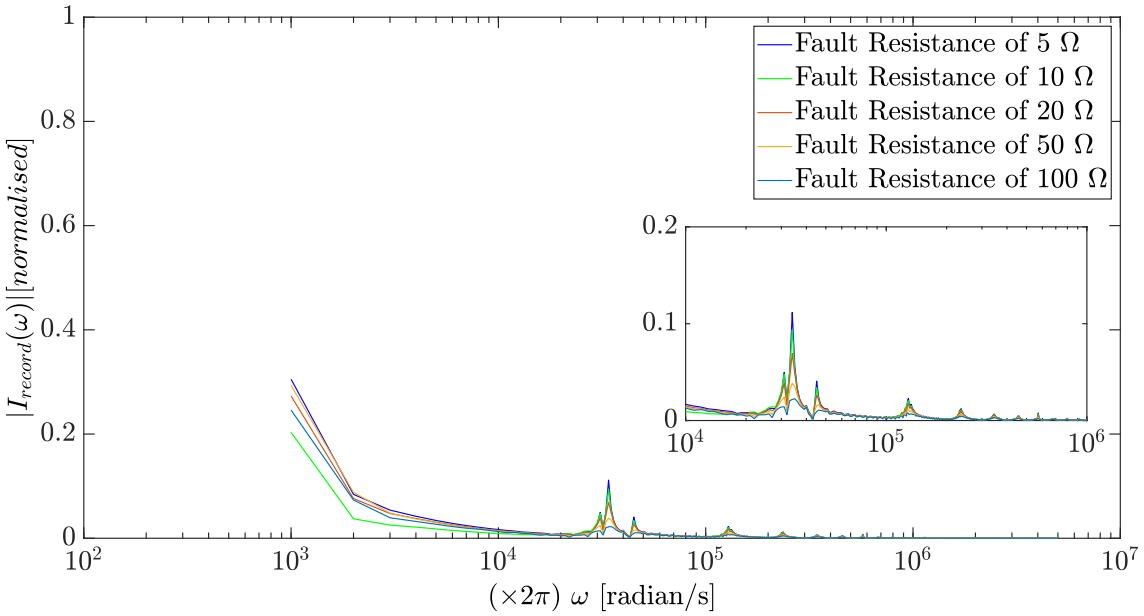

Source: Author

The magnitude spectra in Figures 72 to 76 show, as in Section 5.3, that the magnitude of the fault-induced resonances trended to be as lower as higher is the fault resistance.

Figure 74 – Magnitude spectra of the recorded currents by the current transformer for the single-phase-to-ground faults at node 808(1) for different fault resistances with the cut-off frequency of 1 kHz

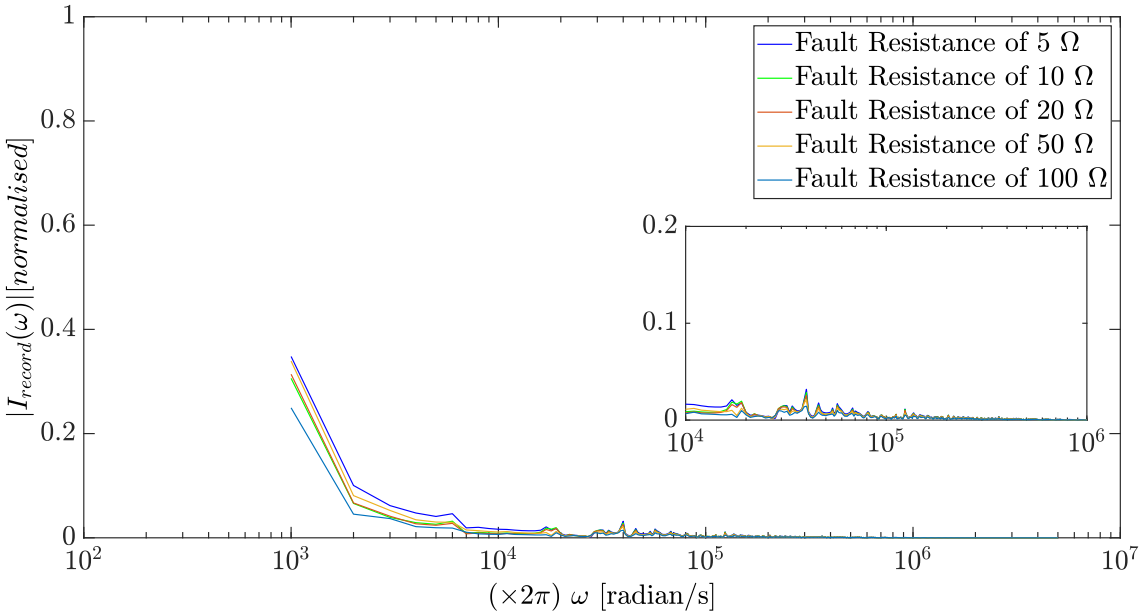

Source: Author

Figure 75 – Magnitude spectra of the recorded currents by the current transformer for the single-phase-to-ground faults at node 812(1) for different fault resistances with the cut-off frequency of 1 kHz

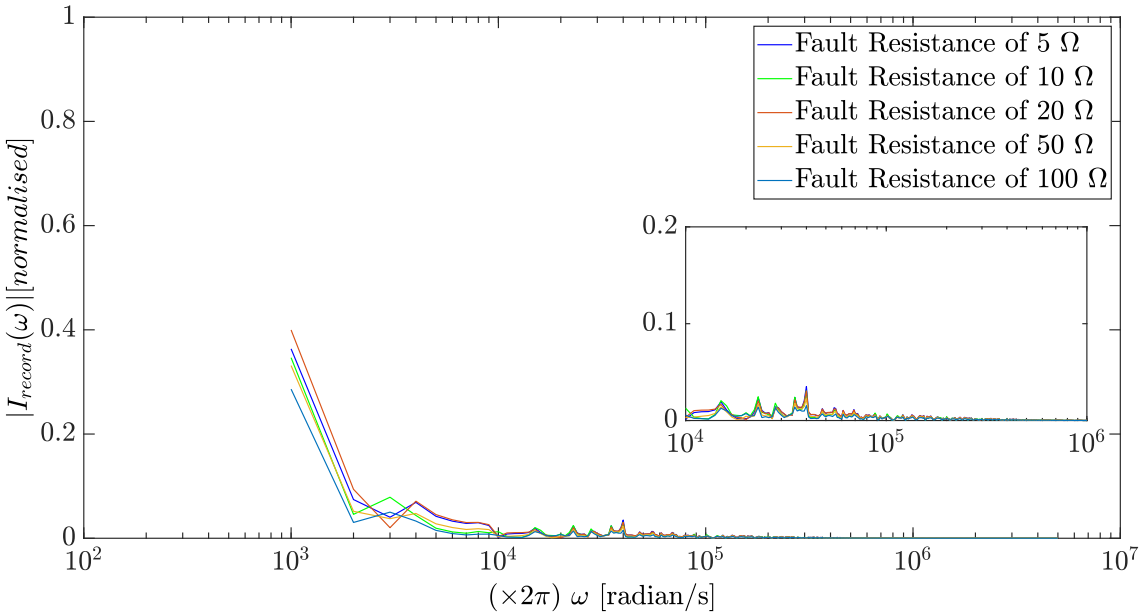

Source: Author

It can likewise be compared to the spectra for fault resistances of 1 Ω in Figures 67 to 71 for the cut-off frequency of 1 kHz. Again, these changes in the spectrum content

Figure 76 – Magnitude spectra of the recorded currents by the current transformer for the single-phase-to-ground faults at node 814i for different fault resistances with the cut-off frequency of 1 kHz

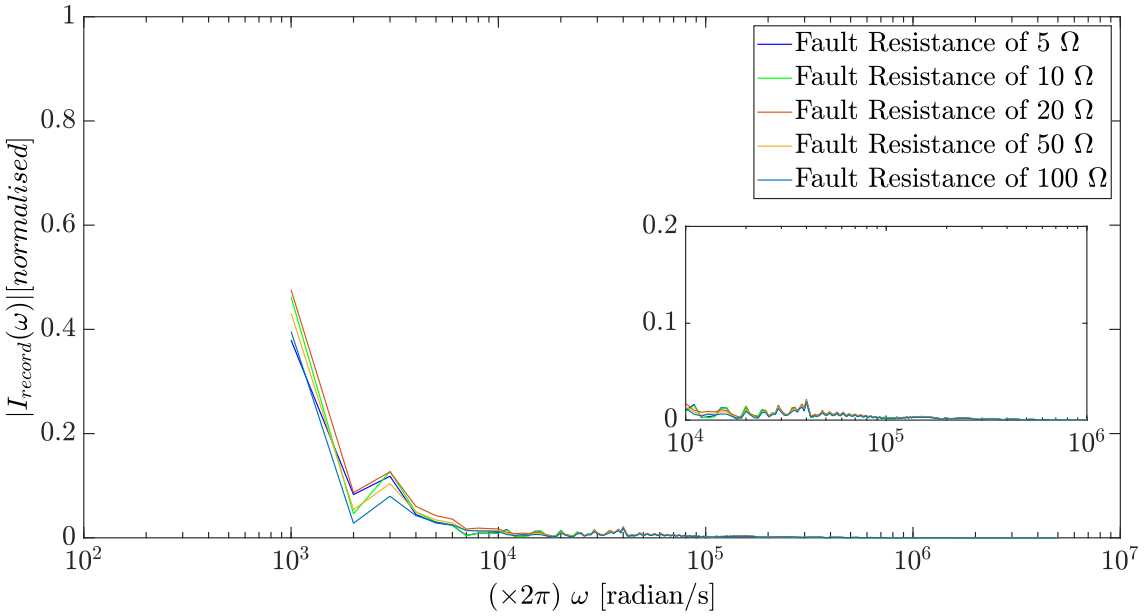

Source: Author

might be the cause of the worse performance of the method with higher fault resistances, for the fault resistances of 50 Ω and 100 Ω lead to a higher decrease in the resonances' magnitudes. The influence of the fault resistance for the fault location on the distribution network section was smaller than in the HVDC cases.

6 CONCLUSION

The present work presented several studies on cases of fault location applying the EMTR method to evaluate its behaviour and capabilities. Two simple systems of overhead single-conductor lines with different lengths are considered in the initial analyses, first conducted in the frequency domain through analytical formulations. Then, the method is evaluated on one of these simple systems in the time domain through simulations in an EMTP-type tool, the EMTP-RV. After, the numerical modelling of an HVDC transmission link and a section of an electric power distribution network was built using the sophisticated models of the electrical components available in the software to resemble realistic cases. Double- and single-end forms of the method were applied, using measurements of the fault-induced EMTs at both extremities of the cable and lines or only at a single one, respectively.

The results from the analytical evaluations showed the effectiveness of the metrics given by $\mathcal{P}_i(x_g)$, $\mathcal{E}_i(x_g)$, $\angle V(x_g, \omega)$, $\mathcal{E}_v(x_g)$, and $\rho_{HH}(x_g)$ in many cases with three different frequency and spatial steps in both systems. However, also pointed out drawbacks of $\mathcal{P}_i(x_g)$, $\mathcal{E}_i(x_g)$, and $\mathcal{E}_v(x_g)$, mainly concerning to cases where the resistive component of the system lines is high relatively to the inductive component. Besides, the impact of the distance of the fault to the probe ends was observed, mostly considering a $1,000$-km line.

The analyses on the simple system in the time domain using $\mathcal{P}_i(x_g)$ and $\mathcal{E}_i(x_g)$ returned similar results taken in the analytical cases, from which the correspondence between the frequency-domain formulation and the EMTP-type numerical modelling was verified. The dependence of the performance of both metrics on the fault distance was observed again for the single-end form of the method and its relation to the length of the recording signal. The double-end recording presented less dependence.

The studies on the HVDC system considered the influence of the filtering of the signal used in the TR process, the fault resistance, and the change of the type of the cable model in the RT simulations, in addition to the influence of the length of the signal, the fault distance, and the fault type. Yet, the studies on the section of the distribution network likewise considered the influence of the filtering of the signal, the fault resistance, the

fault distance and the fault type. The $\mathcal{P}_i(x_g)$ and $\mathcal{E}_i(x_g)$ metrics were used for the fault-location estimation in the studies on both systems. The numerical modelling in the HVDC system had the converter stations modelled and the WB model was used for the cable. The WB model was also applied to the overhead lines in the distribution network section.

In the case of the HVDC system, a cut-off frequency of $1\ \mathrm{kHz}$ for the applied HP filter returned more fault locations correctly estimated. Information related to the fault location was not cut off the spectral content of the signal with $1\ \mathrm{kHz}$. Fault resistances of $5\ \Omega$, $10\ \Omega$, and $50\ \Omega$ led to worse performance, which might be caused by the lowering of the magnitude of the fault-induced resonances. This showed a great shortcoming of both $\mathcal{P}_i(x_g)$ and $\mathcal{E}_i(x_g)$. The change to the CP model for the cable in the RT simulations did not present higher performance for the method. The double-end approach of the method returned lower average and maximum errors on the fault-location estimations in all cases. The results for pole-to-ground and pole-to-pole faults were almost the same.

In the case of the section of the distribution network, the average error on the fault-location estimations was the lowest with the filtering at $3\ \mathrm{kHz}$. The fault-induced resonances present on the EMTs were within the range from $1\ \mathrm{kHz}$ to $10\ \mathrm{kHz}$ for faults at locations farther than $10\ \mathrm{km}$ from the probe end. The cut-off at $3\ \mathrm{kHz}$ did not filter these resonances, whereas it occurred with the filtering with higher cut-off frequencies. The performance of the method benefited from the 3-kHz filter, especially for the faults at far distances. Compared to the HVDC cases, higher fault resistances than $1\ \Omega$ less impacted the performance of the method in all cases. The fault type strongly influenced the results. For instance, the fault-locations estimations had a lower average error for three-phase-to-ground faults than for single-phase-to-ground ones. That is linked to the modal components related to each fault type and the coupling between the phases of the lines, the latter higher than the one of the HVDC system.

From all the results, the overall conclusions of the present thesis are:

- The performance of the most applied metric of the EMTR method for fault location on electric power systems, $\mathcal{E}_i(x_g)$, is very dependent on the distance from the probe ends of the signal used in the TR process to the location of the fault in the presence of propagation losses on the system. It is in a degree that faults farther than a distance of something like $30\ \mathrm{km}$ away from a probe might not have their location correctly estimated. The reach of the method may not be much longer with other metrics, such as $\mathcal{P}_i(x_g)$, which also works through data from RT simulations in an unmatched medium. The results of some of the cases showed similar performance for $\mathcal{P}_i(x_g)$ and $\mathcal{E}_i(x_g)$, indeed.

  Therefore, the use of more than one probe should increase the performance of the method by these metrics, as $30\ \mathrm{km}$ is a distance shorter than the lengths of cables and lines of some power systems. That was observed comparing the results of

double- and single-end forms of the method for the single-conductor and the HVDC systems. In these cases, the probes were at the ends of the system, but they can either be spaced between them by some distance, for instance.

- The length of the signal used in the RT simulations influences the fault-location estimations for the approach with unmatched media. Longer signals tend to lead to higher performance. Therefore, the signal should be as longer as possible.

- The spectral content of the signal used in the TR process determines the performance of the EMTR method. The behaviour of the method is directly related to the fault-induced resonances, which are dependent, e.g., on the system characteristics and the distance from the probe ends to the faults.

  The more information on the fault location is recorded, the higher should be the probability of correct estimation of the fault location. However, lower frequencies might hinder the method's performance given that they are normally not related to the fault, and an HP filter might necessarily be applied to the signal, for instance. In this case, the cut-off frequency used for the filter must be evaluated according to the system rather than arbitrarily chosen. That might be a complex decision because it can involve tests to assess the best value. However, filtering at something like 2 kHz or 3 kHz can generally be a good choice, considering a filter of Butterworth type (the type used here).

- The fault resistance might or not strongly influence the method's performance, which occurs depending on the case applied. The fault resistance decreases the magnitude of the fault-induced resonances according to the magnitude of the resistance value. That can impact the fault-location estimations once the information on the fault location is worsened. Therefore, faults with high resistances are possibly not correctly located by the EMTR method the farther the fault is from the probe ends. That was what happened in the cases of fault resistances higher than 1 Ω in the evaluated HVDC system. Nonetheless, the same impact of the fault resistance was not observed in the cases of the power distribution network.

- The fault type also might or not impact the results of the method, according to the case applied. The fault type is related to the modal components in the fault-induced EMTs. Ground faults yield the ground mode, which is slower than the aerial ones and tends to worsen the performance of the estimations. However, the fault type's influence depends on the coupling between the impedance of the phases of the lines or poles of the cables of the system, as comparing the results from the HVDC system and the distribution network section. For such coupling of a distribution network, the method will return less accuracy on the estimations of

locations of asymmetric ground faults, such as single-phase-to-ground and double-phase-to-ground ones.

- From all the results of this thesis and the considerations above, the EMTR method seems to be limited when applied to fault-location procedures on electric power systems like those of the evaluations in this thesis in the same conditions. The application of the method returned acceptable values of errors for the fault-location estimations only in some studied cases.

  In contrast to the EMTR-based fault-location method, there are currently many other methods presented in the literature on fault location that did not present the same shortcomings in the cases where they were applied. One could expect the same good results of those other methods for the studied cases in this thesis if they were implemented. In a plain supposition, even in the cases where the EMTR method worked, the results by other methods might be more accurate with a lower cost of computational implementation. And it is likely since some of those studies were based on similar cases to the ones herein.

  Following this critical view, the EMTR-based fault-location one needs to be developed to be a better alternative to the current methods for the contexts and conditions considered, and this is related to the metrics applied for the estimation and/or the way these are applied. That is true mainly if the fault-induced EMTs are recorded at only a single probe and long cables or lines form the system, i.e., longer than 30 km, or if it has branches. Otherwise, if many probes record the signal used in the method or the system is formed by only a cable or line whose length is shorter than 30 km, the EMTR method might be a better option against other methods.

  Notwithstanding, any affirmations concerning the comparisons lack verification through similar assessments, which was not done in this work once it focused entirely on the EMTR method. That other methods also have limitations that can lead to poor performance is something acknowledged. Moreover, the literature about the EMTR method highlighted its capabilities and placed the method as a promising alternative for fault location on power systems. Therefore, the method can be a good choice for fault location in other similar cases to those studied here. The results of this thesis came from the analyses of the advantages and limitations of the EMTR method considering complex numerical models for a large number of cases, which was a different perspective.

Future research on the EMTR-based fault-location method applied to power systems can advance towards the development of new metrics, further deeper studies, and the mathematical description of the ways some parameters influence the method's behaviour and how some existent metrics work.

Regarding the development of new metrics, these would need to return estimations of the fault locations with percentage errors equal to or less than 5%, for instance, and:

- to be independent or weakly dependent on the distance from the fault to the probe(s). The method needs to cover extensions of real power systems, i.e., longer than about $30\,\mathrm{km}$. Indeed, this is crucial for the application to transmission systems. Besides, metrics working in a single-end approach of the method would be more suitable for real implementations (considering the advantages that the single-end methods have against the multi-end ones).

- to be independent or weakly dependent on the topology of the system. To have metrics applicable to either distribution or transmission systems, highly branched or loop networks, with single or multiple power sources, is advantageous.

- to be independent or weakly dependent on the knowledge of the parameters of the system. The parameters of the cables, lines, transformers, and other power system components are not truly equal to the nominal ones, given the ageing and fabrication aspects. Also, the parameters of the soil are not fully known in many cases, among others.

- to have a defined form of implementation concerning the steps of any required signal processing. It includes, e.g., what kind of filtering and windowing would be needed.

- to be robust against noise present on the signal. Signals from field recording have noise added which might hamper the method's performance.

- to be robust against fault parameters that can damper the fault-location information present on the EMTs. High fault resistances and low values of fault-inception angle might hamper the method's performance.

Regarding further deeper studies of the method's application, these can bring:

- the application of the metric based on the bounded-phase property in (CODINO *et al.*, 2017) on time-domain data, either from simulations or field measurements. The argument of $\angle V_f(\omega)$ was presented in the method's literature applied in the frequency domain. There is neither a described form of how to apply the argument of $\angle V_f(\omega)$ in the time domain nor studies that show results from such an application. Whether the length, the sampling frequency, the filtering, or the windowing of the signal would impact the metric's performance is not known, nor is the impact of noise.

- analysis of the influence of signal-processing parameters and noise, etc., on the performance of the metric based on the mirrored minimum energy property in (WANG *et al.*, 2017). These aspects have not been covered in any work.

- analysis of the influence of modelling considering frequency-dependent parameters, either in the frequency or time domain, on the performance of the metrics based on the bounded-phase and the mirrored-minimum energy properties. Both works in (CODINO *et al.*, 2017) and (WANG *et al.*, 2017) did not consider such cases.

- the extension of the application of the metrics based on the bounded-phase and the mirrored minimum energy properties to more complex topologies than were presented in (CODINO *et al.*, 2017) and (WANG *et al.*, 2017). The application of the argument of $\angle V_f(\omega)$ in (CODINO *et al.*, 2017) was on a single-conductor and a wye-shape inhomogeneous power network. A system with more branches can be tested so. Still, the mirrored minimum energy property was applied in (WANG *et al.*, 2017) only on a single-conductor system, given the characteristic of the metric. If this metric is able to be improved to be employed in branched systems is not known. Also, both metrics were not applied to three-phase systems.

- analysis of how the choice of different GFLs to the actual fault locations influences the method's performance by any of the existing metrics or other new ones that come to exist. The GFLs fall in the same positions as the actual fault locations in the works of the method's literature. However, the actual fault locations are not known in real fault cases. Therefore, it is truly not reasonable to expect that a set of discrete GFLs likely arbitrarily chosen has the corresponding location of a fault in all cases.

- analysis of how the lack of knowledge of the true values of the parameters of the system impacts the performance of the existing metrics, similar to what is commented above for a new metric.

Regarding missing mathematical descriptions, new works can show those about:

- the metric based on the mirrored minimum energy property. The mathematical demonstration of the principles behind the metric's behaviour was not brought in (WANG *et al.*, 2017), as it was in (CODINO *et al.*, 2017) for the metric based on the bounded-phase property. It seems that the metric was empirically developed. The mathematical description might help improve the metric in such way mentioned above.

- the influence of the spectral content of the signal, as its bandwidth, on the existing and new metrics. The influence of the filtering was observed in the present thesis, and so was the influence of the bandwidth presented for some metrics in (HE;

COZZA; XIE, 2020a,b; COZZA; HE; XIE, 2021b). However, how it mathematically translates is not fully covered. Again, the mathematical demonstration of the influence of the parameters that describe the signal on the performance of the metrics might help both improve them and develop new ones.

Surely future research on the EMTR method can take other directions than those cited above. They were only examples of open topics related to the present thesis seen as encouraging.

REFERENCES

ABBOUD, L. **Time Reversal techniques applied to wire fault detection and location in wire networks**. 2012. Thesis (Doctorate of Physics) — Supélec, 2012. (2012SUPL0002).

ABBOUD, L.; COZZA, A.; PICHON, L. A Noniterative Method for Locating Soft Faults in Complex Wire Networks. **IEEE Transactions on Vehicular Technology**, [S.l.], v. 62, n. 3, p. 1010–1019, Mar. 2013.

ALBERT, D. G.; LIU, L.; MORAN, M. L. Time reversal processing for source location in an urban environment. **The Journal of the Acoustical Society of America**, [S.l.], v. 118, n. 2, p. 616–619, 2005.

AMETANI, A. *et al.* **Power System Transients**: theory and applications. 2nd. ed. Boca Raton, USA: CRC Press, 2016. 600 p.

AN, J. *et al.* An Effective EMTR-Based High-Impedance Fault Location Method for Transmission Lines. **IEEE Transactions on Electromagnetic Compatibility**, [S.l.], v. 63, n. 1, p. 268–276, 2021.

ANCELL, G.; PAHALAWATHTHA, N. Effects of frequency dependence and line parameters on single ended travelling wave based fault location schemes. **IEE Proceedings C (Generation, Transmission and Distribution)**, [S.l.], v. 139, p. 332–342(10), July 1992.

ANCELL, G.; PAHALAWATHTHA, N. Maximum likelihood estimation of fault location on transmission lines using travelling waves. **IEEE Transactions on Power Delivery**, [S.l.], v. 9, n. 2, p. 680–689, 1994.

ANDO, M.; SCHWEITZER, E. O.; BAKER, R. A. Development and Field-Data Evaluation of Single-End Fault Locator for Two-Terminal HVDV Transmission Lines-Part 2 : algorithm and evaluation. **IEEE Transactions on Power Apparatus and Systems**, [S.l.], v. PAS-104, n. 12, p. 3531–3537, 1985.

ARTHUR, J. W. The Evolution of Maxwell's Equations from 1862 to the Present Day. **IEEE Antennas and Propagation Magazine**, [S.l.], v. 55, n. 3, p. 61–81, 2013.

AURANGZEB, M.; CROSSLEY, P.; GALE, P. Fault location on a transmission line using high frequency travelling waves measured at a single line end. *In*: IEEE POWER ENGINEERING SOCIETY WINTER MEETING. CONFERENCE PROCEEDINGS (CAT. NO.00CH37077), 2000., 2000. **Proceedings [...]** [S.l.: s.n.], 2000. v. 4, p. 2437–2442 vol.4.

BAUM, C. *et al.* **Numerical results for multiconductor transmission-line networks, Interaction Note 322**. Albuquerque, USA: Air Force Weapons Laboratory, 1977. 41 p.

BEWLEY, L. **Traveling Waves on Transmission Systems**. [S.l.]: J. Wiley & Sons, 1933.

BEWLEY, L. V. Traveling Waves on Transmission Systems. **Transactions of the American Institute of Electrical Engineers**, [S.l.], v. 50, n. 2, p. 532–550, 1931.

BO, Z. *et al.* Accurate fault location and protection scheme for power cable using fault generated high frequency voltage transients. *In*: MEDITERRANEAN ELECTROTECHNICAL CONFERENCE ON INDUSTRIAL APPLICATIONS IN POWER SYSTEMS, COMPUTER SCIENCE AND TELECOMMUNICATIONS (MELECON 96), 8., 1996. **Proceedings [...]** [S.l.: s.n.], 1996. v. 2, p. 777–780 vol.2.

BO, Z.; WELLER, G.; REDFERN, M. Accurate fault location technique for distribution system using fault-generated high-frequency transient voltage signals. **IEE Proceedings - Generation, Transmission and Distribution**, [S.l.], v. 146, p. 73–79(6), Jan. 1999.

BOGERT, B. Demonstration of Delay Distortion Correction by Time-Reversal Techniques. **IRE Transactions on Communications Systems**, [S.l.], v. 5, n. 3, p. 2–7, 1957.

BOLLEN, M. H. **Understanding Power Quality Problems**: voltage sags and interruptions. [S.l.]: Wiley-IEEE Press, 2000. 672 p.

BORGHETTI, A. *et al.* On the use of continuous-wavelet transform for fault location in distribution power systems. **International Journal of Electrical Power & Energy Systems**, [S.l.], v. 28, n. 9, p. 608–617, 2006. Selection of Papers from 15th Power Systems Computation Conference, 2005.

BORGHETTI, A. *et al.* Continuous-Wavelet Transform for Fault Location in Distribution Power Networks: definition of mother wavelets inferred from fault originated transients. **IEEE Transactions on Power Systems**, [S.l.], v. 23, n. 2, p. 380–388, 2008.

BORGHETTI, A. *et al.* Integrated Use of Time-Frequency Wavelet Decompositions for Fault Location in Distribution Networks: theory and experimental validation. **IEEE Transactions on Power Delivery**, [S.l.], v. 25, n. 4, p. 3139–3146, 2010.

BRAHMA, S. Fault location scheme for a multi-terminal transmission line using synchronized Voltage measurements. **IEEE Transactions on Power Delivery**, [S.l.], v. 20, n. 2, p. 1325–1331, 2005.

BRANIN, F. Computer methods of network analysis. **Proceedings of the IEEE**, [S.l.], v. 55, n. 11, p. 1787–1801, 1967a.

BRANIN, F. Transient analysis of lossless transmission lines. **Proceedings of the IEEE**, [S.l.], v. 55, n. 11, p. 2012–2013, 1967b.

CASSEREAU, D.; FINK, M. Time-reversal of ultrasonic fields. III. Theory of the closed time-reversal cavity. **IEEE Transactions on Ultrasonics, Ferroelectrics, and Frequency Control**, [S.l.], v. 39, n. 5, p. 579–592, 1992.

CHEN, Z.; MAUN, J.-C. Artificial neural network approach to single-ended fault locator for transmission lines. **IEEE Transactions on Power Systems**, [S.l.], v. 15, n. 1, p. 370–375, 2000.

CHEN, Z. *et al.* Properties of Direct-Time and Reversed-Time Transfer Functions to Locate Disturbances Along Power Transmission Lines. *In*: IEEE MILAN POWERTECH, 2019., 2019. **Proceedings [...]** [S.l.: s.n.], 2019. p. 1–6.

CHRISTOPHER, E. *et al.* Fault Location in a Zonal DC Marine Power System Using Active Impedance Estimation. **IEEE Transactions on Industry Applications**, [S.l.], v. 49, n. 2, p. 860–865, 2013.

CHRISTOPOULOS, C.; THOMAS, D.; WRIGHT, A. Scheme, based on travelling-waves, for the protection of major transmission lines. **IEE Proceedings C (Generation, Transmission and Distribution)**, [S.l.], v. 135, p. 63–73(10), Jan. 1988.

CODINO, A. *et al.* An Alternative Method for Locating Faults in Transmission Line Networks Based on Time Reversal. **IEEE Transactions on Electromagnetic Compatibility**, [S.l.], v. 59, n. 5, p. 1601–1612, 2017.

COMMITTEE, I. P. S. R. Automatic Reclosing of Transmission Lines. **IEEE Transactions on Power Apparatus and Systems**, [S.l.], v. PAS-103, n. 2, p. 234–245, 1984.

COSTA, F. *et al.* Mathematical development of the sampling frequency effects for improving the two-terminal traveling wave-based fault location. **International Journal of Electrical Power & Energy Systems**, [S.l.], v. 115, p. 105502, 2020.

COZZA, A.; HE, S.-Y.; XIE, Y.-Z. Surge Compression for Improved Fault Location Accuracy in Full Transient-Based Methods. **IEEE Sensors Journal**, [S.l.], v. 21, n. 2, p. 995–1008, 2021a.

COZZA, A.; HE, S.-Y.; XIE, Y.-Z. Impact of Propagation Losses on Fault Location Accuracy in Full Transient-Based Methods. **IEEE Transactions on Power Delivery**, [S.l.], v. 36, n. 1, p. 383–396, 2021b.

CROSSLEY, P.; MCLAREN, P. Distance Protection Based on Travelling Waves. **IEEE Transactions on Power Apparatus and Systems**, [S.l.], v. PAS-102, n. 9, p. 2971–2983, 1983.

DA COSTA, L. A.; DA SILVA GAZZANA, D.; LEBORGNE, R. C. Fault Location on Point-to-Point HVDC Transmission System by the Electromagnetic Time-Reversal-Based Method. *In*: IEEE INTERNATIONAL CONFERENCE ON ENVIRONMENT AND ELECTRICAL ENGINEERING AND 2021 IEEE INDUSTRIAL AND COMMERCIAL POWER SYSTEMS EUROPE (EEEIC / I&CPS EUROPE), 2021., 2021. **Proceedings [...]** [S.l.: s.n.], 2021. p. 1–6.

DA COSTA, L. A.; GAZZANA, D. S.; LEBORGNE, R. C. Fault Location by the Electromagnetic-Time Reversal Method Using the Fault Clearing Transients. *In*: IEEE INTERNATIONAL CONFERENCE ON ENVIRONMENT AND ELECTRICAL ENGINEERING AND 2022 IEEE INDUSTRIAL AND COMMERCIAL POWER SYSTEMS EUROPE (EEEIC / I&CPS EUROPE), 2022., 2022. **Proceedings [...]** [S.l.: s.n.], 2022. p. 1–6.

DA COSTA, L. A. *et al.* Incipient Fault Location in Underground Distribution Networks Using Electromagnetic Time Reversal. *In*: IEEE INTERNATIONAL CONFERENCE ON ENVIRONMENT AND ELECTRICAL ENGINEERING AND 2020 IEEE INDUSTRIAL AND COMMERCIAL POWER SYSTEMS EUROPE (EEEIC / I&CPS EUROPE), 2020., 2020. **Proceedings [...]** [S.l.: s.n.], 2020. p. 1–6.

DE ROSNY, J.; LEROSEY, G.; FINK, M. Theory of Electromagnetic Time-Reversal Mirrors. **IEEE Transactions on Antennas and Propagation**, [S.l.], v. 58, n. 10, p. 3139–3149, 2010.

DENG, F.; LI, X.; ZENG, X. Single-ended travelling wave protection algorithm based on full waveform in the time and frequency domains. **IET Generation, Transmission & Distribution**, [S.l.], v. 12, p. 3680–3691(11), Aug. 2018.

DERODE, A.; TOURIN, A.; FINK, M. Limits of time-reversal focusing through multiple scattering: long-range correlation. **The Journal of the Acoustical Society of America**, [S.l.], v. 107, n. 6, p. 2987–2998, 2000.

DEWE, M.; SANKAR, S.; ARRILLAGA, J. The application of satellite time references to HVDC fault location. **IEEE Transactions on Power Delivery**, [S.l.], v. 8, n. 3, p. 1295–1302, 1993.

DRAEGER, C.; FINK, M. One-Channel Time Reversal of Elastic Waves in a Chaotic 2D-Silicon Cavity. **Phys. Rev. Lett.**, [S.l.], v. 79, p. 407–410, July 1997.

DYAB, W. M. G. *et al.* A Critical Look at the Principles of Electromagnetic Time Reversal and its Consequences. **IEEE Antennas and Propagation Magazine**, [S.l.], v. 55, n. 5, p. 28–62, 2013.

ERIKSSON, L.; SAHA, M. M.; ROCKEFELLER, G. D. An Accurate Fault Locator with Compensation for Apparent Reactance in the Fault Resistance Resulting from Remote-End Infeed. **IEEE Power Engineering Review**, [S.l.], v. PER-5, n. 2, p. 44–44, 1985.

FARSHAD, M.; SADEH, J. A Novel Fault-Location Method for HVDC Transmission Lines Based on Similarity Measure of Voltage Signals. **IEEE Transactions on Power Delivery**, [S.l.], v. 28, n. 4, p. 2483–2490, 2013.

FERRAZ, R. G. *et al.* Arc fault location: a nonlinear time varying fault model and frequency domain parameter estimation approach. **International Journal of Electrical Power & Energy Systems**, [S.l.], v. 80, p. 347–355, 2016.

FILOMENA, A. D. *et al.* Fault location for underground distribution feeders: an extended impedance-based formulation with capacitive current compensation. **International Journal of Electrical Power & Energy Systems**, [S.l.], v. 31, n. 9, p. 489–496, 2009. Power Systems Computation Conference (PSCC) 2008.

FINK, M. Time reversal of ultrasonic fields. I. Basic principles. **IEEE Transactions on Ultrasonics, Ferroelectrics, and Frequency Control**, [S.l.], v. 39, n. 5, p. 555–566, 1992.

FINK, M. Time-reversed acoustics. **Scientific American**, [S.l.], v. 281, n. 5, p. 91–97, 1999.

FINK, M. *et al.* Self focusing in inhomogeneous media with time reversal acoustic mirrors. *In*: IEEE ULTRASONICS SYMPOSIUM,, 1989. **Proceedings [...]** [S.l.: s.n.], 1989. p. 681–686 vol.2.

FOREST, M.; HOEFER, W. TLM synthesis of microwave structures using time reversal. *In*: IEEE MTT-S MICROWAVE SYMPOSIUM DIGEST, 1992., 1992. **Proceedings [...]** [S.l.: s.n.], 1992. p. 779–782 vol.2.

FUNABASHI, T. *et al.* Digital fault location for parallel double-circuit multi-terminal transmission lines. **IEEE Transactions on Power Delivery**, [S.l.], v. 15, n. 2, p. 531–537, 2000.

FURSE, C. M. *et al.* Fault Diagnosis for Electrical Systems and Power Networks: a review. **IEEE Sensors Journal**, [S.l.], v. 21, n. 2, p. 888–906, 2021.

GAZZANA, D. *et al.* An integrated technique for fault location and section identification in distribution systems. **Electric Power Systems Research**, [S.l.], v. 115, p. 65–73, 2014. Special issue based on selected expanded contributions from the 10th International Conference on Power System Transients (IPST).

GIRGIS, A.; HART, D.; PETERSON, W. A new fault location technique for two- and three-terminal lines. **IEEE Transactions on Power Delivery**, [S.l.], v. 7, n. 1, p. 98–107, 1992.

GRACIA, J.; MAZON, A.; ZAMORA, I. Best ANN structures for fault location in single-and double-circuit transmission lines. **IEEE Transactions on Power Delivery**, [S.l.], v. 20, n. 4, p. 2389–2395, 2005.

GREENWOOD, A. **Electrical Transients in Power Systems**. [S.l.]: Wiley, 1991.

HE, S.-Y.; COZZA, A.; XIE, Y.-Z. Electromagnetic Time Reversal as a Correlation Estimator: improved metrics and design criteria for fault location in power grids. **IEEE Transactions on Electromagnetic Compatibility**, [S.l.], v. 62, n. 2, p. 598–611, 2020a.

HE, S.-Y.; COZZA, A.; XIE, Y.-Z. On the Spatial Resolution of Fault-Location Techniques Based on Full-Fault Transients. **IEEE Transactions on Power Delivery**, [S.l.], v. 35, n. 3, p. 1527–1540, 2020b.

HE, S.-Y. *et al.* Norm Criteria in the Electromagnetic Time Reversal Technique for Fault Location in Transmission Lines. **IEEE Transactions on Electromagnetic Compatibility**, [S.l.], v. 60, n. 5, p. 1240–1248, 2018.

HERRERA-OROZCO, A. *et al.* Incipient fault location formulation: a time-domain system model and parameter estimation approach. **International Journal of Electrical Power & Energy Systems**, [S.l.], v. 90, p. 112–123, 2017.

HSU, Y.-Y. *et al.* An expert system for locating distribution system faults. **IEEE Transactions on Power Delivery**, [S.l.], v. 6, n. 1, p. 366–372, 1991.

IBE, A. O.; CORY, B. J. A Travelling Wave-Based Fault Locator for Two- and Three-Terminal Networks. **IEEE Transactions on Power Delivery**, [S.l.], v. 1, n. 2, p. 283–288, 1986.

IEEE Guide for Automatic Reclosing on AC Distribution and Transmission Lines. **IEEE Std C37.104-2022 (Revision of IEEE Std C37.104-2012)**, [S.l.], p. 1–82, 2022.

INSTITUTE OF ELECTRICAL AND ELECTRONIC ENGINEERS. **IEEE PES Test Feeder**. Available in: <https://cmte.ieee.org/pes-testfeeders/resources/>. Accessed on: 16th January 2021.

INSTITUTE OF ELECTRICAL AND ELECTRONIC ENGINEERS. **IEEE P1547.1/D6**: IEEE Draft Standard for Validation of Computational Electromagnetics Computer Modeling and Simulations. 2021. 1–50 p.

IURINIC, L. U.; FERRAZ, R. G.; BRETAS, A. S. Characteristic frequency of travelling waves applied for transmission lines fault location estimation. *In*: IEEE GRENOBLE CONFERENCE, 2013., 2013. **Proceedings [...]** [S.l.: s.n.], 2013. p. 1–5.

IURINIC, L. U. *et al.* Distribution Systems High-Impedance Fault Location: a parameter estimation approach. **IEEE Transactions on Power Delivery**, [S.l.], v. 31, n. 4, p. 1806–1814, 2016.

IZYKOWSKI, J.; ROSOLOWSKI, E.; SAHA, M. M. Locating faults in parallel transmission lines under availability of complete measurements at one end. **IEE Proceedings - Generation, Transmission and Distribution**, [S.l.], v. 151, p. 268–273(5), Mar. 2004.

IZYKOWSKI, J. *et al.* Accurate Noniterative Fault-Location Algorithm Utilizing Two-End Unsynchronized Measurements. **IEEE Transactions on Power Delivery**, [S.l.], v. 26, n. 2, p. 547–555, 2011.

JACKSON, J. **Classical Electrodynamics**. [S.l.]: Wiley, 1998.

JÄRVENTAUSTA, P.; VERHO, P.; PARTANEN, J. Using fuzzy sets to model the uncertainty in the fault location process of distribution networks. **IEEE Transactions on Power Delivery**, [S.l.], v. 9, n. 2, p. 954–960, 1994.

JIA, K.; THOMAS, D.; SUMNER, M. Impedance-based earth fault location for a non-directly grounded distribution systems. **IET Generation, Transmission & Distribution**, [S.l.], v. 6, p. 1272–1280(8), Dec. 2012.

JIA, K.; THOMAS, D.; SUMNER, M. A New Single-Ended Fault-Location Scheme for Utilization in an Integrated Power System. **IEEE Transactions on Power Delivery**, [S.l.], v. 28, n. 1, p. 38–46, 2013a.

JIA, K.; THOMAS, D. W. P.; SUMNER, M. A New Double-Ended Fault-Location Scheme for Utilization in Integrated Power Systems. **IEEE Transactions on Power Delivery**, [S.l.], v. 28, n. 2, p. 594–603, 2013b.

JOHNS, A. New ultra-high-speed directional comparison technique for the protection of e.h.v. transmission lines. **IEE Proceedings C (Generation, Transmission and Distribution)**, [S.l.], v. 127, p. 228–239(11), July 1980.

KAFAL, M.; COZZA, A. Multifrequency TR-MUSIC Processing to Locate Soft Faults in Cables Subject to Noise. **IEEE Transactions on Instrumentation and Measurement**, [S.l.], v. 69, n. 2, p. 411–418, Feb. 2020.

KAFAL, M.; COZZA, A.; PICHON, L. Locating Multiple Soft Faults in Wire Networks Using an Alternative DORT Implementation. **IEEE Transactions on Instrumentation and Measurement**, [S.l.], v. 65, n. 2, p. 399–406, Feb. 2016.

KAFAL, M.; COZZA, A.; PICHON, L. Locating Faults With High Resolution Using Single-Frequency TR-MUSIC Processing. **IEEE Transactions on Instrumentation and Measurement**, [S.l.], v. 65, n. 10, p. 2342–2348, Oct. 2016.

KAFAL, M. *et al.* A Review on the Application of the Time Reversal Theory to Wire Network and Power System Diagnosis. *In*: IEEE INTERNATIONAL INSTRUMENTATION AND MEASUREMENT TECHNOLOGY CONFERENCE (I2MTC), 2019., 2019. **Proceedings [...]** [S.l.: s.n.], 2019. p. 1–6.

KASZTENNY, B.; ROSTRON, J. Circuit breaker ratings — A primer for protection engineers. *In*: ANNUAL CONFERENCE FOR PROTECTIVE RELAY ENGINEERS (CPRE), 2018., 2018. **Proceedings [...]** [S.l.: s.n.], 2018. p. 1–13.

KAWADY, T.; STENZEL, J. A practical fault location approach for double circuit transmission lines using single end data. **IEEE Transactions on Power Delivery**, [S.l.], v. 18, n. 4, p. 1166–1173, 2003.

KORMYLO, J.; JAIN, V. Two-pass recursive digital filter with zero phase shift. **IEEE Transactions on Acoustics, Speech, and Signal Processing**, [S.l.], v. 22, n. 5, p. 384–387, 1974.

KOSMAS, P.; RAPPAPORT, C. Time reversal with the FDTD method for microwave breast cancer detection. **IEEE Transactions on Microwave Theory and Techniques**, [S.l.], v. 53, n. 7, p. 2317–2323, 2005.

KOSMAS, P.; RAPPAPORT, C. A matched-filter FDTD-based time reversal approach for microwave breast cancer detection. **IEEE Transactions on Antennas and Propagation**, [S.l.], v. 54, n. 4, p. 1257–1264, 2006a.

KOSMAS, P.; RAPPAPORT, C. FDTD-based time reversal for microwave breast cancer Detection-localization in three dimensions. **IEEE Transactions on Microwave Theory and Techniques**, [S.l.], v. 54, n. 4, p. 1921–1927, 2006b.

KUAN, K.; WARWICK, K. Real-time expert system for fault location on voltage underground distribution cables. **IEE Proceedings C (Generation, Transmission and Distribution)**, [S.l.], v. 139, p. 235–240(5), May 1992.

LEROSEY, G. *et al.* Time Reversal of Electromagnetic Waves. **Phys. Rev. Lett.**, [S.l.], v. 92, p. 193904, May 2004.

LEWIS, L. J. Traveling Wave Relations Applicable to Power-System Fault Locators. **Transactions of the American Institute of Electrical Engineers**, [S.l.], v. 70, n. 2, p. 1671–1680, 1951.

LIU, D.; KROLIK, J.; CARIN, L. Electromagnetic Target Detection in Uncertain Media: time-reversal and minimum-variance algorithms. **IEEE Transactions on Geoscience and Remote Sensing**, [S.l.], v. 45, n. 4, p. 934–944, 2007.

LIU, D. *et al.* Electromagnetic time-reversal imaging of a target in a cluttered environment. **IEEE Transactions on Antennas and Propagation**, [S.l.], v. 53, n. 9, p. 3058–3066, 2005.

LIU, D. *et al.* Electromagnetic Time-Reversal Source Localization in Changing Media: experiment and analysis. **IEEE Transactions on Antennas and Propagation**, [S.l.], v. 55, n. 2, p. 344–354, 2007.

LOPES, F. V. *et al.* Real-Time Traveling-Wave-Based Fault Location Using Two-Terminal Unsynchronized Data. **IEEE Transactions on Power Delivery**, [S.l.], v. 30, n. 3, p. 1067–1076, 2015.

LUGRIN, G. *et al.* On the Location of Lightning Discharges Using Time Reversal of Electromagnetic Fields. **IEEE Transactions on Electromagnetic Compatibility**, [S.l.], v. 56, n. 1, p. 149–158, 2014.

LUGRIN, G. *et al.* Electromagnetic time reversal applied to fault detection: the issue of losses. *In*: IEEE INTERNATIONAL SYMPOSIUM ON ELECTROMAGNETIC COMPATIBILITY (EMC), 2015., 2015. **Proceedings [...]** [S.l.: s.n.], 2015. p. 209–212.

MAGNAGO, F.; ABUR, A. Fault location using wavelets. **IEEE Transactions on Power Delivery**, [S.l.], v. 13, n. 4, p. 1475–1480, 1998.

MAHSEREDJIAN, J.; DINAVAHI, V.; MARTINEZ, J. A. Simulation Tools for Electromagnetic Transients in Power Systems: overview and challenges. **IEEE Transactions on Power Delivery**, [S.l.], v. 24, n. 3, p. 1657–1669, 2009.

MANESH, H. M. *et al.* A new method to locate faults in power networks based on Electromagnetic Time Reversal. *In*: IEEE 13TH INTERNATIONAL WORKSHOP ON

SIGNAL PROCESSING ADVANCES IN WIRELESS COMMUNICATIONS (SPAWC), 2012., 2012. **Proceedings [...]** [S.l.: s.n.], 2012. p. 469–474.

MARTINEZ-VELASCO, J. A. **Power System Transients**: parameter determination. 1st. ed. Boca Raton, USA: CRC Press, 2010. 644 p.

MCLAREN, P. G.; RAJENDRA, S. Travelling-Wave Techniques Applied to the Protection of Teed Circuits:- multi-phase/multi-circuit sytstem. **IEEE Transactions on Power Apparatus and Systems**, [S.l.], v. PAS-104, n. 12, p. 3551–3557, 1985a.

MCLAREN, P. G.; RAJENDRA, S. Travelling-Wave Techniques Applied to the Protection of Teed Circuits:- principle of travelling-wave techniques. **IEEE Transactions on Power Apparatus and Systems**, [S.l.], v. PAS-104, n. 12, p. 3544–3550, 1985b.

MIANO, G.; MAFFUCCI, A. (Ed.). **Transmission Lines and Lumped Circuits**. San Diego, USA: Academic Press, 2001. 503 p. (Electromagnetism).

MOMOH, J.; DIAS, L.; LAIRD, D. An implementation of a hybrid intelligent tool for distribution system fault diagnosis. **IEEE Transactions on Power Delivery**, [S.l.], v. 12, n. 2, p. 1035–1040, 1997.

NAGASAWA, T. *et al.* Development of a new fault location algorithm for multi-terminal two parallel transmission lines. **IEEE Transactions on Power Delivery**, [S.l.], v. 7, n. 3, p. 1516–1532, 1992.

NOVOSEL, D. *et al.* Unsynchronized two-terminal fault location estimation. **IEEE Transactions on Power Delivery**, [S.l.], v. 11, n. 1, p. 130–138, 1996.

NUNES, J. *et al.* Distribution systems high impedance fault location: a spectral domain model considering parametric error processing. **International Journal of Electrical Power & Energy Systems**, [S.l.], v. 109, p. 227–241, 2019.

OPPENHEIM, A.; WILLSKY, A.; YOUNG, I. **Signals and Systems**. Englewood Cliffs, USA: Prentice-Hall, 1983. 796 p. (Prentice-Hall Signal Processing Series: Advanced monographs).

ORLANDI, A.; RACHIDI, F.; PAOLONE, M. Extension of the Unmatched-Media Time Reversal Method to Locate Soft Faults in Transmission Lines. **IEEE Transactions on Electromagnetic Compatibility**, [S.l.], v. 60, n. 5, p. 1539–1545, 2018.

ORLANDI, A. *et al.* Feature selective validation (FSV) for validation of computational electromagnetics (CEM). part II- assessment of FSV performance. **IEEE Transactions on Electromagnetic Compatibility**, [S.l.], v. 48, n. 3, p. 460–467, 2006.

OROZCO-HENAO, C. *et al.* Active distribution network fault location methodology: a minimum fault reactance and fibonacci search approach. **International Journal of Electrical Power & Energy Systems**, [S.l.], v. 84, p. 232–241, 2017.

OROZCO-HENAO, C. *et al.* Towards active distribution networks fault location: contributions considering der analytical models and local measurements. **International Journal of Electrical Power & Energy Systems**, [S.l.], v. 99, p. 454–464, 2018.

PAITHANKAR, Y.; SANT, M. A new algorithm for relaying and fault location based on autocorrelation of travelling waves. **Electric Power Systems Research**, [S.l.], v. 8, n. 2, p. 179–185, 1985.

PAUL, C. R. **Analysis of Multiconductor Transmission Lines**. 2nd. ed. New Jersey, USA: Wiley-IEEE Press, London, 2007. 821 p.

POLJAK, D.; NEKHOUL, B.; DRISSI, K. E. K. Some remarks related to first 150 years of Maxwell's equations. *In*: INTERNATIONAL CONFERENCE ON SOFTWARE, TELECOMMUNICATIONS AND COMPUTER NETWORKS (SOFTCOM), 2015., 2015. **Proceedings [...]** [S.l.: s.n.], 2015. p. 48–55.

RACHIDI, F.; RUBINSTEIN, M.; PAOLONE, M. **Electromagnetic Time Reversal**: application to electromagnetic compatibility and power systems. [S.l.]: Wiley, 2017. 304 p.

RAMOS, M. J. *et al.* Distribution networks HIF location: a frequency domain system model and wls parameter estimation approach. **Electric Power Systems Research**, [S.l.], v. 146, p. 170–176, 2017.

RANJBAR, A.; SHIRANI, A.; FATHI, A. A new approach for fault location problem on power lines. **IEEE Transactions on Power Delivery**, [S.l.], v. 7, n. 1, p. 146–151, 1992.

RAZZAGHI, R. **Fast Simulation of Electromagnetic Transients in Power Systems Numerical Solvers and their Coupling with the Electromagnetic Time Reversal Process**. 2016. 205 p. Thesis (Doctorate of Science) — École Polytechnique Fédérale de Lausanne, Lausanne, Switzerland, 2016.

RAZZAGHI, R.; RACHIDI, F.; PAOLONE, M. Single-end FPGA-based fault location system for radial/meshed AC/DC networks based on the electromagnetic time reversal theory. *In*: IEEE MANCHESTER POWERTECH, 2017., 2017. **Proceedings [...]** [S.l.: s.n.], 2017. p. 1–7.

RAZZAGHI, R. *et al.* An Efficient Method Based on the Electromagnetic Time Reversal to Locate Faults in Power Networks. **IEEE Transactions on Power Delivery**, [S.l.], v. 28, n. 3, p. 1663–1673, 2013a.

RAZZAGHI, R. *et al.* On the use of electromagnetic time reversal to locate faults in series-compensated transmission lines. *In*: IEEE GRENOBLE CONFERENCE, 2013., 2013b. **Proceedings [...]** [S.l.: s.n.], 2013b. p. 1–5.

RAZZAGHI, R. *et al.* Fault location in multi-terminal HVDC networks based on Electromagnetic Time Reversal with limited time reversal window. *In*: POWER SYSTEMS COMPUTATION CONFERENCE, 2014., 2014. **Proceedings [...]** [S.l.: s.n.], 2014. p. 1–7.

RAZZAGHI, R. *et al.* An automated FPGA real-time simulator for power electronics and power systems electromagnetic transient applications. **Electric Power Systems Research**, [S.l.], v. 141, p. 147–156, 2016.

RAZZAGHI, R. *et al.* Assessment of the Influence of Losses on the Performance of the Electromagnetic Time Reversal Fault Location Method. **IEEE Transactions on Power Delivery**, [S.l.], v. 32, n. 5, p. 2303–2312, 2017.

SAHA, M. M.; IZYKOWSKI, J. J.; ROSOLOWSKI, E. **Fault Location on Power Networks**. London, UK: Springer, London, 2010. 432 p.

SALIM, R. H. *et al.* Hybrid Fault Diagnosis Scheme Implementation for Power Distribution Systems Automation. **IEEE Transactions on Power Delivery**, [S.l.], v. 23, n. 4, p. 1846–1856, 2008.

SALIM, R. H. *et al.* Extended Fault-Location Formulation for Power Distribution Systems. **IEEE Transactions on Power Delivery**, [S.l.], v. 24, n. 2, p. 508–516, 2009.

SALIM, R.; SALIM, K.; BRETAS, A. Further improvements on impedance-based fault location for power distribution systems. **IET Generation, Transmission & Distribution**, [S.l.], v. 5, p. 467–478(11), Apr. 2011.

SCHREINER, K. E.; FUNK, H. L.; HOPNER, E. Automatic Distortion Correction for Efficient Pulse Transmission. **IBM Journal of Research and Development**, [S.l.], v. 9, n. 1, p. 20–30, 1965.

SCHWEITZER ENGINEERING LABORATORIES. **Ultra-high-speed transmission line relay traveling-wave fault locator high-resolution event recorder**. [S.l.]: Schweitzer Engineering Laboratories, 2019. Available in: <https://selinc.com/products/T400L/>. Accessed on: 18th January 2022.

SCHWEITZER ENGINEERING LABORATORIES. **SEL-T400L Time Domain Line Protection**. [S.l.]: Schweitzer Engineering Laboratories, 2019. Available in: <https://selinc.com/products/T400L/>. Accessed on: 29th August 2023.

SCOTT, I. **Developments in time-reversal of electromagnetic fields using the transmission-line modelling method**. 2010. 238 p. Thesis (Doctorate of Philosophy) — University of Nottingham, Nottingham, United Kingdom, 2010.

SHEHAB-ELDIN, E.; MCLAREN, P. Travelling wave distance protection-problem areas and solutions. **IEEE Transactions on Power Delivery**, [S.l.], v. 3, n. 3, p. 894–902, 1988.

SHORT, T. A. **Electric Power Distribution Handbook**. 2nd. ed. Boca Raton, USA: CRC Press, 2014. 898 p.

SNIEDER, R. **Imaging of Complex Media with Acoustic and Seismic Waves**. Berlin, Heidelberg: Springer Berlin Heidelberg, 2002. p. 1–16.

SORRENTINO, R.; ROSELLI, L.; MEZZANOTTE, P. Time reversal in finite difference time domain method. **IEEE Microwave and Guided Wave Letters**, [S.l.], v. 3, n. 11, p. 402–404, 1993.

SORRENTINO, R.; SO, P. P.; HOEFER, W. J. Numerical Microwave Synthesis by Inversion of the TLM Process. *In*: EUROPEAN MICROWAVE CONFERENCE, 1991., 1991. **Proceedings [...]** [S.l.: s.n.], 1991. v. 2, p. 1273–1277.

STYVAKTAKIS, E.; BOLLEN, M.; GU, I. A fault location technique using high frequency fault clearing transients. **IEEE Power Engineering Review**, [S.l.], v. 19, n. 5, p. 58–60, 1999.

SWIFT, G. W. The Spectra of Fault-Induced Transients. **IEEE Transactions on Power Apparatus and Systems**, [S.l.], v. PAS-98, n. 3, p. 940–947, 1979.

TAKAGI, T. *et al.* A New Alogorithm of an Accurate Fault Location for EHV/UHV Transmission Lines: part i - fourier transformation method. **IEEE Transactions on Power Apparatus and Systems**, [S.l.], v. PAS-100, n. 3, p. 1316–1323, 1981.

TAKAGI, T. *et al.* A New Algorithm of an Accurate Fault Location for EHV/UHV Transmission Lines: part ii - laplace transform method. **IEEE Transactions on Power Apparatus and Systems**, [S.l.], v. PAS-101, n. 3, p. 564–573, 1982a.

TAKAGI, T. *et al.* Development of a New Type Fault Locator Using the One-Terminal Voltage and Current Data. **IEEE Transactions on Power Apparatus and Systems**, [S.l.], v. PAS-101, n. 8, p. 2892–2898, 1982b.

TZIOUVARAS, D.; ROBERTS, J.; BENMOUYAL, G. New multi-ended fault location design for two- or three-terminal lines. *In*: SEVENTH INTERNATIONAL CONFERENCE ON DEVELOPMENTS IN POWER SYSTEM PROTECTION (IEE), 2001., 2001. **Proceedings [...]** [S.l.: s.n.], 2001. p. 395–398.

WANG, Z. *et al.* Using electromagnetic time reversal to locate faults in transmission lines: Definition and application of the "Mirrored Minimum Energy" property. *In*: INTERNATIONAL SYMPOSIUM ON ELECTROMAGNETIC COMPATIBILITY - EMC EUROPE, 2017., 2017. **Proceedings [...]** [S.l.: s.n.], 2017. p. 1–6.

WANG, Z. *et al.* A Full-Scale Experimental Validation of Electromagnetic Time Reversal Applied to Locate Disturbances in Overhead Power Distribution Lines. **IEEE Transactions on Electromagnetic Compatibility**, [S.l.], v. 60, n. 5, p. 1562–1570, 2018a.

WANG, Z. *et al.* Electromagnetic Time Reversal Applied to Fault Location: on the properties of back-injected signals. *In*: POWER SYSTEMS COMPUTATION CONFERENCE (PSCC), 2018., 2018b. **Proceedings [...]** [S.l.: s.n.], 2018b. p. 1–7.

WANG, Z. *et al.* Time reversal applied to fault location in power networks: Pilot test results and analyses. **International Journal of Electrical Power & Energy Systems**, [S.l.], v. 114, p. 105382, 2020a.

WANG, Z. *et al.* Electromagnetic Time Reversal Similarity Characteristics and Its Application to Locating Faults in Power Networks. **IEEE Transactions on Power Delivery**, [S.l.], v. 35, n. 4, p. 1735–1748, 2020b.

WANG, Z. *et al.* A review of time reversal-based methods applied to fault location in power networks. **Frontiers in Energy Research**, [S.l.], v. 10, 2022.

WATSON, N.; ARRILLAGA, J. **Power Systems Electromagnetic Transients Simulation**. [S.l.]: Institution of Engineering and Technology, 2003. (Energy Engineering).

WEDEPOHL, L.; MOHAMED, S. Multiconductor transmission lines. Theory of natural modes and fourier integral applied to transient analysis. **Proceedings of the Institution of Electrical Engineers**, [S.l.], v. 116, p. 1553–1563(10), Sept. 1969.

WESTINGHOUSE ELECTRIC CORPORATION. **Electrical Transmission and Distribution Reference Book**. East Pittsburgh, USA: Westinghouse Electric Corporation, 1964. 824 p.

WU, F.; THOMAS, J.-L.; FINK, M. Time reversal of ultrasonic fields. Il. Experimental results. **IEEE Transactions on Ultrasonics, Ferroelectrics, and Frequency Control**, [S.l.], v. 39, n. 5, p. 567–578, 1992.

YU, C.-S. An Unsynchronized Measurements Correction Method for Two-Terminal Fault-Location Problems. **IEEE Transactions on Power Delivery**, [S.l.], v. 25, n. 3, p. 1325–1333, 2010.

ZAMORA, I. *et al.* Fault location on two-terminal transmission lines based on voltages. **IEE Proceedings - Generation, Transmission and Distribution**, [S.l.], v. 143, p. 1–6(5), Jan. 1996.

ZHAI, H. *et al.* An Electronic Circuit System for Time-Reversal of Ultra-Wideband Short Impulses Based on Frequency-Domain Approach. **IEEE Transactions on Microwave Theory and Techniques**, [S.l.], v. 58, n. 1, p. 74–86, 2010.

APPENDIX A FIGURES OF RESULTS FROM THE FREQUENCY-DOMAIN STUDY CASES ON THE SINGLE-CONDUCTOR NON-BRANCHED TRANSMISSION-LINE SYSTEM

Figures 77 to 88 show the results by $\mathcal{P}_i(x_g)$ for $\ell = 10$ km, with Δx_f and Δx_g equal to 1 km, 100 m, and 10 m, and for $\ell = 1,000$ km, with 100 km, 10 km, and 1 km, where $\Delta\omega$ is $2,000\pi$ rad/s, 200π rad/s, and 20π rad/s. As mentioned in Section 5.1, x_f (along the abscissa axis) and x_g (along the ordinate axis) in the *colormaps* matrices are the real fault locations and the GFLs, respectively, and the axes' points are shown according to the distance to the probe end at 0 km.

Figure 77 – $\mathcal{P}_i(x_g)$ normalised for $\ell = 10$ km with $\Delta x_f = \Delta x_g = 1$ km and double-end recording

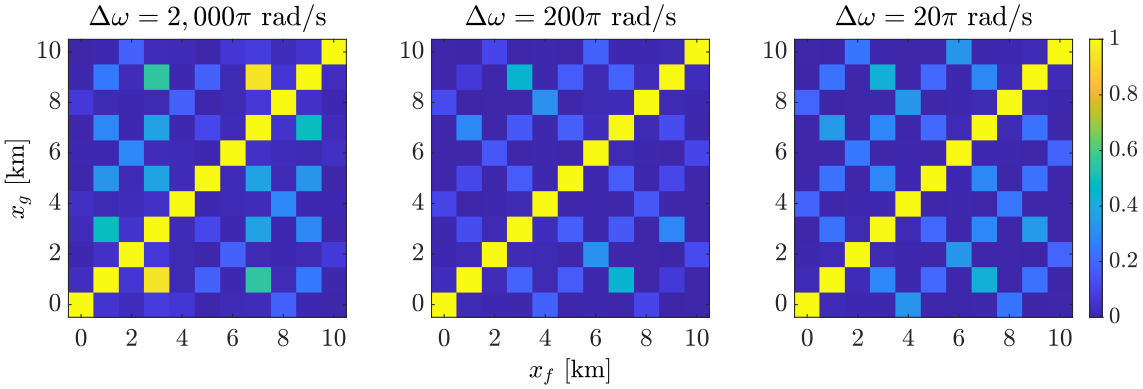

Source: Author

Figures 89 to 96 show the results by $\mathcal{E}_i(x_g)$ and $\mathcal{P}_i(x_g)$ for $\ell = 10$ km and $\Delta x_f = \Delta x_g = 100$ m, and for $\ell = 1,000$ km and $\Delta x_f = \Delta x_g = 10$ km, with $\Delta\omega = 200\pi$ rad/s.

Figures 97 to 102 show $\rho_{HH}(x_g)$ for $\ell = 10$ km, with Δx_f and Δx_g equal to 1 km, 100 m, and 10 m, and for $\ell = 1,000$ km, with 100 km, 10 km, and 1 km, where $\Delta\omega$ is $2,000\pi$ rad/s, 200π rad/s, and 20π rad/s.

Figures 103 and 104 show the results of $\rho_{HH}(x_g)$ for $\ell = 10$ km and $\ell = 1,000$ km,

Figure 78 – $\mathcal{P}_i(x_g)$ normalised for $\ell = 10$ km with $\Delta x_f = \Delta x_g = 1$ km and single-end recording

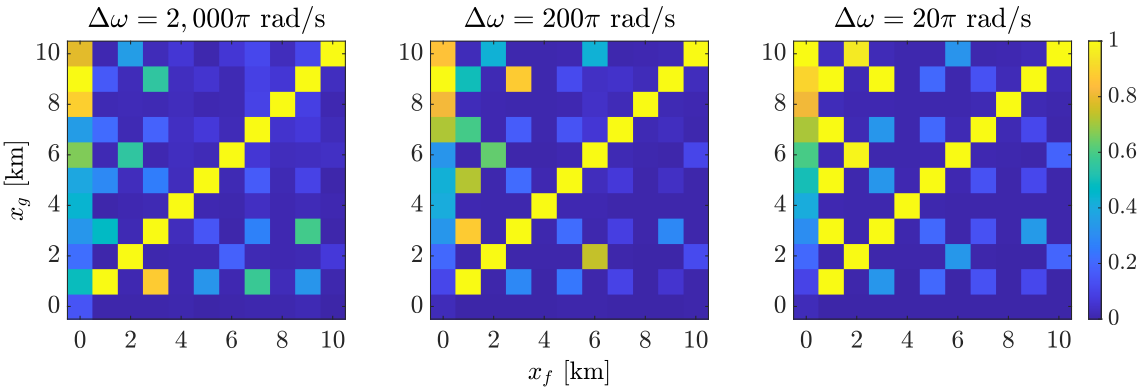

Source: Author

Figure 79 – $\mathcal{P}_i(x_g)$ normalised for $\ell = 1,000$ km with $\Delta x_f = \Delta x_g = 100$ km and double-end recording

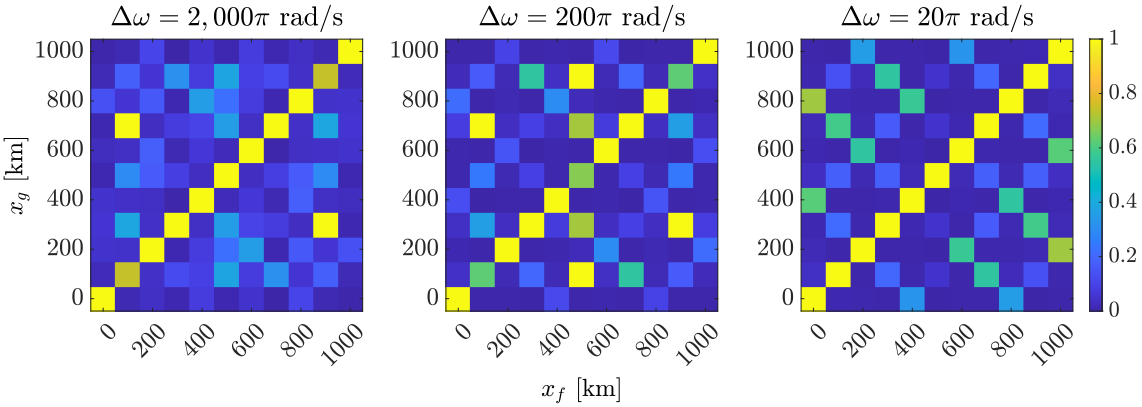

Source: Author

with Δx_g equal to 100 m and 10 m respectively, and with $\Delta\omega = 200\pi$ rad/s, for r/x_l equal to the eight values of $1/20$, $1/10$, $1/4$, 1, $1/2$, 2, 4, and 10.

Figure 80 – $\mathcal{P}_i(x_g)$ normalised for $\ell = 1,000$ km with $\Delta x_f = \Delta x_g = 100$ km and single-end recording

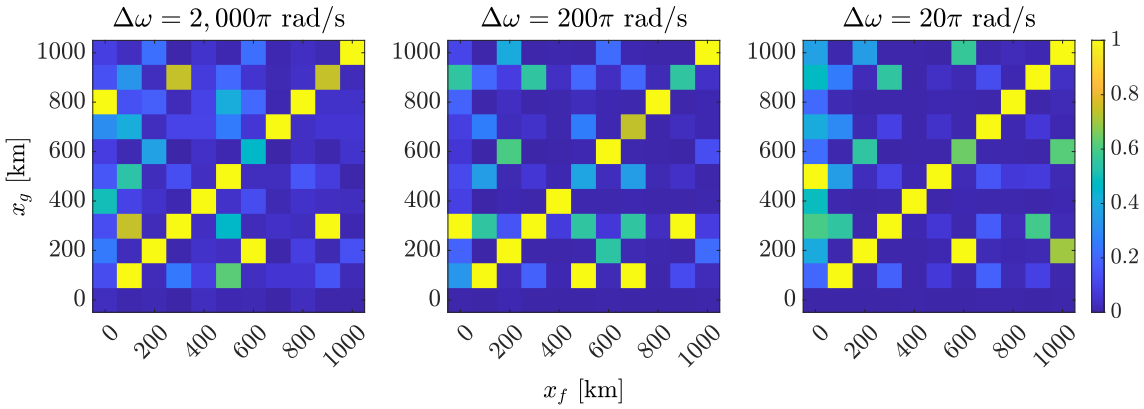

Source: Author

Figure 81 – $\mathcal{P}_i(x_g)$ normalised for $\ell = 10$ km with $\Delta x_f = \Delta x_g = 100$ m and double-end recording

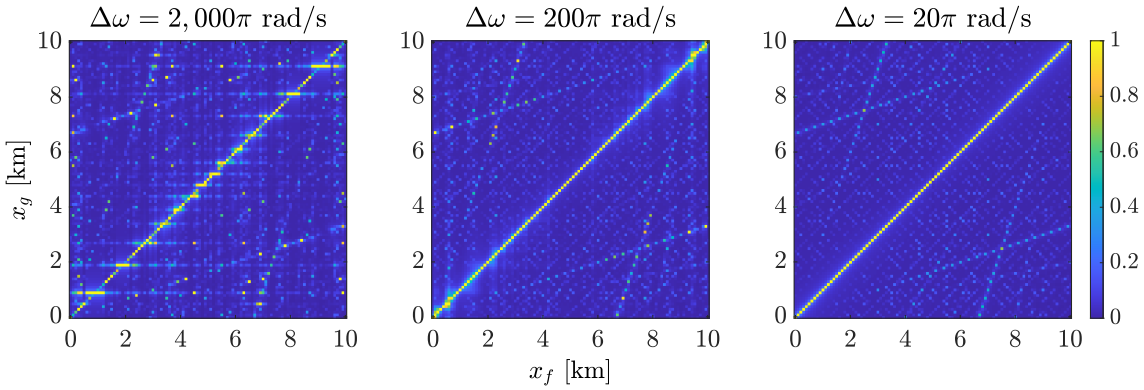

Source: Author

Figure 82 – $\mathcal{P}_i(x_g)$ normalised for $\ell = 10$ km with $\Delta x_f = \Delta x_g = 100$ m and single-end recording

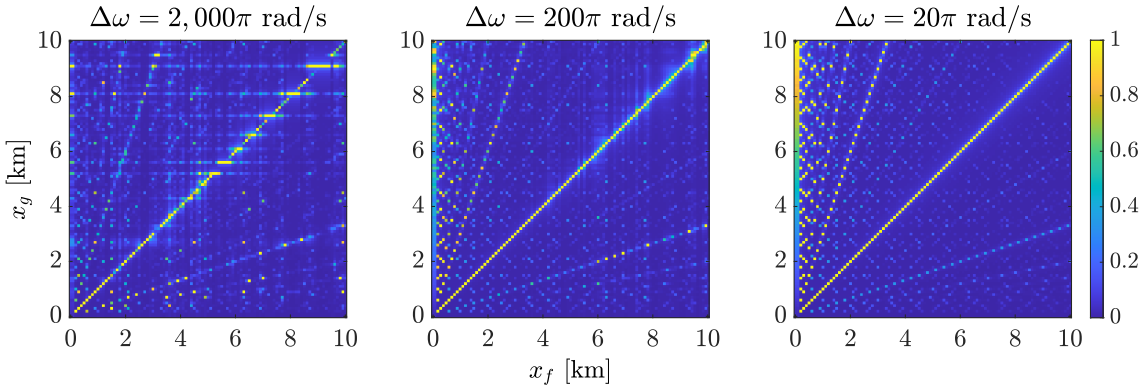

Source: Author

Figure 83 – $\mathcal{P}_i(x_g)$ normalised for $\ell = 1,000$ km with $\Delta x_f = \Delta x_g = 10$ km and double-end recording

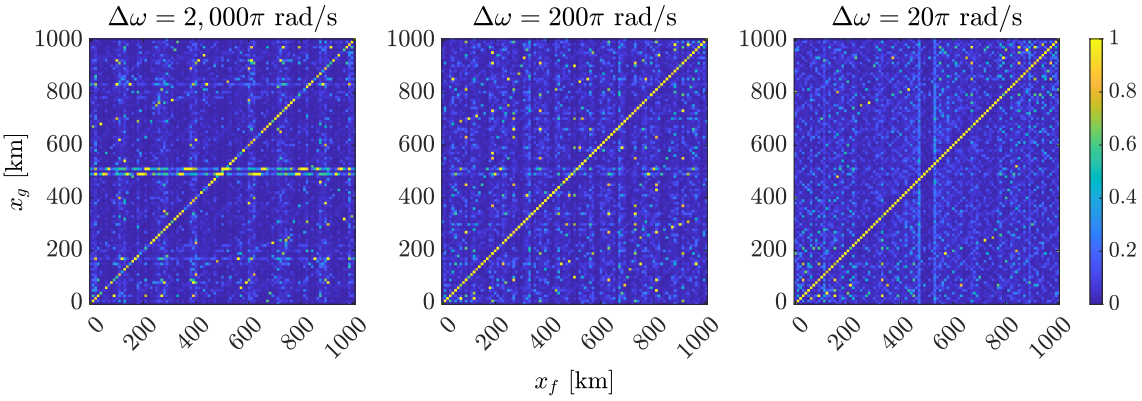

Source: Author

Figure 84 – $\mathcal{P}_i(x_g)$ normalised for $\ell = 1,000$ km with $\Delta x_f = \Delta x_g = 10$ km and single-end recording

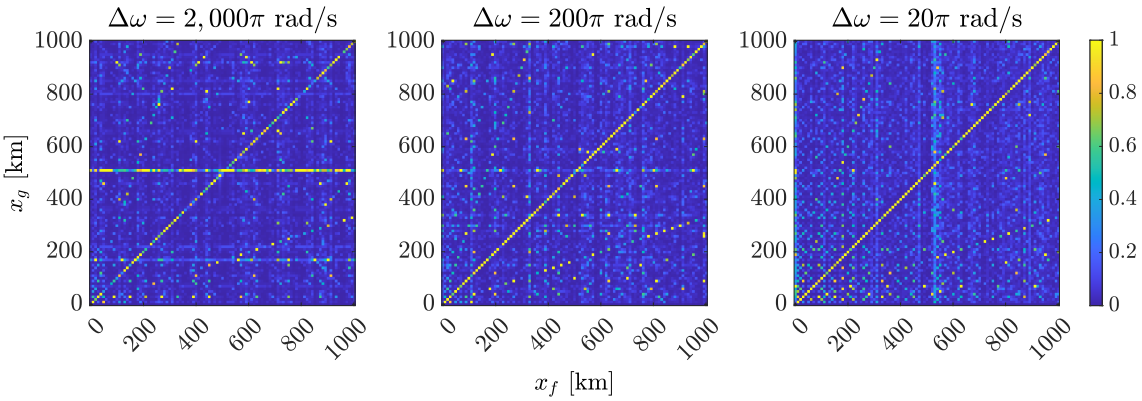

Source: Author

Figure 85 – $\mathcal{P}_i(x_g)$ normalised for $\ell = 10$ km with $\Delta x_f = \Delta x_g = 10$ m and double-end recording

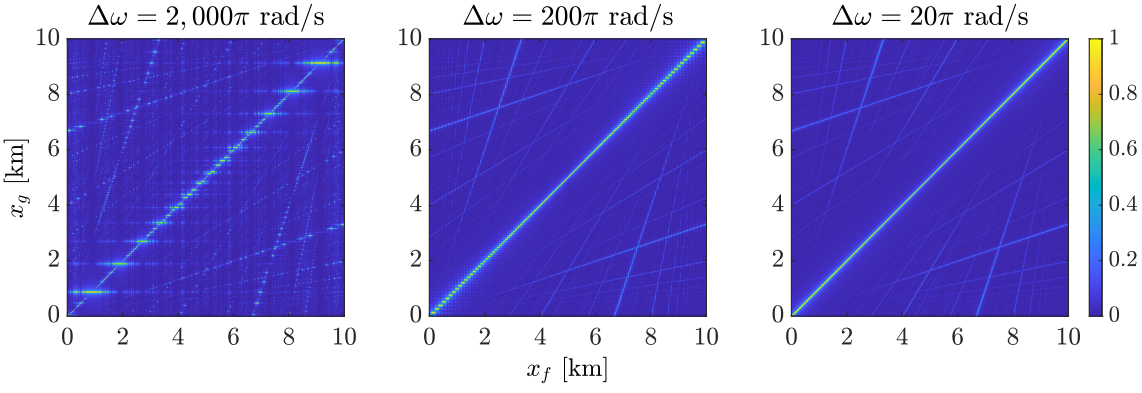

Source: Author

Figure 86 – $\mathcal{P}_i(x_g)$ normalised for $\ell = 10$ km with $\Delta x_f = \Delta x_g = 10$ m and single-end recording

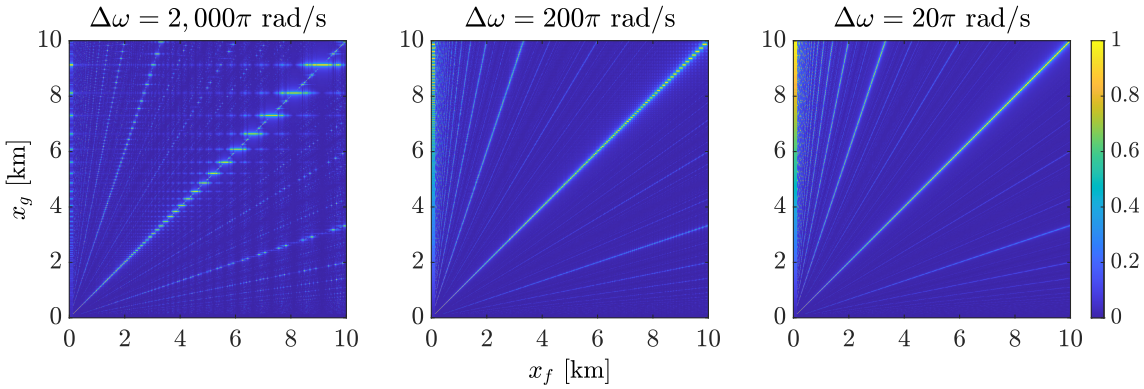

Source: Author

Figure 87 – $\mathcal{P}_i(x_g)$ normalised for $\ell = 1,000$ km with $\Delta x_f = \Delta x_g = 1$ km and double-end recording

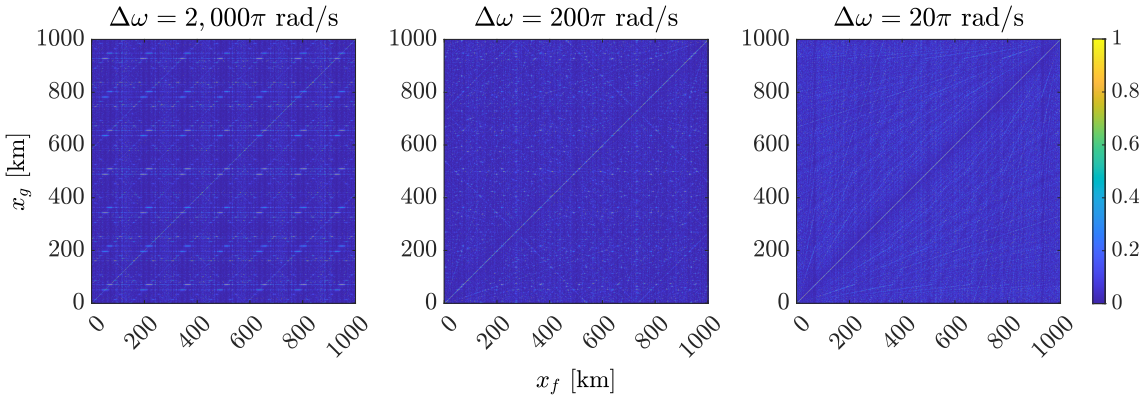

Source: Author

Figure 88 – $\mathcal{P}_i(x_g)$ normalised for $\ell = 1,000$ km with $\Delta x_f = \Delta x_g = 1$ km and single-end recording

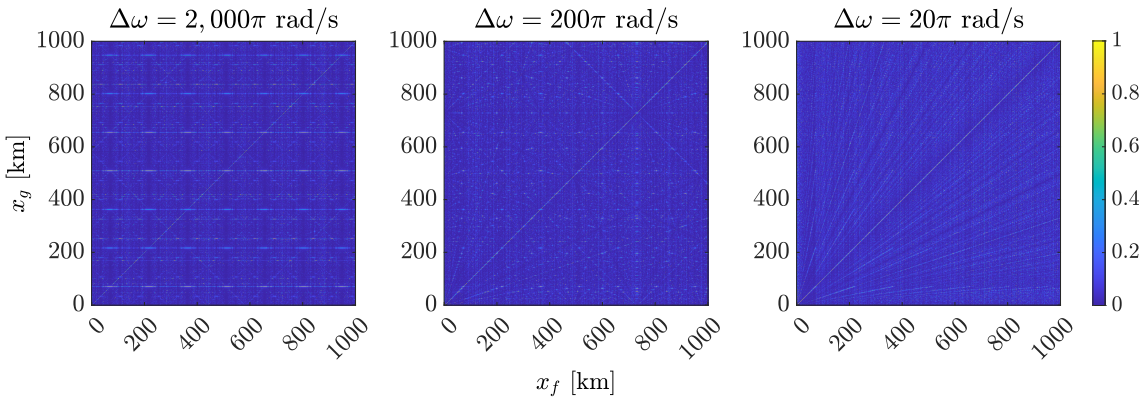

Source: Author

Figure 89 – $\mathcal{E}_i(x_g)$ normalised for $\ell = 10$ km for eight values of r/x_l and double-end recording

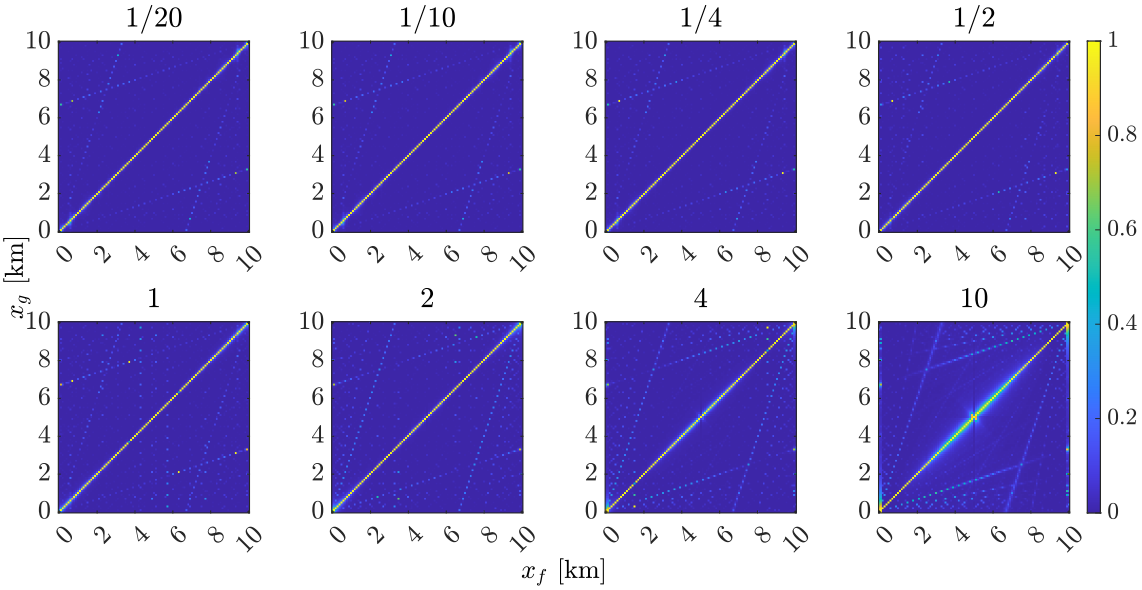

Source: Author

Figure 90 – $\mathcal{E}_i(x_g)$ normalised for $\ell = 10$ km for eight values of r/x_l and single-end recording

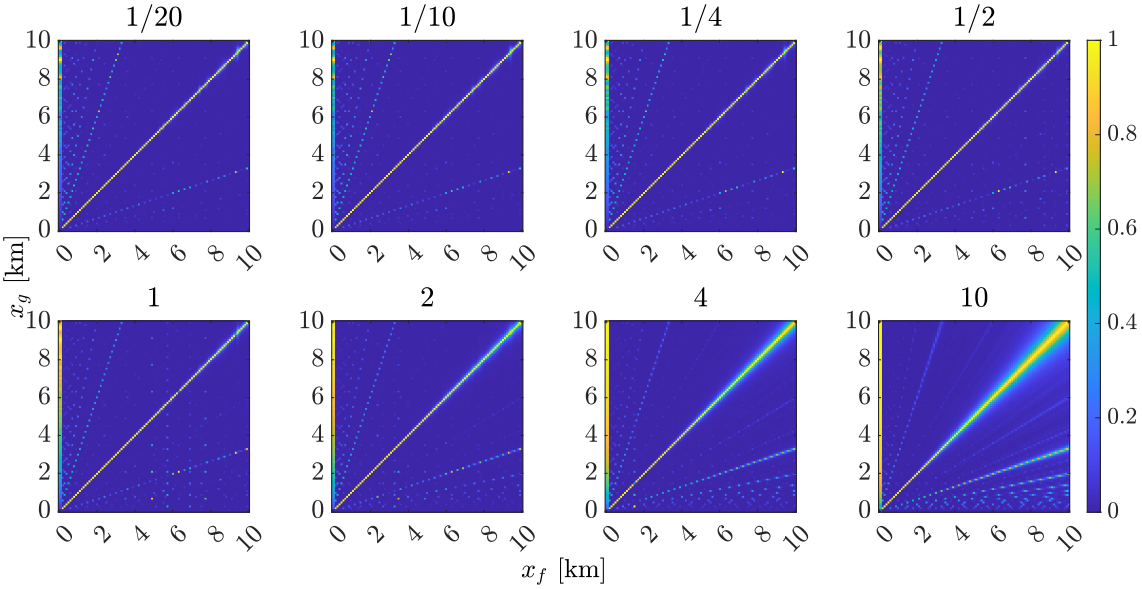

Source: Author

Figure 91 – $\mathcal{E}_i(x_g)$ normalised for $\ell = 1,000$ km for eight values of r/x_l and double-end recording

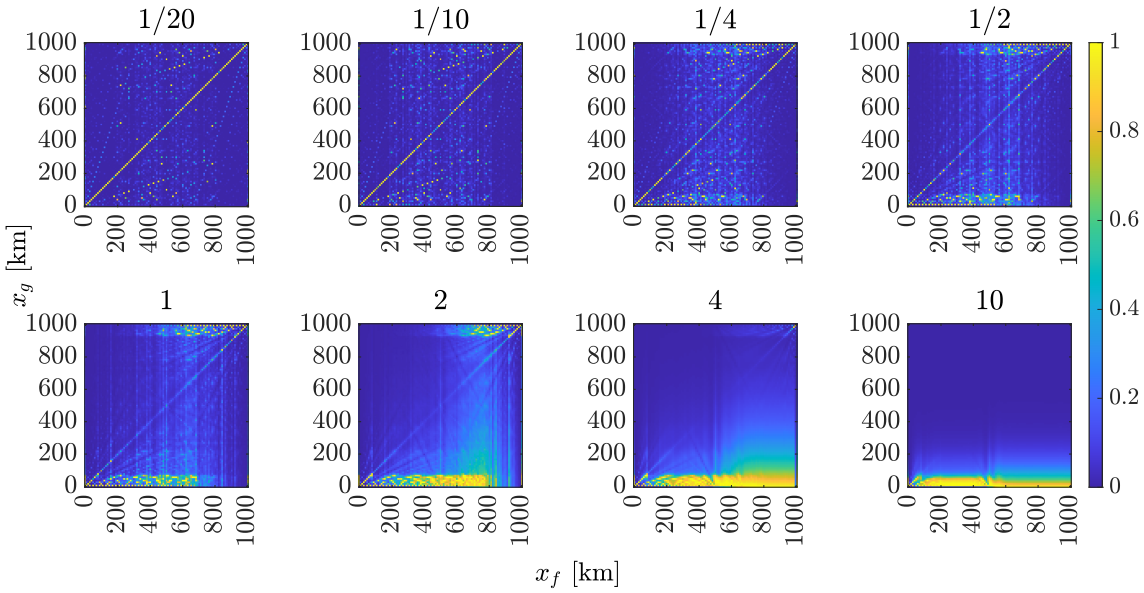

Source: Author

Figure 92 – $\mathcal{E}_i(x_g)$ normalised for $\ell = 1,000$ km for eight values of r/x_l and single-end recording

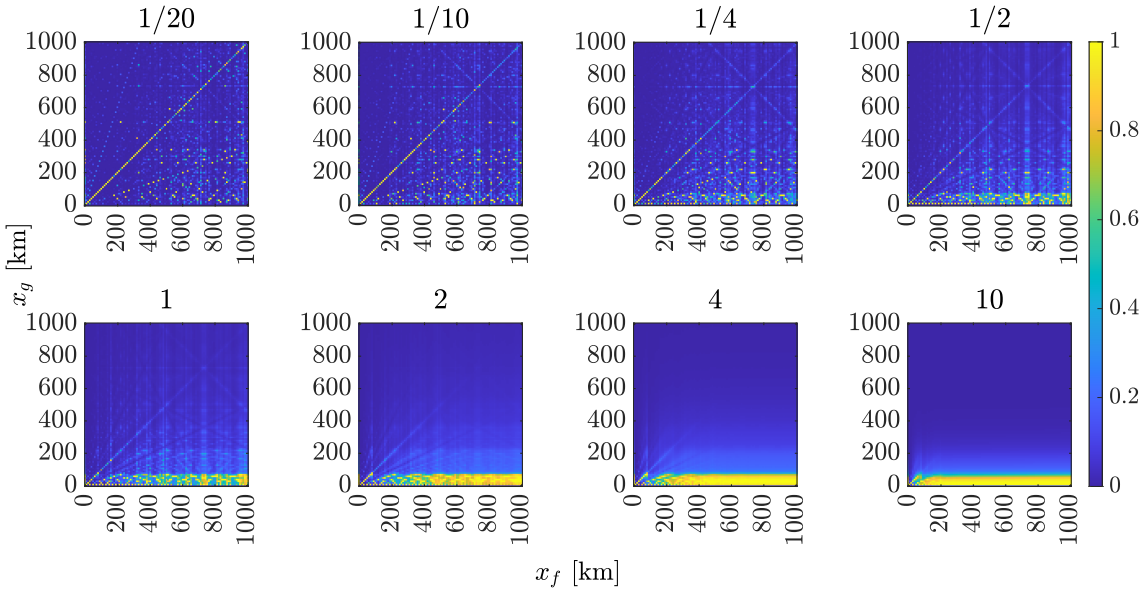

Source: Author

Figure 93 – $\mathcal{P}_i(x_g)$ normalised for $\ell = 10$ km for eight values of r/x_l and double-end recording

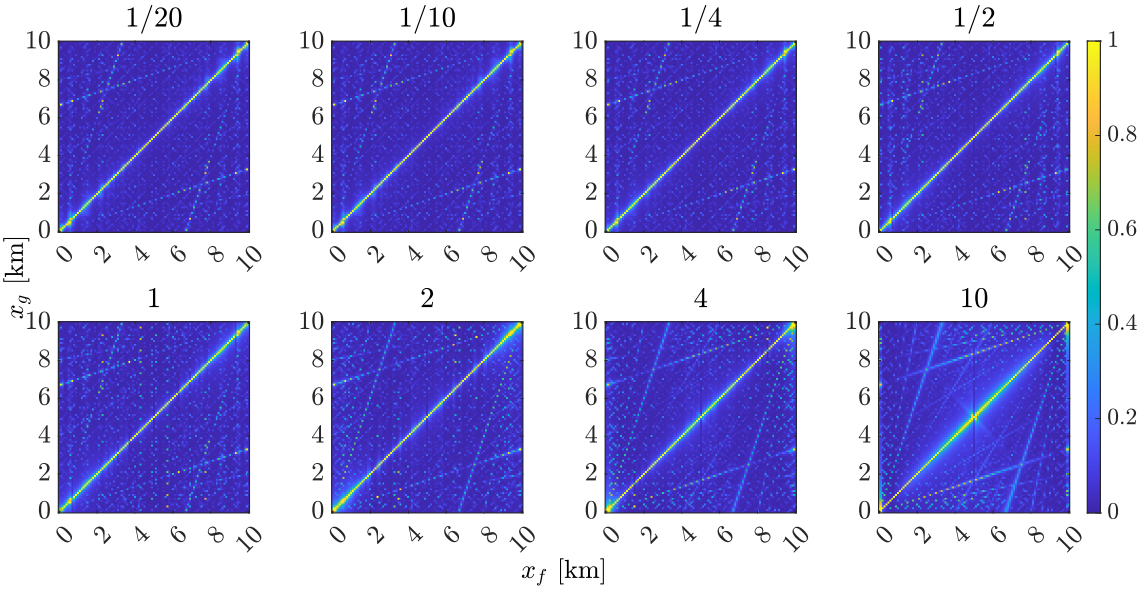

Source: Author

Figure 94 – $\mathcal{P}_i(x_g)$ normalised for $\ell = 10$ km for eight values of r/x_l and single-end recording

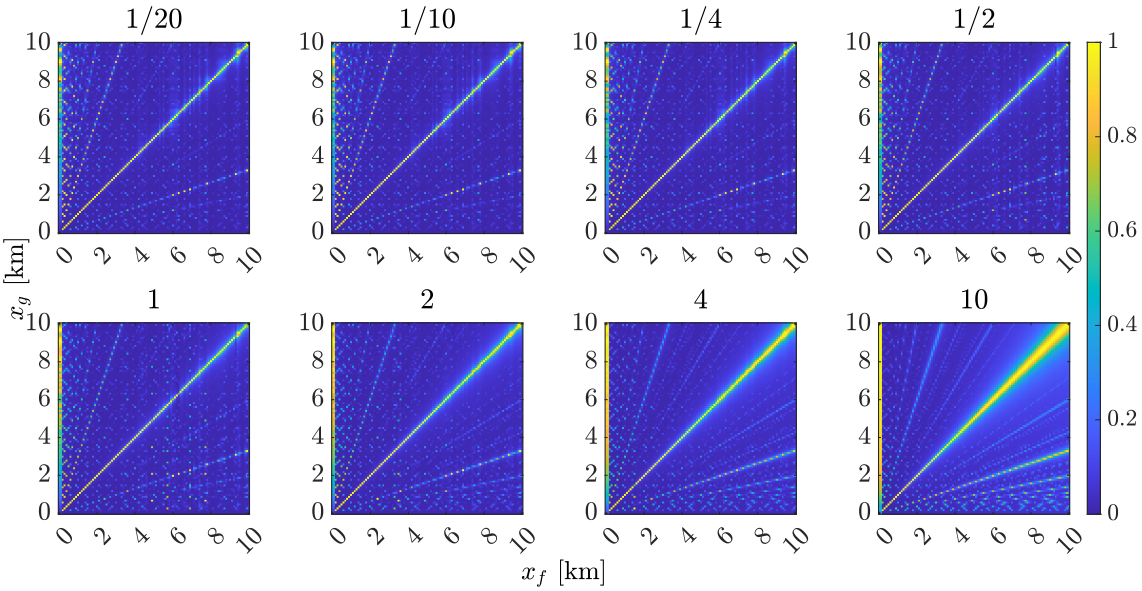

Source: Author

Figure 95 – $\mathcal{P}_i(x_g)$ normalised for $\ell = 1,000$ km for eight values of r/x_l and double-end recording

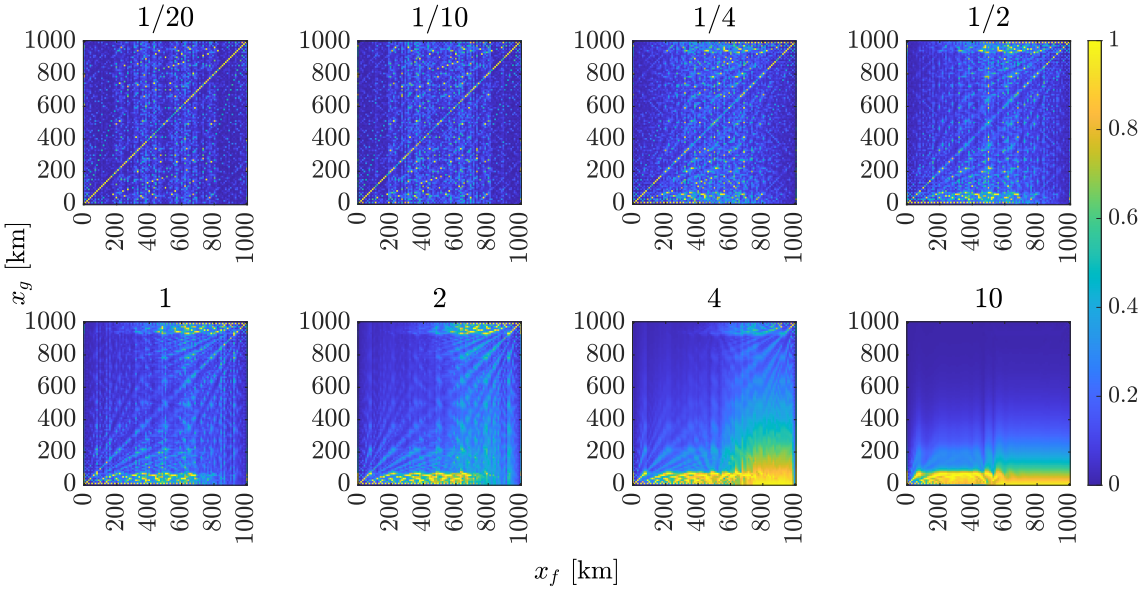

Source: Author

Figure 96 – $\mathcal{P}_i(x_g)$ normalised for $\ell = 1,000$ km for eight values of r/x_l and single-end recording

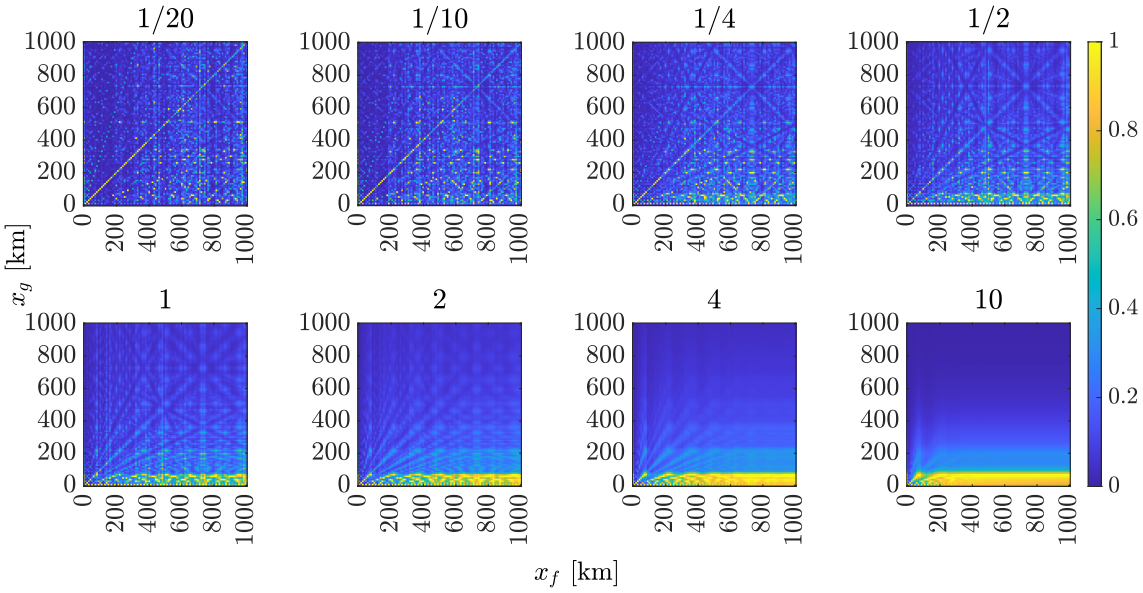

Source: Author

Figure 97 – $\rho_{HH}(x_g)$ for $\ell = 10$ km with $\Delta x_f = \Delta x_g = 1$ km

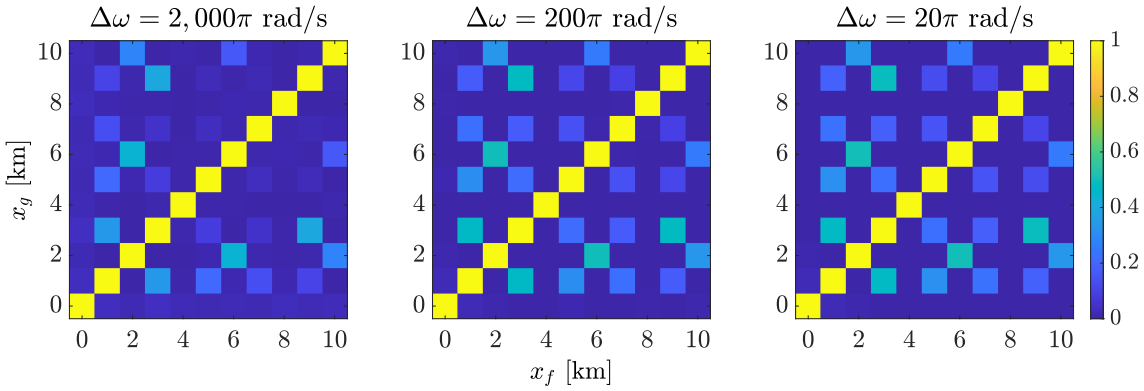

Source: Author

Figure 98 – $\rho_{HH}(x_g)$ for $\ell = 1,000$ km with $\Delta x_f = \Delta x_g = 100$ km

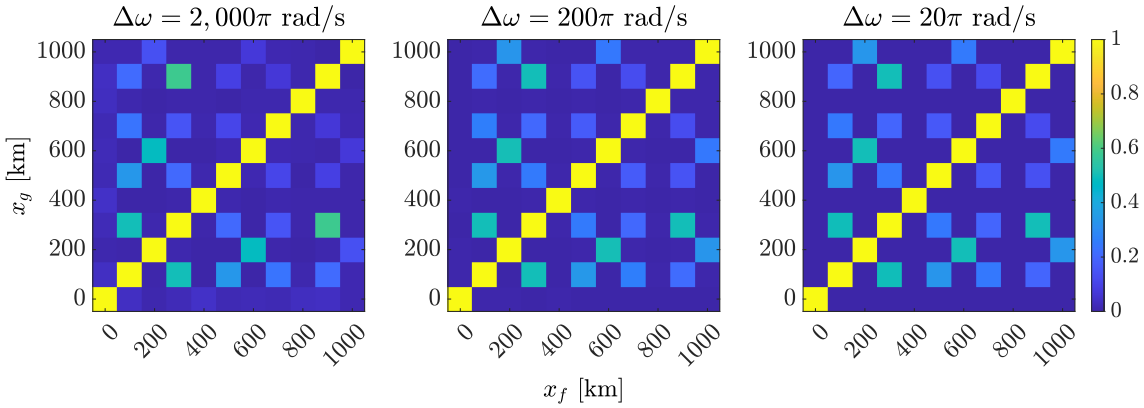

Source: Author

Figure 99 – $\rho_{HH}(x_g)$ for $\ell = 10$ km with $\Delta x_f = \Delta x_g = 100$ m

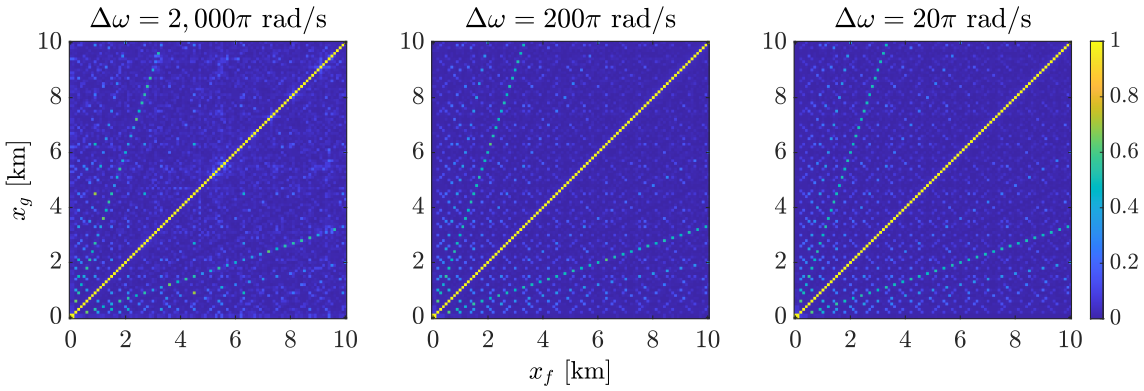

Source: Author

Figure 100 – $\rho_{HH}(x_g)$ for $\ell = 1,000$ km with $\Delta x_f = \Delta x_g = 10$ km

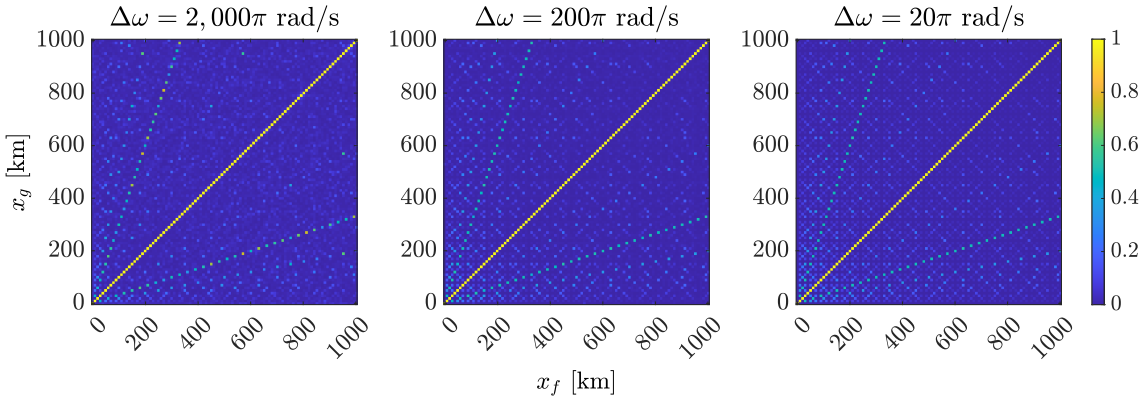

Source: Author

Figure 101 – $\rho_{HH}(x_g)$ for $\ell = 10$ km with $\Delta x_f = \Delta x_g = 10$ m

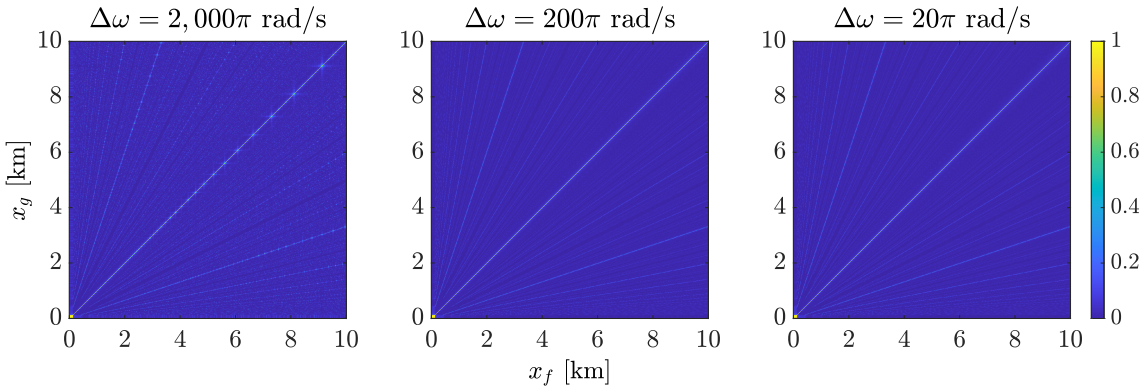

Source: Author

Figure 102 – $\rho_{HH}(x_g)$ for $\ell = 1,000$ km with $\Delta x_f = \Delta x_g = 1$ km

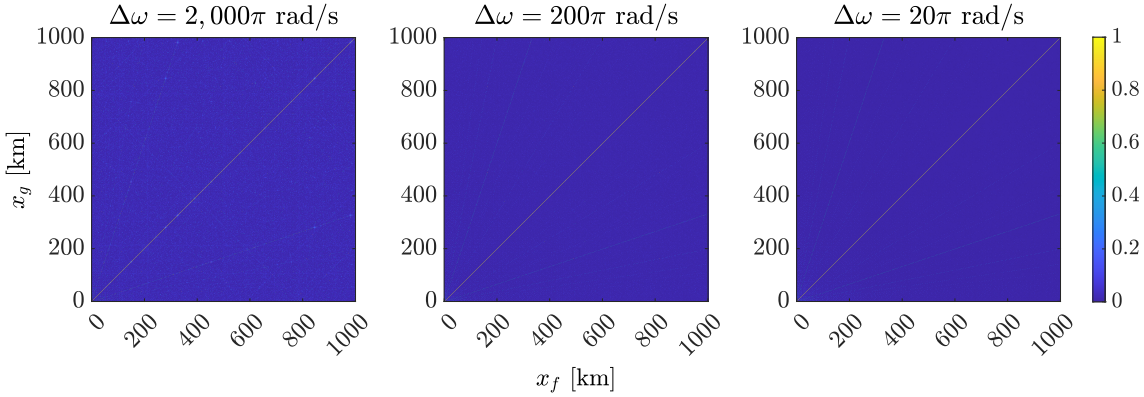

Source: Author

Figure 103 – $\rho_{HH}(x_g)$ for three positions and for eight values of r/x_l, with $\ell = 10$ km

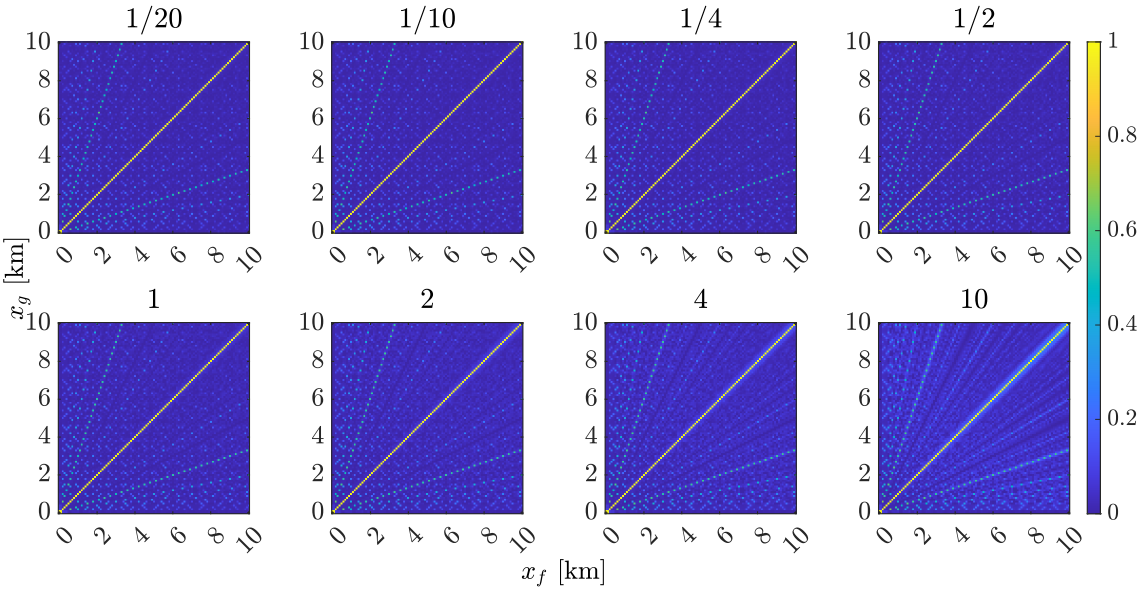

Source: Author

Figure 104 – $\rho_{HH}(x_g)$ for three positions and for eight values of r/x_l, with $\ell = 1,000$ km

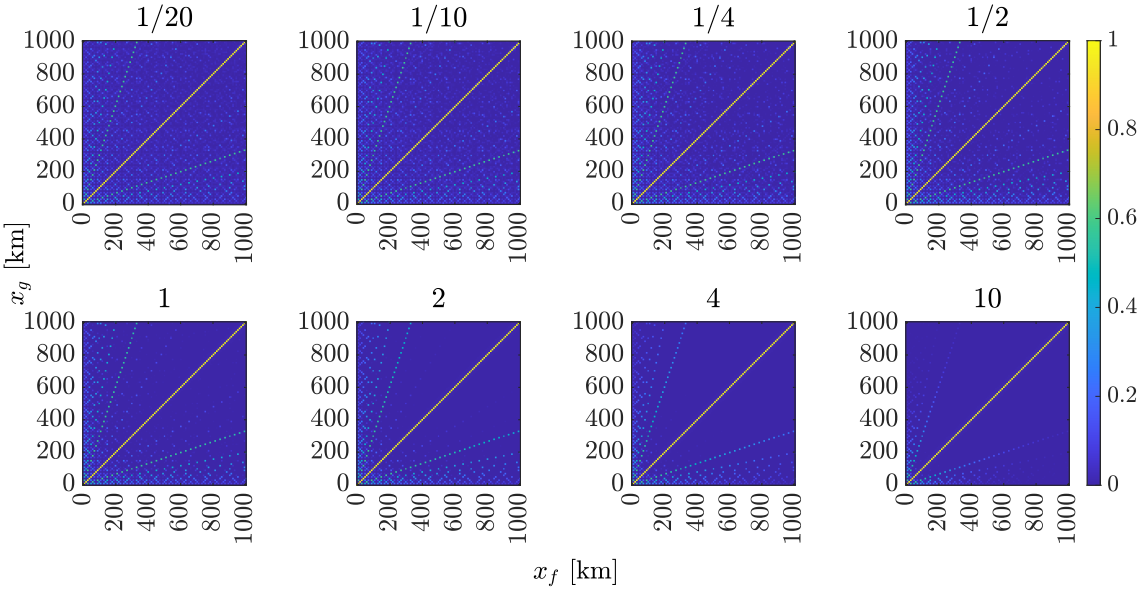

Source: Author

APPENDIX B MODELLING DATA AND SIMULATION PARAMETERS OF THE TIME-DOMAIN STUDY CASES ON THE POINT-TO-POINT HVDC TRANSMISSION SYSTEM IN THE EMTP-RV

EMTP-RV enables choosing some checkbox options and parameters' values related to the software's simulations. These are in the menu *Simulation Options*. The following options and parameters were chosen for the time-domain simulations of the EMTR method for the study cases on the point-to-point HVDC transmission system:

- *Basic Data*
  - *Find Steady-state solution and start from steady-state* [*sic*] was checked;
    - *Start Steady-state solution from Load-Flow solution* [*sic*] was checked — however, there was no load-flow solution, thus appears the message "The Load-Flow solution is not available";
  - *Find Time-domain solution* [*sic*] was checked;
    - *Main time-step* (Δt) equal to 1 µs;
    - *Simulation time:* (t_{max}) equal to 2000 ms [*sic*] ("2000" is the EMTP-RV notation for $2,000$) for the DT simulations, 2 ms for the RT simulations with the recording window of 1 ms and 20 ms for those with the recording window of 10 ms;
  - *Default Power Frequency (Steady-state and Load-Flow)* [*sic*] equal to 50 Hz;
- *Advanced*
  - *Numerical Integration Method*;
    - *Trapezoidal and Backward Euler* was checked;
  - Nothing was changed from the default values in *Solver for control devices* and *Precision control data*;

- *Output*
  - *Plot output (scopes) options*;
    - *Save waveforms* was checked;
    - *Fixed output rate for waveforms* equal to 1;
    - *High precision output* was checked;
    - *Plot file format* as *MPLOT*;
    - *Save scope names* was checked;
    - *Save intermediate time-points* was checked;
  - *ASCII Output options*
    - *HTML output*;
  - *Waitbar Step* [*sic*] equal to 100;
- *Memory*
  - *Predicted number of nonzeros* [*sic*] equal to 10 *(scaling factor)*;
  - *Offset for sparse matrix storage (electrical network)* equal to 100 *(extra cells)*;
  - *Predicted number of nonzeros (control system)* [*sic*] equal to 5 *(scaling factor)*;
  - *Predicted number of nodes* equal to 200.

Two black boxes model the ac sources at both ends of the HVDC link in the DT simulations. The black boxes[1] were composed of an *AC voltage source and impedance* part and a *Load-Flow Bus* part[2]. The options and parameters of the *AC voltage source and impedance* part were the following:

- *Source*
  - *Generic 3-phase voltage source data* [*sic*] was checked;
    - *Phase A*
      - V_m equal to $\frac{400\times\sqrt{2}}{\sqrt{3}}$ kV, or approximately 326598.63 kV;
      - f equal to 50 Hz;
      - θ equal to $0°$;
      - t_{start} equal to -1 s;

[1] The use of black boxes was not really necessary in this case since they model a simple component. This system is an example of the application cases of EMTP-RV, and the components were the same as the original.

[2] As the study cases were performed through fault simulations, the load-flow solution was also not really necessary.

        - t_{stop} equal to $1E15$ s [*sic*] ("$1E15$" is the EMTP-RV notation for 1.00×10^{15});
    - *Phase B*
        - V_m equal to $\frac{400 \times \sqrt{2}}{\sqrt{3}}$ kV;
        - f equal to 50 Hz;
        - θ equal to $-120°$;
        - t_{start} equal to -1 s;
        - t_{stop} equal to $1E15$ s [*sic*];
    - *Phase C*
        - V_m equal to $\frac{400 \times \sqrt{2}}{\sqrt{3}}$ kV;
        - f equal to 50 Hz;
        - θ equal to $120°$;
        - t_{start} equal to -1 s;
        - t_{stop} equal to $1E15$ s [*sic*];
    - *balanced* was checked;
    - *Load-Flow solution device* [*sic*] — the slack bus given by the *Load-Flow Bus* part was the option chosen, noted as *Slack:LF2* ("LF2" was the name of the slack bus);

- *Impedance*
    - *Impedance data input* was checked;
        - *Impedance real part — Sequence Data Input* was checked — *R*;
            - *Zero* equal to $\frac{400^2}{10{,}000 \times \sqrt{(101)}}$ Ω, approximately 1.59 Ω;
            - *Positive* equal to $\frac{400^2}{10{,}000 \times \sqrt{(101)}}$ Ω;
            - *Negative* equal to $\frac{400^2}{10{,}000 \times \sqrt{(101)}}$ Ω;
        - *Impedance imaginary part — Sequence Data Input* was checked — *L*;
            - *Zero* equal to $\frac{10 \times 400^2}{2 \times \pi \times 50 \times 10{,}000 \times \sqrt{(101)}}$ H, approximately 0.05 H;
            - *Positive* equal to $\frac{10 \times 400^2}{2 \times \pi \times 50 \times 10{,}000 \times \sqrt{(101)}}$ H;
            - *Negative* equal to $\frac{10 \times 400^2}{2 \times \pi \times 50 \times 10{,}000 \times \sqrt{(101)}}$ H;
- The options of the other tabs were default or not checked.

The options and parameters of the *Load-Flow bus* part were the following:

- *Values*
    - *Bus type* as *Slack bus*;

  - *Frequency* equal to 50 Hz;
  - *Controlled Voltage* equal to $\frac{400\times\sqrt{2}}{\sqrt{3}}$ kV (equal to V_m — this could be done by *#Vm#*);
  - *Controlled Phase* equal to 0 deg;
  - *Retrieve Impedance data from (reference)* as *VwZ1* (this the name of the *AC voltage source and impedance* part);
    * *Source impedance R — Sequence Data* was checked — *R*;
      · *Zero* equal to $\frac{400^2}{10{,}000\times\sqrt{(101)}}$ Ω, approximately 1.59 Ω;
      · *Positive* equal to $\frac{400^2}{10{,}000\times\sqrt{(101)}}$ Ω;
      · *Negative* equal to $\frac{400^2}{10{,}000\times\sqrt{(101)}}$ Ω;
    * *Impedance imaginary L — Sequence Data* was checked — *L*;
      · *Zero* equal to $\frac{10\times400^2}{2\times\pi\times50\times10{,}000\times\sqrt{(101)}}$ H, approximately 0.05 H;
      · *Positive* equal to $\frac{10\times400^2}{2\times\pi\times50\times10{,}000\times\sqrt{(101)}}$ H;
      · *Negative* equal to $\frac{10\times400^2}{2\times\pi\times50\times10{,}000\times\sqrt{(101)}}$ H;

- The options of the other tabs were default or not checked.

The black boxes were each connected to other black boxes at both ends of the link. Those were only composed of one *PQm* part, the three-phase meter for active and reactive periodic power. The options and parameters of the two *PQm* parts were the following:

- *Data*
  - *Use Global Data* was checked;
  - *Initial Parameters-Values: Text mode input*
    * *freq = oGlobalData.DefaultFrequency;*
    * *Pic = 0*;
    * *Qic = 0*;
    * *Pscope=1;*
    * *Qscope=1;*

- *Options*
  - *Copy options to other masks*
    * *Accept global data update in Read-Only subcircuits* was checked;
  - *Configuration options*
    * *Hide 'Rules/Calculations' area* was checked;

    - *Hide 'Variables to transmit' section* was checked;

Downstream the *PQm* parts were the converter stations. For the *MMC station* parts that model them, the options and parameters were the following:

- *Main data*
  - *Type of model :* [*sic*] as *Model 3 - Switching Function of Arm*;
  - *Configuration :* [*sic*] as *Monopolar*;
  - *Rated power* equal to $1000\ \mathrm{MVA}$; [*sic*] ("1000" is the EMTP-RV notation for $1,000$);
  - *AC primary voltage* [*sic*] equal to $400\ \mathrm{kVRMSLL}$ ("kVRMSLL" is the EMTP-RV notation for "line-to-line rms kV");
  - *AC secondary voltage* [*sic*] equal to $320\ \mathrm{kVRMSLL}$;
  - *Frequency* equal to $50\ \mathrm{Hz}$;
  - *DC pole-to-pole voltage* equal to $640\ \mathrm{kV}$;
  - *Transformer reactance* equal to $0.18\ \mathrm{pu}$;
  - *Transformer resistance* equal to $0.001\ \mathrm{pu}$;
  - *MMC arm Inductance* [*sic*] equal to $0.15\ \mathrm{pu}$;
  - *Capacitor energy in each Submodule (SM)* [*sic*] equal to $40\ \mathrm{kJ/MVA}$;
  - *Number of submodules per arm* equal to 400;
  - *Conduction losses of each IGBT/diode* equal to $0.001\ \Omega$;
  - *Connect star point reactor* equal to 1;
  - *Initialization Time* [*sic*] equal to $0.2\ \mathrm{s}$;
  - *LF_Pref* [*sic*] equal to $1\ \mathrm{pu}$ for the converter at the left end of the link and to $-1\ \mathrm{pu}$ for the converter at the right end;
  - *LF_Qref* [*sic*] equal to $0\ \mathrm{pu}$;
  - *Exclude transformer magnetization branch model* was checked.
- *Control data*
  - *Type of Outer Control* as *P control*;
  - *Active power control*
    - *Reference* equal to $1\ \mathrm{pu}$;
    - *Time constant* equal to $0.1\ \mathrm{s}$;
    - *Step value* equal to $-0.1\ \mathrm{pu}$;

    - *Step time* equal to $1E+15$ s ("$1E+15$" is an EMTP-RV notation for 1.00×10^{15});
- *DC voltage control*
    - *Reference* equal to 1 pu;
    - *Time constant* equal to 0.1 s;
    - *Step value* equal to -0.05 pu;
    - *Step time* equal to $1E+15$ s;
- *P/Vdc droop control*
    - *Droop value* ($\Delta Vdc/\Delta P$) equal to 0.2 s;
- $Vac/f(V/F)$ *control*
    - *Reference* equal to 1 pu;
    - *Time constant* equal to 0.1 s;
    - $Xpcc$ equal to 1 pu;
    - *Step value* equal to -0.05 pu;
    - *Step time* equal to $1E+15$ s;
- *Q or Vac Control* as *Q control*;
- *Reactive power control*
    - *Reference* equal to 0 pu;
    - *Time constant* equal to 0.1 s;
    - *Step value* equal to -0.1 pu;
    - *Step time* equal to $1E+15$ s ("$1E+15$" is an EMTP-RV notation for 1.00×10^{15});
- *AC voltage control*
    - *Reference* equal to 1 pu;
    - *Time constant* equal to 0.1 s;
    - *Xpcc* equal to 1 pu for the converter at the left end of the link and to 0.1 pu for the converter at the right end;
    - *Step value* equal to 0.05 pu;
    - *Step time* equal to $1E+15$ s ("$1E+15$" is an EMTP-RV notation for 1.00×10^{15});
- *Inner Current Control Time constant* [*sic*] equal to 0.01 s;
- *I d-q reference limiter*
    - *Priority is given to* as *Reactive power*;
    - *Maximum rated current* equal to 1.1 pu;

        * *Maximum Id reference* equal to 1.1 pu;
        * *Maximum Iq reference* equal to 0.5 pu;
    - *Active Protection system* [*sic*] was checked;
    - *DC current maximum limit protection* equal to 6 pu.

Connected to the *MMC station* parts were the current meters given by the *Current scope and observe* parts, one at each pole at the left end of the link. The only option checked was the following:

- *Scopes*
    - *Time-domain or Frequency scan scopes/td>* [*sic*]
        * *i* was checked;
- No other option of another tab was checked.

Connected to the *Current scope and observe* parts were the *CT* parts that model the current transformers[3] (only on the right side). The options and parameters were the following:

- *Data*
    - *Nominal frequency* equal to 60 Hz;
    - *Transformer data*
        * *Ratio* equal to $1200 : 5$ A (1200 and 5 go each one in different boxes — "1200" is the EMTP-RV notation for $1,200$);
        * *Winding 1 R* equal to 0 Ω;
        * *Winding 1 X* equal to 0 Ω;
        * *Winding 2 R* equal to 0.15 Ω;
        * *Winding 2 X* equal to 0 Ω;
    - *Burden data*
        * Z_{burden} equal to 2 Ω;
        * *Power Factor* equal to 0.5;
    - *Excitation Curve* — current and voltage points form the following table:
    - *Magnetization resistance* [*sic*] equal to 10 MΩ;
- *IC*

[3] Although the voltage signal was used in the studies of the HVDC link, the current transformers were modelled to observe the current signal.

Current (A)	*Voltage* (V)
0.01	6.8
0.02	17
0.03	28
0.05	56
0.1	145
0.16	200
0.2	215
0.5	230
1	235
5	245
10	250

  - *Initial flux* (ϕ_0) equal to 0 Wb — the default value;

- *Scopes*

  - *Winding 2 current (exiting)* was checked;

- *Attributes* — the default options were used.

The current transformers at the left end of the link and the converter station at the right end were then connected to the buses at the ends of the link cable. Also, voltage meters given by the *Voltage scope* part were connected to those buses. The connection to a bus causes a part to have a three-phase form, so the voltage scopes automatically assume the three-phase form. The signals under the TR transformation were from these voltage scopes. Their options were the following:

- *Phase A* was checked;

- *Phase B* was checked;

- *Phase C* was checked;

- As *Per-unit* was not checked, the *Voltage base* field does not influence and has the default value.

The cable of the HVDC link was divided into seventy sections of 1 km, with buses between the sections corresponding to the faulted points (a different connection for each fault case). The *Wideband line/cable* part was used for the cable sections, where model data given by the *Line/Cable Data* part is loaded (a file with an extension "mod"). The options and parameters of the *Wideband line/cable* part were the following:

- *Data*

  - *Number of phases* equal to 4;

  - *Model data* — here the file with the model data was loaded by the button *Select data file*;
  - *Save data file names using relative path* [*sic*] was checked;

- *IC* — the default options and values were kept;

- *Drawing*

  - *Distance between wires* equal to 140;
  - *Line length* equal to 770;
  - *Lower the left (+) side* equal to 0;
  - *Lower the right side* equal to 0;
  - *Show pin (wire) numbers (wires were numbered from top to down)*;

- *Attributes* — the default options were used.

The options and parameters of the *line/cable data* part were the following:

- *Conductors*

  - *Geometrical data and materials* as *Insulated cable*;
  - *Insulated cables*
    * *Single-core (SC) cables* equal to 2;
    * *Pipe-type (PT) cables* equal to 0;
  - *Soil*
    * *Resistivity* equal to $100\ \Omega\,\mathrm{m}$;
    * *Relative permeability* (μ_r) equal to 1;
    * *Relative permittivity* (ε_r) equal to 1;
  - *Length*
    * *Units* as *Metric*;
    * *Line/Cable length* equal to $1\ \mathrm{km}$;
  - *List of tables — Single-core cables* was checked

- *Model*

  - *Modeling options* [*sic*]
    * *Model* as *Wideband* or *CP* for the RT simulations when the CP model is used;

Table 40 – Single-core (SC) cable main data [*sic*]

Cabe	*Number of conductors*	*Horizontal position (*m*)*	*Ground depth (*m*)*	*Radius (*cm*)*
1	2	-0.25	-1.33	$63.9e-1$[1]
2	2	0.25	-1.33	$63.9e-1$

[1] "$63.9e-1$" is an EMTP-RV notation for 63.9×10^{-1} in the table of the cable data.

Table 41 – Single-core (SC) cable conductors/insulators data [*sic*]

Cabe	*Conductor*	*Phase*	*Inner radius (*cm*)*	*Outer radius (*cm*)*	*Conductor resistivity (*Ohm m *)*	*Conductor relative permeability*	*Conductor relative permittivity*	*Insulator relative permittivity*	*Insulatorloss factor*
1	1	1	0	$32.0e-1$	$1.72e-8$	1	1	2.5	0.0004
1	2	2	$56.9e-1$[1]	$58.2e-1$	$2.83e-8$	1	1	2.5	0.0004
2	1	3	0	$32.0e-1$	$1.72e-8$	1	1	2.5	0.0004
2	2	4	$56.9e-1$	$58.2e-1$	$2.83e-8$	1	1	2.5	0.0004

[1] "$56.9e-1$" is an EMTP-RV notation for 56.9×10^{-1} in the table of the cable data. It is the same for the other values in the table.

    - *Model frequency* equal to 1000 ("1000" is the EMTP-RV notation for $1,000$) — this parameter is only available when the CP model is used (*CP* is chosen in *Model*);

- *Frequency range* — these options are only available when the WB model is used (*Wideband* is chosen in *Model*)
    - f_{min} equal to $.01$ Hz;
    - *Points/decade* equal to 20;
    - *Decades* equal to 10;
    - f_{max} equal to $100E6$ Hz ("$100E6$" is the EMTP-RV notation for 10×10^6);
- *Wideband Fitting* — these options are only available when the WB model is used (*Wideband* is chosen in *Model*)
    - *Convergence tolerance* equal to 1% (the "$\%$" is not written);
    - *Cable model correction* was checked;
    - *Residue/Pole threshold* equal to 1000 ("1000" is the EMTP-RV notation for $1,000$);
    - *DC correction* was checked.

The *AC voltage source and impedance*, *Load-Flow Bus*, *PQm*, *MMC station*, *Current scope and observe*, and *CT* parts were only present in the modelling of the DT simula-

tions. In the RT simulations, there was the source with the time-reversed signal at only the right end of the link, for the single-end form of the method, or at both ends, for the double-end form of the method.

Table function voltage source parts model the source with the time-reversed signal in the RT simulations, one for each pole of the HVDC system (there is no three-phase version of the same part). Thereby, there were two at the left end of the link for the single-end form of the method and two at each end for the double-end. The options and parameters were the following:

- *Data*
  - t_{start} equal to 0 s;
  - t_{stop} equal to 1 ms;
  - *Use File input* [*sic*] was checked — the time-reversed signal of each respective pole and system end was loaded as MATLAB-generated files with the points of time and voltage data pairs in a two-column table, with the extension "dat";
- No other option of another tab was checked.

The *Table function voltage source* parts were connected to single-phase resistors (*RLC:R* part). The resistors were connected to the buses at the ends of the cable link (in the single-end form of the method, the resistors at the right end were connected to the end bus and the ground since there was no source at the right end). The resistors were the equivalent of high input impedances against high-frequency EMTs at the line extremities formed by the converters and the ac-side components, such as transformers. The options and parameters for these *RLC:R* parts in the RT simulations were the following:

- *Values*
  - R equal to 10 kΩ;

The pole-to-ground faults were modelled with an ideal three-phase switch (*Ideal switch* part) connected to a three-phase resistor (*RLC:R* part). Slightly different, the pole-to-pole faults were modelled with an ideal three-phase switch connected to a three-phase resistor, and from this resistor, a single-phase switch was connected across two phases. The components were in the three-phase form even though the fault was at a single pole, for the fault switch was connected to the buses corresponding to the faulted points between the cable sections. However, only the parameters of one phase have values to represent the pole-to-ground fault, while ones of two phases do for the pole-to-pole faults. The others have extreme values.

The options and parameters for the *Ideal switch* part in the DT and RT simulations for pole-to-ground faults were the following:

- *Data*
  - *Phase A*
    - t_{close} equal to 1 s in the DT simulations and -1 s in the RT simulations;
    - t_{open} equal to $1E15$ s [*sic*];
    - I_{margin} equal to 0 A;
  - *Phase B*
    - t_{close} equal to $1E15$ s;
    - t_{open} equal to $1E15$ s;
    - I_{margin} equal to 0 A;
  - *Phase C*
    - t_{close} equal to $1E15$ s;
    - t_{open} equal to $1E15$ s;
    - I_{margin} equal to 0 A;
- *Scopes*
  - *A*
    - v was checked;
    - i was checked;
  - *B*
    - v was checked;
    - i was checked;
  - *C*
    - v was checked;
    - i was checked.

The options and parameters for the *RLC:R* part in the DT and RT simulations for pole-to-ground faults were the following:

- *Values*
  - *Resistor*
    - *Phase A*
      - R equal to $1\ \Omega$, $5\ \Omega$, $10\ \Omega$, and $50\ \Omega$ in the DT simulations, and $1\ \Omega$ in the RT simulations;
    - *Phase B*

        - R equal to $1\ \Omega$, $5\ \Omega$, $10\ \Omega$, and $50\ \Omega$ in the DT simulations, and $1\ \Omega$ in the RT simulations;
    - *Phase C*
        - R equal to $1\ \Omega$, $5\ \Omega$, $10\ \Omega$, and $50\ \Omega$ in the DT simulations, and $1\ \Omega$ in the RT simulations;
    - *balanced* was checked.

The options and parameters for the *Ideal switch* part in the three-phase form in the DT and RT simulations for pole-to-pole faults were the following:

- *Data*
    - *Phase A*
        - t_{close} equal to $1\ \mathrm{s}$ in the DT simulations and $-1\ \mathrm{s}$ in the RT simulations;
        - t_{open} equal to $1E15\ \mathrm{s}$;
        - I_{margin} equal to $0\ \mathrm{A}$;
    - *Phase B*
        - t_{close} equal to $1\ \mathrm{s}$ in the DT simulations and $-1\ \mathrm{s}$ in the RT simulations;
        - t_{open} equal to $1E15\ \mathrm{s}$;
        - I_{margin} equal to $0\ \mathrm{A}$;
    - *Phase C*
        - t_{close} equal to $1E15\ \mathrm{s}$;
        - t_{open} equal to $1E15\ \mathrm{s}$;
        - I_{margin} equal to $0\ \mathrm{A}$;
- *Scopes*
    - *A*
        - i was checked in the RT simulations;
    - *B*
        - i was checked in the RT simulations;

The options and parameters for the *Ideal switch* part in the single-phase form in the DT and RT simulations for pole-to-pole faults were the following:

- *Data*
    - t_{close} equal to $1\ \mathrm{s}$ in the DT simulations and $-1\ \mathrm{s}$ in the RT simulations;
    - t_{open} equal to $1E15\ \mathrm{s}$;

  - I_{margin} equal to 0 A;

- *Scopes*

  - i was checked in the RT simulations;

The options and parameters for the *RLC:R* part in the DT and RT simulations for pole-to-pole faults were the following:

- *Values*

  - *Resistor*

    * *Phase A*

      · R equal to $0.5\ \Omega$, $2.5\ \Omega$, $5\ \Omega$, and $25\ \Omega$ in the DT simulations, and $0.5\ \Omega$ in the RT simulations;

    * *Phase B*

      · R equal to $0.5\ \Omega$, $2.5\ \Omega$, $5\ \Omega$, and $25\ \Omega$ in the DT simulations, and $0.5\ \Omega$ in the RT simulations;

    * *Phase C*

      · R equal to $0.5\ \Omega$, $2.5\ \Omega$, $5\ \Omega$, and $25\ \Omega$ in the DT simulations, and $0.5\ \Omega$ in the RT simulations;

    * *balanced* was checked.

APPENDIX C FIGURES OF RESULTS FROM THE TIME-DOMAIN STUDY CASES ON THE POINT-TO-POINT HVDC TRANSMISSION SYSTEM

Figures 105 to 120 show the results for pole-to-ground and pole-to-pole faults for the cases where the fault resistance is changed and the WB model is used in both DT and RT stages.

Figure 105 – Results by $\mathcal{P}_i(x_g)$ for pole-to-ground faults with different resistances, double-end recording and $T = 10$ ms

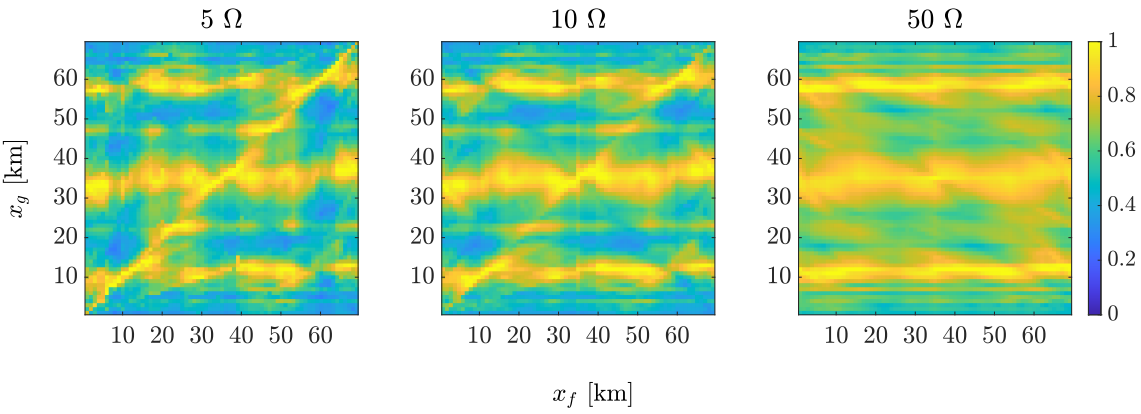

Source: Author

Figures 121 to 128 show the results for pole-to-ground and pole-to-pole faults for the cases where the cut-off frequency of the HP filter is changed, and the WB model is used in the DT stage and the CP model in the RT stage.

Figure 106 – Results by $\mathcal{P}_i(x_g)$ for pole-to-ground faults with different resistances, double-end recording and $T = 1$ ms

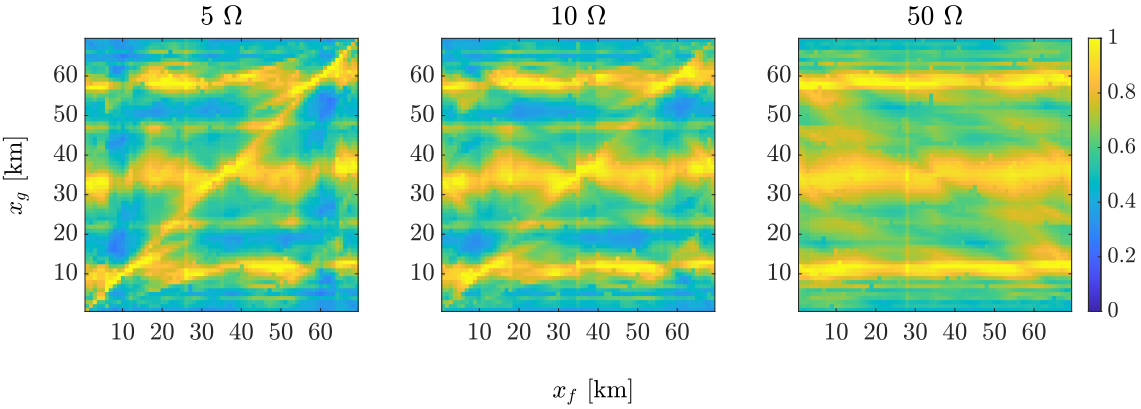

Source: Author

Figure 107 – Results by $\mathcal{P}_i(x_g)$ for pole-to-ground faults with different resistances, single-end recording and $T = 10$ ms

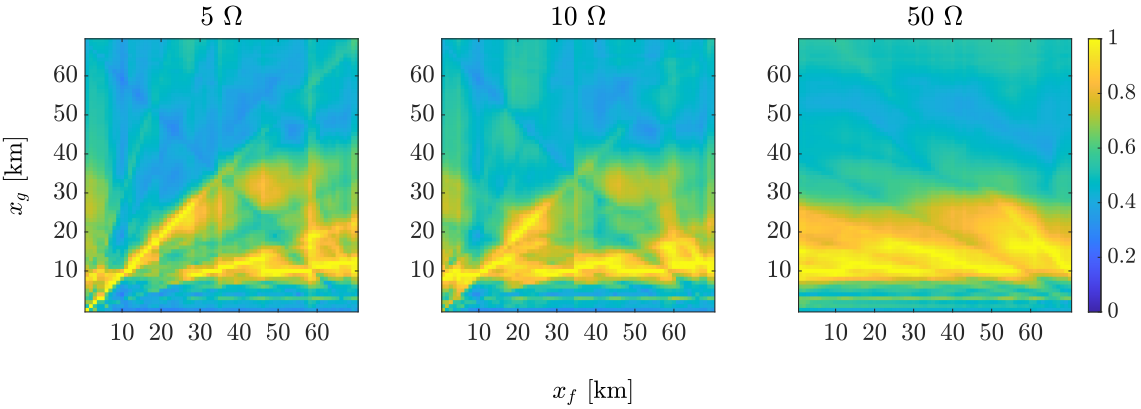

Source: Author

Figure 108 – Results by $\mathcal{P}_i(x_g)$ for pole-to-ground faults with different resistances, single-end recording and $T = 1$ ms

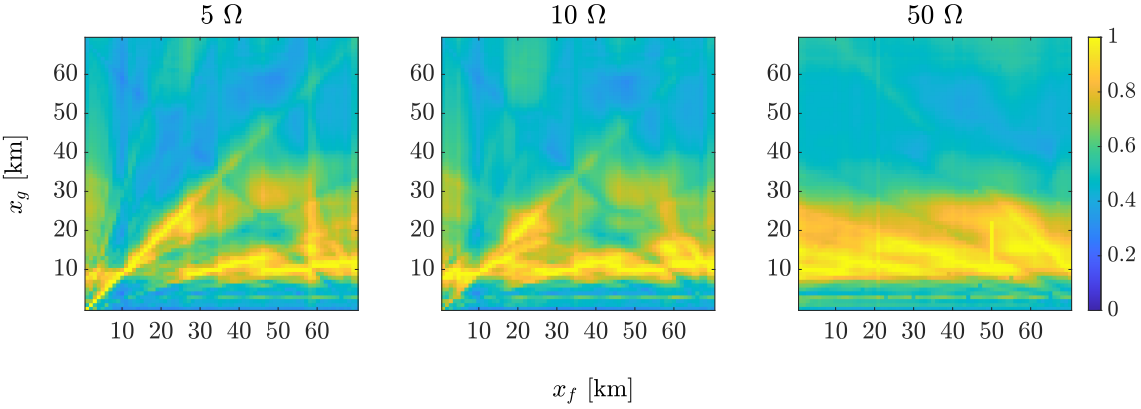

Source: Author

Figure 109 – Results by $\mathcal{E}_i(x_g)$ for pole-to-ground faults with different resistances, double-end recording and $T = 10$ ms

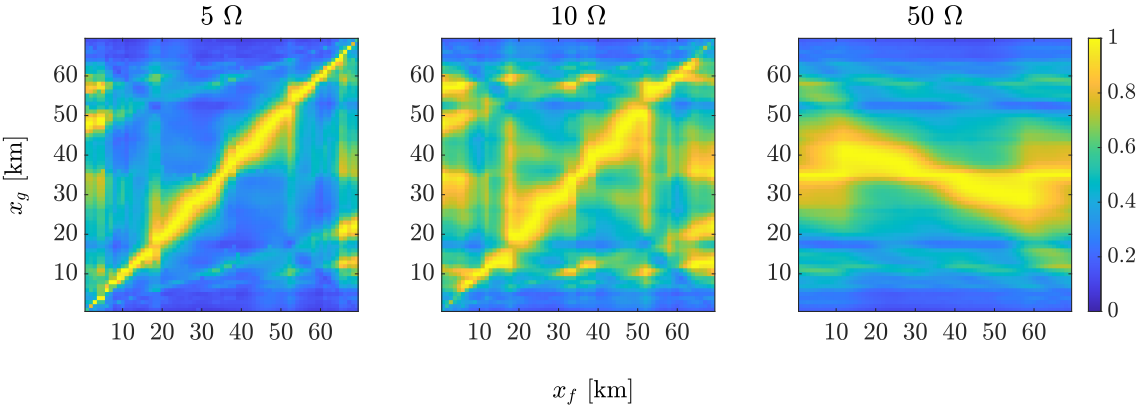

Source: Author

Figure 110 – Results by $\mathcal{E}_i(x_g)$ for pole-to-ground faults with different resistances, double-end recording and $T = 1$ ms

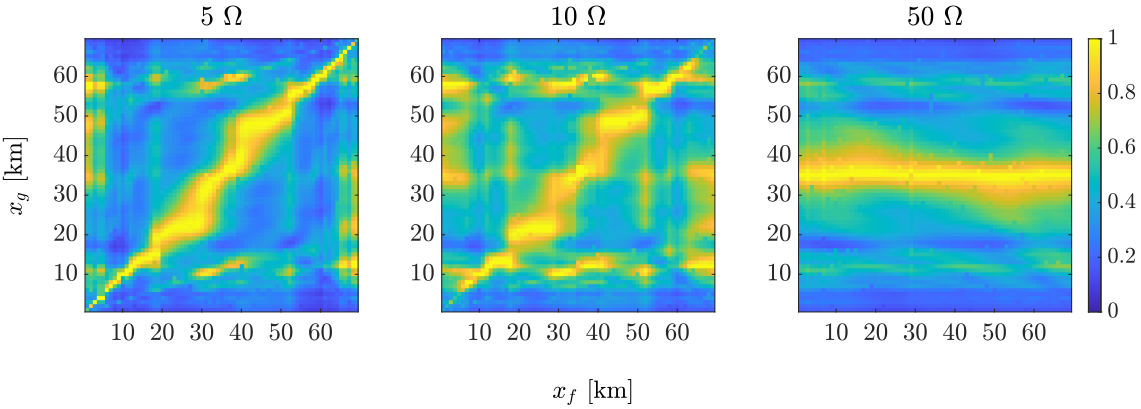

Source: Author

Figure 111 – Results by $\mathcal{E}_i(x_g)$ for pole-to-ground faults with different resistances, single-end recording and $T = 10$ ms

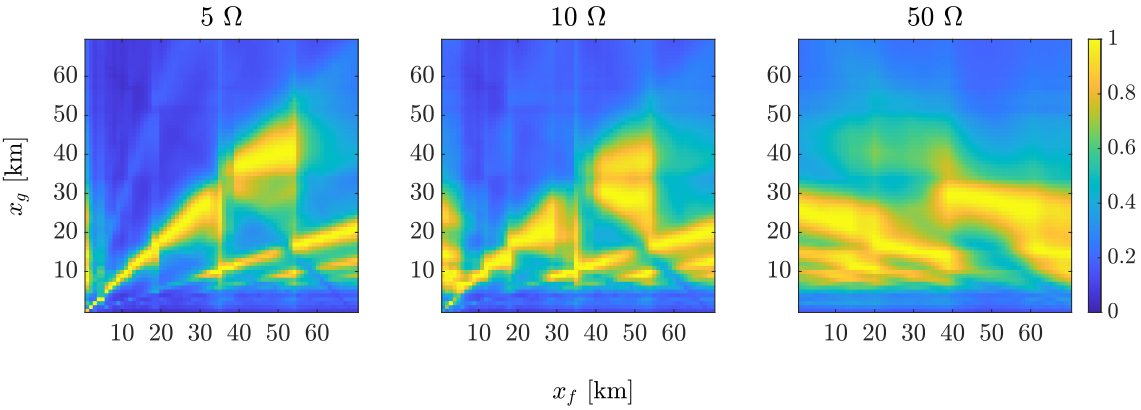

Source: Author

Figure 112 – Results by $\mathcal{E}_i(x_g)$ for pole-to-ground faults with different resistances, single-end recording and $T = 1$ ms

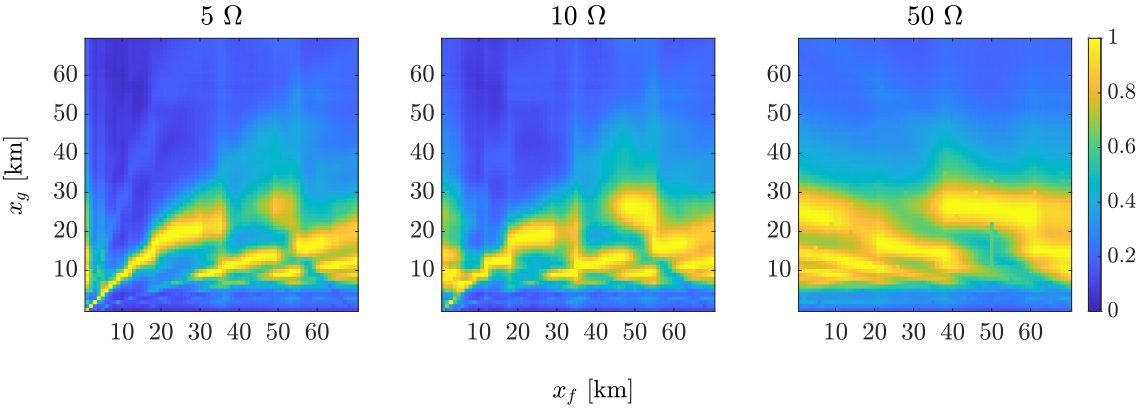

Source: Author

Figure 113 – Results by $\mathcal{P}_i(x_g)$ for pole-to-pole faults with different resistances, double-end recording and $T = 10$ ms

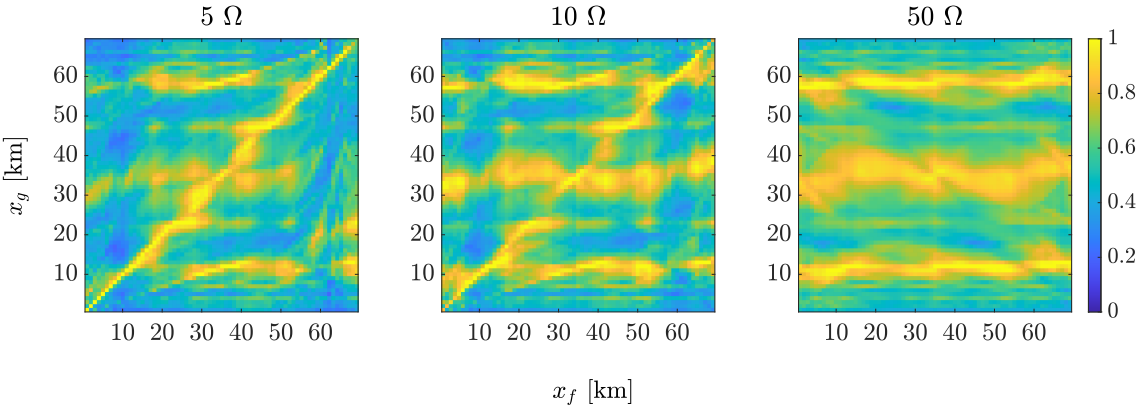

Source: Author

Figure 114 – Results by $\mathcal{P}_i(x_g)$ for pole-to-pole faults with different resistances, double-end recording and $T = 1$ ms

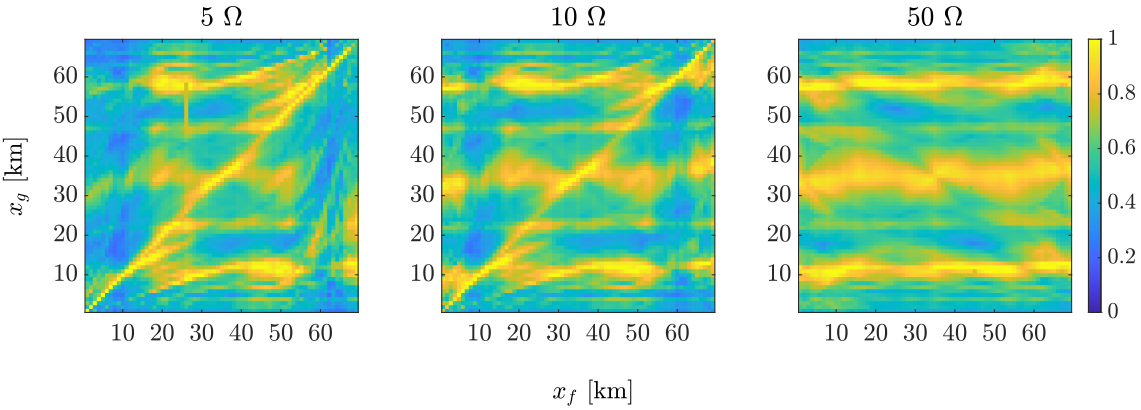

Source: Author

Figure 115 – Results by $\mathcal{P}_i(x_g)$ for pole-to-pole faults with different resistances, single-end recording and $T = 10$ ms

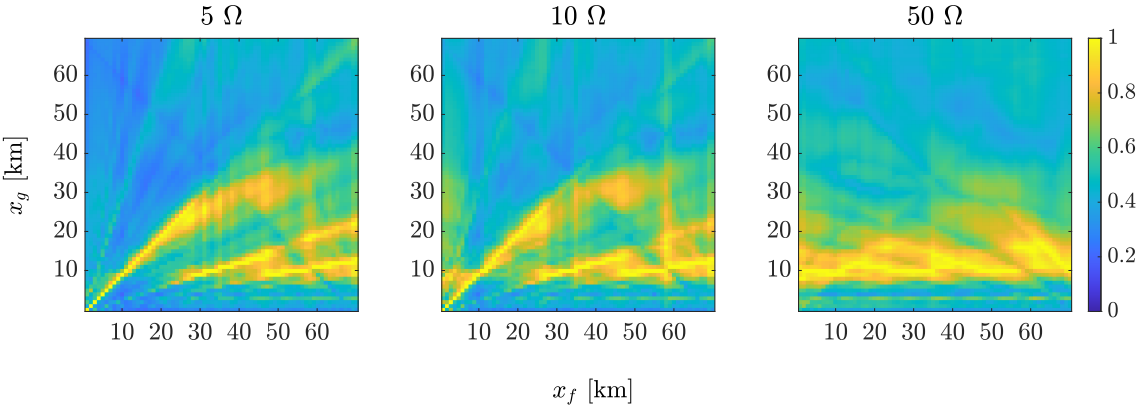

Source: Author

Figure 116 – Results by $\mathcal{P}_i(x_g)$ for pole-to-pole faults with different resistances, single-end recording and $T = 1$ ms

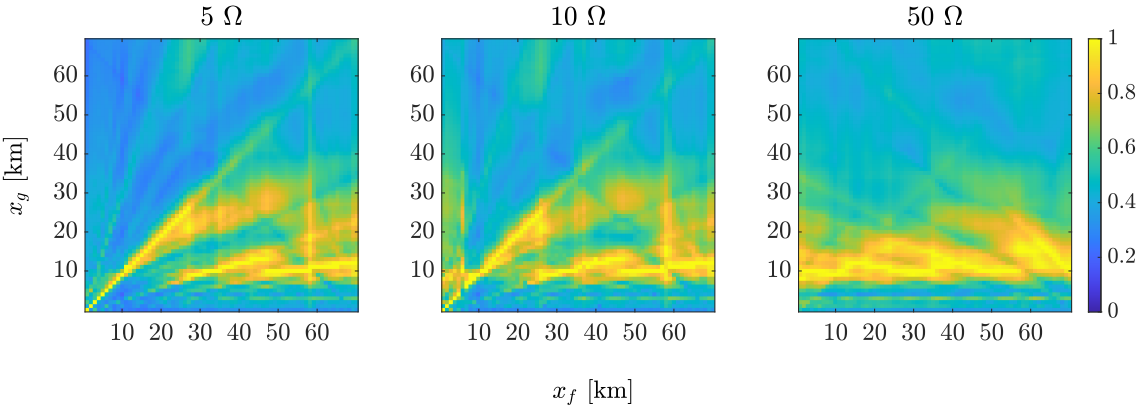

Source: Author

Figure 117 – Results by $\mathcal{E}_i(x_g)$ for pole-to-pole faults with different resistances, double-end recording and $T = 10$ ms

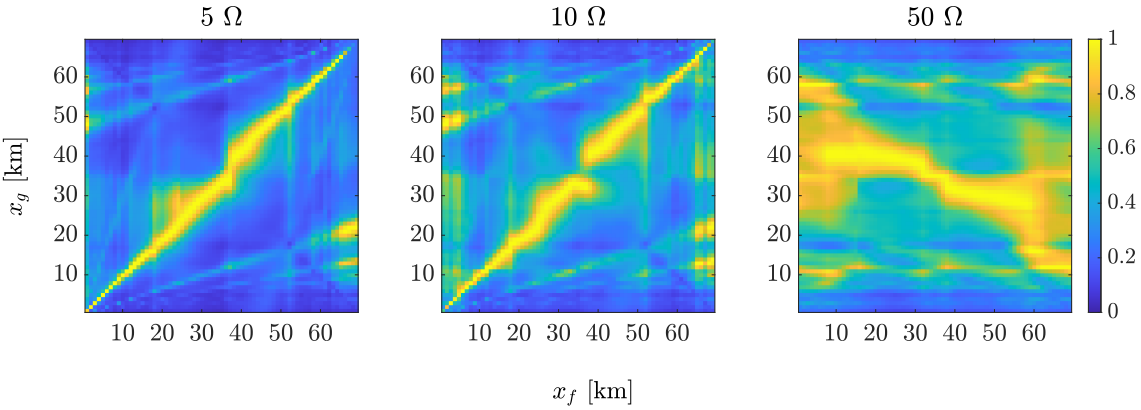

Source: Author

Figure 118 – Results by $\mathcal{E}_i(x_g)$ for pole-to-pole faults with different resistances, double-end recording and $T = 1$ ms

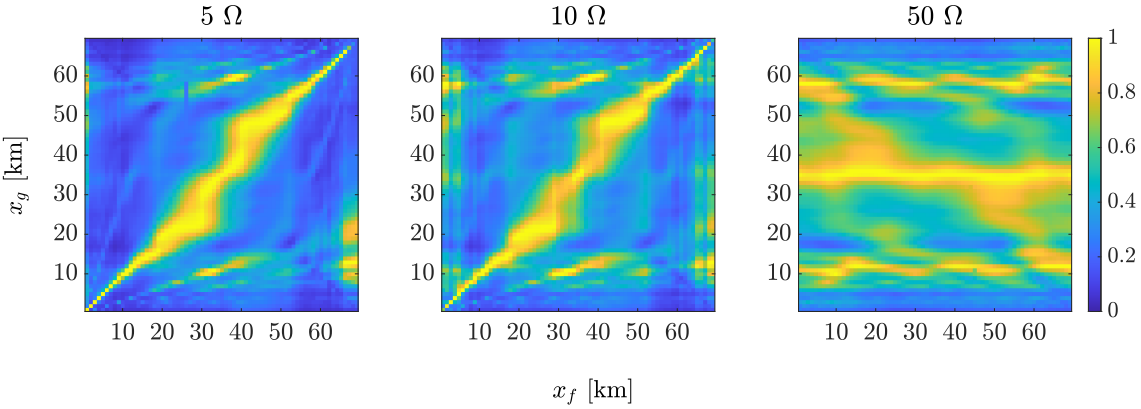

Source: Author

Figure 119 – Results by $\mathcal{E}_i(x_g)$ for pole-to-pole faults with different resistances, single-end recording and $T = 10$ ms

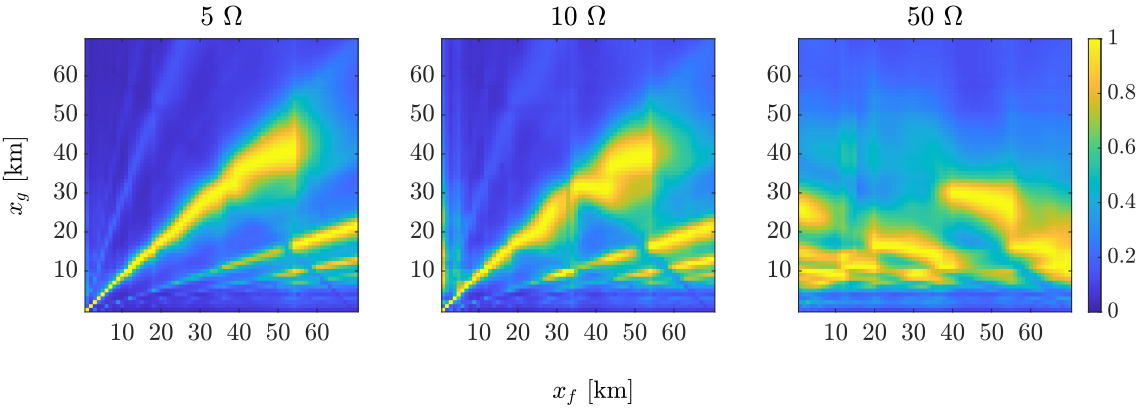

Source: Author

Figure 120 – Results by $\mathcal{E}_i(x_g)$ for pole-to-pole faults with different resistances, single-end recording and $T = 1$ ms

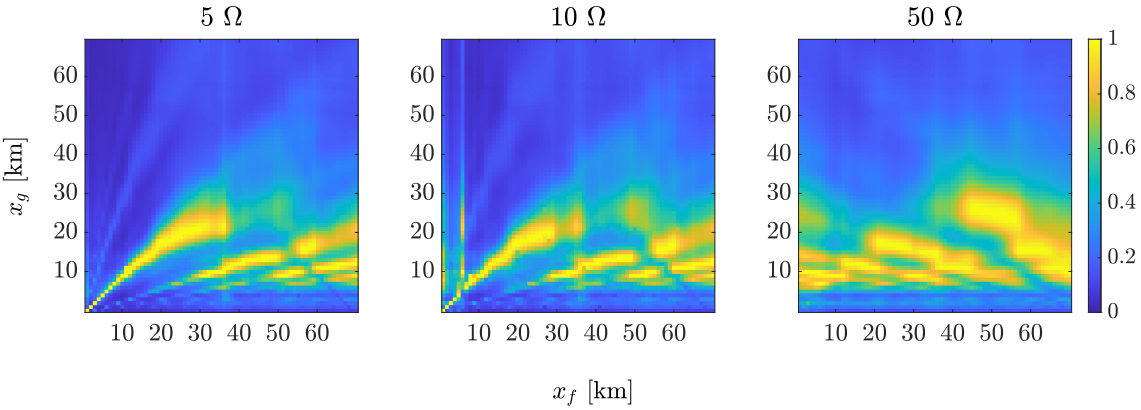

Source: Author

Figure 121 – Results by $\mathcal{P}_i(x_g)$ for pole-to-ground faults with different cut-off frequencies and $T = 10$ ms, changing the cable model in the RT stage

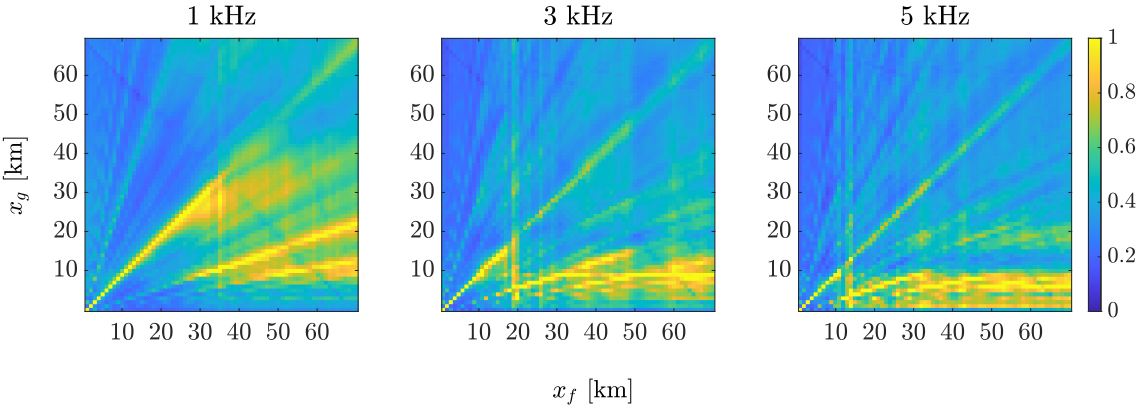

Source: Author

Figure 122 – Results by $\mathcal{P}_i(x_g)$ for pole-to-ground faults with different cut-off frequencies and $T = 1$ ms, changing the cable model in the RT stage

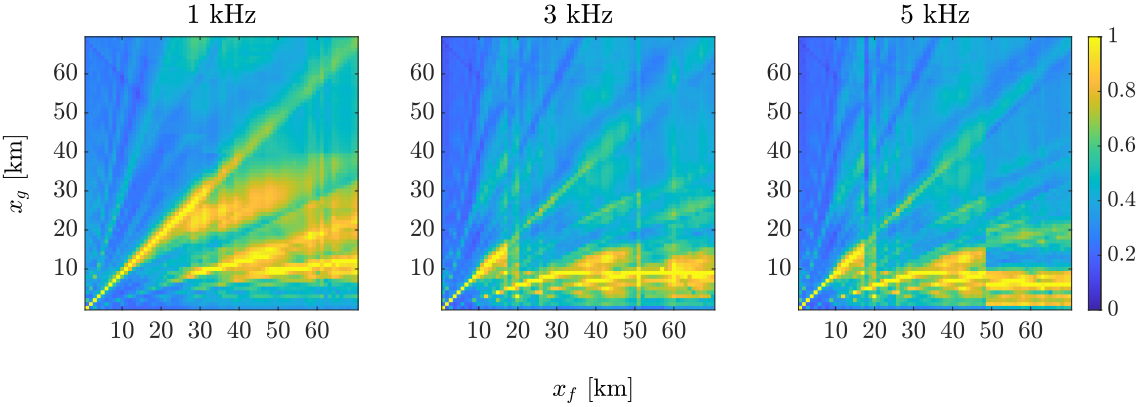

Source: Author

Figure 123 – Results by $\mathcal{E}_i(x_g)$ for pole-to-ground faults with different cut-off frequencies and $T = 10$ ms, changing the cable model in the RT stage

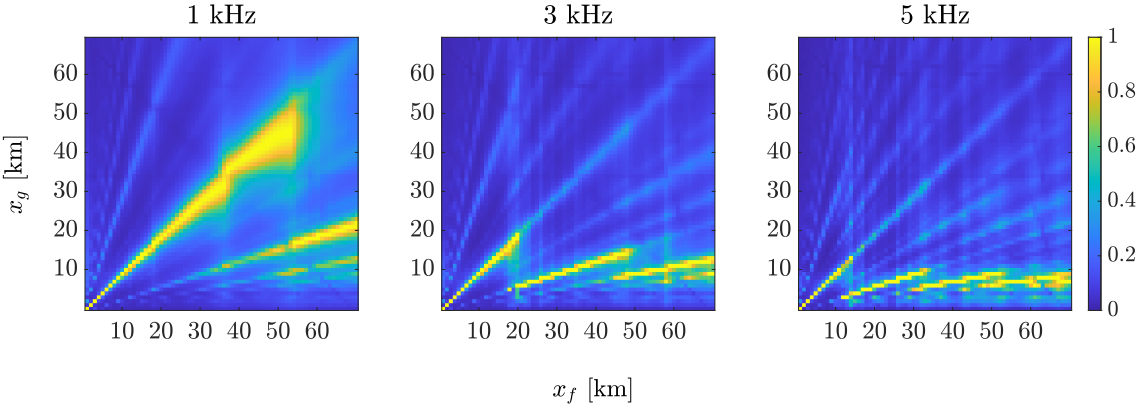

Source: Author

Figure 124 – Results by $\mathcal{E}_i(x_g)$ for pole-to-ground faults with different cut-off frequencies and $T = 1$ ms, changing the cable model in the RT stage

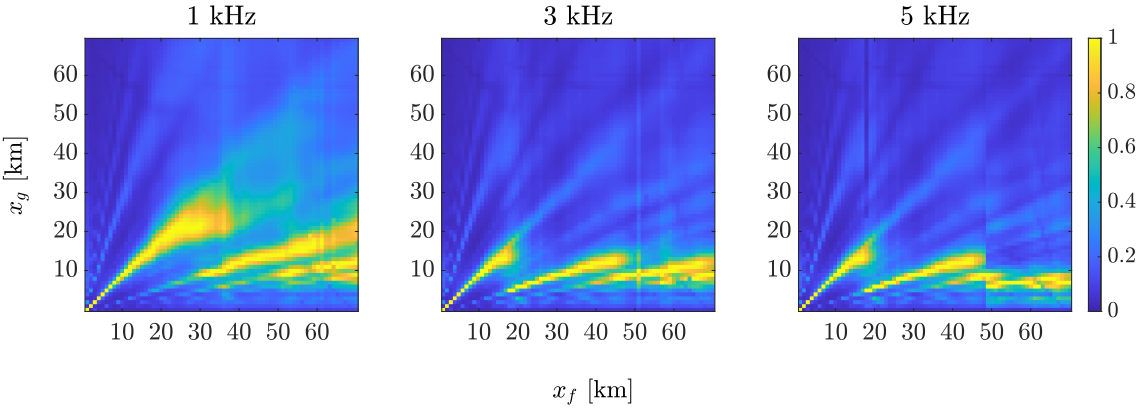

Source: Author

Figure 125 – Results by $\mathcal{P}_i(x_g)$ for pole-to-pole faults with different cut-off frequencies and $T = 10$ ms, changing the cable model in the RT stage

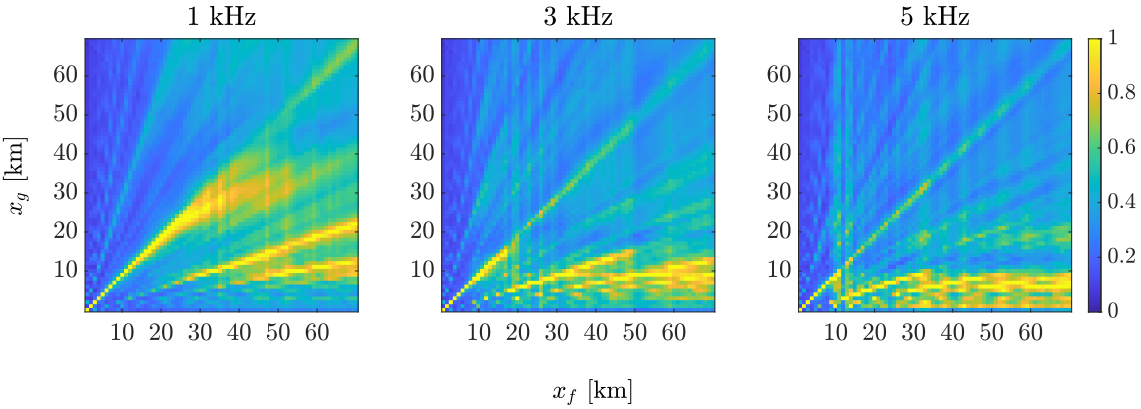

Source: Author

Figure 126 – Results by $\mathcal{P}_i(x_g)$ for pole-to-pole faults with different cut-off frequencies and $T = 1$ ms, changing the cable model in the RT stage

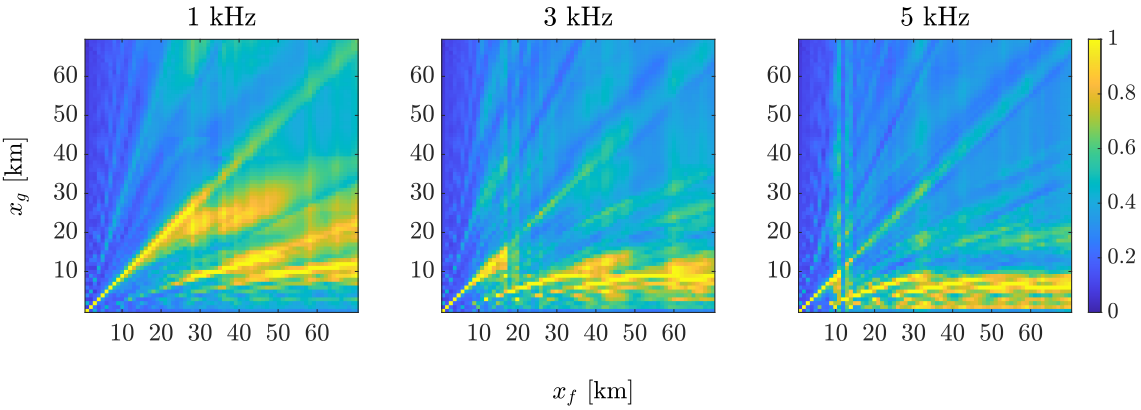

Source: Author

Figure 127 – Results by $\mathcal{E}_i(x_g)$ for pole-to-pole faults with different cut-off frequencies and $T = 10$ ms, changing the cable model in the RT stage

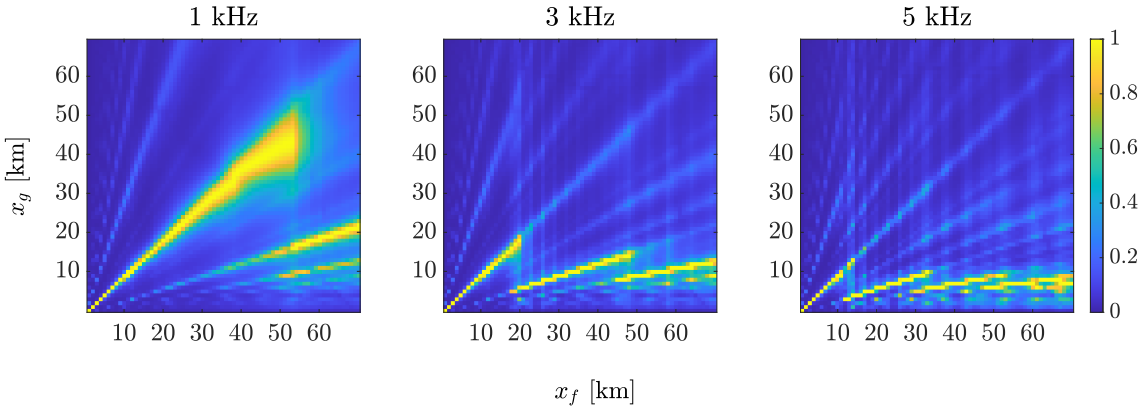

Source: Author

Figure 128 – Results by $\mathcal{E}_i(x_g)$ for pole-to-pole faults with different cut-off frequencies and $T = 1$ ms, changing the cable model in the RT stage

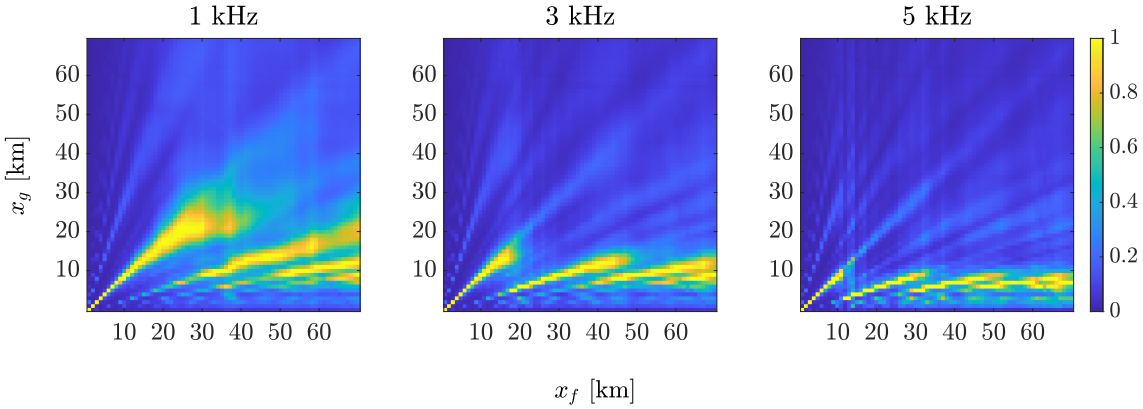

Source: Author

APPENDIX D MODELLING DATA AND SIMULATION PARAMETERS OF THE TIME-DOMAIN STUDY CASES ON THE ELECTRIC POWER DISTRIBUTION NETWORK IN THE EMTP-RV

The following options and parameters were chosen for the time-domain simulations of the EMTR method for the study cases on the electric power distribution network:

- *Basic Data*
  - *Find Steady-state solution and start from steady-state* [*sic*] was checked;
  - *Find Time-domain solution* [*sic*] was checked;
    - *Main time-step* (Δt) equal to 0.1 µs;
    - *Simulation time:* (t_{max}) equal to 100 ms for the DT simulations and 2 ms for the RT simulations;
  - *Default Power Frequency (Steady-state and Load-Flow)* [*sic*] equal to 60 Hz;
- *Advanced*
  - *Numerical Integration Method*;
    - *Trapezoidal* was checked;
  - Nothing was changed from the default values in *Solver for control devices* and *Precision control data*;
- *Output*
  - *Plot output (scopes) options*;
    - *Save waveforms* was checked;
    - *Fixed output rate for waveforms* equal to 1;
    - *High precision output* was checked;
    - *Plot file format* as *MPLOT*;

        * *Save scope names* was checked;
        * *Save intermediate time-points* was checked;
    - *ASCII Output options*
        * *HTML output*;
    - *Waitbar Step* [*sic*] equal to 100;

- *Memory*
    - *Predicted number of nonzeros* [*sic*] equal to 10 *(scaling factor)*;
    - *Offset for sparse matrix storage (electrical network)* equal to 100 *(extra cells)*;
    - *Predicted number of nonzeros (control system)* [*sic*] equal to 5 *(scaling factor)*;
    - *Predicted number of nodes* equal to 200.

An *AC voltage source and impedance* part models the unique ac source of the power distribution network. The options and parameters of the *AC voltage source and impedance* part were the following:

- *Source*
    - *Generic 3-phase voltage source data* [*sic*] was checked;
        * *Phase A*
            · V_m equal to 69 kVRMSLL [*sic*] ("kVRMSLL" is the EMTP-RV notation for "line-to-line rms kV");
            · f equal to 60 Hz;
            · θ equal to 0 deg [*sic*] ("deg" is the EMTP-RV notation for degree);
            · t_{start} equal to -1 s;
            · t_{stop} equal to $1E15$ s [*sic*] ("$1E15$" is the EMTP-RV notation for 1.00×10^{15});
        * *Phase B*
            · V_m equal to 69 kVRMSLL [*sic*];
            · f equal to 60 Hz;
            · θ equal to -120 deg [*sic*];
            · t_{start} equal to -1 s;
            · t_{stop} equal to $1E15$ s [*sic*];
        * *Phase C*
            · V_m equal to 69 kVRMSLL [*sic*];
            · f equal to 60 Hz;
            · θ equal to 120 deg [*sic*];

        - t_{start} equal to -1 s;
        - t_{stop} equal to $1E15$ s [*sic*];
      - *balanced* was checked;
      - *Show 3-phase ground pin* was checked;

- *Impedance*

  - *Impedance data input* was checked;

    - *Impedance real part — Sequence Data Input* was checked — *R*;
      - *Zero* equal to $\frac{0.4\times69{,}000^2}{3{,}000\times1{,}000{,}000\times\sqrt{0.26}}$ Ω, approximately 0.59 Ω;
      - *Positive* equal to $\frac{0.4\times69{,}000^2}{3{,}000\times1{,}000{,}000\times\sqrt{0.26}}$ Ω;
      - *Negative* equal to $\frac{0.4\times69{,}000^2}{3{,}000\times1{,}000{,}000\times\sqrt{0.26}}$ Ω;
    - *Impedance imaginary part — Sequence Data Input* was checked — *L*;
      - *Zero* equal to $\frac{69{,}000^2}{3{,}000\times1{,}000{,}000\times\sqrt{0.26}}$ Ω, approximately 0.59 Ω;
      - *Positive* equal to $\frac{69{,}000^2}{3{,}000\times1{,}000{,}000\times\sqrt{0.26}}$ Ω;
      - *Negative* equal to $\frac{69{,}000^2}{3{,}000\times1{,}000{,}000\times\sqrt{0.26}}$ Ω;

- The options of the other tabs were default or not checked.

The ac source was then connected to the three-phase transformer "Tr1", modelled with the *three-phase nameplate input* part. The options and parameters were the following:

- *Data*

  - *Basic data*

    - *Connection Type* as *DY* $-30°$;
    - *Nominal power* equal to $\frac{2.5}{3}$ MVA (the *three-phase nameplate input* part is three separate single-phase units);
    - *Nominal frequency* equal to 60 Hz;
    - *Winding 1 voltage* equal to 69 kV RMSLL ("kV RMSLL" is another EMTP-RV notation for "line-to-line rms kV";
    - *Winding 2 voltage* equal to 24.9 kV RMSLL;
    - *Tap ratio* [*sic*] equal to 1;
    - *Winding R* equal to 0.01 pu;
    - *Winding X* equal to 0.08 pu;
    - *Winding impedance on winding 1* equal to 0.9 and was checked;

  - *Magnetization data* [*sic*] as *Current-Flux* and *pu-pu* — current and flux points form the following table:

*Current (*pu*)*	*Flux (*pu*)*
0.002	1
0.01	1.075
0.025	1.15
0.05	1.2
0.1	1.23
2	1.72

        - L_{sat} equal to 0.3 pu;
        - *Magnetization resistance* [*sic*] equal to 500 pu;

- *IC*
    - *Initial flux* (ϕ_0) *phase A* equal to 0 pu — the default value;
    - *Initial flux* (ϕ_0) *phase B* equal to 0 pu — the default value;
    - *Initial flux* (ϕ_0) *phase C* equal to 0 pu — the default value;

- No other option of another tab was checked.

The connection "DY" means a delta connection on the high-voltage side and a wye connection on the low-voltage side. The "neutral" point of the wye connection (the common point) was directly connected to the ground in the modelling (connected through a null resistance, modelling a solidly earthing system).

The *RLC:C non polarized* parts model the stray capacitances between the transformer' windings of the high and low voltage sides and between the windings of both sides to the ground, in the "Pi" representation, externally connected to the transformer. The options and parameters for the capacitor between the windings of the high-voltage side to the ground were the following:

- *Data*
    - *Phase A*
        - C equal to 2.4624337995 nF;
    - *Phase B*
        - C equal to 2.4624337995 nF;
    - *Phase C*
        - C equal to 2.4624337995 nF;
    - *balanced* was checked;

- *IC*

  - There was no initial conditions — the value 0 V (the default value) was used for all phases;

- No other option of another tab was checked.

The options and parameters for the capacitor between the transformer's windings of the high- and low-voltage sides were the following:

- *Data*
  - *Phase A*
    - C equal to 1.6293379964 nF;
  - *Phase B*
    - C equal to 1.6293379964 nF;
  - *Phase C*
    - C equal to 1.6293379964 nF;
  - *balanced* was checked;
- *IC*
  - There was no initial conditions — the value 0 V (the default value) was used for all phases;
- No other option of another tab was checked.

The options and parameters for the capacitor between the windings of the low-voltage side to the ground were the following:

- *Data*
  - *Phase A*
    - C equal to 3.8017886582 nF;
  - *Phase B*
    - C equal to 3.8017886582 nF;
  - *Phase C*
    - C equal to 3.8017886582 nF;
  - *balanced* was checked;
- *IC*
  - There was no initial conditions — the value 0 V (the default value) was used for all phases;

- No other option of another tab was checked.

Connected to the *three-phase nameplate input* part was a current meter given by the *Current scope and observe* part. The only option checked was the following:

- *Scopes*
  - *Time-domain or Frequency scan scopes* [*sic*] — *i* was checked;
    - i
      - *Phase A* was checked;
      - *Phase B* was checked;
      - *Phase C* was checked;
- No other option of another tab was checked.

Connected to the *Current scope and observe* part was the *CT* part that models the current transformer. It has the three-phase form (*3-phase Wye-connected versions* [*sic*]) since it was connected to a three-phase component and the bus 800, where the first line (800-802) was connected. The options and parameters were the following:

- *Data*
  - *Nominal frequency* equal to $60\ \mathrm{Hz}$;
  - *Transformer data*
    - *Ratio* equal to $200 : 5\ \mathrm{A}$ (200 and 5 go each one in different boxes);
    - *Winding 1 R* equal to $0\ \Omega$;
    - *Winding 1 X* equal to $0\ \Omega$;
    - *Winding 2 R* equal to $0.15\ \Omega$;
    - *Winding 2 X* equal to $0\ \Omega$;
  - *Burden data*
    - Z_{burden} equal to $2\ \Omega$;
    - *Power Factor* equal to 0.5;
  - *Excitation Curve* — current and voltage points form the following table:
  - *Magnetization resistance* [*sic*] equal to $10\ \mathrm{M}\Omega$;
- *IC*
  - *Initial flux* (ϕ_0) equal to $0\ \mathrm{Wb}$ — the default value;
- *Scopes*
  - *Winding 2 current (exiting)* was checked;

Current (A)	*Voltage* (V)
0.01	6.8
0.02	17
0.03	28
0.05	56
0.1	145
0.16	200
0.2	215
0.5	230
1	235
5	245
10	250

- *Attributes* — the default options were used.

The signal used in the TR transformation was the current signal measured through this current transformer.

A voltage meter given by the *Voltage scope* part was also connected to the bus 800, where the *CT* part was. The voltage scope assumes the three-phase form with the connection to the bus. The options were the following:

- *Phase A* was checked;
- *Phase B* was checked;
- *Phase C* was checked;
- As *Per-unit* was not checked, the *Voltage base* field does not influence and has the default value.

The lines 800-802 and 802-806 and sections of lines 806-808, 808-810, 808-812, and 812-814i were connected by buses, where the faults were simulated. The *Wideband line/cable* part was used for lines 800-802 and 802-806, and all sections of lines 806-808, 808-810, 808-812, and 812-814i. The model data for the lines and sections was given by the *Line/Cable Data* part, which generates a file with an extension "mod". The files are then loaded to the *Wideband line/cable* parts. The options and parameters of the *Wideband line/cable* part were the following:

- *Data*
  - *Number of phases* equal to 4 for the three-phase lines and sections and 2 for the single-phase ones;
  - *Model data* — here the file with the model data was loaded by the button *Select data file*;

  - *Save data file names using relative path* [*sic*] was checked;

- *IC* — the default options and values were kept;

- *Drawing*

  - *Distance between wires* equal to 140;
  - *Line length* equal to 1330;
  - *Lower the left (+) side* equal to 0;
  - *Lower the right side* equal to 0;
  - *Show pin (wire) numbers (wires were numbered from top to down)*;

- *Attributes* — the default options were used.

The options and parameters of the *line/cable data* part for the lines 800-802, 802-806, and the sections of the lines 806-808, 808-812, and 812-814 were the following:

- *Conductors*

  - *Geometrical data and materials* as *Overhead line*;
  - *Overhead lines*
    * *Single-wire (W) conductors* equal to 4;
    * *Bundled (B) conductors* equal to 0;
    * *Conductor characteristic* as *DC resistance*;
  - *Soil*
    * *Resistivity* equal to $100\ \Omega\,\mathrm{m}$;
    * *Relative permeability (μ_r)* equal to 1;
    * *Relative permittivity (ε_r)* equal to 1;
  - *Length*
    * *Units* as *English*;
    * *Line/Cable length* equal to $\frac{2580}{5280}\ \mathrm{mi}$ for the line 800-802, $\frac{1730}{5280}\ \mathrm{mi}$ for the line 802-806, $\frac{32{,}230}{12\times5280}\ \mathrm{mi}$ for the twelve sections of the line 806-808, $\frac{37{,}500}{14\times5280}\ \mathrm{mi}$ for the fourteen sections of the line 808-812, and $\frac{29{,}730}{12\times5280}\ \mathrm{mi}$ for the twelve sections of the line 812-814;
  - *List of tables — Overhead single-wire conductors* was checked

- *Model*

  - *Modeling options* [*sic*]

Table 42 – Overhead line, Single-wire (W) conductors [*sic*]

Conductor	*Phase*	*Horizontal position* (ft)	*Height* (ft)	*Radius* (in)	*DC resistance* (Ohm/mile)	*Conductor relative permeability*	*Conductor relative permittivity*
1	1	−1	28	0.1990	0.974	1	1
2	2	−3.5	28	0.1990	0.974	1	1
3	3	3.5	28	0.1990	0.974	1	1
4	4	0.5	24	0.1990	0.974	1	1

        - *Model* as *Wideband*;
    - *Frequency range*
        - f_{min} equal to 0.001 Hz;
        - *Points/decade* equal to 10;
        - *Decades* equal to 10;
        - f_{max} equal to $10E6$ Hz [*sic*] ("$10E6$" is the EMTP-RV notation for 10×10^6);
    - *Options*
        - *Proximity effect* was checked;
        - *Earth return path* was checked;
    - *Wideband Fitting*
        - *Convergence tolerance* equal to 1% (the "$\%$" is not written);
        - *DC correction* was checked.

The options and parameters of the *line/cable data* part for the sections of the lines 808-810 were similar to those for the lines 800-802, 802-806, and the sections of the lines 806-808, 808-812, and 812-814. The differences were the following:

- *Conductors*
    - *Geometrical data and materials* as *Overhead line*;
    - *Overhead lines*
        - *Single-wire (W) conductors* equal to 2;
    - *Length*
        - *Line/Cable length* equal to $\frac{5{,}804}{2\times5280}$ mi for the two sections of the line 808-810;
    - *List of tables — Overhead single-wire conductors* was checked

Table 43 – Overhead line, Single-wire (W) conductors [*sic*]

Conductor	*Phase*	*Horizontal position* (ft)	*Height* (ft)	*Radius* (in)	*DC resistance* (Ohm/mile)	*Conductor relative permeability*	*Conductor relative permittivity*
1	1	0	29	0.1250	2.47	1	1
2	2	0.5	24	0.1250	2.47	1	1

The *RLC:R-L* part models the distributed loads connected to phases *B* and *C* between buses 802 and 806, and phase *B* between buses 808 and 810. The distributed feature of the loads was modelled splitting the loads between the two respective buses, i.e., dividing their values in half. The *RLC:R-L* parts were used in the single-phase form since they were connected directly to the phases. The options and parameters for the loads at phase *B* at buses 802 and 806 were the following:

- *Values*
  - *RL branch*
    - R equal to $\Re(\frac{\frac{24{,}900}{\sqrt{3}}^2}{\frac{30{,}000}{2}-j\frac{15{,}000}{2}})\ \Omega$;
    - L equal to $\Im(\frac{\frac{24{,}900}{\sqrt{3}}^2}{\frac{30{,}000}{2}-j\frac{15{,}000}{2}})\ \Omega$;
- *IC*
  - There was no initial conditions — the value 0 A (the default value) was used for i_0 for L;
- No other option of another tab was checked.

The options and parameters for the loads at phase *C* at buses 802 and 806 were the following:

- *Values*
  - *RL branch*
    - R equal to $\Re(\frac{\frac{24{,}900}{\sqrt{3}}^2}{\frac{25{,}000}{2}-j\frac{14{,}000}{2}})\ \Omega$;
    - L equal to $\Im(\frac{\frac{24{,}900}{\sqrt{3}}^2}{\frac{25{,}000}{2}-j\frac{14{,}000}{2}})\ \Omega$;
- *IC*
  - There was no initial conditions — the value 0 A (the default value) was used for i_0 for L;
- No other option of another tab was checked.

The *AC voltage source and impedance* and *CT* parts were not present in the modelling of the RT simulations. The source with the time-reversed signal was used in the RT simulations instead of the ac source.

Three *Table function current source* parts model the source with the time-reversed signal in the RT simulations, one for each phase once there was no correspondent three-phase form. They were all connected to a bus. The options and parameters were the following:

- *Data*
  - t_{start} equal to 0 s;
  - t_{stop} equal to 1 ms;
  - *Use File input* [*sic*] was checked — the time-reversed signal of each respective phase was loaded as a MATLAB-generated file in each RT simulation, with the points of time and current data pairs in a two-column table, with the extension "dat";
- *Scopes*
  - *Time-domain or Frequency scan scopes/td>* [*sic*]
    - *i* was checked;
- No other option of another tab was checked.

A three-phase resistor given by the *RLC:R* part was connected to the bus in parallel with the *Table function current source* parts (connected to the same bus and the ground). The resistors model the high input impedance against high-frequency EMTs given by the transformer "Tr1". The connection of the resistor was in parallel once the time-reversed signals were current signals, not voltage ones. The options and parameters were the following:

- *Values*
  - *Phase A*
    - R equal to 100 kΩ;
  - *Phase B*
    - R equal to 100 kΩ;
  - *Phase C*
    - R equal to 100 kΩ;
  - *balanced* was checked;

- No other option of another tab was checked.

Upstream to the *Table function current source* parts were a three-phase transformer, modelled with the *three-phase nameplate input* part. This transformer was similar to the "Tr1" of the DT modelling. It was modelled in the RT simulations to resemble the same blocking behaviour of the EMTs of the DT simulations. The options and parameters were the following:

- *Data*
  - *Basic data*
    - *Connection Type* as *YgYg*;
    - *Nominal power* equal to $\frac{2.5}{3}$ MVA (the *three-phase nameplate input* part is three separate single-phase units);
    - *Nominal frequency* equal to 60 Hz;
    - *Winding 1 voltage* equal to 24.9 kV RMSLL ("kV RMSLL" is another EMTP-RV notation for "line-to-line rms kV";
    - *Winding 2 voltage* equal to 24.9 kV RMSLL;
    - *Tap ratio* [*sic*] equal to 1;
    - *Winding R* equal to 0.01 pu;
    - *Winding X* equal to 0.08 pu;
    - *Winding impedance on winding 1* equal to 0.9 and was checked;
  - *Magnetization data* [*sic*] as *Current-Flux* and *pu-pu* — current and flux points form the following table:

*Current (*pu*)*	*Flux (*pu*)*
0.002	1
0.01	1.075
0.025	1.15
0.05	1.2
0.1	1.23
2	1.72

    - *Magnetization resistance* [*sic*] equal to 500 pu;
- *IC*
  - *Initial flux* (ϕ_0) *phase A* equal to 0 pu — the default value;
  - *Initial flux* (ϕ_0) *phase B* equal to 0 pu — the default value;
  - *Initial flux* (ϕ_0) *phase C* equal to 0 pu — the default value;

- No other option of another tab was checked.

As in the DT simulations, the *RLC:C non polarized* parts model the stray capacitances between the transformer' windings of the high and low voltage sides and between the windings of both sides to the ground, in the "Pi" representation, externally connected to the transformer. The options and parameters for the capacitor between the windings of the high-voltage side to the ground were the following:

- *Data*
  - *Phase A*
    - C equal to 3.7646860634 nF;
  - *Phase B*
    - C equal to 3.7646860634 nF;
  - *Phase C*
    - C equal to 3.7646860634 nF;
  - *balanced* was checked;
- *IC*
  - There was no initial conditions — the value 0 V (the default value) was used for all phases;
- No other option of another tab was checked.

The options and parameters for the capacitor between the transformer's windings of the high- and low-voltage sides were the following:

- *Data*
  - *Phase A*
    - C equal to 1.6293379964 nF;
  - *Phase B*
    - C equal to 1.6293379964 nF;
  - *Phase C*
    - C equal to 1.6293379964 nF;
  - *balanced* was checked;
- *IC*
  - There was no initial conditions — the value 0 V (the default value) was used for all phases;

- No other option of another tab was checked.

The options and parameters for the capacitor between the windings of the low-voltage side to the ground were the following:

- *Data*
  - *Phase A*
    - C equal to 3.7646860634 nF;
  - *Phase B*
    - C equal to 3.7646860634 nF;
  - *Phase C*
    - C equal to 3.7646860634 nF;
  - *balanced* was checked;
- *IC*
  - There was no initial conditions — the value 0 V (the default value) was used for all phases;
- No other option of another tab was checked.

Also, connected to the *three-phase nameplate input* part was a current meter given by the *Current scope and observe* part. The only option checked was the following:

- *Scopes*
  - *Time-domain or Frequency scan scopes/td*> [*sic*] — *i* was checked;
    - i
      - *Phase A* was checked;
      - *Phase B* was checked;
      - *Phase C* was checked;
- No other option of another tab was checked.

The *Current scope and observe* part was connected to the bus 800 (where the line 800-802 was connected).

The single-phase-to-ground, double-phase-to-ground, and three-phase-to-ground faults were modelled with an ideal three-phase switch (*Ideal switch* part) connected to a three-phase resistor (*RLC:R* part). The phase-to-phase faults were modelled with an ideal three-phase switch connected to a three-phase resistor and a single-phase switch was connected across two phases of this same resistor. The components were in the three-phase form since the fault switch was connected to the buses in each fault simulation.

The single-phase-to-ground faults were simulated only at phase *A*, whilst the phase-to-phase and double-phase-to-ground faults were simulated only involving phases *A* and *B*. The three-phase-to-ground faults involve all three phases *A*, *B*, and *C*. Only the parameters of the phases involved in the fault have values to represent the fault, whereas the parameters of the phases not involved have extreme values.

The fault-inception angles for all faults were given around 90° of phase *A*, for each fault location. It means that the time instant of the simulation of the fault was different for some locations. These times are in Table 44:

The options and parameters for the *Ideal switch* part in the DT and RT simulations for single-phase-to-ground faults were the following:

- *Data*
  - *Phase A*
    - t_{close} equal to the value in Table 44 for the respective fault location in the DT simulations and -1 s in the RT simulations;
    - t_{open} equal to $1E15$ s [*sic*];
    - I_{margin} equal to 0 A;
  - *Phase B*
    - t_{close} equal to $1E15$ s;
    - t_{open} equal to $1E15$ s;
    - I_{margin} equal to 0 A;
  - *Phase C*
    - t_{close} equal to $1E15$ s;
    - t_{open} equal to $1E15$ s;
    - I_{margin} equal to 0 A;
- *Scopes*
  - *A*
    - v was checked;
    - i was checked;
  - *B*
    - v was checked;
    - i was checked;
  - *C*
    - v was checked;

        * i was checked.

The options and parameters for the *RLC:R* part in the DT and RT simulations for single-phase-to-ground faults were the following:

- *Values*
  - *Resistor*
    * *Phase A*
      · R equal to $1\ \Omega$, $5\ \Omega$, $10\ \Omega$, $20\ \Omega$, $50\ \Omega$, and $100\ \Omega$ in the DT simulations, and $1\ \Omega$ in the RT simulations;
    * *Phase B*
      · R equal to $1\ \Omega$, $5\ \Omega$, $10\ \Omega$, $20\ \Omega$, $50\ \Omega$, and $100\ \Omega$ in the DT simulations, and $1\ \Omega$ in the RT simulations;
    * *Phase C*
      · R equal to $1\ \Omega$, $5\ \Omega$, $10\ \Omega$, $20\ \Omega$, $50\ \Omega$, and $100\ \Omega$ in the DT simulations, and $1\ \Omega$ in the RT simulations;
    * *balanced* was checked.

The options and parameters for the *Ideal switch* part in the three-phase form in the DT and RT simulations for phase-to-phase faults were the following:

- *Data*
  - *Phase A*
    * t_{close} equal to the value in Table 44 for the respective fault location in the DT simulations and $-1\ \mathrm{s}$ in the RT simulations;
    * t_{open} equal to $1E15\ \mathrm{s}$;
    * I_{margin} equal to $0\ \mathrm{A}$;
  - *Phase B*
    * t_{close} equal to the value in Table 44 for the respective fault location in the DT simulations and $-1\ \mathrm{s}$ in the RT simulations;
    * t_{open} equal to $1E15\ \mathrm{s}$;
    * I_{margin} equal to $0\ \mathrm{A}$;
  - *Phase C*
    * t_{close} equal to $1E15\ \mathrm{s}$;
    * t_{open} equal to $1E15\ \mathrm{s}$;
    * I_{margin} equal to $0\ \mathrm{A}$;

- *Scopes*
  - *A*
    - v was checked in the RT simulations;
    - i was checked in the DT and RT simulations;
  - *B*
    - v was checked in the RT simulations;
    - i was checked in the DT and RT simulations;
  - *C*
    - v was checked in the RT simulations;
    - i was checked in the RT simulations;

The options and parameters for the *Ideal switch* part in the single-phase form in the DT and RT simulations for phase-to-phase faults were the following:

- *Data*
  - t_{close} equal to -1 s in the DT and RT simulations;
  - t_{open} equal to $1E15$ s;
  - I_{margin} equal to 0 A;
- *Scopes*
  - *Time-domain or Frequency scan scopes*
    - i was checked in the DT RT simulations;

The options and parameters for the *RLC:R* part in the DT and RT simulations for phase-to-phase faults were the following:

- *Values*
  - *Resistor*
    - *Phase A*
      - R equal to $0.5\ \Omega$, $2.5\ \Omega$, $5\ \Omega$, $10\ \Omega$, $25\ \Omega$, and $50\ \Omega$ in the DT simulations, and $0.5\ \Omega$ in the RT simulations;
    - *Phase B*
      - R equal to $0.5\ \Omega$, $2.5\ \Omega$, $5\ \Omega$, $10\ \Omega$, $25\ \Omega$, and $50\ \Omega$ in the DT simulations, and $0.5\ \Omega$ in the RT simulations;
    - *Phase C*

            - R equal to $0.5\ \Omega$, $2.5\ \Omega$, $5\ \Omega$, $10\ \Omega$, $25\ \Omega$, and $50\ \Omega$ in the DT simulations, and $0.5\ \Omega$ in the RT simulations;
        - *balanced* was checked.

The options and parameters for the *Ideal switch* part in the DT and RT simulations for double-phase-to-ground faults were the following:

- *Data*
  - *Phase A*
    - t_{close} equal to the value in Table 44 for the respective fault location in the DT simulations and -1 s in the RT simulations;
    - t_{open} equal to $1E15$ s [*sic*];
    - I_{margin} equal to 0 A;
  - *Phase B*
    - t_{close} equal to the value in Table 44 for the respective fault location in the DT simulations and -1 s in the RT simulations;
    - t_{open} equal to $1E15$ s;
    - I_{margin} equal to 0 A;
  - *Phase C*
    - t_{close} equal to $1E15$ s;
    - t_{open} equal to $1E15$ s;
    - I_{margin} equal to 0 A;
- *Scopes*
  - *A*
    - v was checked;
    - i was checked;
  - *B*
    - v was checked;
    - i was checked;
  - *C*
    - v was checked;
    - i was checked.

The options and parameters for the *RLC:R* part in the DT and RT simulations for double-phase-to-ground faults were identical to those for single-phase-to-ground faults. The options and parameters for the *Ideal switch* part in the DT and RT simulations for three-phase-to-ground faults were the following:

- *Data*
  - *Phase A*
    - t_{close} equal to the value in Table 44 for the respective fault location in the DT simulations and -1 s in the RT simulations;
    - t_{open} equal to $1E15$ s [*sic*];
    - I_{margin} equal to 0 A;
  - *Phase B*
    - t_{close} equal to the value in Table 44 for the respective fault location in the DT simulations and -1 s in the RT simulations;
    - t_{open} equal to $1E15$ s;
    - I_{margin} equal to 0 A;
  - *Phase C*
    - t_{close} equal to the value in Table 44 for the respective fault location in the DT simulations and -1 s in the RT simulations;
    - t_{open} equal to $1E15$ s;
    - I_{margin} equal to 0 A;
- *Scopes*
  - *A*
    - v was checked;
    - i was checked;
  - *B*
    - v was checked;
    - i was checked;
  - *C*
    - v was checked;
    - i was checked.

The options and parameters for the *RLC:R* part in the DT and RT simulations for three-phase-to-ground faults were identical to those for single-phase-to-ground faults.

Table 44 – Fault-inception times respective to the fault locations of the power distribution network in the DT stage

Location	Time Instant [s]
Bus 800	0.03473760
Bus 802	0.03473780
Bus 806	0.03473800
After the first section of the line 806-808	0.03473830
After the second section of the line 806-808	0.03473850
After the third section of the line 806-808	0.03473870
After the fourth section of the line 806-808	0.03473890
After the fifth section of the line 806-808	0.03473910
After the sixth section of the line 806-808	0.03473920
After the seventh section of the line 806-808	0.03473930
After the eighth section of the line 806-808	0.03473940
After the ninth section of the line 806-808	0.03473960
After the 10th section of the line 806-808	0.03473980
After the 11th section of the line 806-808	0.03473990
Bus 808	0.03474010
After the first section of the line 808-812	0.03474020
After the second section of the line 808-812	0.03474020
After the third section of the line 808-812	0.03474020
After the fourth section of the line 808-812	0.03474020
After the fifth section of the line 808-812	0.03474030
After the sixth section of the line 808-812	0.03474030
After the seventh section of the line 808-812	0.03474040
After the eighth section of the line 808-812	0.03474040
After the ninth section of the line 808-812	0.03474050
After the 10th section of the line 808-812	0.03474050
After the 11th section of the line 808-812	0.03474060
After the 12th section of the line 808-812	0.03474060
After the 13th section of the line 808-812	0.03474070
Bus 812	0.03474080
After the first section of the line 812-814	0.03474080
After the second section of the line 812-814	0.03474080
After the third section of the line 812-814	0.03474090
After the fourth section of the line 812-814	0.03474090
After the fifth section of the line 812-814	0.03474100
After the sixth section of the line 812-814	0.03474100
After the seventh section of the line 812-814	0.03474100
After the eighth section of the line 812-814	0.03474100
After the ninth section of the line 812-814	0.03474100
After the 10th section of the line 812-814	0.03474090
After the 11th section of the line 812-814	0.03474090
Bus 814	0.03474090

APPENDIX E FIGURES OF RESULTS FROM THE TIME-DOMAIN STUDY CASES ON THE ELECTRIC POWER DISTRIBUTION NETWORK

Figures 129 to 138 present the results for single-phase-to-ground faults.

Figure 129 – Results by $\mathcal{P}_i(x_g)$ for single-phase-to-ground faults with the cut-off frequency of 1 kHz

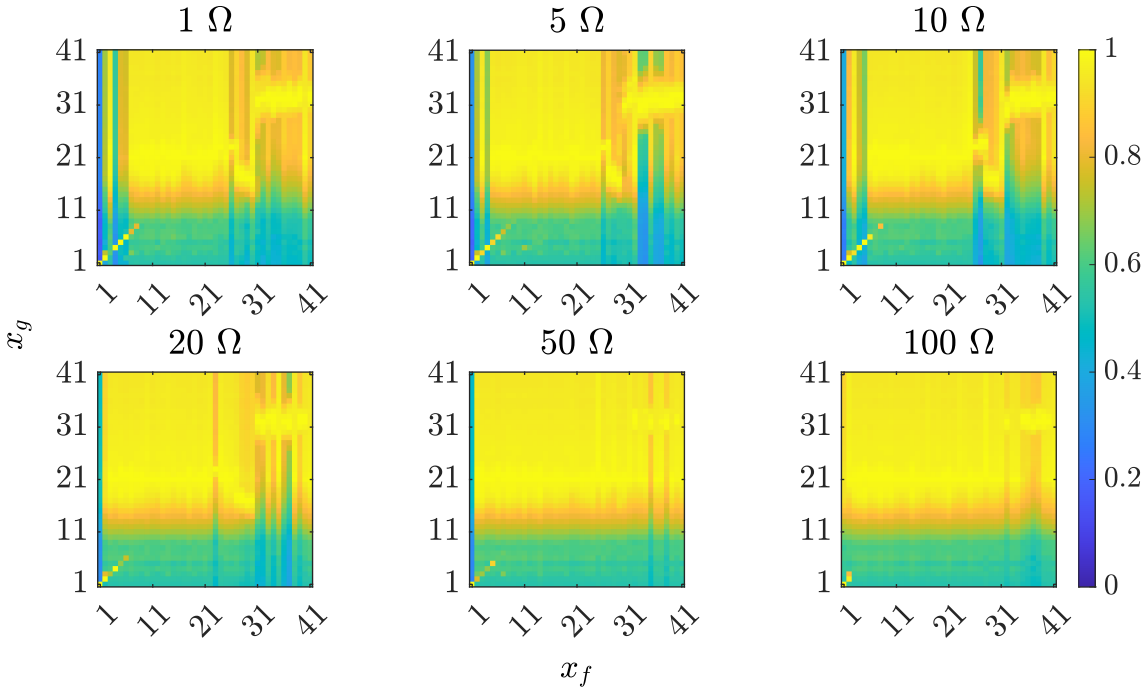

Source: Author

Similarly, the results for phase-to-phase faults are presented in Figures 139 to 148.

Still, the results for double-phase-to-ground faults are presented in Figures 149 to 158.

Finally, the results for three-phase-to-ground faults are presented in Figures 159 to 168.

The points of both abscissa and ordinate axes in Figures 129 to 168 are the representative indices of the fault locations in Figure 66. Figures 129 and 160 show that the

Figure 130 – Results by $\mathcal{E}_i(x_g)$ for single-phase-to-ground faults with the cut-off frequency of 1 kHz

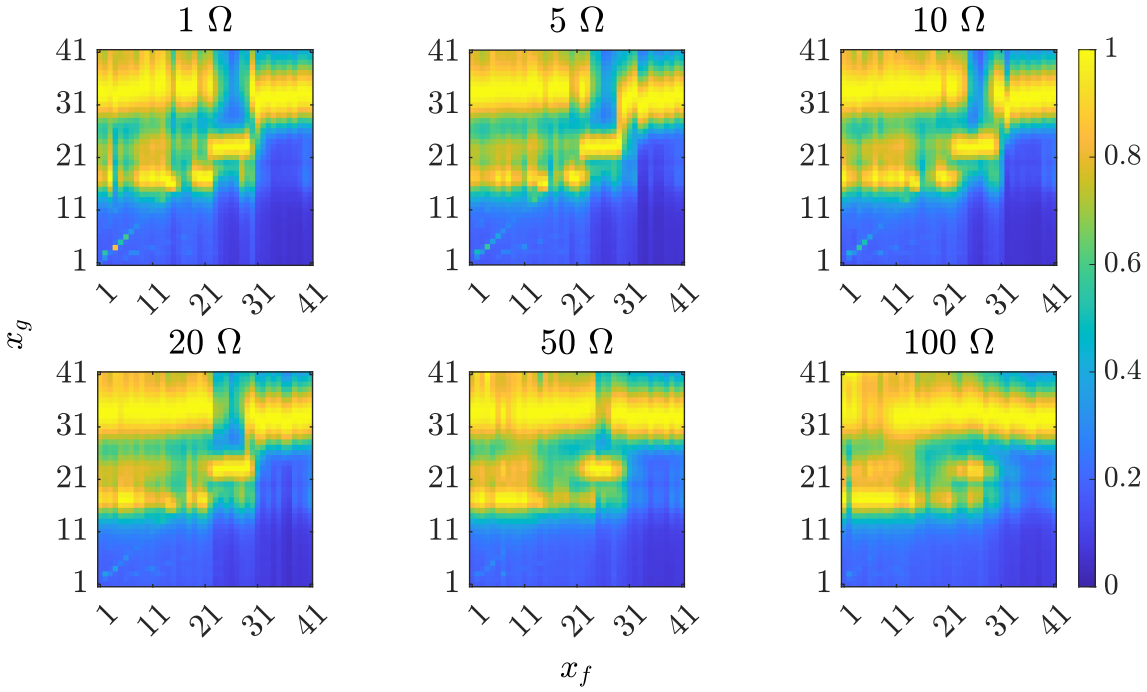

Source: Author

Figure 131 – Results by $\mathcal{P}_i(x_g)$ for single-phase-to-ground faults with the cut-off frequency of 3 kHz

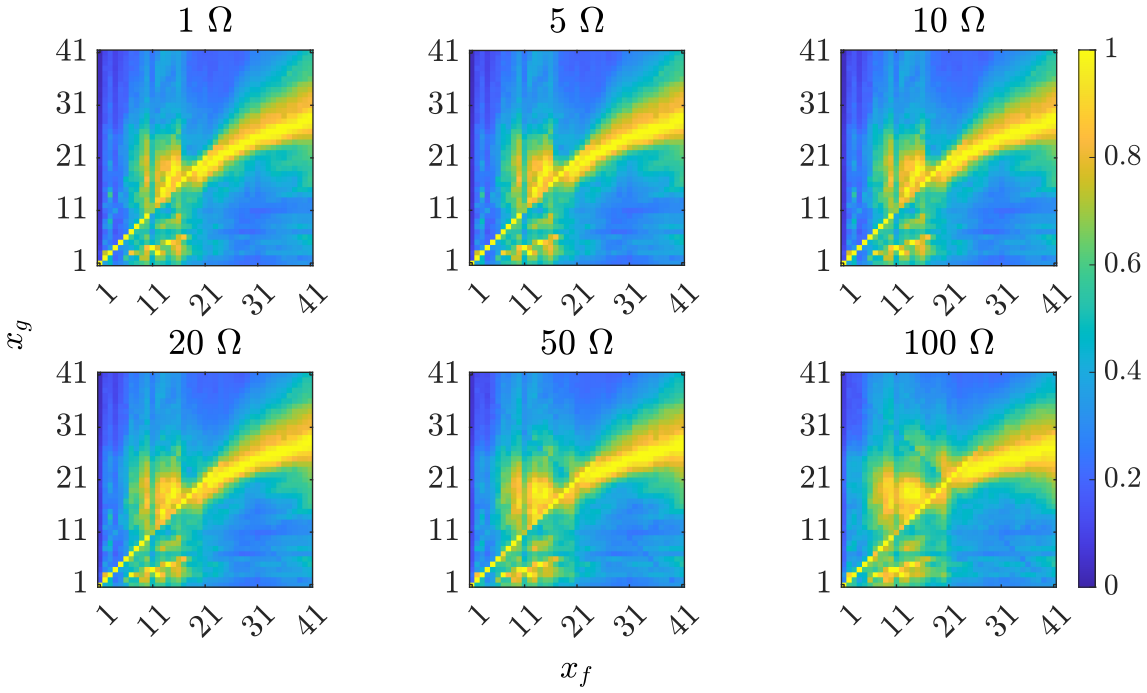

Source: Author

Figure 132 – Results by $\mathcal{E}_i(x_g)$ for single-phase-to-ground faults with the cut-off frequency of 3 kHz

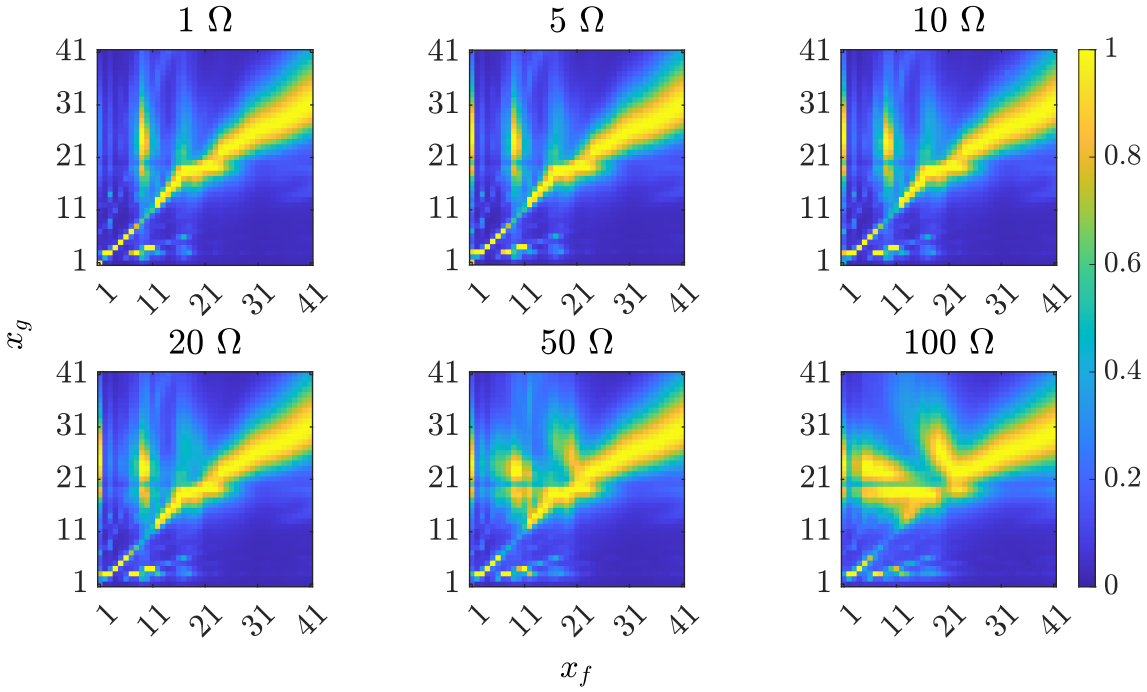

Source: Author

Figure 133 – Results by $\mathcal{P}_i(x_g)$ for single-phase-to-ground faults with the cut-off frequency of 5 kHz

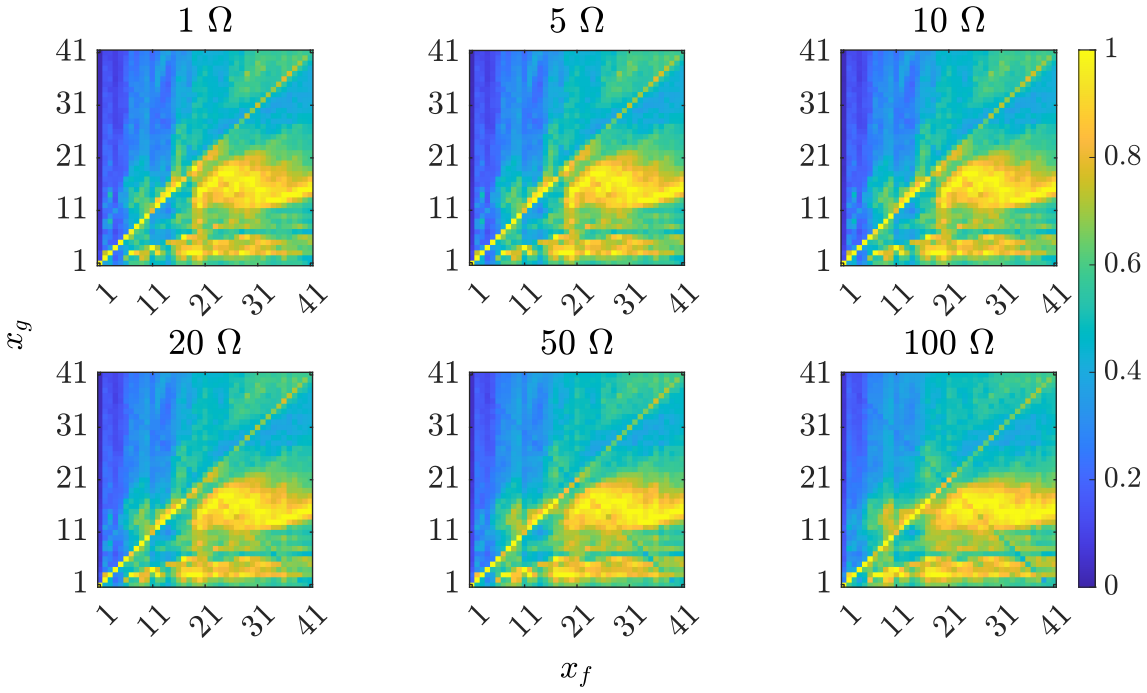

Source: Author

Figure 134 – Results by $\mathcal{E}_i(x_g)$ for single-phase-to-ground faults with the cut-off frequency of 5 kHz

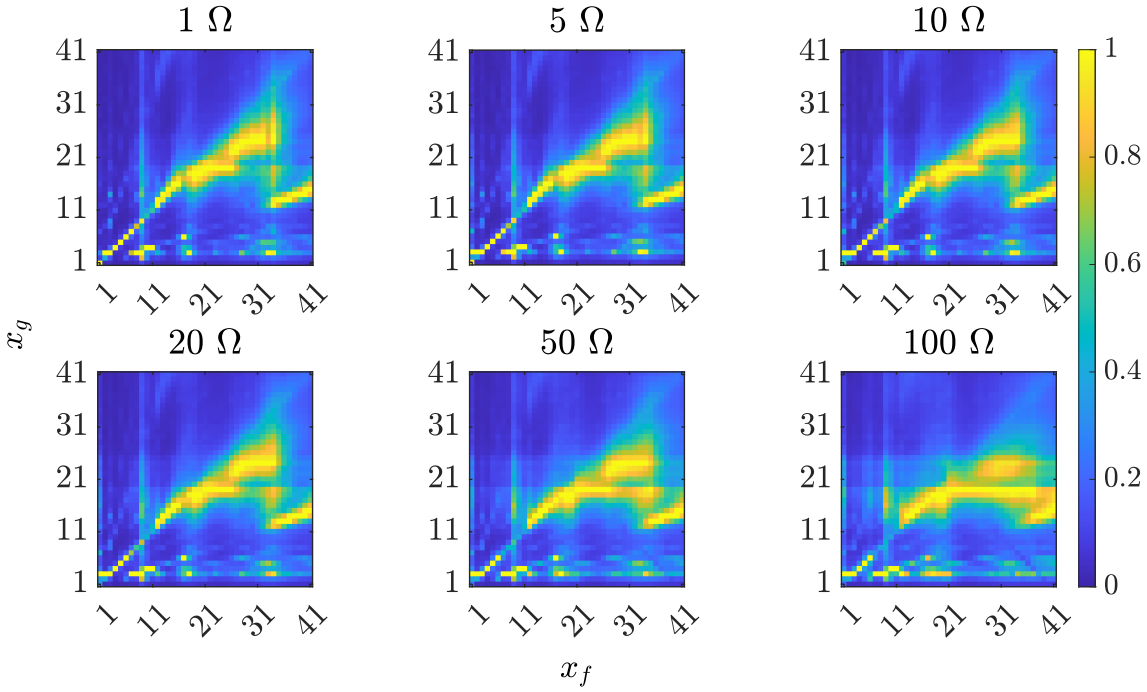

Source: Author

Figure 135 – Results by $\mathcal{P}_i(x_g)$ for single-phase-to-ground faults with the cut-off frequency of 7 kHz

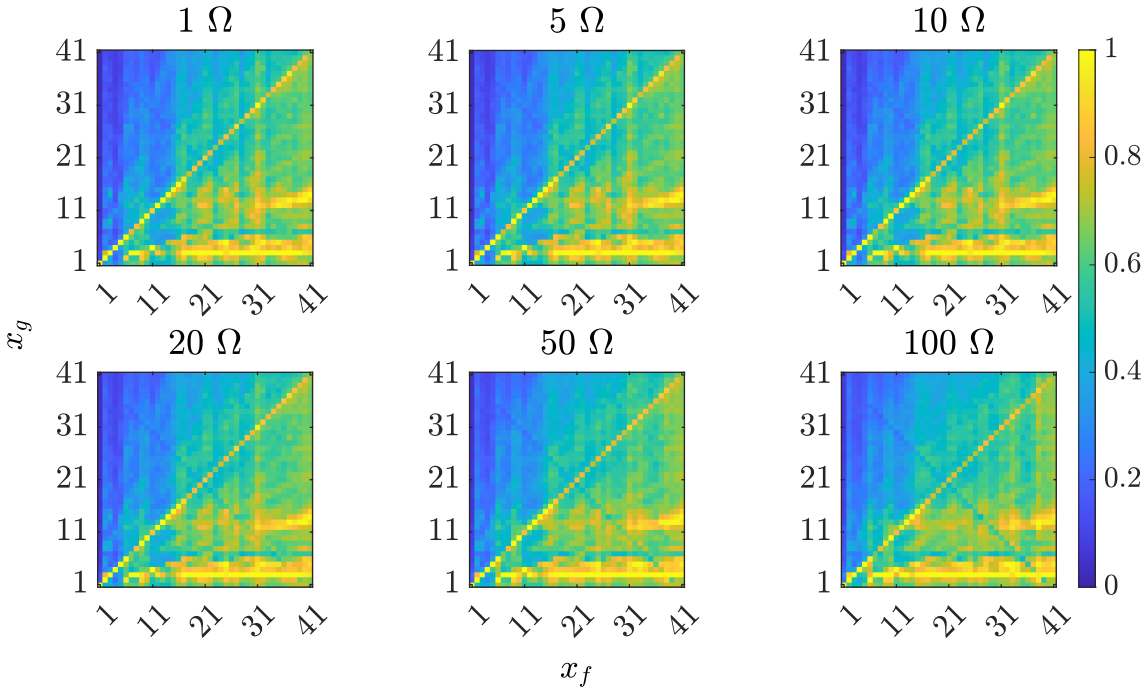

Source: Author

Figure 136 – Results by $\mathcal{E}_i(x_g)$ for single-phase-to-ground faults with the cut-off frequency of 7 kHz

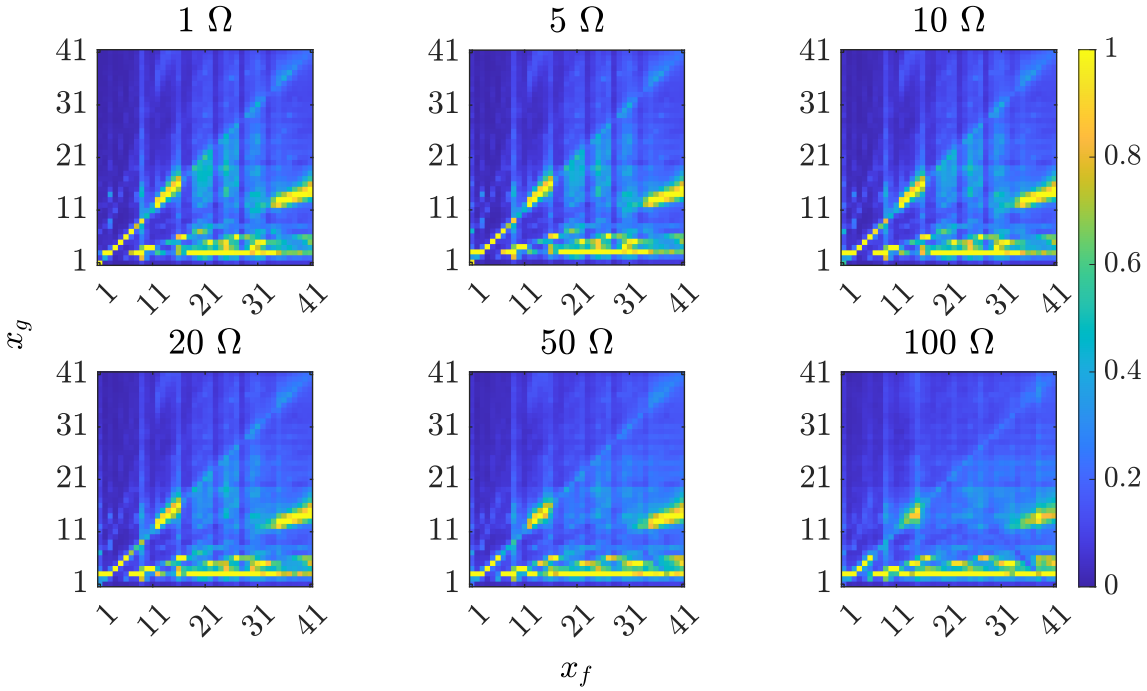

Source: Author

Figure 137 – Results by $\mathcal{P}_i(x_g)$ for single-phase-to-ground faults with the cut-off frequency of 9 kHz

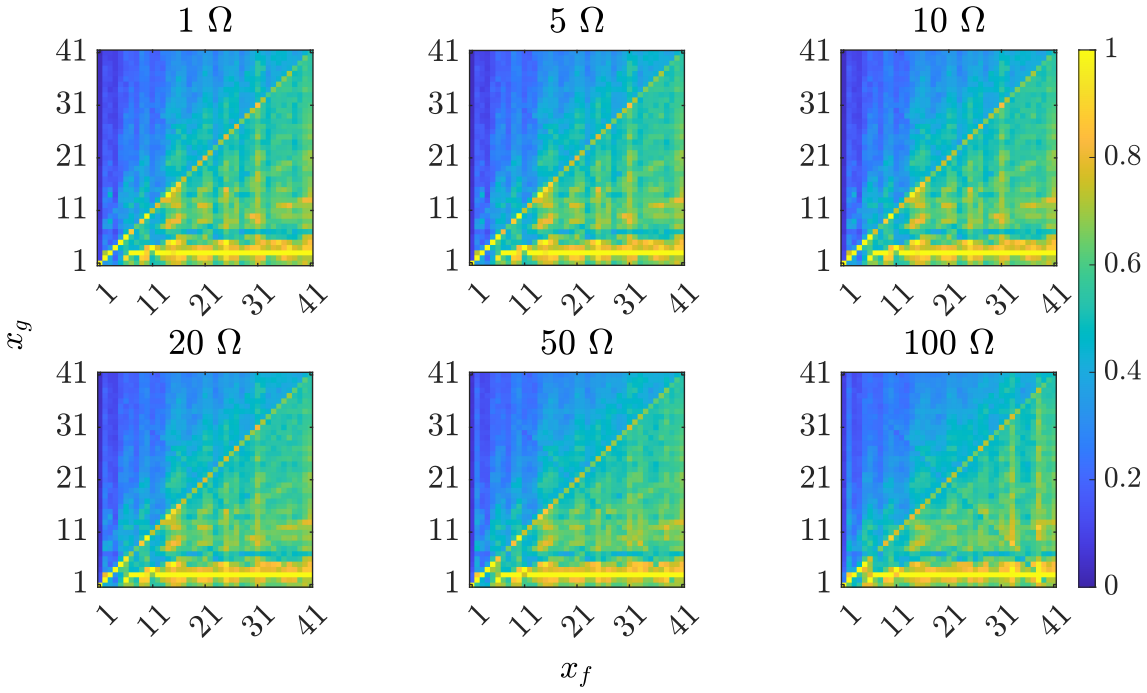

Source: Author

Figure 138 – Results by $\mathcal{E}_i(x_g)$ for single-phase-to-ground faults with the cut-off frequency of 9 kHz

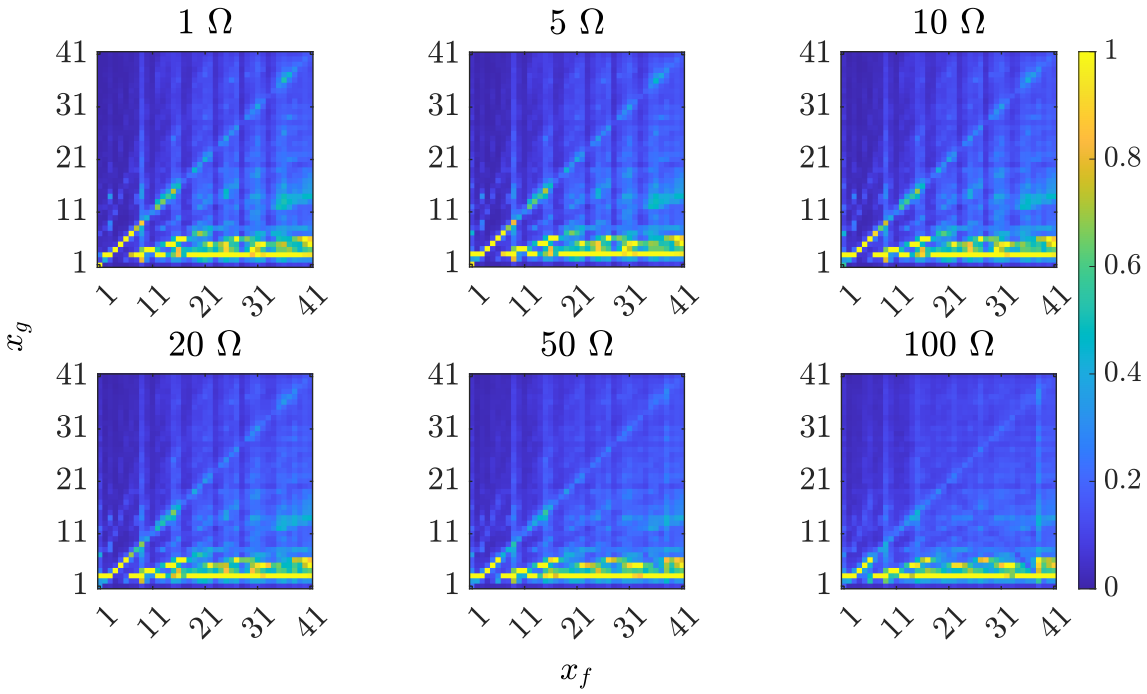

Source: Author

Figure 139 – Results by $\mathcal{P}_i(x_g)$ for phase-to-phase faults with the cut-off frequency of 1 kHz

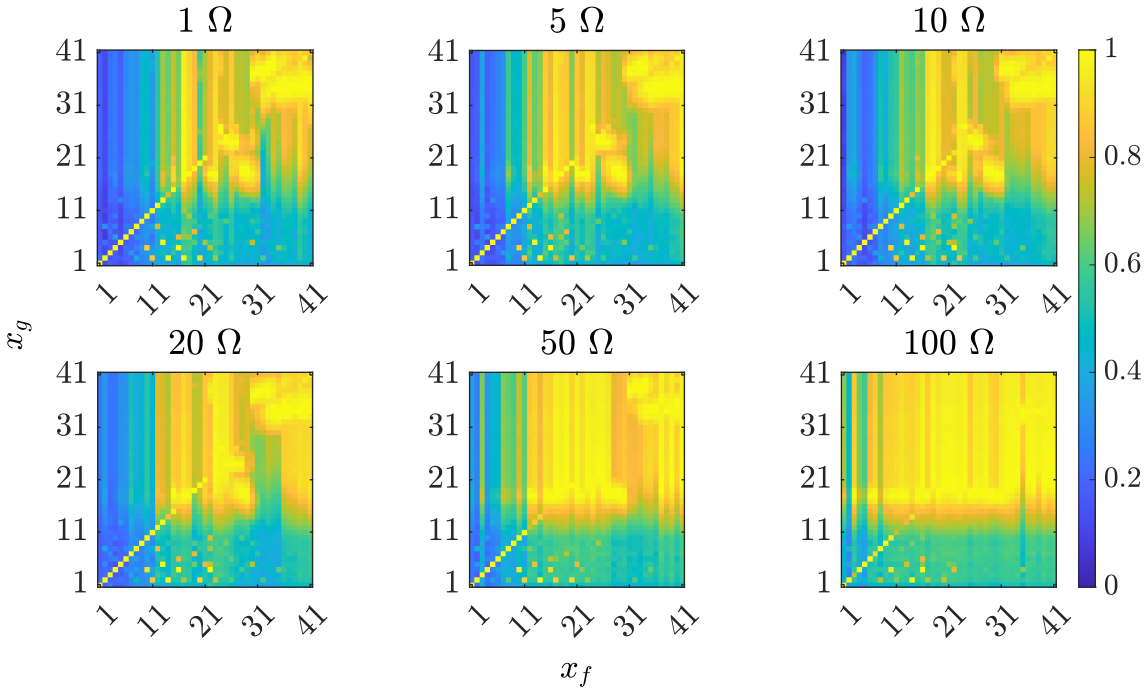

Source: Author

Figure 140 – Results by $\mathcal{E}_i(x_g)$ for phase-to-phase faults with the cut-off frequency of 1 kHz

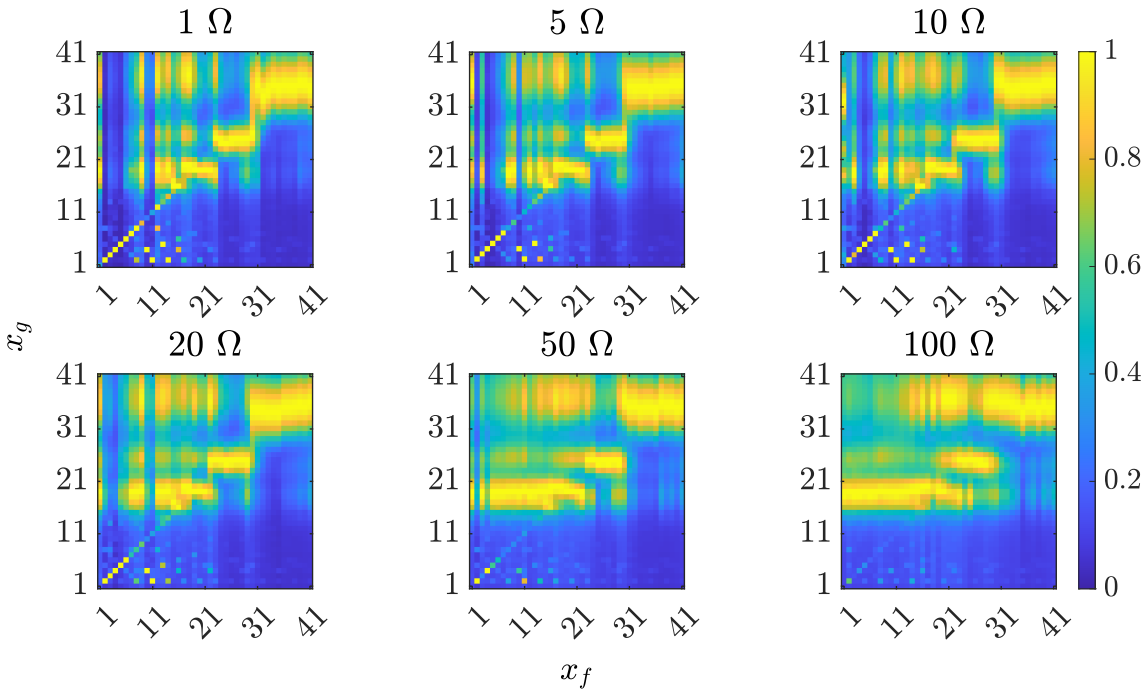

Source: Author

Figure 141 – Results by $\mathcal{P}_i(x_g)$ for phase-to-phase faults with the cut-off frequency of 3 kHz

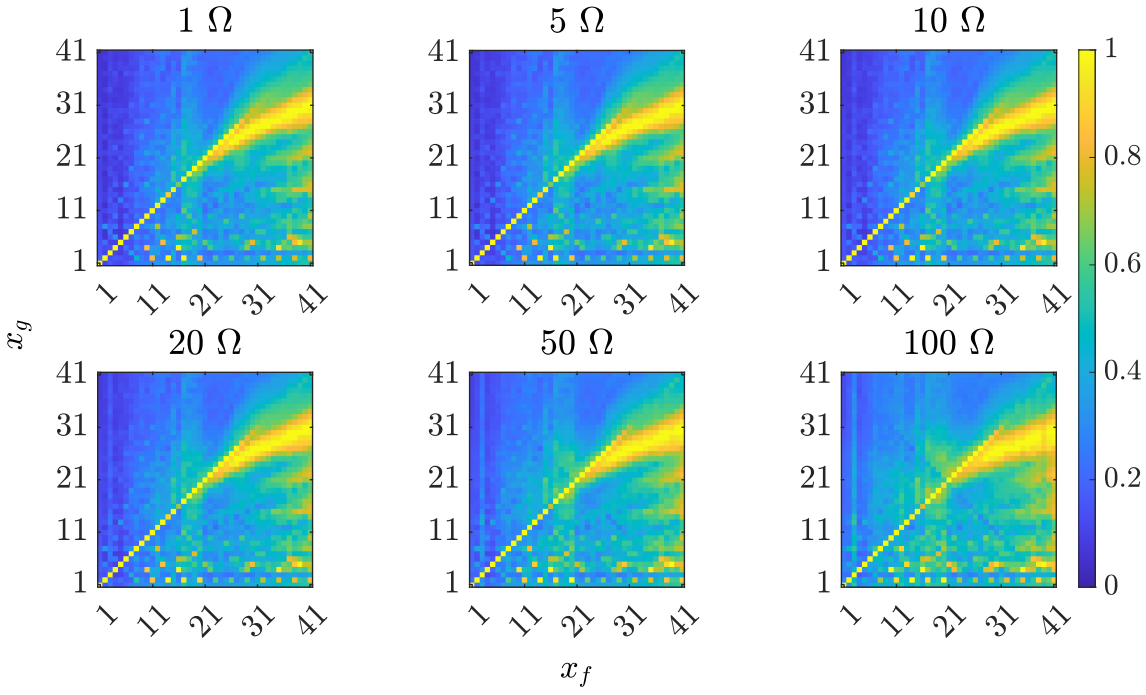

Source: Author

Figure 142 – Results by $\mathcal{E}_i(x_g)$ for phase-to-phase faults with the cut-off frequency of 3 kHz

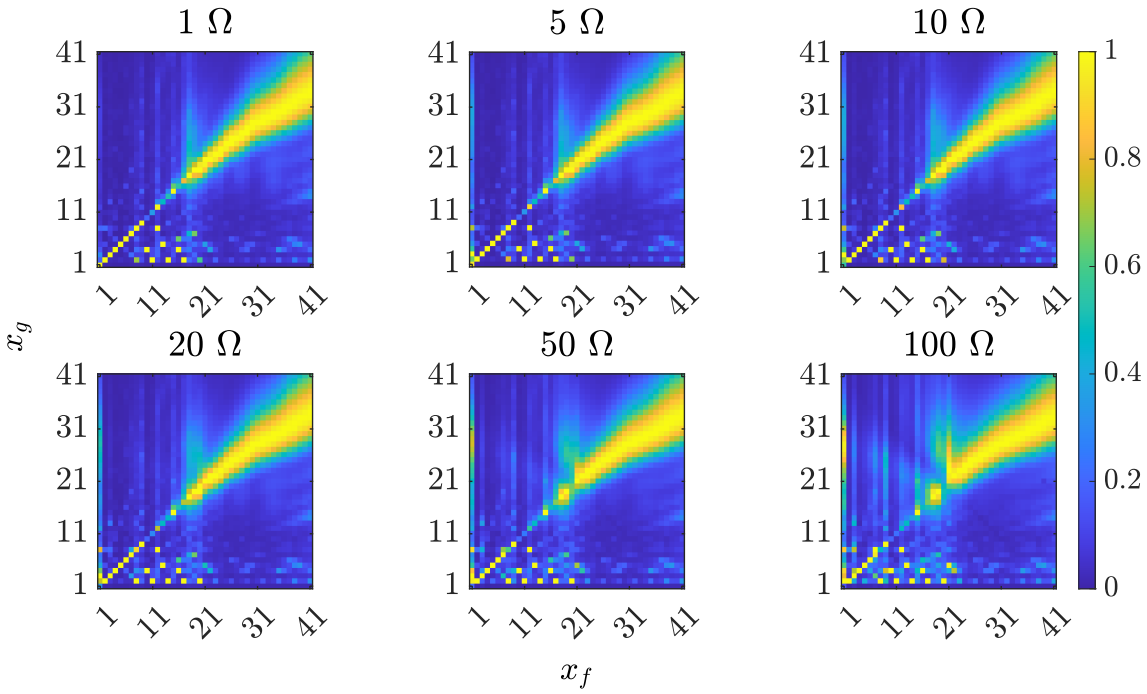

Source: Author

Figure 143 – Results by $\mathcal{P}_i(x_g)$ for phase-to-phase faults with the cut-off frequency of 5 kHz

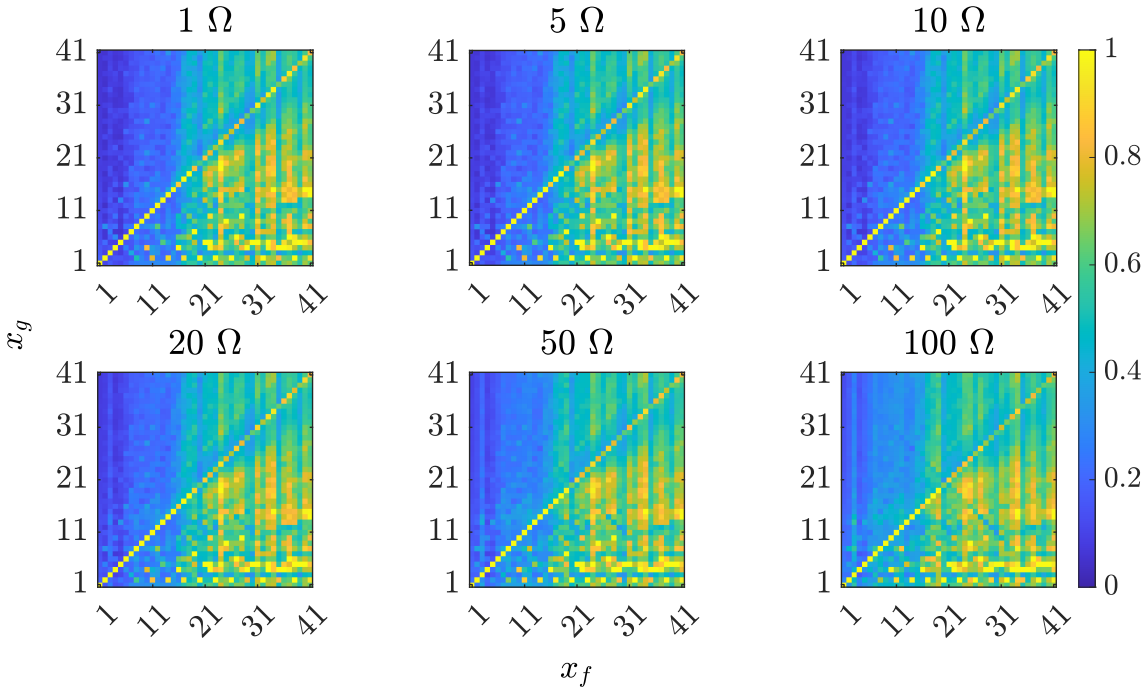

Source: Author

Figure 144 – Results by $\mathcal{E}_i(x_g)$ for phase-to-phase faults with the cut-off frequency of 5 kHz

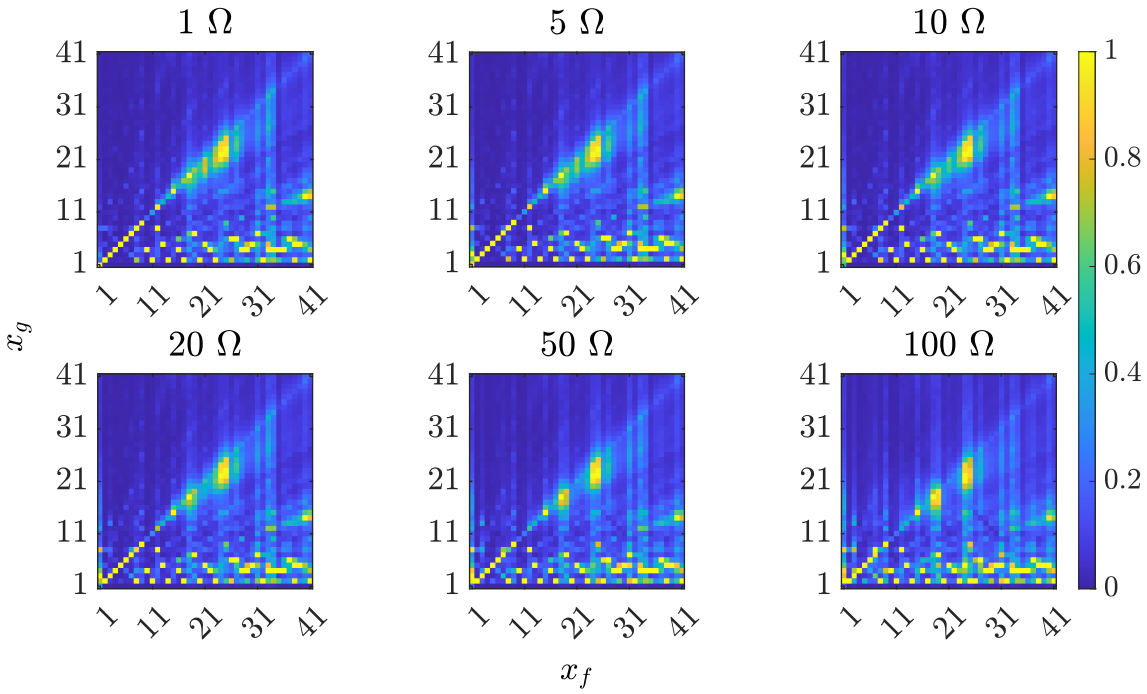

Source: Author

Figure 145 – Results by $\mathcal{P}_i(x_g)$ for phase-to-phase faults with the cut-off frequency of 7 kHz

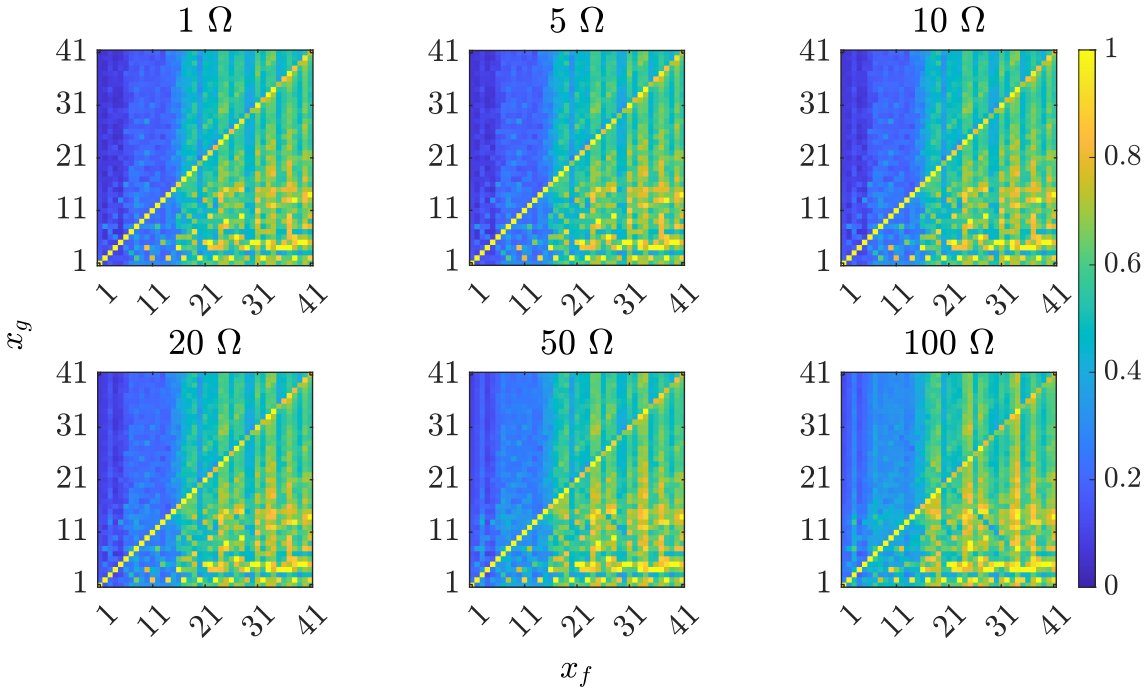

Source: Author

Figure 146 – Results by $\mathcal{E}_i(x_g)$ for phase-to-phase faults with the cut-off frequency of 7 kHz

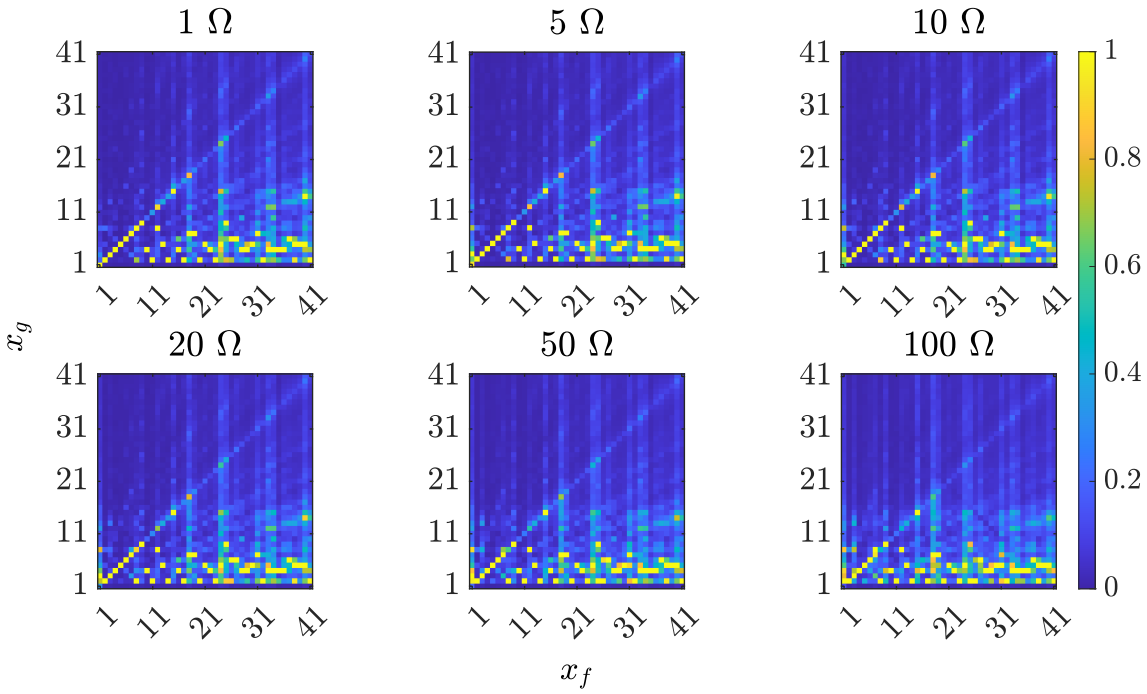

Source: Author

Figure 147 – Results by $\mathcal{P}_i(x_g)$ for phase-to-phase faults with the cut-off frequency of 9 kHz

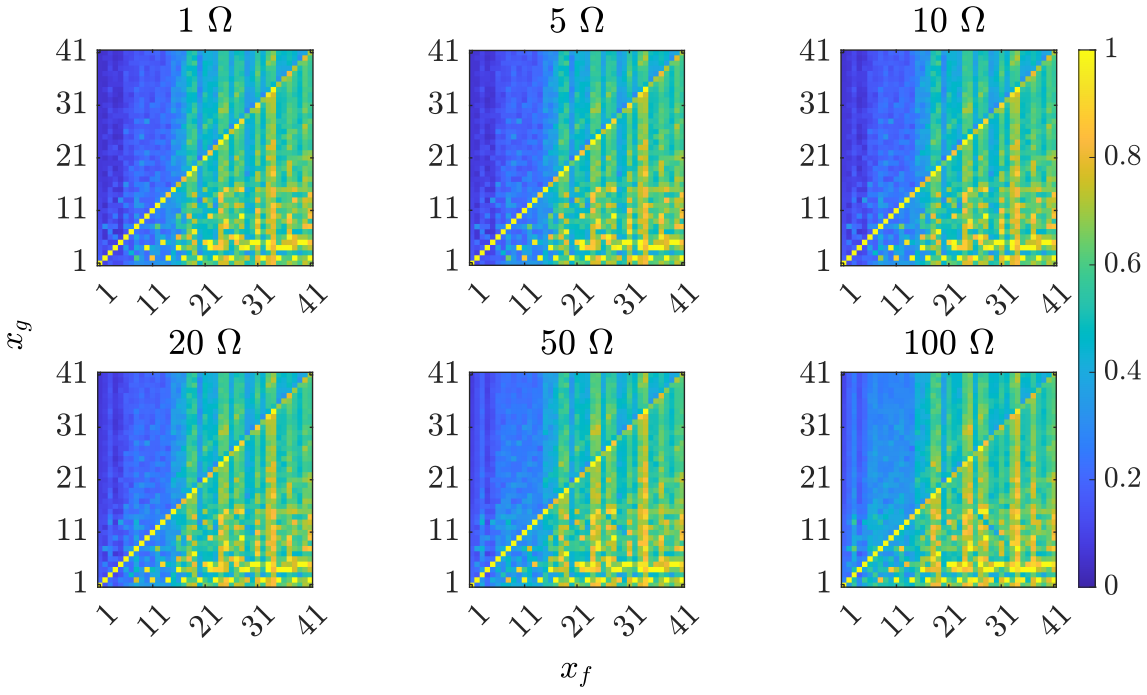

Source: Author

Figure 148 – Results by $\mathcal{E}_i(x_g)$ for phase-to-phase faults with the cut-off frequency of 9 kHz

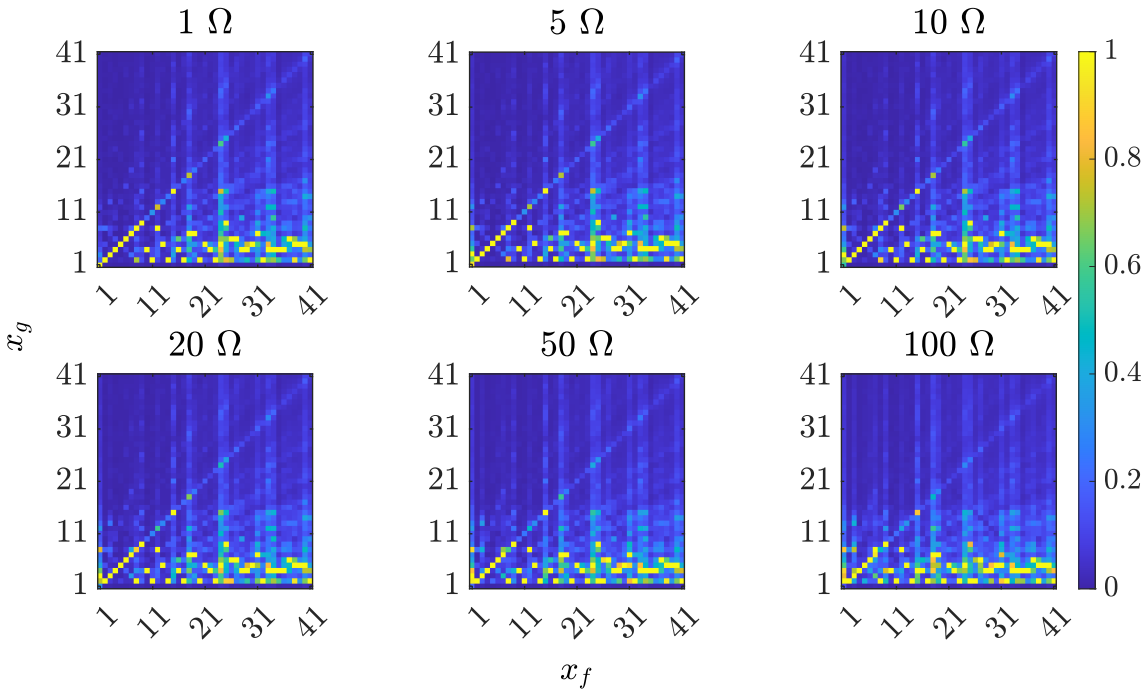

Source: Author

Figure 149 – Results by $\mathcal{P}_i(x_g)$ for double-phase-to-ground faults with the cut-off frequency of 1 kHz

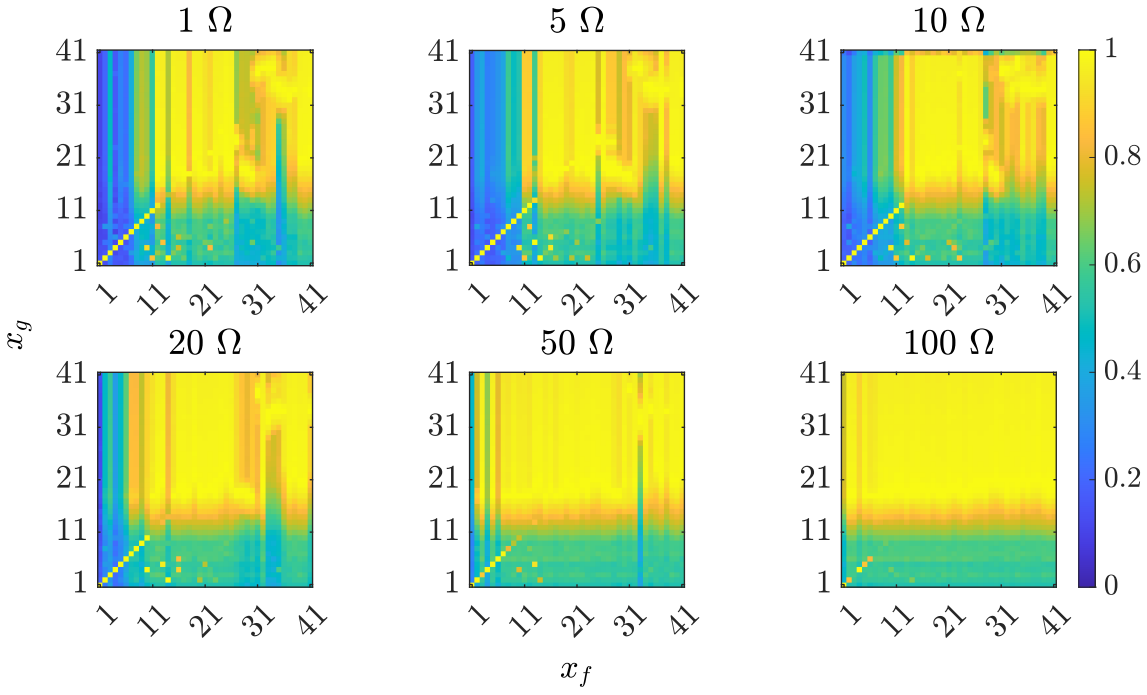

Source: Author

Figure 150 – Results by $\mathcal{E}_i(x_g)$ for double-phase-to-ground faults with the cut-off frequency of 1 kHz

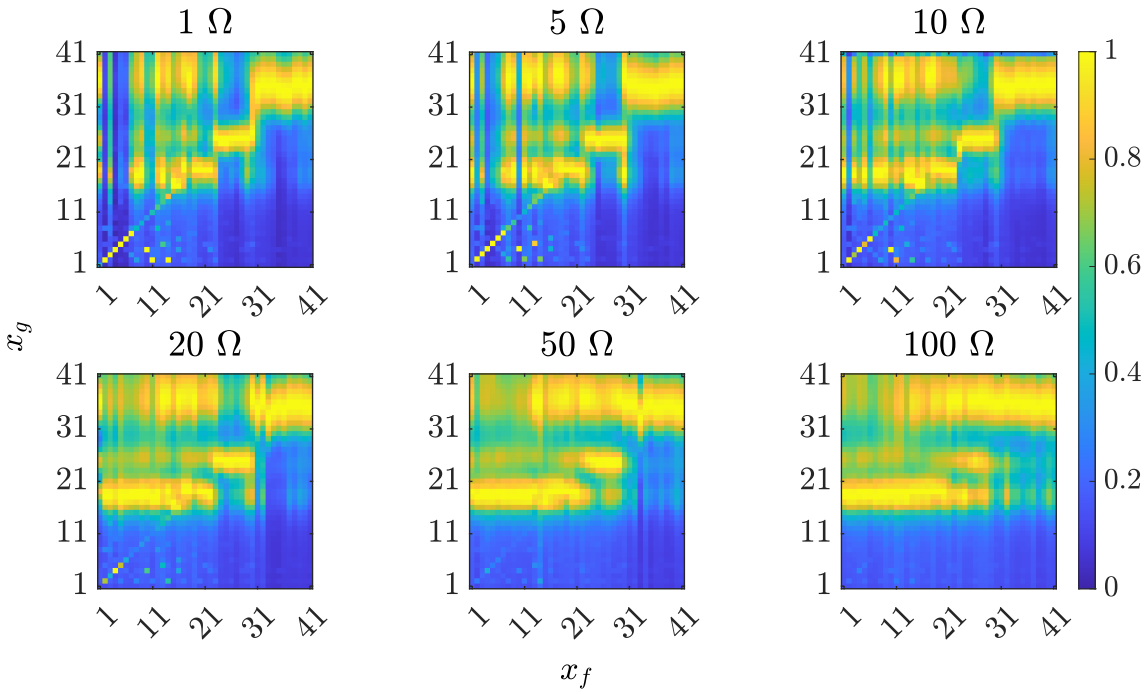

Source: Author

Figure 151 – Results by $\mathcal{P}_i(x_g)$ for double-phase-to-ground faults with the cut-off frequency of 3 kHz

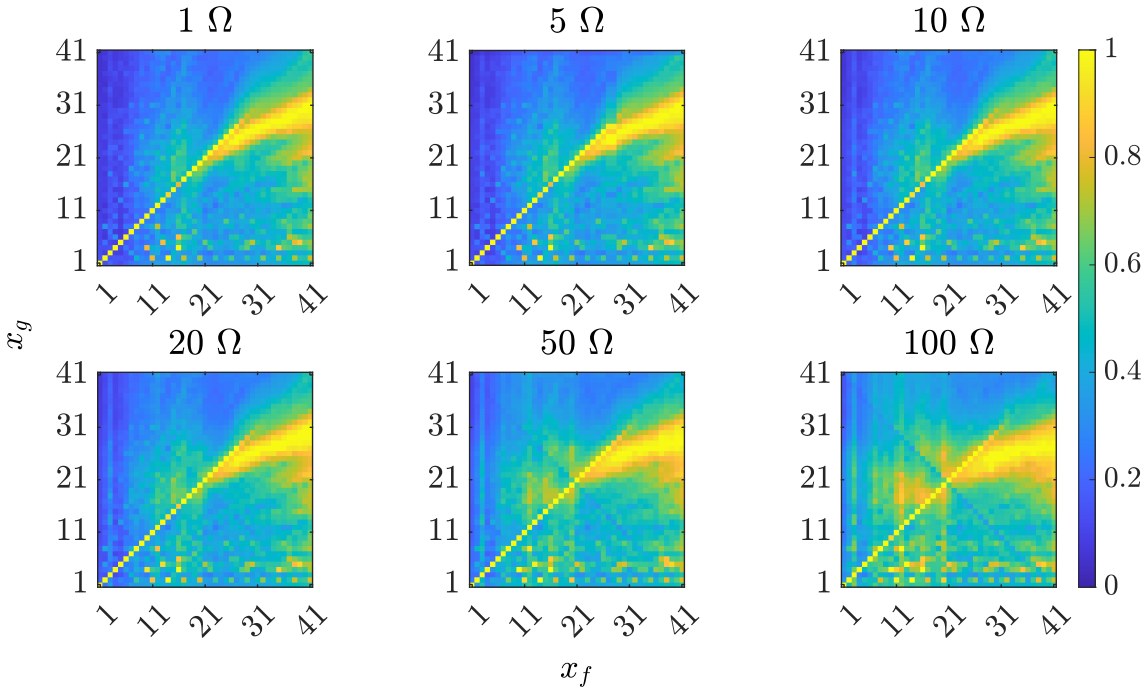

Source: Author

Figure 152 – Results by $\mathcal{E}_i(x_g)$ for double-phase-to-ground faults with the cut-off frequency of 3 kHz

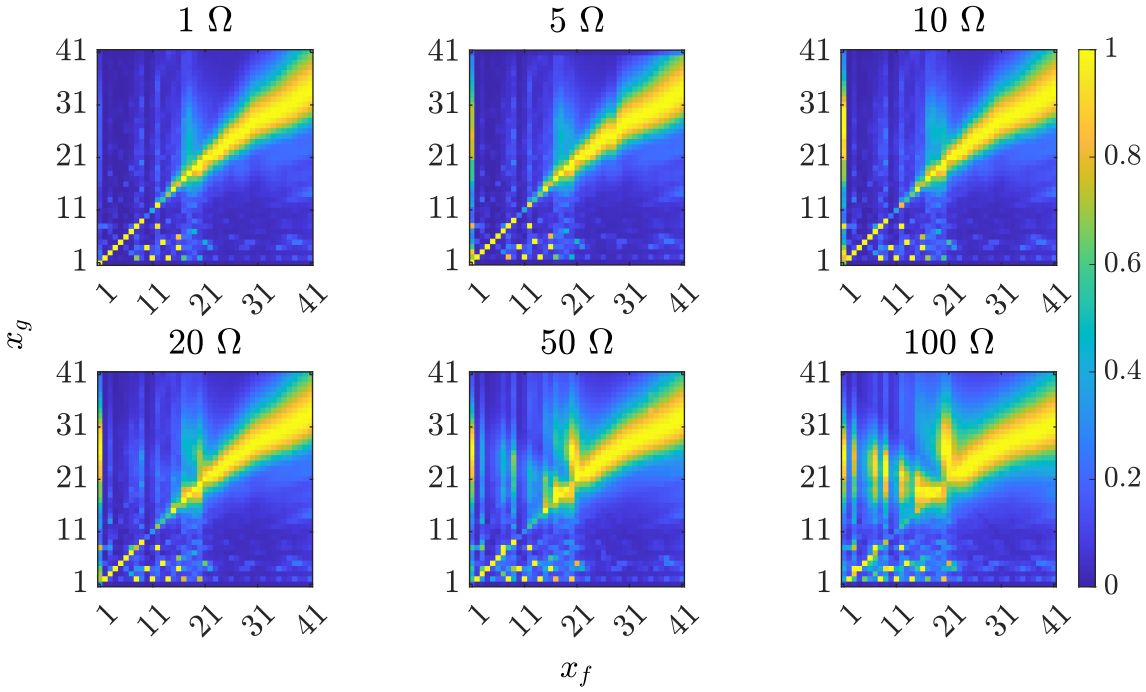

Source: Author

Figure 153 – Results by $\mathcal{P}_i(x_g)$ for double-phase-to-ground faults with the cut-off frequency of 5 kHz

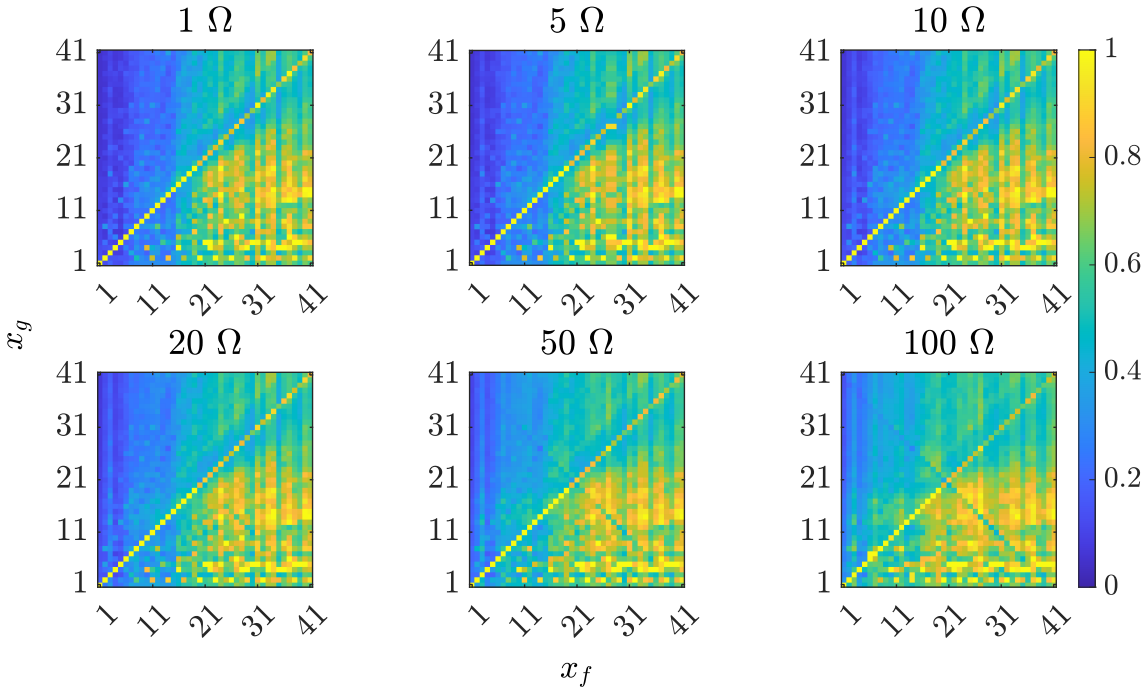

Source: Author

Figure 154 – Results by $\mathcal{E}_i(x_g)$ for double-phase-to-ground faults with the cut-off frequency of 5 kHz

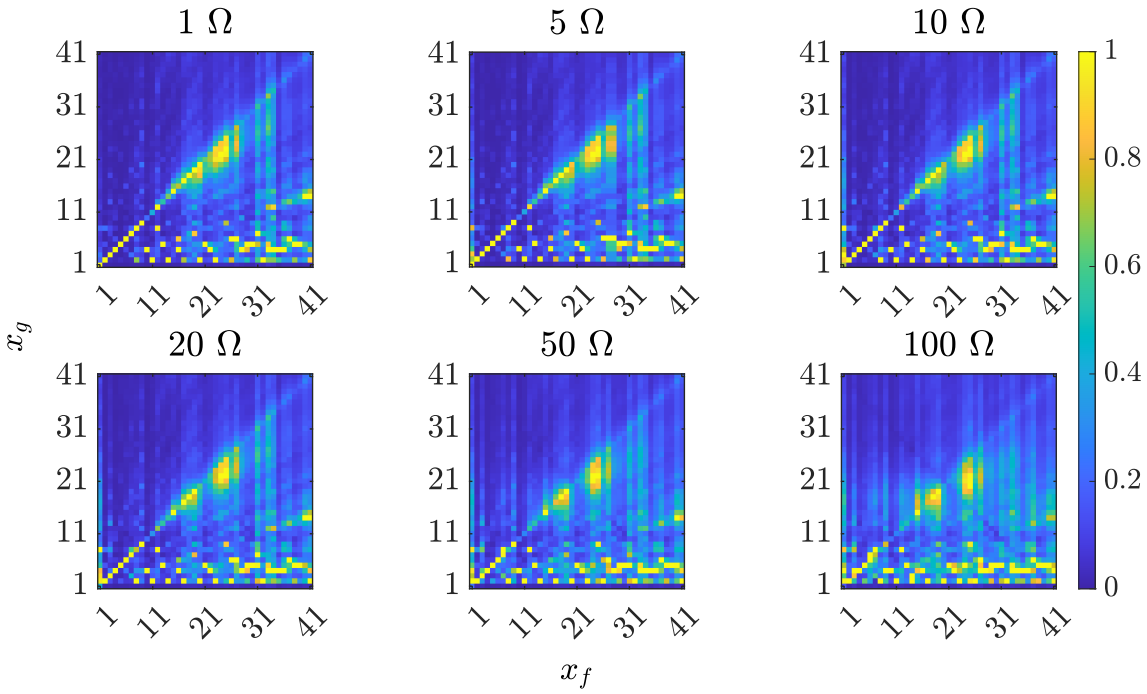

Source: Author

Figure 155 – Results by $\mathcal{P}_i(x_g)$ for double-phase-to-ground faults with the cut-off frequency of 7 kHz

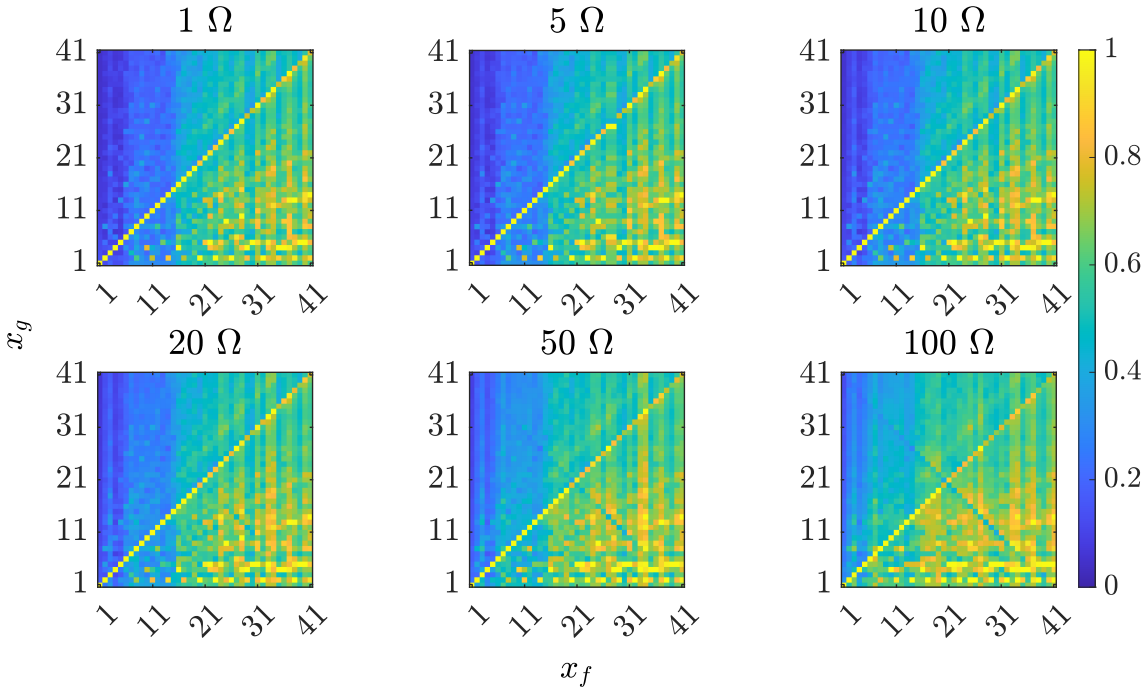

Source: Author

Figure 156 – Results by $\mathcal{E}_i(x_g)$ for double-phase-to-ground faults with the cut-off frequency of 7 kHz

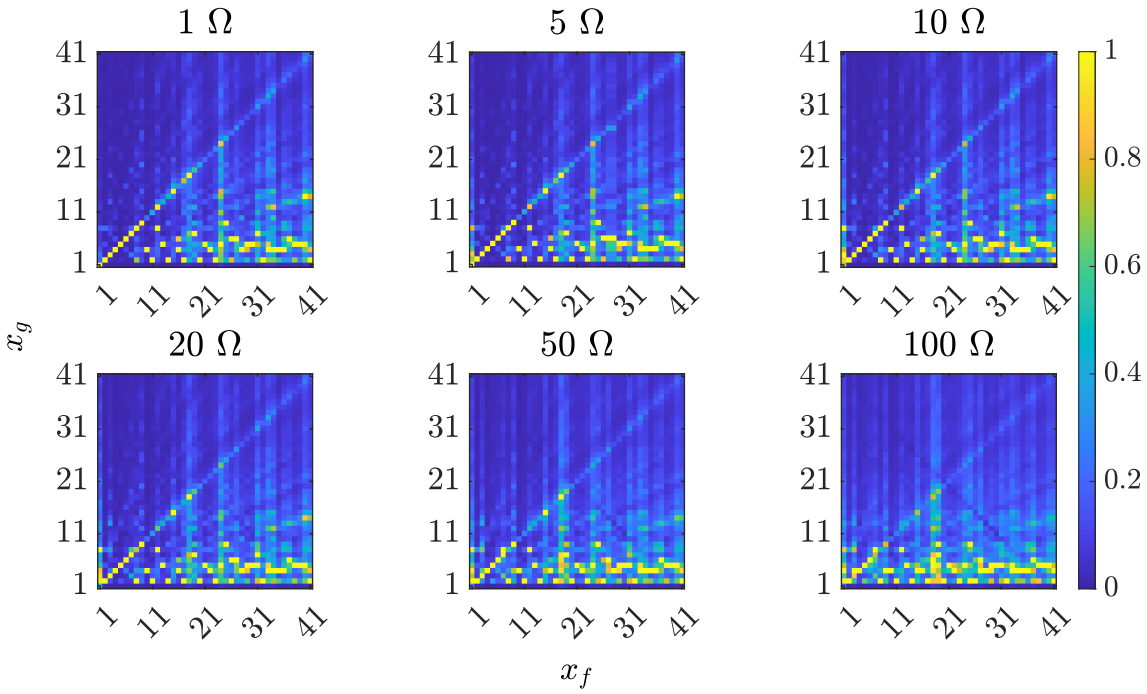

Source: Author

Figure 157 – Results by $\mathcal{P}_i(x_g)$ for double-phase-to-ground faults with the cut-off frequency of 9 kHz

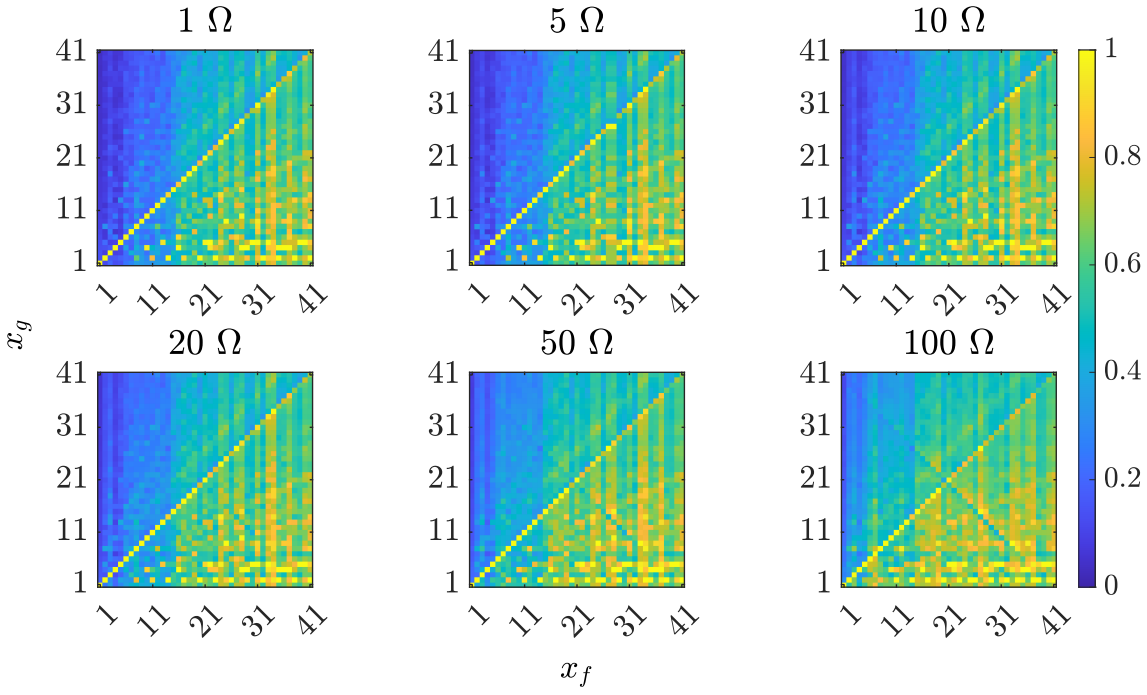

Source: Author

Figure 158 – Results by $\mathcal{E}_i(x_g)$ for double-phase-to-ground faults with the cut-off frequency of 9 kHz

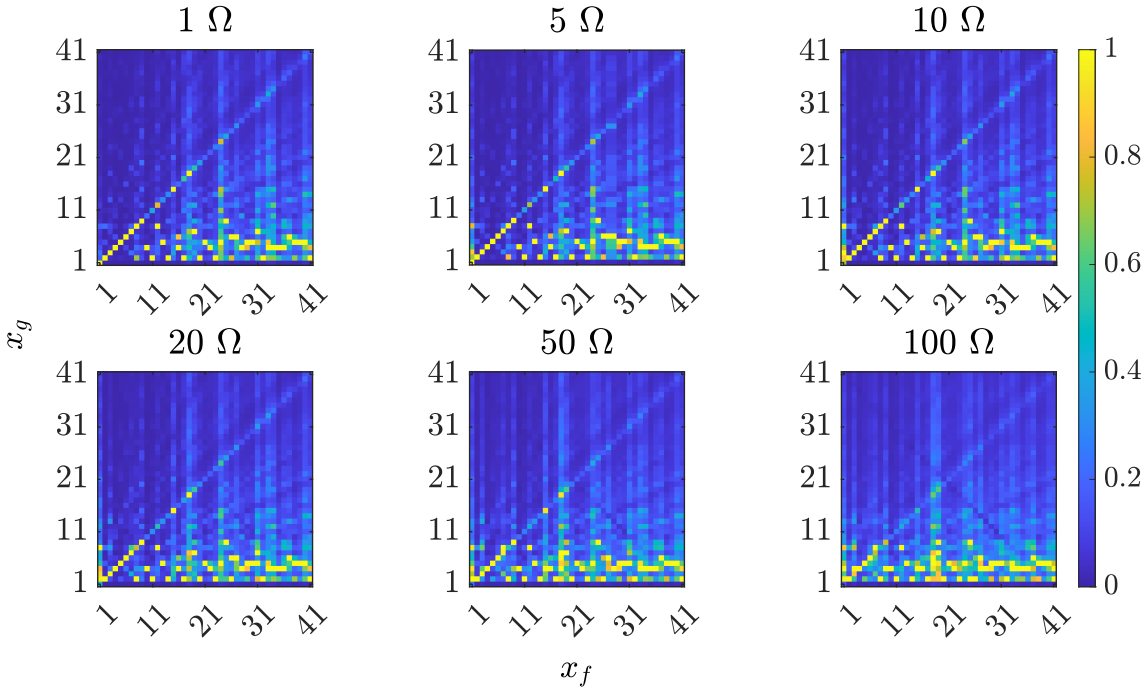

Source: Author

Figure 159 – Results by $\mathcal{P}_i(x_g)$ for three-phase-to-ground faults with the cut-off frequency of 1 kHz

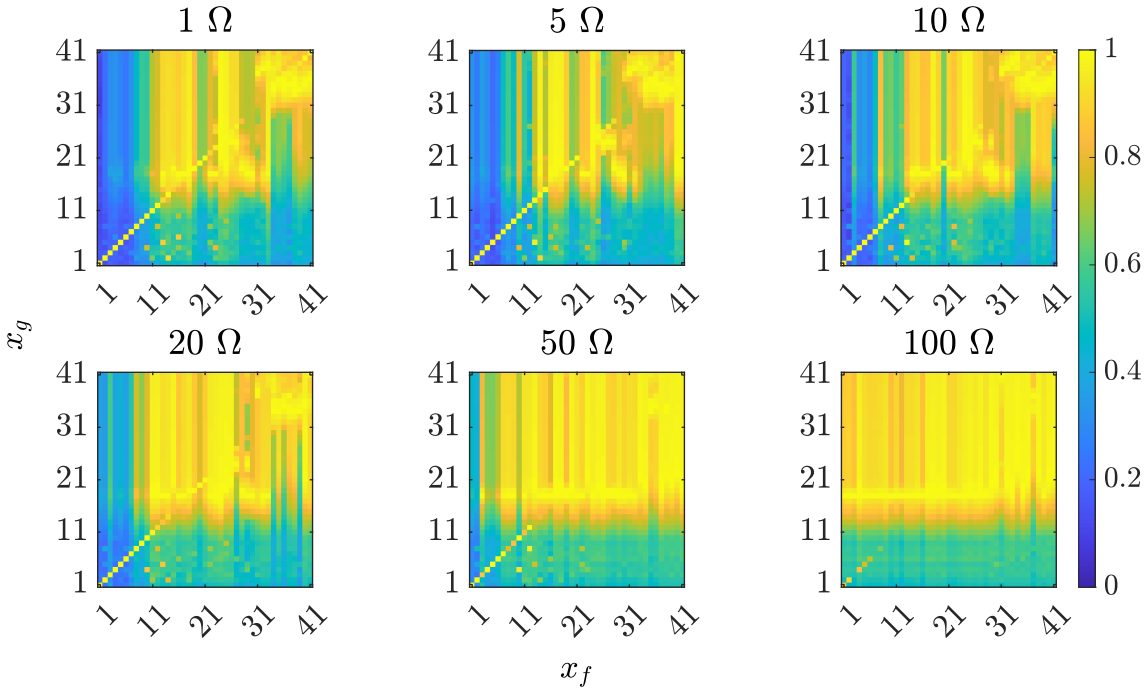

Source: Author

Figure 160 – Results by $\mathcal{E}_i(x_g)$ for three-phase-to-ground faults with the cut-off frequency of 1 kHz

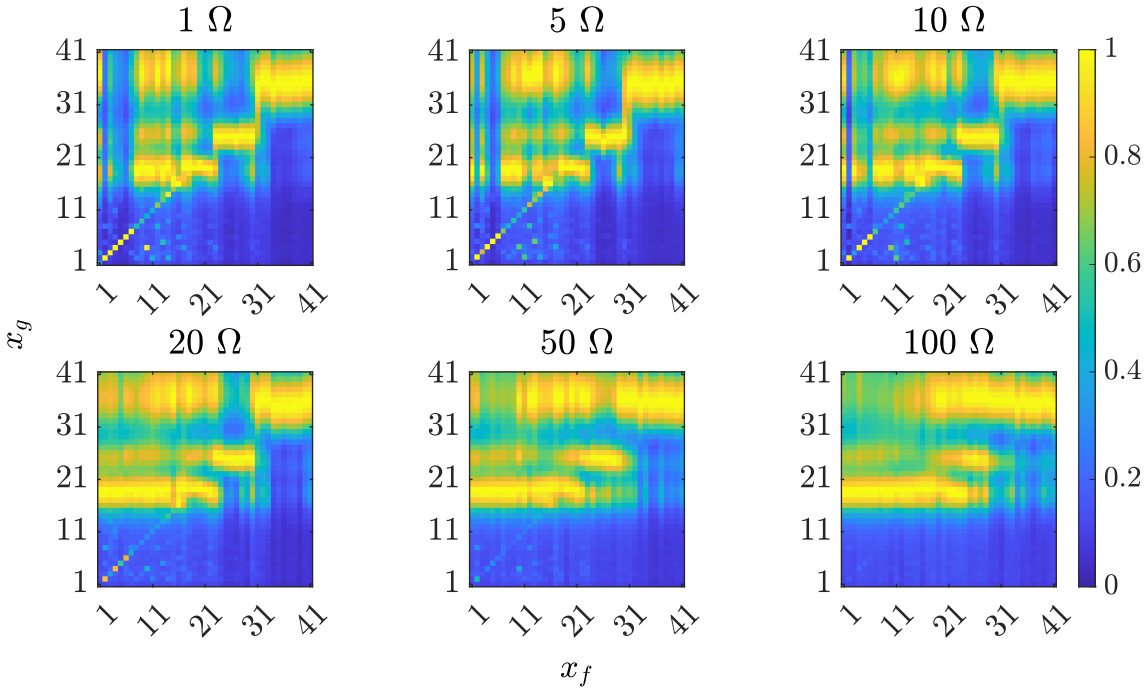

Source: Author

Figure 161 – Results by $\mathcal{P}_i(x_g)$ for three-phase-to-ground faults with the cut-off frequency of 3 kHz

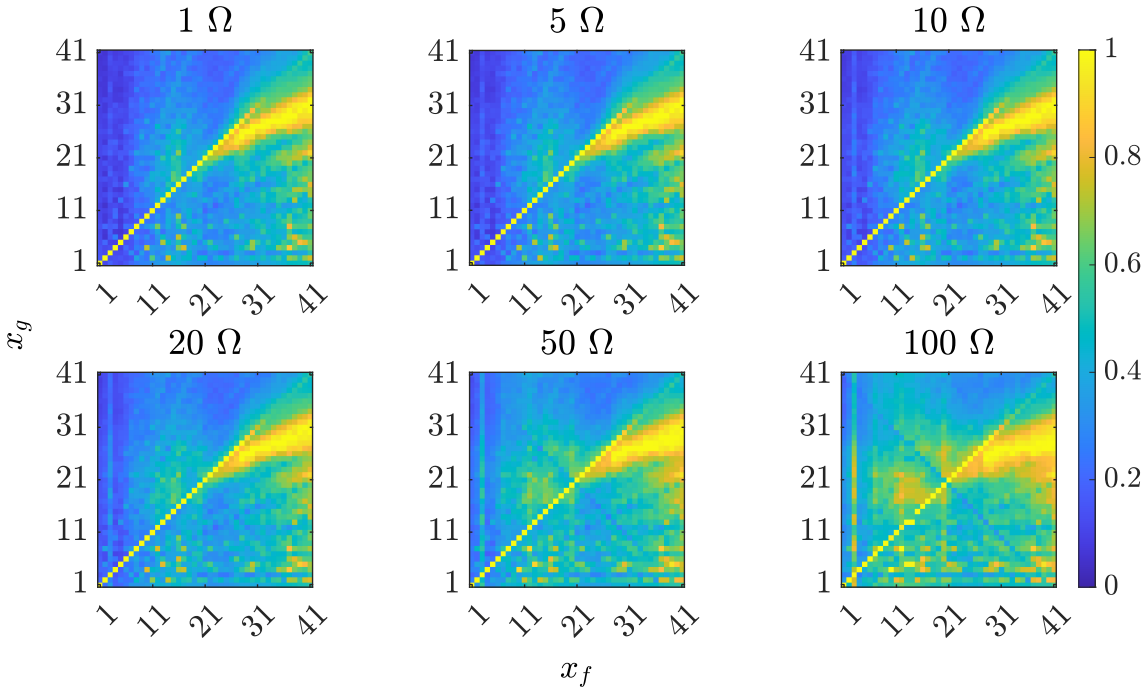

Source: Author

Figure 162 – Results by $\mathcal{E}_i(x_g)$ for three-phase-to-ground faults with the cut-off frequency of 3 kHz

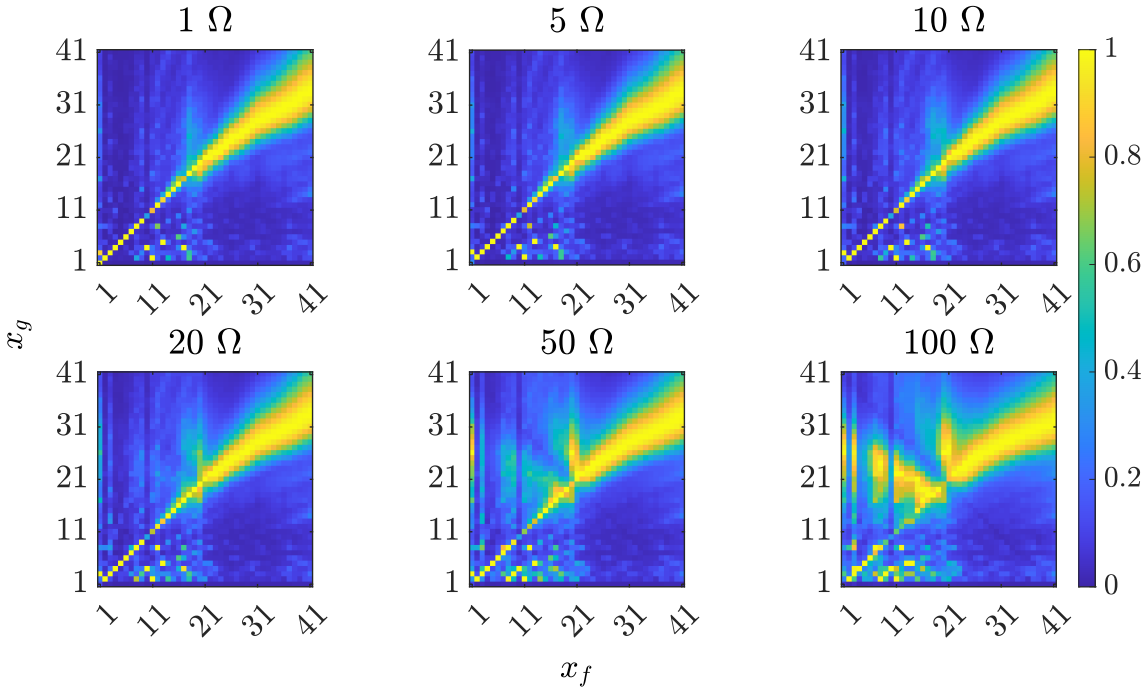

Source: Author

Figure 163 – Results by $\mathcal{P}_i(x_g)$ for three-phase-to-ground faults with the cut-off frequency of 5 kHz

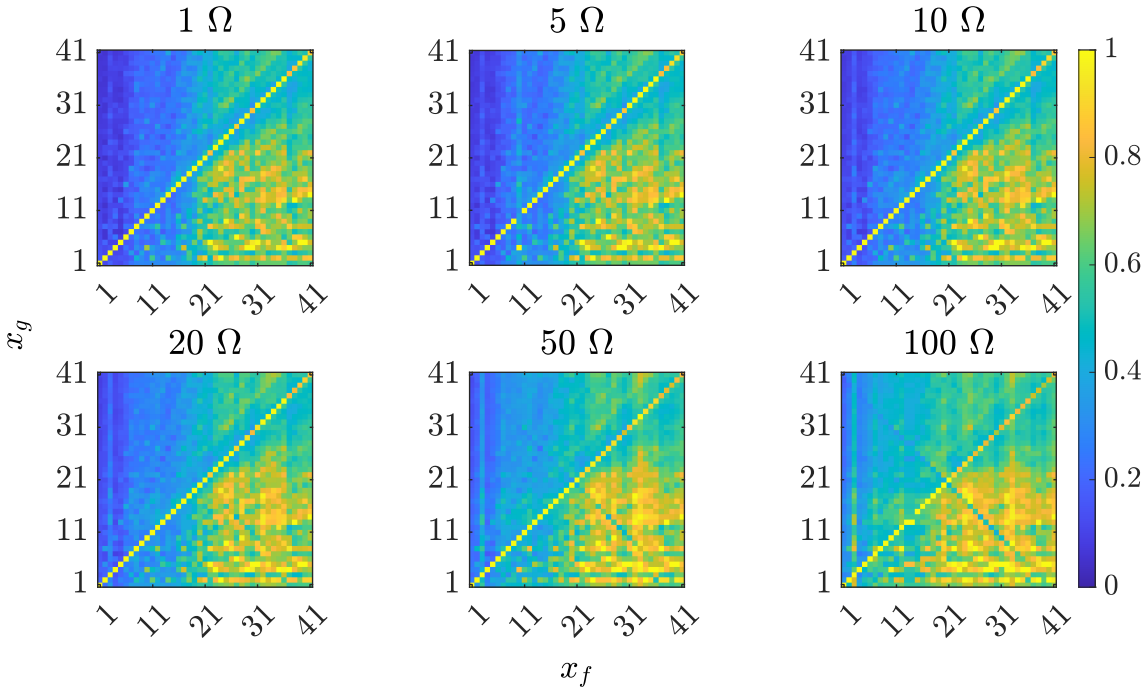

Source: Author

Figure 164 – Results by $\mathcal{E}_i(x_g)$ for three-phase-to-ground faults with the cut-off frequency of 5 kHz

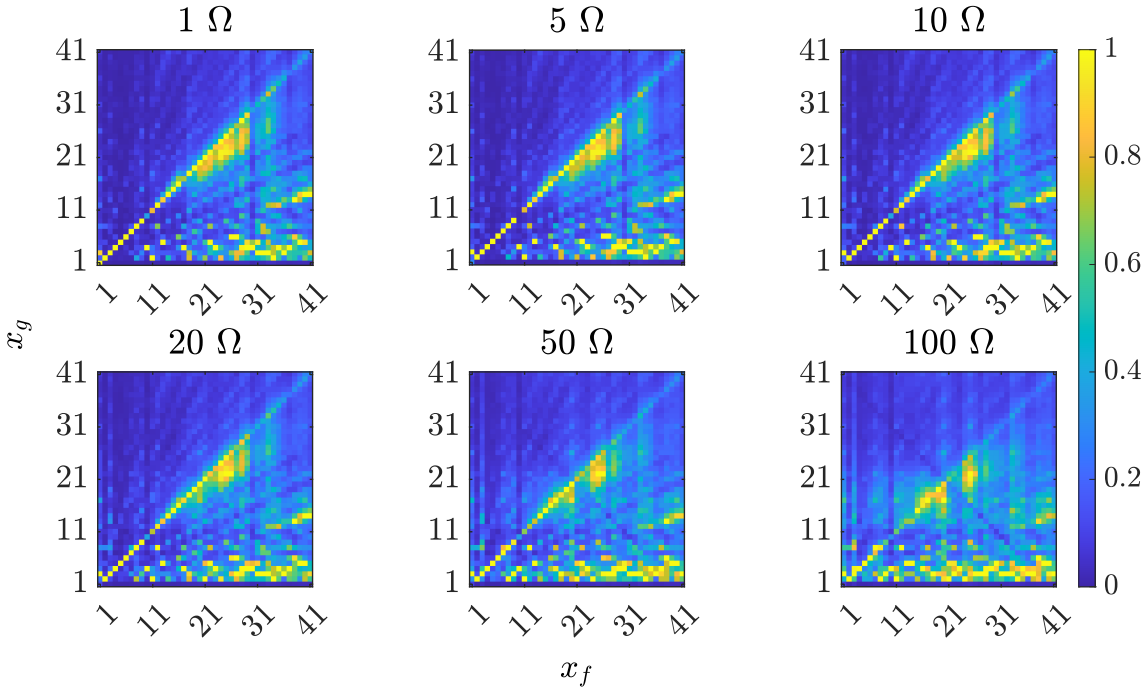

Source: Author

Figure 165 – Results by $\mathcal{P}_i(x_g)$ for three-phase-to-ground faults with the cut-off frequency of 7 kHz

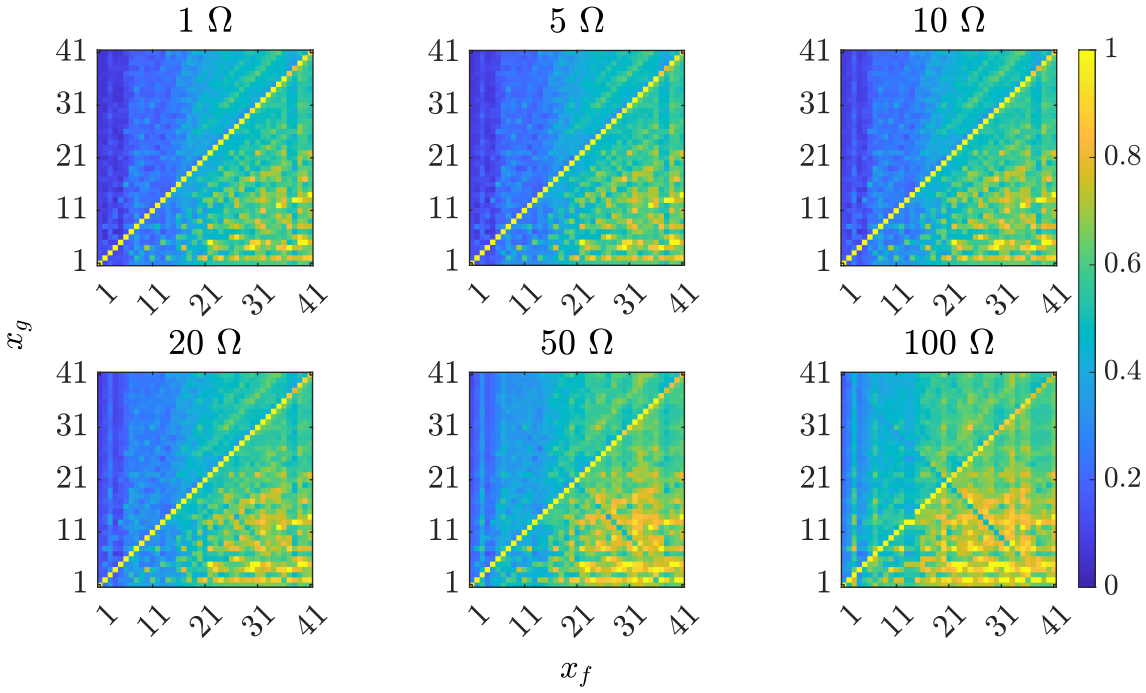

Source: Author

Figure 166 – Results by $\mathcal{E}_i(x_g)$ for three-phase-to-ground faults with the cut-off frequency of 7 kHz

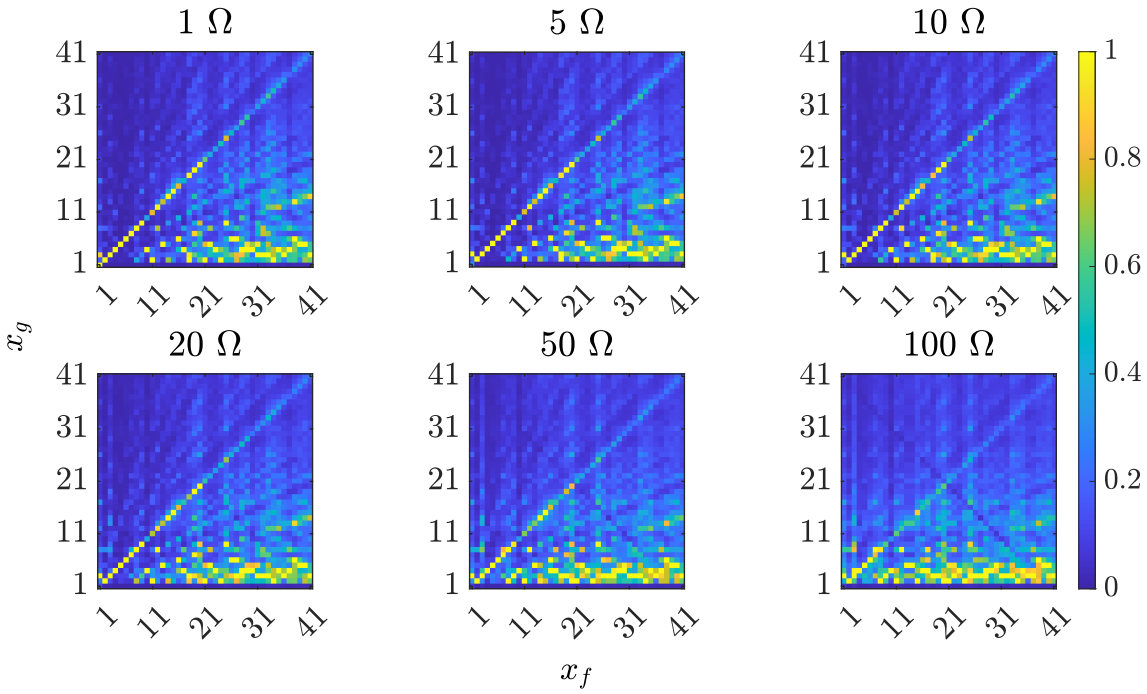

Source: Author

Figure 167 – Results by $\mathcal{P}_i(x_g)$ for three-phase-to-ground faults with the cut-off frequency of 9 kHz

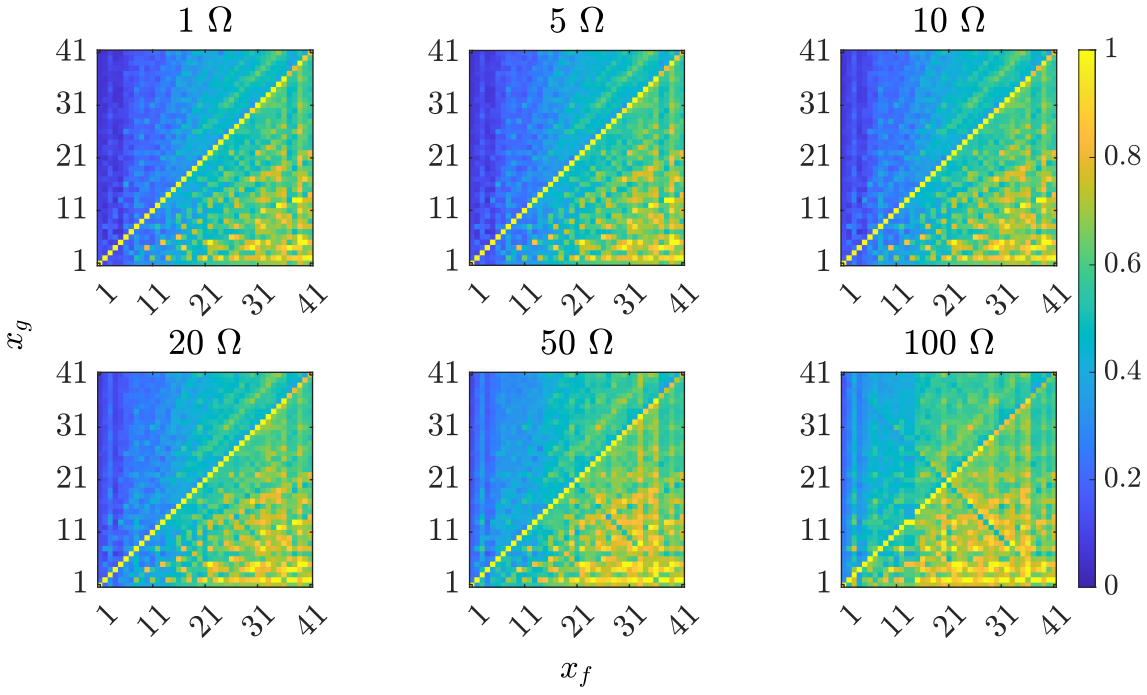

Source: Author

Figure 168 – Results by $\mathcal{E}_i(x_g)$ for three-phase-to-ground faults with the cut-off frequency of 9 kHz

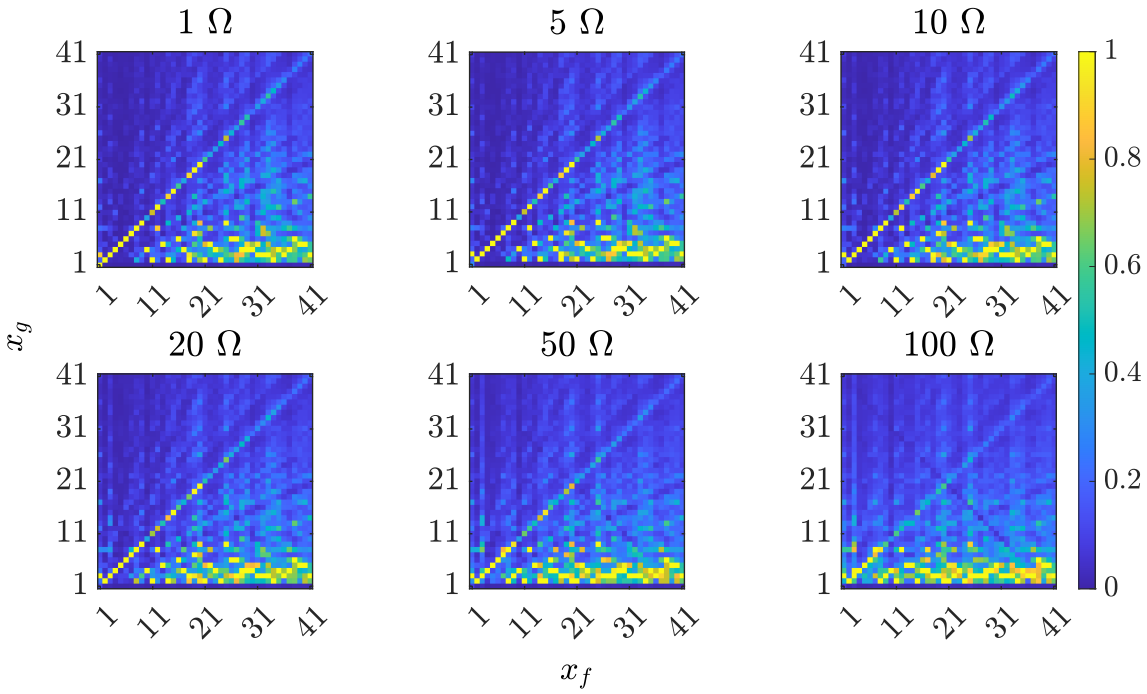

Source: Author

estimated fault locations downstream of the farthest correct one deviated from the main diagonal and some fell at points near the probe end of the system. The same also occurs with the filtering at 3 kHz to 9 kHz. The deviated estimations in some cases were virtually given in more than one point of the network section for the same actual fault location, with both criteria. Also, the main diagonal is noticeable in many cases even though the fault-location estimation was not correct for many points given the secondary picks of $\mathcal{P}_i(x_g)$ and $\mathcal{E}_i(x_g)$.

APPENDIX F RELATED PUBLICATIONS BY THE THESIS'S AUTHOR

Part of the research by the author's thesis related to the studies here happened to be published as conference articles, which are listed below. The studies in (DA COSTA; DA SILVA GAZZANA; LEBORGNE, 2021) were shown improved and extended in the present thesis. The studies in (DA COSTA *et al.*, 2020) and (DA COSTA; GAZZANA; LEBORGNE, 2022) were not covered here.

- (DA COSTA *et al.*, 2020) – L. A. da Costa, D. S. Gazzana, R. C. Leborgne and D. W. P. Thomas, "Incipient Fault Location in Underground Distribution Networks Using Electromagnetic Time Reversal," 2020 IEEE International Conference on Environment and Electrical Engineering and 2020 IEEE Industrial and Commercial Power Systems Europe (EEEIC / I&CPS Europe), Madrid, Spain, 2020, pp. 1-6, doi: 10.1109/EEEIC/ICPSEurope49358.2020.9160622.

- (DA COSTA; DA SILVA GAZZANA; LEBORGNE, 2021) – L. A. Da Costa, D. Da Silva Gazzana and R. C. Leborgne, "Fault Location on Point-to-Point HVDC Transmission System by the Electromagnetic Time-Reversal-Based Method," 2021 IEEE International Conference on Environment and Electrical Engineering and 2021 IEEE Industrial and Commercial Power Systems Europe (EEEIC / I&CPS Europe), Bari, Italy, 2021, pp. 1-6, doi: 10.1109/EEEIC/ICPSEurope51590.2021.9584483.

- (DA COSTA; GAZZANA; LEBORGNE, 2022) – L. A. da Costa, D. S. Gazzana and R. C. Leborgne, "Fault Location by the Electromagnetic-Time Reversal Method Using the Fault Clearing Transients," 2022 IEEE International Conference on Environment and Electrical Engineering and 2022 IEEE Industrial and Commercial Power Systems Europe (EEEIC / I&CPS Europe), Prague, Czech Republic, 2022, pp. 1-6, doi: 10.1109/EEEIC/ICPSEurope54979.2022.9854780.